# Appendix H:

## Report

Project no. **INCO-CT-2006-026283-OPSA**

Project title:
**Centre of Excellence for Optical Spectroscopy Applications in Physics, Material Science and Environmental Protection**

# Copies of papers published in the scientific journals within the whole duration of the OPSA Project

# List of papers published in scientific journals:

**1. Z. V. Popović, Z. Dohčević-Mitrović, M. J. Konstantinović, M. Šćepanović**
*Raman scattering characterization of nano-powders and nano-wires (rods)*
Journal of Raman Spectroscopy **38**, 750 (2007).

**2. Z.V. Popović, A. Milutinović, N. Romčević**
*Spin-assisted photoluminescence of polycrystalline* $\alpha$*-MnSe*
J. Luminescence **128** (2008) 142-146.

**3. Z. V. Popović, Z. Dohčević-Mitrović, A. Cros and A. Cantarero**
*Raman scattering study of the anharmonic effects in* $CeO_2$ *nanocrystals*
Journal of Physics: Condensed Mater**19** (2007) 496209 (9pp)

**4. R. Kostić, S. Aškrabić, Z. Dohčević-Mitrović, Z.V. Popović**
*Low-frequency Raman Scattering from* $CeO_2$ *Nanoparticles*
Applied Physics A**90**, 679-83 (2008).

**5. Z. Dohčević-Mitrović, M. Radović, M. Šćepanović, M. Grujić-Brojčin, Z. V. Popović, B. Matović and S. Bošković**
*Temperature-dependent Raman study of* $Ce_{0.75}Nd_{0.25}O_{2-\delta}$ *nanocrystals*
Applied Physics Letters **91** 203118 (2007).

**6. M. Radović, Z. Dohčević-Mitrović, M. Šćepanović, M. Grujić-Brojčin, B. Matović, S. Bošković, Z. V. Popović,**
*Raman study of Ba-doped ceria nanopowders*
Science of Sintering **39** (2007) 281-286.

**7. M. Šćepanović, M. Grujić-Brojčin, Z. Dohčević-Mitrović, K. Vojisavljevic, T Sreckovic, Z. V. Popović**
*The effects of Nonstoichiometry on optical properties of oxide nanopowders*
Acta Physica Polonica A, **112** (2007) 1013.

**8. S. Aškrabić, R. Kostić, Z. Dohčević-Mitrović, Z.V. Popović**
*Raman scattering from low-frequency phonons confined in* $CeO_2$ *nanoparticles*
Journal of Physics: Conference Series **92** (2007) 012042.

**9. Z. Dohčević-Mitrović, Z.V. Popović and M. Šćepanović**
*Anharmonicity Effects in Nanocrystals Studied by Raman Scattering Spectroscopy*
Acta Physica Polonica **A116** (2009) 36

**10. M. Grujić-Brojčin, M.J. Šćepanović, Z.D. Dohcević-Mitrović and Z.V. Popović**
*Use of Phonon Confinement Model in Simulation of Raman Spectra of Nanostructured Materials*
Acta Physica Polonica **A116** (2009) 51

**11. R. Kostić**
*Raman Scattering from Acoustic Phonons Confined in Spherical Nanoparticles*
Acta Physica Polonica **A116** (2009) 62

**12. M. Radović, Z. Dohčević-Mitrović, N. Paunović, M. Šćepanović, B. Matović and Z.V. Popović** *Effect of* $Fe^{2+}$ *(*$Fe^{3+}$*) Doping on Structural Properties of* $CeO_2$ *Nanocrystals*
Acta Physica Polonica **A116** (2009) 84

**13. M. Šćepanović, S. Aškrabić, M. Grujić-Brojčin, A. Golubović, Z. Dohčević-Mitrović, A. Kremenović and Z.V. Popović**
*Low Frequency Raman Spectroscopy of Pure and La Doped* $TiO_2$ *Nanopowders Synthesized by Sol Gel Method*
Acta Physica Polonica **A116** (2009)99

**14. S. Askrabic, Z. D. Dohcevic-Mitrovic, M. Radovic, M. Scepanovic, Z. V. Popovic,**
*Phonon-phonon interactions in* $Ce_{0.85}Gd_{0.15}O_{2-\delta}$ *nanocrystals studied by Raman spectroscopy*
JOURNAL OF RAMAN SPECTROSCOPY **40** (2009): 650-655

**15. M. J. Šcepanovic, M. Grujic-Brojcin, Z. D. Dohcevic-Mitrovic and Z. V. Popovic**
*Characterization of Anatase TiO2 Nanopowder by Variable-Temperature Raman Spectroscopy*
Science of Sintering, **41** (2009) 67-73

**16. A. Golubovic, M. Šcepanovic, A. Kremenevic, S. Aškrabic, V. Berec, Z. Dohcevic-Mitrovic, and Z. V. Popovic**
*Raman study of the variation in anatase structure of TiO2 nanopowders due to changes of sol-gel synthesis conditions*
J. Sol-Gel Sci Technol **49** (2009) 311-319

**17. M. Šćepanović, S. Aškrabić, V. Berec, A. Golubović, Z. Dohcević-Mitrović, A. Kremenović and Z.V. Popović**
*Characterization of La-Doped* $TiO_2$ *Nanopowders by Raman Spectroscopy*
Acta Physica Polonica A **115** (2009) 771.

JOURNAL OF RAMAN SPECTROSCOPY
*J. Raman Spectrosc.* 2007; **38**: 750–755
DOI: 10.1002/jrs.1696

JRS

# Raman scattering characterization of nanopowders and nanowires (rods)

**Z. V. Popović,[1]* Z. Dohčević-Mitrović,[1] M. J. Konstantinović[1,2] and M. Šćepanović[1]**

[1] Center for Solid State Physics and New Materials, Institute of Physics, 11080 Belgrade, Pregrevica 118, Serbia
[2] SCK CEN, Studiecentrum voor Kernenergie, Boeretang 200, B-2400 Mol, Belgium

Received 1 August 2006; Accepted 11 December 2006

**We study nanograin size confinement effects, the effect of the increase of local temperature and strain, and substitutional and nonstoichiometry effects on the Raman spectra in Ce(Ba,Nd,Gd)$O_2$ nanopowders obtained by self-propagating, room-temperature synthesis, and silicon nanowires obtained by the electrochemical etching process. The local temperature was monitored by measuring the Stokes/anti-Stokes peak ratio. We found large wavenumber shifts, up to 10 (30) $cm^{-1}$, and broadenings, up to 40 (20) $cm^{-1}$, of the first-order Raman-active modes of Ce(M)$O_2$ (n-Si), which we attribute to confinement and strain effects (laser heating). The phonon softening and phonon linewidth are calculated using a phenomenological model, which takes into account disorder effects through the breakdown of the k = 0 Raman-scattering selection rule, and also anharmonicity, which is incorporated through the three- and four-phonon anharmonic processes. Very good agreement with experimental data is obtained for the calculated spectra of $CeO_2$ with nanograin sizes of about 7 nm, taking into account particle size distribution, as well as an increase in the anisotropy constants with respect to those of bulk materials.**

**KEYWORDS:** Raman scattering; $CeO_2$-doped nanopowders; Si nanowires (rods)

## INTRODUCTION

Raman spectroscopy is a powerful tool for characterization of nanosized materials and structures. This technique is widely used for the study of phonon confinement effects, the effect of the increase of local temperature, strain and substitutional effects, porosity and nonstoichiometry in different types of nanomaterials. Recent progress in the use of Raman spectroscopy for nanomaterial characterization is summarized in Ref. 1. We shall demonstrate here how the Raman spectroscopic method can be used for the characterization of nanopowdered oxides like $CeO_2$ and silicon nanowires (pillars). The large phonon softening and broadening observed in these nanomaterials are compared with calculated spectra obtained from the phenomenological model that takes into account disorder effects through the breakdown of the $\mathbf{k} = 0$ Raman-scattering selection rule, and also anharmonicity, which is incorporated through the three- and four-phonon processes. This analysis clearly shows that the strong shift and broadening of the Raman peaks are dominated by the anharmonic effects, while confinement plays a secondary role.

## EXPERIMENTAL

Self-propagating, room-temperature synthesis was used in order to produce ceria and ceria-doped nanopowders with Ba, Gd and Nd of high quality with a narrow size particle distribution in the nanometer range. The detailed powder preparation procedure is already described in our recent publications.[2,3] The silicon samples used in this investigation are made of an array of silicon nanoclusters obtained by low-energy cluster beam deposition[4] and of nanowires (nanopillars, nanorods) obtained by the electrochemical etching process.[5] Figure 1(a) shows a scanning electron micrograph (SEM) of a typical part of the Si nanowire sample, while Fig. 1(b) presents an SEM image of $Ce_{0.75}Nd_{0.25}O_2$ powder sample. Nanowires are vertically aligned with a typical length of about 10 μm and a diameter of about 50 to 500 nm. Some nanorods are found to be detached from the nonreacted part of the silicon crystal, lying in the horizontal position on top of the sample.

Micro-Raman spectra were taken with excitation from the 514.5 nm line of an argon ion laser, using variable laser power

---

*Correspondence to: Z. V. Popović, Center for Solid State Physics and New Materials, Institute of Physics, 11080 Belgrade, Pregrevica 118, Serbia. E-mail: zoran.popovic@phy.bg.ac.yu

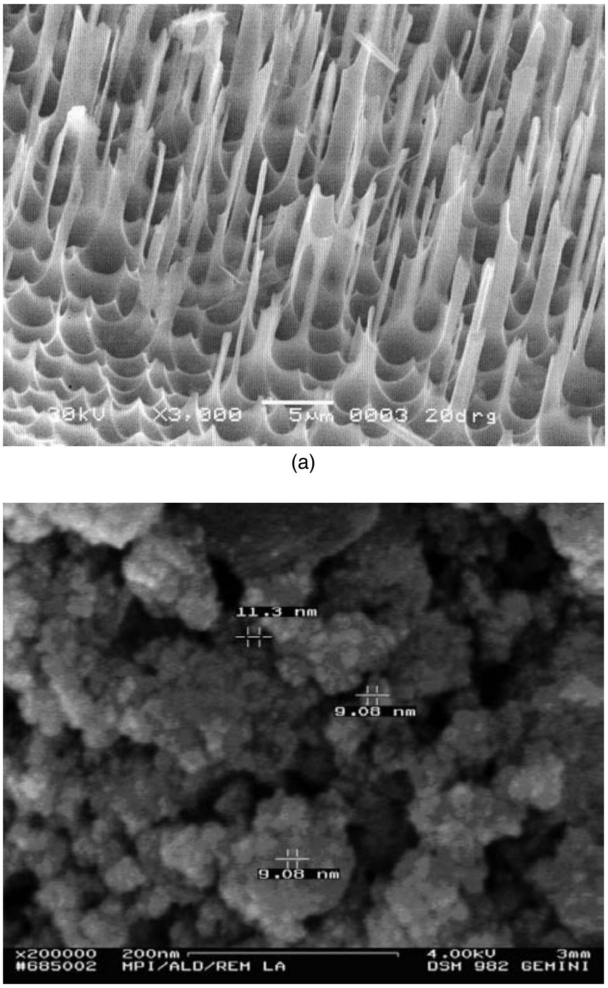

(a)

(b)

**Figure 1.** SEM picture of the Si nanowires (a) and $Ce_{0.75}Nd_{0.25}O_2$ sample (b).

at the sample surface from 10 to 500 mW. The Raman spectra were measured in the backscattering configuration and analyzed using a JY T64000 and DILOR triple spectrometer with a liquid-nitrogen-cooled charge-coupled device detector. For high-temperature measurements, we used a Linkam TS 1500 microscope heating stage.

## RESULTS AND DISCUSSION

The *phonon confinement model* is used to compare experimental data with theoretical predictions in nanomaterials. According to this model, owing to the relaxation of the $q \approx 0$ selection rule for finite-sized crystals, the Raman intensity $I(\omega)$ is calculated over the whole Brillouin zone (assumed to be spherical) by the following relation:[2,6]

$$I(\omega) = \sum_{1}^{3} \int_{0}^{\infty} \rho(L) dL \times \int_{BZ} \frac{\exp(-q^2\xi^2)}{[\omega - (\omega_i(q) + \Delta\omega_i(q, L))]^2 + [\Gamma_0/2]^2} d^3q \quad (1)$$

where $\rho(L)$ is the particle size distribution, $q$ is the wave vector expressed in units of $\pi/a$ ($a$ is the effective unit cell parameter), $L$ is the grain size, and $\Gamma_0$ is the intrinsic linewidth of the Raman mode in the bulk crystal. The Gaussian correlation length, $\xi$, is an adjustable parameter depending on the strength of the confinement in different nanomaterials. This parameter ranges from $\xi = L/2\sqrt{2}$ for the Richter confinement model[7] to $\xi = L/4\pi$ in the Campbell and Fauchet model[8] where $L$ is the diameter of the spherical particle. A more detailed analysis between the correlation length and grain size is presented in the work of Kosacki *et al.*[9] Note that inhomogeneous strain (change in lattice parameter with particle size) is introduced into the model through term $\Delta\omega_i(q, L)$ in Eqn (1) to explain properly the shift and mode broadening, while the sum is taken over the allowed Raman modes (in a case of $CeO_2$, $i = 3$, because the $F_{2g}$ mode is triply degenerate).

The influence of anharmonic effects on the Raman spectra of the materials under consideration is taken into account via three- and four-phonon anharmonic processes.[10]

$$\omega(k, T) = \omega_0 + A\left[1 + \frac{2}{e^{\hbar\omega/2k_BT} - 1}\right] + B\left[1 + \frac{3}{e^{\hbar\omega/3k_BT} - 1} + \frac{3}{(e^{\hbar\omega/3k_BT} - 1)^2}\right] \quad (2)$$

The phonon linewidth is given by

$$\Gamma(T) = C\left[1 + \frac{2}{e^{\hbar\omega/2k_BT} - 1}\right] + D\left[1 + \frac{3}{e^{\hbar\omega/3k_BT} - 1} + \frac{3}{(e^{\hbar\omega/3k_BT} - 1)^2}\right] \quad (3)$$

where $A$, $B$, $C$ and $D$ are anharmonic constants.

### $CeO_2$

Ultrafine ceria ($CeO_2$) powder has attracted considerable research interest as a material for solid oxide fuel cells that can operate at intermediate temperatures (500–700 °C). The Raman spectrum of the $CeO_2$ powder sample is presented in Fig. 2 together with Raman spectra of the polycrystalline sample and different spectra obtained by calculations.[2] Phonon confinement, strain, size distribution, defects and variations in phonon relaxation with particle size can contribute to the changes in the Raman peak position and linewidth of the 465 $cm^{-1}$ ($F_{2g}$) symmetry mode. At first we have used Cambell's confinement model (stronger confinement function than in Richter's model) to explain the evolution of the Raman lineshape (wavenumber shift, broadening, asymmetry) in $CeO_{2-\delta}$ nanopowders. However, this simple confinement model could not give a good fit for experimental spectra of $CeO_{2-\delta}$, as we have demonstrated in Fig. 2. The lattice constant of $CeO_{2-\delta}$ nanoparticles has been found to be larger than the corresponding bulk value.[2] The lattice relaxation with decreasing particle size, due to the

DOI: 10.1002/jrs

microstrain effects is also found in various nanocrystalline materials. Having in mind the lattice parameter change in our nanostructured samples, we used a model proposed by Spanier *et al.*[11], which, in the first approximation, considered the strain to be uniform within each particle. This average strain produces changes in the lattice parameter and affects the Raman peak position. The Raman mode for the fluorite structure, centered at $\omega_i$, shifts by $\Delta\omega_i = -3\gamma_i(q)\omega_i(q)[\Delta a/a_0]$, where $\gamma_i$ is a mode Grüneisen parameter and $\Delta a$ is the measured change of lattice parameter with respect to the bulk value $a_0$. Nevertheless, the model based on the average strain effect did not give a good fit of the Raman spectra of our $CeO_{2-\delta}$ nanopowder samples.

According to the comprehensive model developed by Spanier *et al.*[11] for the Raman spectra of ceria nanoparticles, the dispersion in particle size must be taken into account. The size distribution produces a dispersion of the lattice parameter and appearance of inhomogeneous strain. The combined effects of inhomogeneous strain and phonon confinement can produce an even larger shift and asymmetric broadening of the Raman modes. To explain properly the higher shift to lower wavenumbers and the width ($\sim$40 $cm^{-1}$) of the $F_{2g}$ mode observed in our ceria sample than those in Ref. 11, we included the effect of inhomogeneous strain using a Gaussian size-distribution function centered at the mean grain size $L_0$ with a width $w = 0.52L_0$, based on the work of Santos and Torriani.[12] The Raman line position is determined essentially by the mean grain size, while the asymmetry in the Raman mode is caused by the dispersion in grain sizes. The resulting Raman intensity now can be expressed as double integral, Eqn (1), where the sum is taken over the three allowed Raman modes with $\omega_i(q = 0) = 465\ cm^{-1}$. The natural full width of the $F_{2g}$ mode is $\Gamma_0 = 10\ cm^{-1}$, while the average particle diameter value is taken to be $L_0 = 7$ nm, which perfectly matches the $F_{2g}$ mode position. The phonon dispersion of the $F_{2g}$ mode, $\omega_i(q)$, is represented by parabolic fits to Nakajima dispersion curves[13] for $CeO_2$. To simulate the shift and linewidth of the $F_{2g}$ mode in $CeO_2$ nanopowders, a higher degree of phonon confinement was applied, i.e. $\xi \sim L/8\sqrt{5}$. The calculated Raman spectrum (solid line) for ceria nanopowder together with experimental data (dotted line) is presented in Fig. 2. As can be seen from Fig. 2, we achieved a very good agreement between the experimental and theoretical curves. Therefore, we concluded that the peak position and the linewidth of our $CeO_2$ nanopowder can be very well explained by combined effect of phonon confinement and inhomogenous strain using a higher degree of phonon confinement, while Spanier *et al.*[11] explained sufficiently well only the linewidth of the $F_{2g}$ mode but not its position using the same boundary condition for the Gaussian localization function. The simulated Raman spectra based on Cambell's and Spanier's models for the averaged strain are also presented in Fig. 2 for comparison. The additional Raman peak around 595 $cm^{-1}$ is already seen in pure ceria nanopowders[14] and is attributed to the defect spaces, which include oxygen vacancies.[15,16] This intrinsic $O^{2-}$ vacancies originate from the nonstoichiometry of nanocrystalline ceria powders. The relatively weak intensity of this mode points towards the presence of relatively few vacancies in our sample. Therefore, we supposed that peak position and linewidth changes owing to vacancies are not very significant.

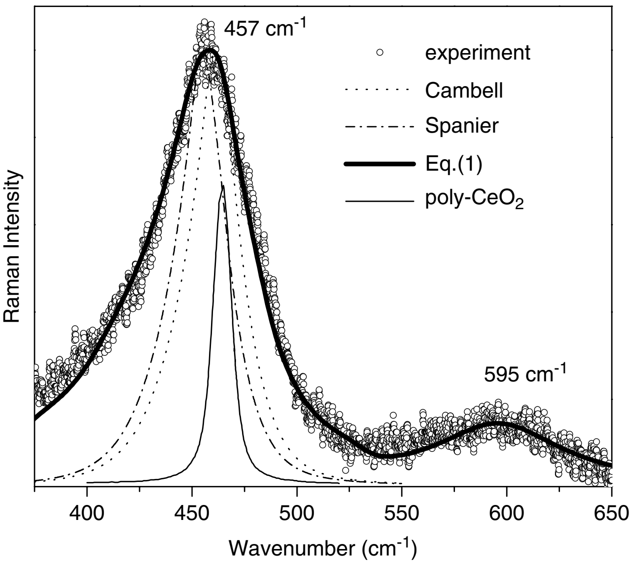

**Figure 2.** First-order Raman spectrum of $CeO_2$ nanopowder (open circles) and the fitted spectrum (full line) using the combined effect of inhomogeneous strain and confinement together with simulated spectra based on Cambell's and Spanier's models for the averaged strain. The peak, at $\sim$595 $cm^{-1}$, is associated with the intrinsic oxygen vacancies in ceria nanopowders.

In order to reduce the nonstoichiometry and inhomogeneous strain, we heated our $CeO_{2-\delta}$ sample up to 1100 °C. Raman spectra measured upon heating and cooling show remarkable differences, which comprise wavenumber, linewidth and lineshape differences (Fig. 3).

During the heating, we found that Raman mode wavenumber of nanosized $CeO_2$ sample continuously decreased (empty squares in Fig. 3), and this part of our work is consistent with that of Spanier *et al.*[11] In addition, the line shape became less asymmetrical as the temperature increased, and at about 900 °C it became totally symmetric. Upon cooling, the energy of the $F_{2g}$ mode increases (full squares in Fig. 3), reaching the value of 464.3 $cm^{-1}$ at room temperature. The linewidth (FWHM) decreases as the temperature decreases, down to 9 $cm^{-1}$ at room temperature. These values are very close to the corresponding values of $CeO_2$ single crystals,[6] what leads us to conclude that our sample transforms from the nano- into the polycrystalline state by the above-mentioned heat treatment. Furthermore, the temperature dependence of the mode energy and broadening corresponds well with those of the calculated spectra

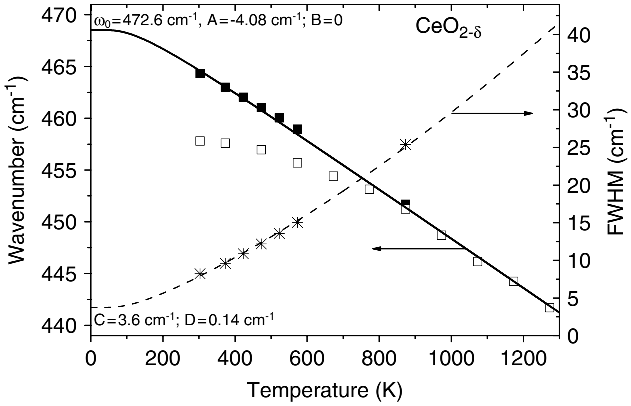

**Figure 3.** Energy (squares) and broadening (asterisks) of the $F_{2g}$ Raman mode in $CeO_2$ *vs* temperature. Lines are calculated spectra using Eqn (2) (solid line) and Eqn (3) (dashed line) with the parameters indicated in the figure.

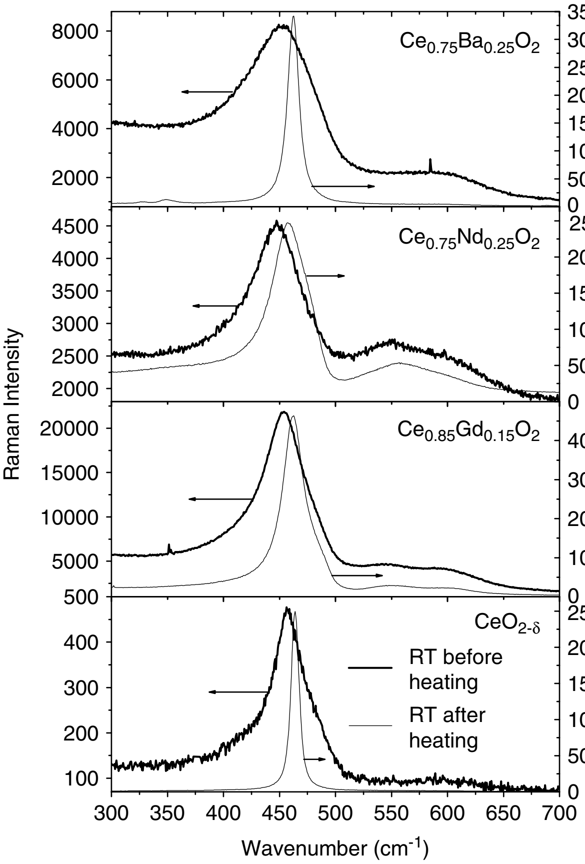

**Figure 4.** Raman spectra of cerium oxide-doped samples at room temperature before and after annealing at 1000 °C.

(solid and dashed lines) based only on anharmonic effects (Eqns (2) and (3)), while the additional Raman mode at 595 cm$^{-1}$ disappears. This means that all 'nano' effects such as nonstoichiometry, inhomogeneous strain, structure defects, etc. are removed by the heat treatment.

Figure 4 shows Raman spectra of $CeO_{2-\delta}$ and Ce (Nd, Gd, Ba)$O_{2-\delta}$ samples at room temperature before and after the heat treatment. It is interesting to note that Raman modes of only the $CeO_2$ and Ce(Ba)$O_2$ samples become symmetric after annealing and are almost at the same position as in the bulk sample. The Raman mode in the Nd-doped sample stays asymmetric, although the mode frequency shifts to higher energies, while linewidth becomes smaller (Fig. 5). Besides the $F_{2g}$ mode at about 450 cm$^{-1}$, the additional mode at about 550 cm$^{-1}$ becomes very intense on cooling. We attribute this mode to the presence of additional $O^{2-}$ vacancies introduced into the ceria lattice by the substitution of $Ce^{4+}$ ions with $Nd^{3+}$ ions in order to keep charge neutrality.[3]

The most interesting case is that of $Ce_{0.85}Gd_{0.15}O_2$. After annealing, the Raman mode becomes narrow but asymmetrical (Fig. 4). By deconvolution using the Lorentzian line profile technique, we have found that this mode consists of two modes with wavenumbers 464 and 487 cm$^{-1}$. Because of that, we paid special attention to the $CeO_2$–$Gd_2O_3$ system. In Fig. 6(a), we show the X-ray diffraction (XRD) patterns of three different samples of the $CeO_2$–$Gd_2O_3$ system. According to the experimental XRD data, there is no difference in the pattern for 20 and 40% of $Gd_2O_3$. For 80% of $Gd_2O_3$ some new, very low intensity lines appear (indicated by asterisk in Fig. 6). In Fig. 6(b), we present the calculated XRD spectra for pure $CeO_2$ and $Gd_2O_3$. As can be seen from Fig. 6(b), the diffraction peaks of $CeO_2$ and $Gd_2O_3$ coincide in many cases. As diffraction peaks whose positions differ have not been registered experimentally, the XRD analysis seems to be an inadequate technique for the investigation of the $CeO_2$–$Gd_2O_3$ system. Contrary to that, the Raman spectra of these samples show clear evidence of phase separation even in the lowest $Gd_2O_3$ concentration (20%) case (Fig. 7): namely, the Raman peak of $CeO_2$, which appears at about 464 cm$^{-1}$ in the polycrystalline sample, can be observed in the 20% $Gd_2O_3$ sample at the same wavenumber. Besides this line, one additional mode can easily be resolved at about 487 cm$^{-1}$, which belongs to $Gd_2O_3$. An increase of $Gd_2O_3$ concentration leads to an intensity decrease/increase of $CeO_2$ ($Gd_2O_3$) Raman mode.

## Si nanoclusters and rods

The typical Stokes and anti-Stokes Raman spectra of Si nanowires measured with various laser powers are shown in Fig. 8. The results are fully reproducible whenever the laser power is increased or decreased. With increasing laser power, there is a strong red shift of the first-order phonon mode at 520 cm$^{-1}$, which is accompanied by a substantial broadening. The softening and broadening are large, up to about 30 cm$^{-1}$ and 25 cm$^{-1}$, respectively, for the highest used laser power of about 500 mW. It can also be seen from Fig. 8 that the intensity ratio between the Stokes and anti-Stokes part of the spectrum decreases as the laser power increases. This implies that a dramatic change in the local temperature

DOI: 10.1002/jrs

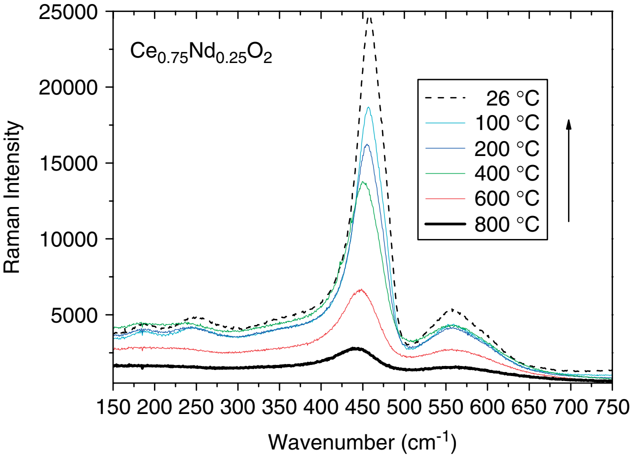

**Figure 5.** Raman spectra of $Ce_{0.75}Nd_{0.25}O_2$ obtained on cooling the sample from 800 °C down to room temperature. This figure is available in colour online at www.interscience.wiley.com/journal/jrs.

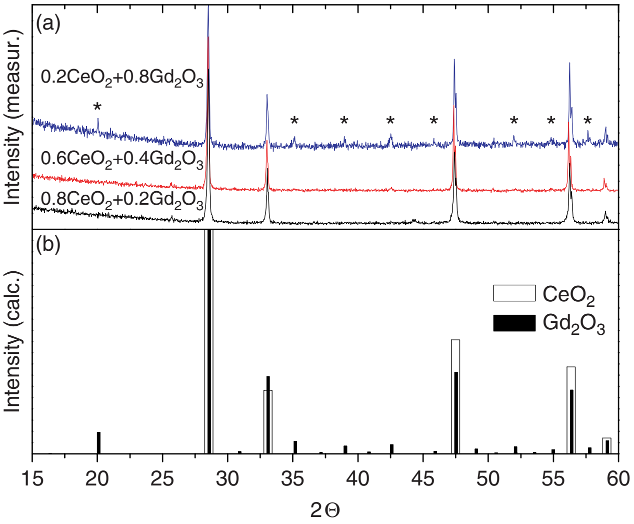

**Figure 6.** (a) XRD patterns of different samples in $CeO_2-Gd_2O_3$ system. (b) Calculated XRD patterns for pure $CeO_2$ and $Gd_2O_3$. This figure is available in colour online at www.interscience.wiley.com/journal/jrs.

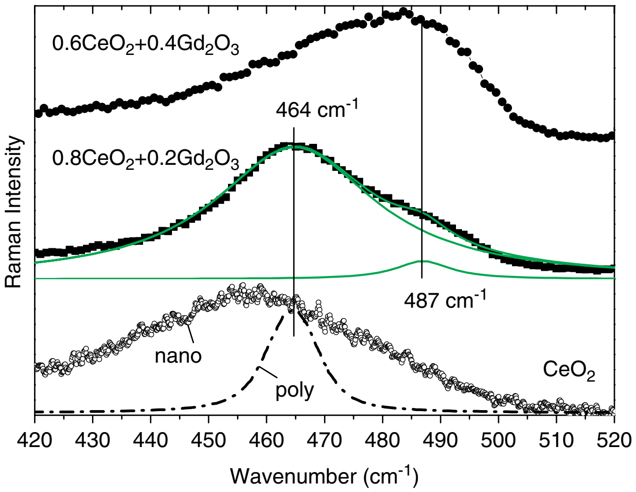

**Figure 7.** Raman spectra of $CeO_2$ polycrystalline and nanosized samples, together with the Raman spectra of 20 and 40% $Gd_2O_3$ samples. This figure is available in colour online at www.interscience.wiley.com/journal/jrs.

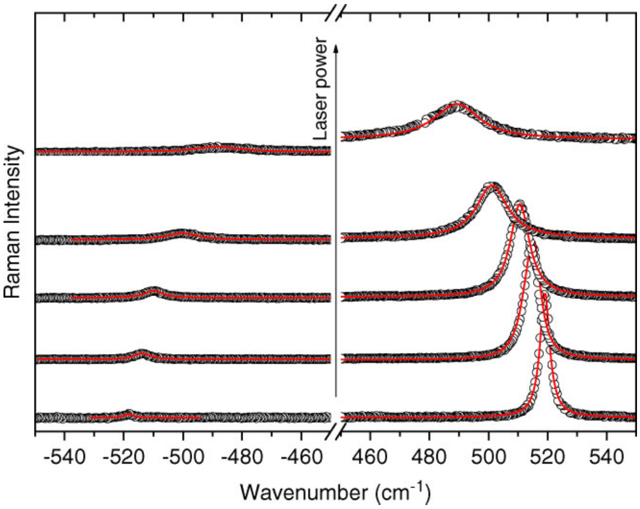

**Figure 8.** The Stokes and anti-Stokes Raman spectra of silicon nanowires measured with different laser power densities. This figure is available in colour online at www.interscience.wiley.com/journal/jrs.

of the nanowires takes place during the measurements, as expected in micro-Raman experiments, in which the laser light is focused on a micrometer-size area. Another important effect directly related to the increase of the local temperature, concerns the phonon lineshapes. Our Raman spectra show that the phonon lineshapes are more or less symmetrical regardless the wavenumber shifts and the broadening, as shown in Fig. 8. This observation is in clear contradiction with the strong asymmetric lineshape expected in the case of quantum phonon confinement.[17]

A comparison between the calculated and measured Raman spectra is also shown in Fig. 8. The calculated curves are obtained by taking the Lorentzian lineshape, which includes the anharmonic effects via three- and four-phonon anharmonic processes (Eqns (2) and (3)). The agreement between the calculation and the experimental data is very good, showing that the shift and broadening arise mainly on account of the local laser heating effect. The temperature change induced by the local heating effect is estimated from the Stokes and anti-Stokes intensity ratio. The wavenumber shift and broadening of the 520 $cm^{-1}$ mode as a function of the temperature are presented in Fig. 9. Similar results are obtained in the case of silicon nanoclusters.[4] The main difference between the Raman

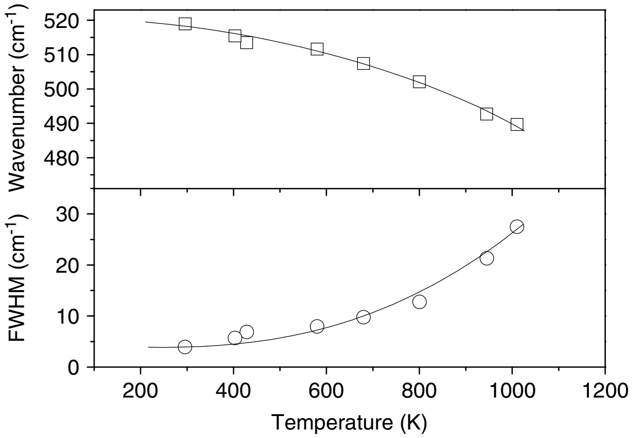

**Figure 9.** The energy and full width at half-maximum of the 520 cm$^{-1}$ mode as a function of temperature in the nanowire. The full lines are guides for the eye.

spectra of nanoclusters and nanowires is the intensity of the hump at the low-wavenumber side of the 520 cm$^{-1}$ peak. The fact that this feature is suppressed in nanowires in comparison to nanoclusters suggests that it might originate from the Raman scattering of amorphous silicon. This can be understood as a consequence of the difference between the preparation techniques. The silicon nanoclusters were produced by laser vaporization technique, which resulted in formation of nanoclusters on top of the amorphous film. On the other hand, the nanowires are produced starting from silicon crystalline material, so the amorphous signal is expected to be much smaller. This analysis clearly shows that the strong shift and broadening of the Raman peak are dominated by the anharmonic effects originating from laser heating, while confinement plays a secondary role.

## CONCLUSION

In conclusion, we have shown that Raman scattering is a very effective nondestructive optical technique for the characterization of nanosized crystalline materials. Raman spectroscopy can easily be used for the size determination of nanoparticles, as well as for the investigation of nanomaterial stoichiometry, microstrain and confinement effects.

## Acknowledgements

This work was supported by the Serbian MSEP under the project No. 141047 and the OPSA-026283 Project within EC FP6 Programme. We would like to express our thanks to Dr B. Matović and Dr S. Bošković who provided XRD data and supplied us with some of the samples. Dr Ana Cros from the University of Valencia helped us with the high-temperature Raman measurements.

## REFERENCES

1. Gouadec D, Colomban P. *Prog. Cryst. Growth Charact. Mater.* 2006; **188** (in press).
2. Dohčević-Mitrović ZD, Šćepanović MJ, Grujić-Brojčin MU, Popović ZV, Bošković SB, Matović BM, Zinkevich MV, Aldinger F. *Solid State Commun.* 2006; **137**: 387.
3. Dohčević-Mitrović ZD, Grujić-Brojčin MU, Šćepanović MJ, Popović ZV, Bošković SB, Matović BM, Zinkevich MV, Aldinger F. *J. Phys.: Condens. Matter* 2006; **18**: S2061.
4. Konstantinović MJ, Bersier S, Wang X, Hayne M, Lievens P, Silverans RE, Moshchalkov VV. *Phys. Rev., B* 2002; **66**: 161311(R).
5. Konstantinovic M.J. *Physica E.* (in press).
6. Weber WH, Hass KC, McBride JR. *Phys. Rev., B* 1993; **48**: 178.
7. Richter H, Wang YP, Ley L. *Solid State Commun.* 1981; **39**: 625.
8. Campbell IH, Fauchet PM. *Solid State Commun.* 1986; **58**: 739.
9. Kosacki I, Suzuki T, Anderson HA, Colomban P. *Solid State Ionics* 2002; **149**: 99.
10. Balkanski M, Wallis RF, Haro E. *Phys. Rev., B* 1983; **28**: 1928.
11. Spanier JE, Robinson RD, Zhang F, Chan SW, Herman IP. *Phys. Rev., B* 2001; **64**: 245407.
12. dos Santos DR, Torriani IL. *Solid State Commun.* 1993; **85**: 307.
13. Nakajima A, Yoshihara A, Ishigame M. *Phys. Rev., B* 1994; **50**: 13297.
14. Hernandez-Alonso MD, Hugria AB, Martinez-Arias A, Coronado JM, Conesa JC, Soria J, Fernandez-Garcia M. *Phys. Chem. Chem. Phys.* 2004; **6**: 3524.
15. McBride JR, Hass KC, Poindexter BD, Weber WH. *J. Appl. Phys.* 1994; **76**: 2435.
16. Lin XM, Li LP, Li GS, Su WH. *Mater. Chem. Phys.* 2001; **69**: 236.
17. Shuker R, Gammon RW. *Phys. Rev. Lett.* 1970; **25**: 222.

Available online at www.sciencedirect.com

ScienceDirect

Journal of Luminescence 128 (2008) 142–146

JOURNAL OF LUMINESCENCE

www.elsevier.com/locate/jlumin

# Spin-assisted photoluminescence of polycrystalline α-MnSe

Z.V. Popović, A. Milutinović*, N. Romčević

*Center for Solid State Physics and New Materials, Institute of Physics, Pregrevica 118, 11080 Belgrade/Zemun, Serbia*

Received 22 June 2007; accepted 22 June 2007
Available online 5 July 2007

**Abstract**

We have studied photoluminescence of α-MnSe in the antiferromagnetic and paramagnetic phases. Two broad, possibly multi-component emission bands centred at about 1.53 and 1.66 eV are observed at 20 K. The frequencies and intensities of these bands show step-like shift in the vicinity of $T_N$. On the basis of difference in peak energies at $T = 1.8$ K and $T_N$ the d–p–d superexchange interaction in excited state is estimated to be $J_{2g(exc)} = 0.918$ meV.

*PACS:* 75.50.Ee; 75.30.Kz; 78.55.−m; 75.30.Et

*Keywords:* Antiferromagnetics; Phase transition; α-MnSe; Photoluminescence; Superexchange interaction

## 1. Introduction

Manganese oxides and chalcogenides, their alloys and superlattices have been of great interest for years because of the relevance of their magnetooptical and transport properties to applications such as infrared detectors, solar cells and spintronic devices in near future [1–4]. At room temperature MnSe has cubic, NaCl-type structure (α-phase), which persists in antiferromagnetic phase, having AFM-II [5] spin ordering, and according to Ref. [3] has Néel temperature of 122 K. In our previous papers [6,7], it was found that $T_N = 90$ K when one-magnon excitation disappears from Raman spectra [6], or between 100 and 170 K (due to thermal histeresis) according to magnetic susceptibility measurements [7]. Some modes in far-infrared reflectivity and Raman spectra connected with spin excitation confirm that antiferromagnetic transition starts about 100 K in polycrystalline α-MnSe [7].

α-MnSe has several optical absorption bands in the visible and near-ultraviolet energy range as a result of crystal-field transitions of $Mn^{2+}$ ion from the ground state ${}^6A_{1g}$ to ${}^4_aT_{1g}$ and ${}^4_aT_{2g}$, and transitions from ${}^4_aA_{1g}$ to ${}^4_aE_g$, ${}^4_bT_{2g}$ and ${}^4_bE_g$ [8]. Although transitions of this type are forbidden by the spin and the parity selection rules, the observed bands are intense. Several mechanisms were supposed for explanation of absorption in manganese compounds with NaCl-type structure. Phonons, spin–orbit interaction or magnons may cause the perturbation of structure and breaking of the inversion symmetry. The magnon sideband absorption arises from the simultaneous creation of $Mn^{2+}$ exciton and magnon. It is proved that short-range magnetic order in MnO exists up to 530 K [9].

In the present work, we investigated photoluminescence (PL) in polycrystalline α-MnSe and show its connection with magnetic ordering. Step-like energy shift of emission bands below $T_N$ demonstrates the correlation with the AFM spin ordering in this material.

## 2. Experiment

Polycrystalline α-MnSe samples were made by sintering technique. Details of sample preparing were published in Ref. [6]. The quality of α-MnSe samples was checked by X-ray diffractometry. No trace of starting elements or impurity phases confirms a good quality of the samples. Photoluminescence was measured using Joben-Yvon U1000 monochromator and conventional photon-counting technique. In order to avoid the sample heating

---

*Corresponding author. Tel.: +381 11 3160346; fax: +381 11 3160531.
*E-mail address:* miluta@phy.bg.ac.yu (A. Milutinović).

0022-2313/$ - see front matter © 2007 Elsevier B.V. All rights reserved.
doi:10.1016/j.jlumin.2007.06.004

we used a line focus. Low-temperature spectra were measured using Leybold closed-cycle helium cryostat.

Reflectivity of α-MnSe was measured using Perkin-Elmer Lambda 19 spectrophotometer at room temperature in the 180–860 nm spectral range.

## 3. Results and discussion

Typical photoluminescence spectra of as-prepared α-MnSe polycrystalline sample are given in Fig. 1. PL spectra in Fig. 1(a) were excited using 476.5 nm line of Ar laser. Besides dominant structure at about 1.52 and 1.65 eV, a very weak band at about 2.41 eV can be observed at lowest temperature 1.8 K. This band disappears at 20 K and it was not possible to evaluate its frequency vs. temperature dependence. PL spectra excited by 488 nm line of Ar-ion laser are presented in Fig. 1(b) in energy range between 1.45 and 1.85 eV. Spectra were recorded by cooling from room temperature. As can be seen in Fig. 1(b), with increasing the temperature intensity of photoluminescence rapidly decreases. Thus, we were not able to analyse spectra recorded at temperatures higher than 120 K. Observed peak is asymmetrical and the deconvolution, given in Fig. 2, shows that it consist of two broad peaks centred at 1.53 and 1.66 eV at the temperature of 20 K. The intensity of the peak at 1.66 eV changes abruptly with increasing temperature and equalises with the intensity of the lower-energy peak over 100 K. With increasing the temperature lower-energy peak has a small, and peak at 1.66 eV well-defined step-like red energy shift passing across Néel point.

On the basis of these photoluminescence measurements, the temperature of antiferromagnetic ordering is roughly estimated to be between 60 K, where the red energy shift is finished, and 100 K, where intensity of peak at about 1.6 eV becomes as low as the intensity of peak at about 1.5 eV. Spectra recorded at temperatures above 150 K were of very low intensity, but two broad weak peaks still can be resolved up to 300 K. Existence of peak at about 1.6 eV at higher temperatures shows that photoluminescence peak at 1.66 eV at low temperatures consists more than one component.

The electron energy scheme for photoluminescence in α-MnSe in investigated energy range is given in Fig. 3. This scheme is in agreement with similar scheme of other Mn-compounds with NaCl crystal structure (and octahedral surrounding). Luminescence bands could be excited via energy transfer by the “d–d” transition from the $^{6}A_{1g}$ ground state into the $^{4}_{a}T_{1g}$ excited state of the Mn$^{2+}$ ions. In α-MnSe, “d–d” transitions are not of pure “d” origin but mixture of Mn 3d$^{5}$ and Se 4p$^{4}$ states [10,11].

From excited Mn$^{2+}$ ions energy is partially transferred in a nonradiative way to localised energy levels. Further deexcitation is radiative. There are two groups of sublevels. The lower one originates of Mn ions in an environment disturbed by defects, impurities, or Mn$^{3+}$ ions [8]. Radiative deexcitation from this group of sublevels forms a broad emission band centred at 1.53 eV. Depending on a sample preparation (time of additional annealing), its position and size vary, compared to the second PL band. It was referred in Ref. [12] that in the time-resolved emission spectra of MnO this band shows exponential decay. Rapid decrease in the emission band intensity with increase in delay and gate from 20 to 156 μs is observed. In the case of our polycrystalline MnSe, under steady-state excitation, this band becomes more pronounced with increasing of temperature due to reducing intensity (and smaller screening) of 1.66 eV band.

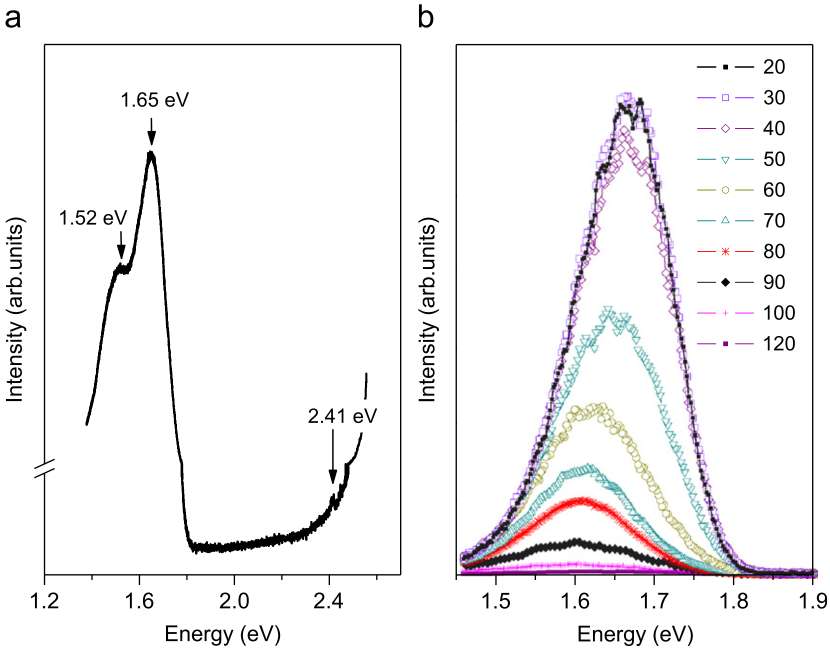

Fig. 1. PL spectra of α-MnSe excited by (a) 476.5 nm line (at $T = 1.8$ K) and (b) 488 nm line of an Ar-ion laser in the temperature range from 20 to 120K.

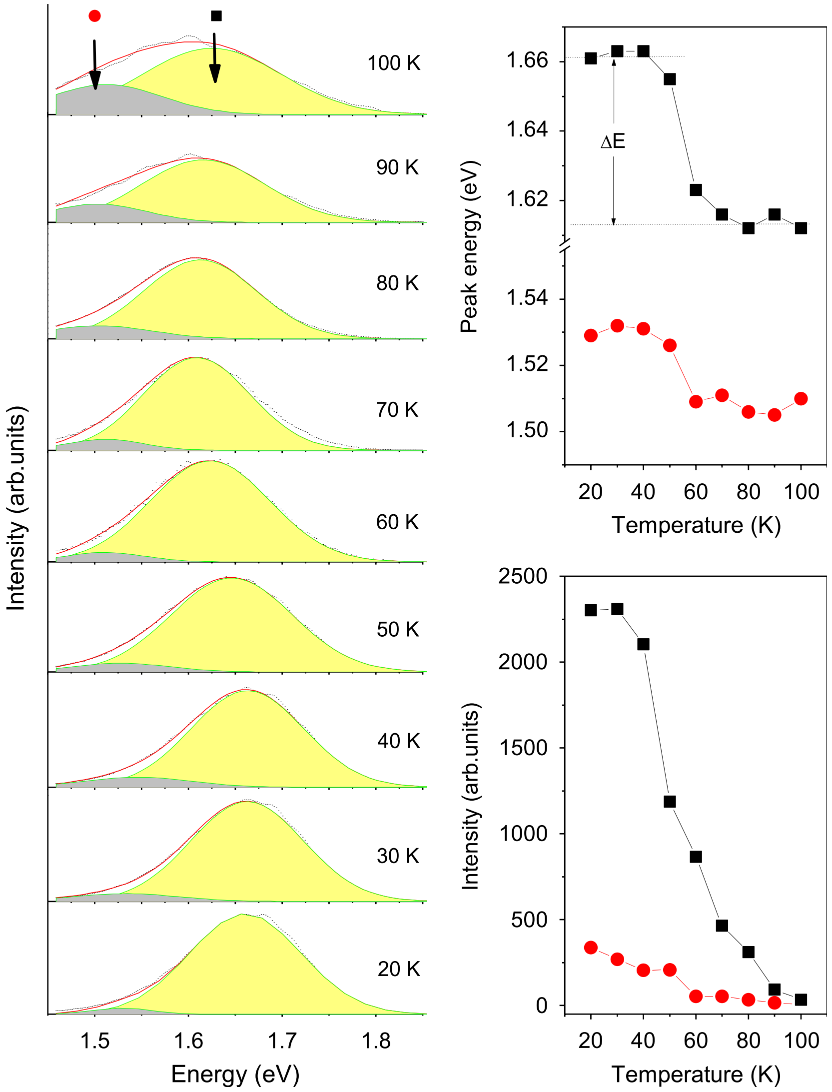

Fig. 2. Deconvoluted PL spectra (left panel) and temperature dependence of the PL peak energies and intensities (right panel).

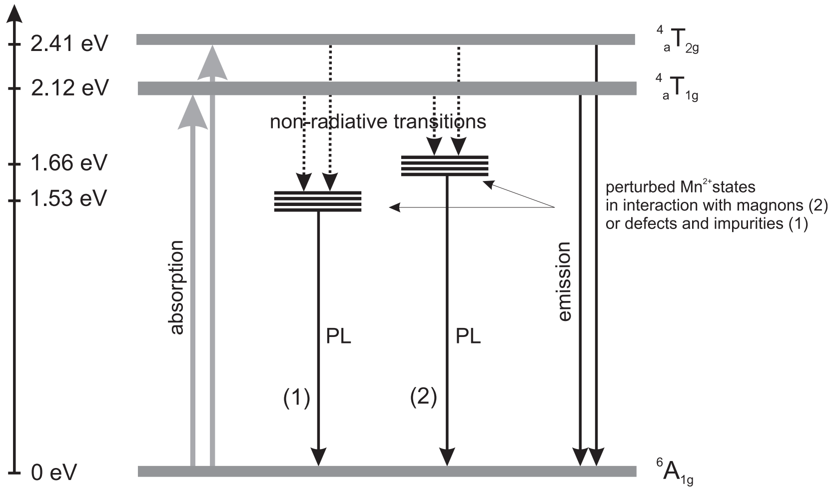

Fig. 3. Possible electron energy scheme of α-MnSe.

The higher localised energy levels originate from perturbed $Mn^{2+}$ states in interaction with magnons. In Ref. [13] it was shown that in MnO second luminescence band can be time resolved in three bands. It is possible that corresponding band in polycrystalline MnSe samples at 1.66 eV comes from many-electron levels, too.

The PL spectra presented in Fig. 4 are an example when the lower PL band is much stronger than the band at 1.66 eV. This sample was not annealed. Its low crystallinity may be the reason for the appearance of an enormous PL band connected with defects and existence of $Mn^{3+}$ ions. In addition, the appearance of new structures at about 1.47 and 2.125 eV (20 K) can be related to interaction of perturbed $Mn^{2+}$ states with several kinds of defects.

Deconvolution of PL spectra from Fig. 4 shows that bands at about 1.51, 1.66 and 2.12 eV have red energy shift passing across $T_N$ (see the right panel of Fig. 4). The intensities of PL bands decrease rapidly between 90 and 100 K, and bands stay hardly visible (in the paramagnetic state) with further increasing of temperature.

We made an additional reflectivity measurement in order to identify emission bands that can be seen at room temperature. Reflectivity spectra of polycrystalline α-MnSe recorded at 300 K in energy range from 1.45 to 6.89 eV is presented in Fig. 5. Arrows indicate several absorption bands. The band at 1.5 eV is very pronounced at 300 K and the band at 1.6 eV is absent, or hardly distinguished, what confirms its predominantly magnetic origin. Weak band at 2.2 eV represents $^6A_1 \rightarrow {}^4T_{1g}$ transition and $^6A_1 \rightarrow {}^4T_{2g}$ is on 2.5 eV. It was referred that in α-MnSe single crystal this excitation band is at 2.41 eV [8]. The band at 3.2 eV corresponds to fundamental band gap energy.

Step-like energy shift $\Delta E$ (see Fig. 2) of the photoluminescence peaks below the Néel temperature, $T_N$, demonstrates the correlation between the antiferromagnetic spin-ordering and the energies of the $Mn^{2+}$ internal transitions. Different relaxation energies for the ground and excited $Mn^{2+}$ states are responsible for this behaviour. In the isomorphic MnS the highest total shift between $T_N$ and 0 K is observed for $^4T_{2g} \rightarrow {}^6A_1$ emission [14] and it can be supposed that in α-MnSe is the same. We could not measure the energy shift of this band in our polycrystalline α-MnSe, but we measure energy difference between 1.8 K and $T_N$ for PL bands at 1.52 and 1.66 eV which are connected with this excitation. An existence of the energy shift of the PL bands indicates that localised energy sublevels of $Mn^{2+}$ ions, perturbed by defects, or by interaction with magnons, are pinned to higher electronic energy levels.

In the case of the NaCl structure, the anions lie on the edges of the cubic fcc cell between the second-nearest magnetic neighbours. As a result, the next-nearest-neighbour interaction (d–p–d superexchange interaction) is usually

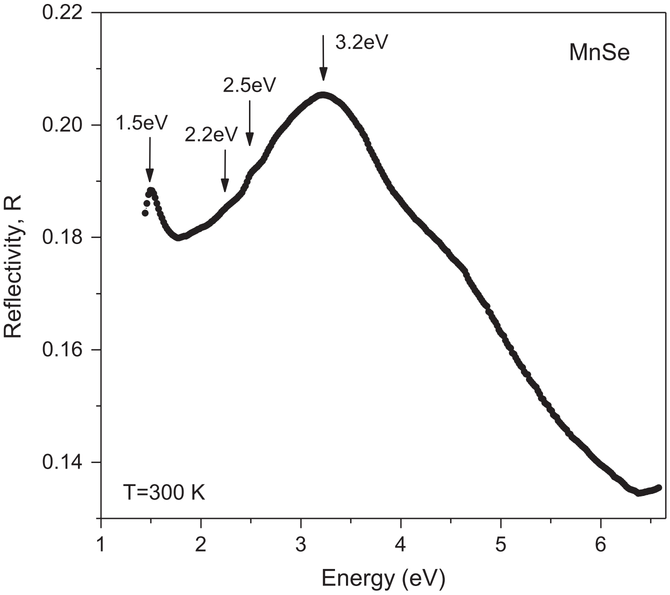

Fig. 5. Room temperature reflectivity spectrum of polycrystalline α-MnSe.

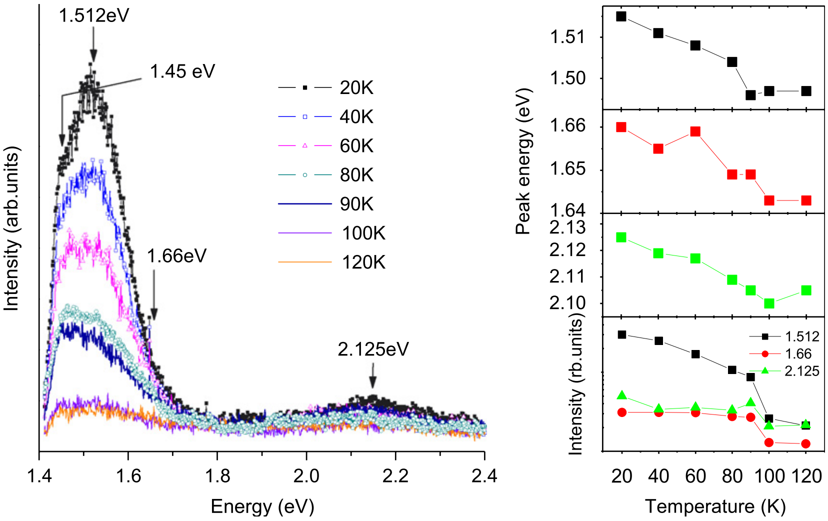

Fig. 4. PL spectra of an unannealed sample in the temperature range 20–120 K (left panel). Temperature dependences of the PL peak energy and intensity (right panel).

stronger than the nearest-neighbour interaction. The magnetic anisotropy energy is expected to be mainly of dipolar origin, and very small compared to the isotropic exchange energy. In the first approximation, energy relaxation of $Mn^{2+}$ ion can be described on the basis of the isotropic part of Hamiltonian neglecting the nearest-neighbour interaction. Energy difference between ground and excited state in this approximation is given by

$$\Delta E = 6(J_{2g}S^2 - J_{2g(exc)}SS'),$$

where $J_{2g(exc)}$ is n–n–n exchange interaction for ground (excited) state; spin $S = 5/2$ for $T = 0$ K, $S' = 3/2$ [10] for excited states; and 6—number of next-nearest neighbours. Value of $J_{2g} = 0.697$ meV corresponds to ground state, as it was estimated in Ref. [6], $\Delta E = 0.0468$ eV is the highest measured value of energy shift for "1.66 eV" PL band (0.0387 eV is the mean value for all PL bands that are connected with $^4T_{1g} \rightarrow {}^6A_1$) and we calculate $J_{2g(exc)} = 0.918$ meV for the highest energy shift of "1.66 eV" PL band and 0.558 meV for mean value for all PL bands that are connected with $^4T_{1g} \rightarrow {}^6A_1$.

The energy shift, $\Delta E$, caused only by spin difference would be much smaller, about 0.01 eV. It seems that the energy shift of PL bands at 1.66 and 2.2 eV passing $T_N$ is mainly caused by varying of exchange integral. The most pronounced component of band at 1.66 eV disappears at higher temperatures, which verifies its connection with long-range spin ordering. Together with weak band that stays at about 1.6 eV (after disappearing a part of PL band connected with long-range ordering), bands at about 1.5 and 2.2 eV stay visible in the paramagnetic phase. Energies and intensities of these two bands show a step-like behaviour near $T_N$ also and it is obvious that these two PL bands are influenced, but not activated by magnons.

## 4. Conclusion

Photoluminescence in polycrystalline α-MnSe shows step-like shift of band energies and intensities below Néel temperature in correlation with the antiferromagnetic spin ordering. The total energy shift of photoluminescence bands is mainly caused by different superexchange energies of the ground and excited $Mn^{2+}$ states. Weak bands at about 1.5, 1.6 and 2.2 eV stay visible in the paramagnetic phase. This fact demonstrates that connection with long-range magnetic ordering is not exclusive in activating of photoluminescence in α-MnSe.

## Acknowledgements

This work is supported by Serbian Ministry of Science under Project no. 141047 and the OPSA-026283 Project within EC FP6 Programme.

## References

[1] S.A. Wolf, D.D. Awschalom, R.A. Buhrman, J.M. Daughton, S. Molnár, M.L. Roukes, A.Y. Chtchelkanova, D.M. Treger, Science 294 (2001) 1488.

[2] D.R. Huffman, R.L. Wild, Phys. Rev. 118 (1966) 526.

[3] R.J. Pollard, V.H. McCann, J.B. Ward, J. Phys. C 16 (1983) 345.

[4] K. Ozawa, S. Anzai, Y. Hamaguchi, Phys. Lett. 20 (1966) 132.

[5] P. Klosowski, T.M. Giebultowicz, J.J. Rhyne, N. Samarth, H. Luo, J. Furdyna, J. Appl. Phys. 69 (1991) 6109.

[6] A. Milutinović, N. Tomić, S. Dević, P. Milutinović, Z.V. Popović, Phys. Rev. B 66 (2002) 012302.

[7] Z.V. Popović, A. Milutinović, Phys. Rev. B 73 (2006) 155203.

[8] W. Heimbrodt, O. Goede, I. Tschentscher, V. Weinhold, A. Klimakow, U. Pohl, K. Jacobs, N. Hoffmann, Physica B 185 (1993) 357.

[9] B. Hermsmeier, J. Osterwalder, D. Freidman, C. Fadley, Phys. Rev. Lett. 62 (1989) 478.

[10] H. Sato, T. Mihara, A. Furuta, M. Tamura, K. Mimura, N. Happo, M. Taniguchi, Y. Ueda, Phys. Rev. B 56 (1997) 7222.

[11] S.-H. Wei, A. Zunger, J. Crys. Growth 86 (1988) 1.

[12] B. Piriou, J. Dexpert-Ghys, S. Mochizuki, J. Phys.: Condens. Matter 6 (1994) 7317.

[13] S. Mochizuki, B. Piriou, J. Dexpert-Ghys, J. Phys.: Condens. Matter 2 (1990) 5225.

[14] W. Heimbrodt, C. Benecke, O. Goede, H.-E. Gumlich, J. Crys. Growth 101 (1990) 911.

IOP PUBLISHING JOURNAL OF PHYSICS: CONDENSED MATTER

J. Phys.: Condens. Matter **19** (2007) 496209 (9pp) doi:10.1088/0953-8984/19/49/496209

# Raman scattering study of the anharmonic effects in $\mathrm{CeO}_{2-y}$ nanocrystals

**Z V Popović**[1], **Z Dohčević-Mitrović**[1], **A Cros**[2] **and A Cantarero**[2]

[1] Center for Solid State Physics and New Materials, Institute of Physics, Pregrevica 118,
11080 Belgrade, Serbia
[2] Materials Science Institute, University of Valencia, P O Box 22085, E-46071, Valencia, Spain

Received 3 May 2007, in final form 17 October 2007
Published 12 November 2007
Online at stacks.iop.org/JPhysCM/19/496209

**Abstract**

We have studied the temperature dependence of the $F_{2g}$ Raman mode phonon frequency and broadening in $\mathrm{CeO}_{2-y}$ nanocrystals. The phonon softening and phonon linewidth are calculated using a model which takes into account the three-and four-phonon anharmonic processes. A detailed comparison of the experimental data with theoretical calculations revealed the predominance of four-phonon anharmonic processes in the temperature dependence of the phonon energy and broadening of the nanocrystals. On the other hand, three-phonon processes dominate the temperature behavior of phonons in polycrystalline samples. The anti-Stokes/Stokes peak intensity ratio was also investigated and found to be smaller for nanosized $\mathrm{CeO}_2$ powders than in the bulk counterpart.

(Some figures in this article are in colour only in the electronic version)

## 1. Introduction

Raman spectroscopy is a powerful tool for characterization of nanosized materials and structures. This technique is widely used for the study of phonon confinement, strain and substitutional effects, porosity, and nonstoichiometry in different kinds of nanomaterials. Recent progress in the use of Raman spectroscopy for nanomaterial characterization is given in [1]. Very few experiments have been carried out to investigate the temperature dependence of Raman mode frequencies and linewidths in nanocrystals [2, 3]. Finite-size effects in nanocrystals are expected to modify the anharmonicity and the phonon decay times. From the temperature-dependent Raman scattering study of nanocrystalline and bulk silicon Mishra and Jain [2] found a higher degree of anharmonicity in Si nanocrystals in comparison with bulk, while Spanier *et al* [4] reported that phonon coupling is not stronger in the $\mathrm{CeO}_{2-y}$ nanoparticle system than that in the bulk counterpart. In addition, to the best of our knowledge, the anharmonicity in very small nanocrystals has not been investigated theoretically yet.

Cerium dioxide ($CeO_2$) has recently attracted a lot of interest as a potential electrolyte in intermediate-temperature solid oxide fuel cells (SOFCs) due to its ability to absorb and release oxygen easily and to exhibit higher ionic conductivity at lower temperatures (500–700 °C) than conventional yttria-stabilized zirconia (YSZ). Therefore it is important to investigate its characteristics at elevated temperatures.

The purpose of this paper is to examine the effect of confinement and temperature-induced changes on vibrational states of $CeO_{2-y}$ nanopowders using Raman spectroscopy. Here we have measured the Raman spectra (Stokes and anti-Stokes) of $CeO_{2-y}$ nanocrystals in the temperature range from room temperature up to 1100 °C. We have found that in nano-$CeO_{2-y}$ the temperature-induced Raman mode frequency shift consists of at least two contributions: the anharmonicity effect, on the one hand, and a phonon frequency change due to the change of nanoparticle size by temperature increase (confinement effect), on the other hand. The anti-Stokes/Stokes intensity ratio is smaller in nano-$CeO_{2-y}$ powders in comparison with the polycrystalline sample. It is supposed that this difference comes from the change of the electronic structure of $CeO_2$ due to the change of the particle size induced by the temperature increase.

## 2. Experimental details

The self-propagating room temperature synthesis method was used to produce $CeO_{2-y}$ nanocrystals of high quality with a narrow size particle distribution in the nanometric range. The details of the sample preparation procedure can be found in our recent publications [5–7]. Micro-Raman spectra were taken in backscattering configuration and analyzed using a Jobin Yvon T64000 spectrometer, equipped with a nitrogen cooled charge-coupled-device detector. As an excitation source we used the 514.5 nm and 488 nm lines of an Ar-ion laser. The high temperature measurements were performed using the Linkam TS 1500 microscope heating stage. Overheating of the sample was avoided by lowering the level of laser power on the sample till no changes of the Raman spectra were observed. The crystal structure of the $CeO_{2-y}$ sample was identified using the powder x-ray diffraction (XRD) method on a Siemens D-5000 XRD diffractometer with Cu K$\alpha$ radiation at room temperature. The average grain size was determined using the Scherrer formula $L = 0.941\lambda/B\cos\Theta$, where $\lambda$ is the wavelength, $B$ is the FWHM of the diffraction peak corrected using the corresponding peak of a micron-sized sample and $\Theta$ is the diffraction angle. The average size of $CeO_{2-y}$ nanocrystals obtained from XRD measurements is $L = 6$ nm.

## 3. Results and discussion

Raman spectra (Stokes and anti-Stokes) of $CeO_{2-y}$ nanocrystals, measured at different temperatures, are shown in figure 1. By heating, the Raman mode frequency continuously decreases and its line shape becomes less asymmetric, becoming totally symmetric at about 900 °C (see the right panel of figure 1).

The particle size effect provokes systematic changes in the Raman spectra of $CeO_{2-y}$ when crystallite size decreases down to 6 nm [4, 6, 8]. The changes of the Raman mode position and shape in nanomaterials are usually studied using the phonon confinement model (PCM) [4, 9]. The evolution of the $F_{2g}$ Raman mode (the mode frequency shift and broadening) strongly depends on the confinement and inhomogeneous strain effects due to the particle size distribution [4, 6]. With decreasing size, the Raman line shifts to lower energy becoming more asymmetric because of the contribution of interior phonons from the entire Brillouin zone ($q \neq 0$). According to this model, due to the relaxation of the $q \simeq 0$ selection rule in

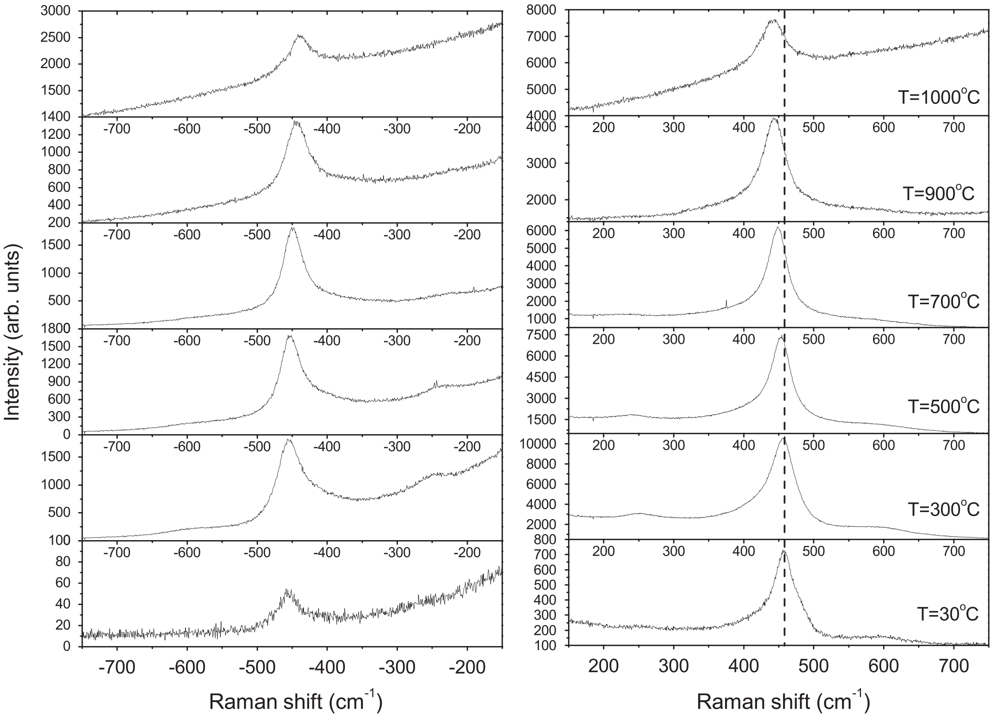

**Figure 1.** Stokes (right panel) and anti-Stokes (left panel) Raman spectra of $CeO_{2-y}$ nanocrystals at different temperatures. Vertical broken line indicates a red shift of $F_{2g}$ Raman active mode with increasing temperature.

finite size crystals, Raman intensity $I(\omega)$ is calculated over the whole Brillouin zone (assumed to be spherical) by the following relation [6]:

$$I(\omega) = \sum_{1}^{3} \int_{0}^{\infty} \rho(L)\,\mathrm{d}L \times \left( \int_{BZ} \exp\left(\frac{-q^2L^2}{8\beta}\right) \frac{\mathrm{d}^3q}{\{\omega - [\omega_i(q) + \Delta\omega_i(q, L)]\}^2 + (\Gamma_0/2)^2} \right) \mathrm{d}L, \qquad (1)$$

where the wavevector $q$ is expressed in units of $2\pi/a$ (where $a$ is the lattice constant of crystalline $CeO_2$), $L$ is the particle diameter and $\Gamma_0$ is the intrinsic linewidth of the Raman mode in the bulk crystal. The factor $\beta$ in equation (1) is an adjustable parameter that reflects the strength of the phonon confinement in the nanomaterials. In our calculations we used the value $\beta = 4\pi^2$. The best fit was obtained for $L = 7.8$ nm, which is in a rather good agreement with XRD results.

In the recent work of Mazali *et al* [10] regarding the Raman spectra of $CeO_2$ nanocrystals dispersed in porous Vycor glass, the authors used the same model as we did to estimate the particle size. Although they used a somewhat simplified dispersion relation model compared with ours [6], the obtained results are similar, demonstrating that the Raman method is a reliable characterization tool for estimating average nanocrystal size.

The Raman peak position is affected by a change of lattice parameter which, on the other hand, depends on particle dimension. The dispersion in particle size produces dispersion in lattice constant. This leads to an inhomogeneous strain and broadening of the Raman peak.

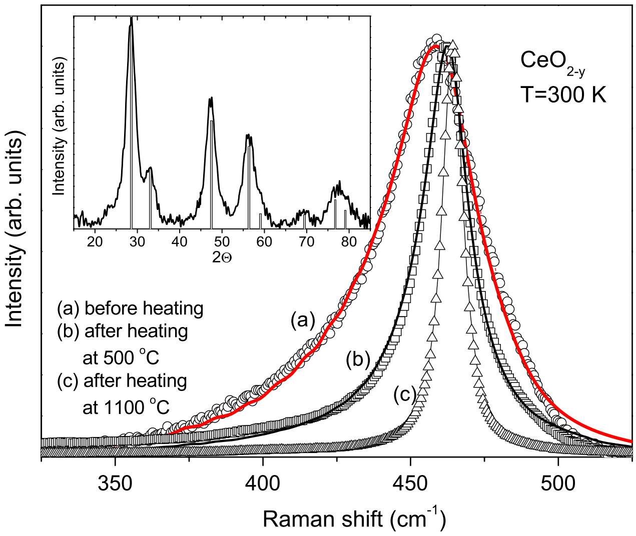

**Figure 2.** Room temperature Raman spectra of $CeO_{2-y}$ nanocrystals before (open circles) and after different heat-treatment (open squares and triangles). Full lines ((a), (b)) are theoretical spectra obtained using equation (1) and a Lorentzian line profile fitting (c). Inset: room temperature x-ray diffraction patterns of $CeO_{2-y}$ nanocrystals together with calculated XRD spectrum obtained for $a = 5.4122$ Å.

The effect of inhomogeneous strain is introduced into the model through the term $\Delta\omega_i(q, L)$ in equation (1), using the particle size distribution function to account for the shift and mode broadening. The sum is taken over three allowed Raman modes since the $F_{2g}$ mode is triple degenerate. A large distribution of nanocrystalline sizes leads to a very large broadening and an asymmetry of the peak, as shown in detail in figure 2(a) (empty circles). In this case a good fit of the experimental line shape cannot be obtained in the framework of the phonon confinement model without including the particle size distribution function $\rho(L)$ in equation (1). We have already discussed in detail the use of this model concerning $CeO_{2-y}$ nanocrystals in [6].

Although the $CeO_{2-y}$ sample is not completely stoichiometric [5, 6] there is no indication that the oxygen deficiency greatly influences the position and linewidth of the $F_{2g}$ Raman mode. According to McBride *et al* [11], with increasing disorder due to the presence of oxygen vacancies, the Raman mode will shift up in frequency (to higher energies) and this is not our case.

The x-ray diffraction patterns of $CeO_{2-y}$ nanocrystals, the inset of figure 2, show a perfect crystallinity. It proves that our sample consists of nanosized $CeO_2$ single crystals, with no amorphous, defect or impurity phases. Such XRD spectra support the work of Hernandez *et al* where they deduced that the samples with average particle size between 3 and 10 nm have fluorite structure similar to the bulk while ceria nanoparticles below 3 nm are strongly disordered materials where the crystalline and amorphous domains exist [8].

In bulk materials, both the frequency and linewidth of optical phonons are found to vary with temperature. This temperature dependence can be attributed to anharmonic terms in the vibrational potential energy. Because of anharmonicity of the lattice forces, an optical mode can interchange energy with other lattice modes and in this way maintain thermal equilibrium. The principal anharmonic interactions are due to the cubic and quartic anharmonic terms, resulting in the splitting of the optical phonon into two or three acoustic phonons, respectively. According to Balkanski *et al* [12] the influence of these anharmonic effects on the Raman

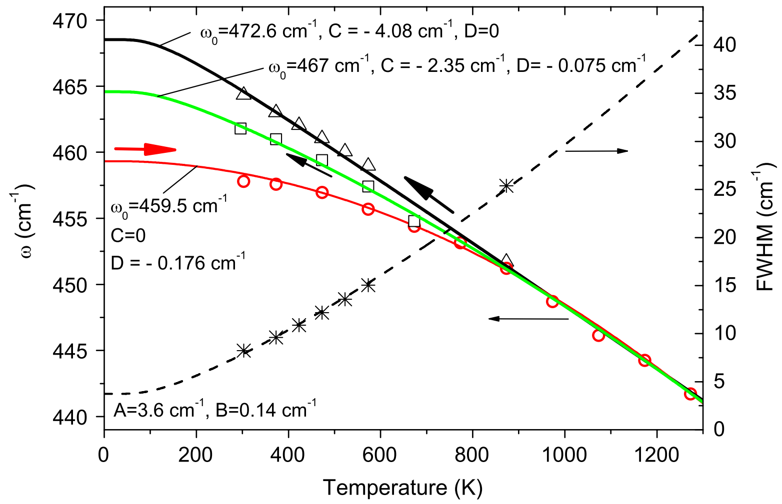

**Figure 3.** Frequency (circles, squares, triangles) and broadening (asterisks) of the $F_{2g}$ Raman mode in $CeO_{2-y}$ versus temperature. The solid (dashed) lines are calculated data using equations (2) and (3) with the fitting parameters indicated in the figure.

spectra in the materials under consideration is taken into account via three-and four-phonon decay processes:

$$\omega(q,T) = \omega_0 + C\left[1 + \frac{2}{e^{\hbar\omega_0/2k_BT} - 1}\right] + D\left[1 + \frac{3}{e^{\hbar\omega_0/3k_BT} - 1} + \frac{3}{(e^{\hbar\omega_0/3k_BT} - 1)^2}\right]. \quad (2)$$

The phonon linewidth is given by

$$\Gamma(T) = A\left[1 + \frac{2}{e^{\hbar\omega_0/2k_BT} - 1}\right] + B\left[1 + \frac{3}{e^{\hbar\omega_0/3k_BT} - 1} + \frac{3}{(e^{\hbar\omega_0/3k_BT} - 1)^2}\right], \quad (3)$$

where $A$, $B$, $C$, and $D$ are anharmonic constants.

Since no theory of anharmonic effects has been developed yet for nanocrystals, we assume that the changes induced by temperature in the phonon vibrational states of the nanocrystals can be well described with the corresponding equations for bulk phonons (equations (2) and (3)).

Figure 3 shows the first-order Raman mode frequency of $CeO_{2-y}$ nanocrystals at different temperatures. By heating, the Raman frequency continuously decreases (open circles in figure 3). In addition, as the temperature increases the line shape becomes less asymmetric, and at about 900 °C it is totally symmetric, as can be observed from figure 1. By cooling, the frequency of the $F_{2g}$ mode increases (open triangles in figure 3), reaching the value of 464.3 $cm^{-1}$ at room temperature. The linewidth (FWHM) decreases with temperature decrease down to 9 $cm^{-1}$ at room temperature. These values are very close to the corresponding values of $CeO_2$ single crystals [13, 14], which leads us to conclude that our sample suffers a transformation from nano- to polycrystalline (see figure 2(c)) by the above-mentioned heating treatment. This means that all effects that arise from the nanometric size of the crystals, such as nonstoichiometry, inhomogeneous strain, confinement, structure defects, etc, are removed by heat treatment.

Equations (2) and (3) have been used to fit the experimental data by suitably choosing the constants $\omega_0$, $A$, $B$, $C$, and $D$, and the agreement between the theoretical curve and experimental points is found to be quite good. It is natural to expect that in bulk materials the contribution of four-phonon processes should be small compared to that of the three-phonon processes [12], i.e. the ratios of $B/A$ and $D/C$ should be small (a few per cent). In addition, in the high temperature limit, the factors multiplying $C$ and $D$ in equation (2) vary as $T$ and $T^2$, respectively. Having this in mind, the results of the fitting procedure applied to the experimental frequency versus temperature dependence of nano-CeO$_{2-y}$ are unexpected. Namely, as can be seen from figure 3, the Raman mode frequency of the nanocrystals (open circles) varies as $T^2$ ($C = 0$, $D = -0.176$ cm$^{-1}$), in the temperature range from 300–1300 K (high temperature limit). Consequently, we can conclude that, at least in CeO$_{2-y}$ nanocrystals, the anharmonicity is dominated by four-phonon processes. The same fitting analysis applied to the polycrystalline CeO$_2$ sample (open triangles in figure 3) showed that a linear dependence with $T$ ($C = -4.08$ cm$^{-1}$, $D = 0$, three-phonon processes) is more suitable for fitting the experimental data. The fact that the value of $D$ for nanocrystals is much larger than that found in polycrystalline CeO$_2$ implies that the different phonon decay channels (four-phonon anharmonic effects) are more important in CeO$_{2-y}$ nanocrystals than in the corresponding bulk. This conclusion could be valid only if the temperature dependence of other effects such as change of grain size (phonon confinement, inhomogeneous strain), or nonstoichiometry were not so important.

According to [15], no significant grain size increase was registered in nano-CeO$_{2-y}$ with temperature increase up to 600 °C. Despite this, we believe that the frequency shift of the Raman mode in our nanocrystalline CeO$_{2-y}$ sample with increasing temperature is also influenced by an increase in grain size. In order to verify this influence we heated the nano-CeO$_{2-y}$ at 500 °C and measured the Raman spectra by cooling it down to room temperature. The corresponding peak frequencies are shown by open squares in figure 3, and the room temperature Raman spectrum, after the mentioned heat treatment, is shown in figure 2 (open squares). It is clear that Raman spectra before and after this heat treatment differ significantly. We fitted both of them with the phonon confinement model described by equation (1) and found that a starting grain size of about $L = 7.8$ nm is almost doubled ($L = 13$ nm) after annealing to 500 °C. Annealing at temperatures higher than 600 °C leads to a grain size increase up to $L = 22$ nm [5, 15], when the nanocrystalline sample transforms into the polycrystalline one. Room temperature Raman spectra of CeO$_2$ after annealing up to 1100 °C is displayed as open triangles in figure 2. This spectrum is totally symmetric with an absence of any of 'nano' effects, i.e. the line frequency and linewidth correspond to the values expected for bulk CeO$_2$. The ratio of the best fit anharmonicity parameters $D/C$ reduces from 'pure' nano to 'pure' polycrystalline phase (see figure 3).

The above discussion should be considered with great care, since it is necessary to take into account that a temperature increase induces two opposite effects on the phonon frequency: a blue shift due to the grain size increase and a red shift due to anharmonicity. To determine which of these mechanisms dominates at different temperature ranges it would be necessary to compare Raman scattering with x-ray diffraction measurements performed on the same sample and at the same temperature. Namely, from the x-ray diffraction data it is possible to estimate the crystallite size (Scherrer equation) separating the effects of size and strain in nano-CeO$_{2-y}$ samples using Williams–Hall plots [16]. Alternatively, a study implying only Raman scattering could be performed by repeating the heating/cooling cycles at various temperatures, and checking the increase of grain size by the use of the phonon confinement model to analyze the Raman shift at room temperature. In this work, this procedure is applied only at a temperature of 500 °C.

We checked the validity of the thermal effects on the phonon modes of the nanocrystals with an analysis of the relative intensities of Stokes and anti-Stokes scattering measured using 514.5 nm and 488 nm lines of an Ar-ion laser. In figure 4 we show the anti-Stokes/Stokes intensity ratio versus temperature for CeO$_{2-y}$ nanocrystals as they are heated (open symbols) and cooled-down (full symbols). This ratio can be written as [12]

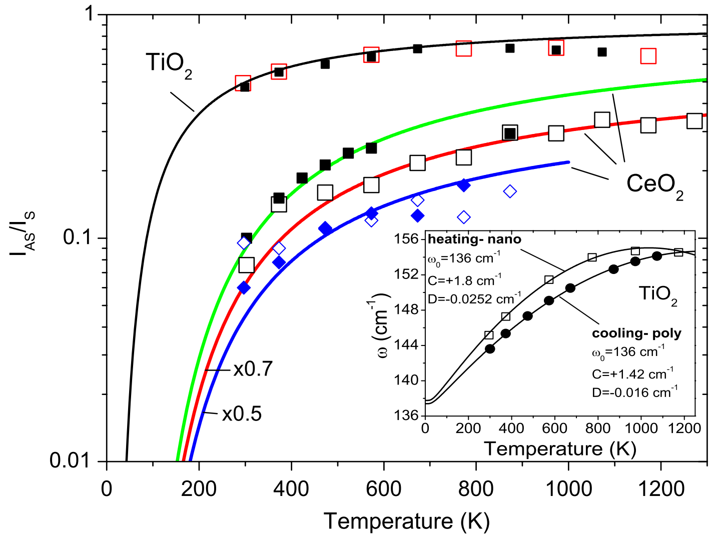

**Figure 4.** Temperature dependence of the anti-Stokes/Stokes intensity ratio for $CeO_{2-y}$ and $TiO_2$ nanocrystalline samples, considering the corrections as discussed in the text. Open (solid) symbols represent data obtained by heating (cooling) of the samples. Squares (diamonds) represent green (blue) Ar-ion laser line measurements. The theoretical curves are represented by solid lines. Inset: frequency versus temperature dependence of $E_g$ symmetry mode of a commercial $TiO_2$ nanocrystalline sample (grain size ∼ 5 nm). Solid lines are the best fit curves, equation (2), for anharmonic parameters indicated in the inset.

$$\frac{I_{\mathrm{AS}}}{I_{\mathrm{S}}} = A\left(\frac{\omega_{\mathrm{AS}}}{\omega_{\mathrm{S}}}\right)^3 \mathrm{e}^{-\hbar\omega_0/k_{\mathrm{B}}T}, \tag{4}$$

and

$$A = \frac{\alpha_{\mathrm{I}} + \alpha_{\mathrm{S}}}{\alpha_{\mathrm{I}} + \alpha_{\mathrm{AS}}} \frac{S(\omega_{\mathrm{I}}, \omega_{\mathrm{AS}})}{S(\omega_{\mathrm{I}}, \omega_{\mathrm{S}})}, \tag{5}$$

where $\alpha_{\mathrm{I}}$, $\alpha_{\mathrm{AS}}$, $\alpha_{\mathrm{S}}$, are the absorption constants at the incident ($\omega_{\mathrm{I}}$), anti-Stokes ($\omega_{\mathrm{AS}}$) and Stokes ($\omega_{\mathrm{S}}$) frequencies, whereas $S(\omega_{\mathrm{I}}, \omega_{\mathrm{AS}})$ and $S(\omega_{\mathrm{I}}, \omega_{\mathrm{S}})$ are the Raman cross sections at the involved frequencies.

In equation (5), $A$ takes into account the frequency dependence of the absorption coefficient and Raman cross sections at the corresponding frequencies. Full lines in figure 4 represent the calculated spectra using equation (4). As can be seen from figure 4, the calculated spectrum for a polycrystalline $CeO_2$ sample fits well with the experimental values taking $A = 1$. For nano-$CeO_{2-y}$ experimental data can be fitted with a correction coefficient which is about 30% smaller than for poly-$CeO_2$ ($A = 0.7$). We believe that this difference most probably comes from different absorption coefficients $\alpha_{\mathrm{AS}}$, $\alpha_{\mathrm{S}}$ of nano-$CeO_{2-y}$. Support for this conclusion is found in [17, 18], where absorption coefficient as well as index of refraction versus wavelength of $CeO_2$ films are presented. There is a significant change of both quantities close to the laser line frequency of 514.5 nm. This means that the anti-Stokes/Stokes intensity ratio is strongly modulated due to a resonance Raman effect in the nano-$CeO_{2-y}$ sample. With the blue line excitation of 488 nm (2.54 eV) resonance effects are even stronger, because the energy of this line is closer to the energy gap value of nanoceria. Ellipsometric or absorption coefficient measurements of nano-$CeO_{2-y}$ at high temperatures can help to resolve this problem. Unfortunately these techniques are not at our disposal for the time being.

We check the validity of equation (4) in the case of commercial nano-$TiO_2$ (grain size $\sim 5$ nm). As can be seen from figure 4, the anti-Stokes/Stokes intensity ratio does not change in the nano-(heating) and poly-(cooling) phase of $TiO_2$ and is well fitted with $A = 1$. Similarly to the case for our $CeO_{2-y}$ sample, we find that the anharmonicity constants $C$ and $D$ as well as the $D/C$ ratio are larger in the nanocrystals than in the polycrystalline phase of $TiO_2$ (see the inset of figure 4), although the changes observed are smaller than in nanocrystalline $CeO_{2-y}$.

A better knowledge of the correction factors is therefore necessary in order to use the anti-Stokes/Stokes ratio as a tool for the determination of temperature in nano-$CeO_{2-y}$ samples. In the case of $TiO_2$, such correction is not necessary. From our measurements we conclude, however, that equation (4) may be applicable for temperature measurements in nanosized materials with similar restrictions as for the bulk samples.

## 4. Conclusion

In conclusion, we have found that at least two contributions are involved in the temperature-induced Raman mode frequency shift of nano-$CeO_{2-y}$: the anharmonicity effect and the phonon frequency change due to the change of nanoparticle size with temperature (confinement effect). The anti-Stokes/Stokes intensity ratio is smaller in $CeO_{2-y}$ nanocrystals in comparison with the polycrystalline sample. This difference probably comes from the change of the electronic structure of $CeO_2$ due to the particle size change induced by the temperature increase, which changes the value of the absorption coefficients at the energies involved in the experiment.

## Acknowledgments

This work was supported by the Serbian Ministry of Science under project no. 141047 and the OPSA-026283 Project within EC FP6 Programme. We would like to express our thanks to Dr B Matović and Dr S Bošković who provided us with some of the samples. Support from the Spanish Ministry of Education (MAT2006-01825-FEDER) is also acknowledged.

## References

[1] Guadec G and Colomban P (eds) 2007 Raman study of nanomaterials *J. Raman Spectrosc.* **38** 597
[2] Mishra P and Jain K P 2000 *Phys. Rev.* B **22** 14790
[3] Konstantinović M J, Bersier S, Wang X, Hayne M, Lievens P, Silverans R E and Moshchalkov V V 2002 *Phys. Rev.* B **66** 161311(R)
[4] Spanier J E, Robinson R D, Zhang F, Chan S W and Herman I P 2001 *Phys. Rev.* B **64** 245407
Zhang F, Chan S W, Spanier J E, Apak E, Jin Q, Robinson R D and Herman I P 2002 *Appl. Phys. Lett* **80** 127
[5] Bošković S, Djurović D, Dohčević-Mitrović Z, Popović Z, Zinkevich M and Aldinger F 2005 *J. Power Sources* **145** 237
[6] Dohčević-Mitrović Z D, Šćepanović M, Grujić-Brojčin M, Popović Z V, Bošković S, Matović B, Zinkevich M and Aldinger F 2006 *Solid State Commun.* **137** 387
[7] Dohčević-Mitrović Z D, Grujić-Brojčin M, Šćepanović M, Popović Z V, Bošković S, Matović B, Zinkevich M and Aldinger F 2006 *J. Phys. Condes. Matter* **18** S2061
[8] Hernandez-Alonso M D, Hugria A B, Martinez-Arias A, Coronado J M, Conesa J C, Soria J and Fernandez-Garcia M 2004 *Phys. Chem. Chem. Phys.* **6** 3524
[9] Campbell I H and Fauchet P M 1986 *Solid State Commun.* **58** 739
[10] Mazali I O, Viana B C, Alves O L, Mendes Filho J and Souza Filho A G 2007 *J. Phys. Chem. Solids* **68** 622
[11] McBride J R, Hass K C, Poindexter B D and Weber W H 1994 *J. Appl. Phys.* **76** 2435
[12] Balkanski M, Wallis R F and Haro E 1983 *Phys. Rev.* B **28** 1928
[13] Sato T and Tateyama S 1982 *Phys. Rev.* B **26** 2257

[14] Weber W H, Hass K C and McBride J R 1993 *Phys. Rev.* B **48** 178
[15] Wang X, Hanson J C, Liu G, Rodriguez J A, Iglesias-Juez A and Fernandez-Garcia M 2004 *J. Chem. Phys.* **121** 5434
[16] Zhou X-D and Huebner W 2001 *Appl. Phys. Lett.* **79** 3512
[17] Kanakaraju S, Mohan S and Sood A K 1997 *Thin Solid Films* **305** 191
[18] Suzuki T, Kosacki I, Petrovsky V and Anderson U 2002 *J. Appl. Phys.* **91** 2308

Appl. Phys. A 90, 679–683 (2008)
DOI: 10.1007/s00339-007-4345-6
**Applied Physics A**
**Materials Science & Processing**

R. KOSTIĆ✉
S. AŠKRABIĆ
Z. DOHČEVIĆ-MITROVIĆ
Z.V. POPOVIĆ

# Low-frequency Raman scattering from $CeO_2$ nanoparticles

Centre for Solid State Physics and New Materials, Institute of Physics, P.O. Box 68, Pregrevica 118, 11080 Belgrade, Serbia

**Received: 23 April 2007/Accepted: 24 October 2007**

**ABSTRACT** Raman scattering measurements were performed on $CeO_2$ nanoparticles at room temperature. Low-frequency modes are assigned to confined acoustic vibrations of spherical $CeO_2$ nanoparticles. Frequencies of these vibrational modes have been calculated in the elastic continuum approximation, which considers a nanoparticle as a homogeneous elastic sphere. We assumed stress-free boundary conditions. The specific dependence of the vibrational frequency on the particle diameter enables the determination of the particle size from the experimental Raman frequency. The particle size value calculated in this way agrees well with the value acquired from the phonon confinement model.

**PACS** 61.46.Df; 73.63.Bd; 63.22.+m

## 1 Introduction

$CeO_2$ is one of the rare-earth oxides having fluorite-type structure. Upon doping with other rare-earth oxides it becomes a good $O^{2-}$ ion conductor at intermediate temperatures (400–700 °C). The electrical properties and chemical reactivity of pure and doped $CeO_2$ nanocrystals make it interesting for applications such as gas sensors, fuel cell electrolyte materials, catalysts for oxygen storage, etc. [1–3]. As this material has attracted a lot of attention, a great improvement in methods of synthesis and characterization has been made in recent years [4–7].

Investigation of size-dependent properties by the Raman scattering technique has been reported simultaneously with methods of synthesis of $CeO_2$ nanocrystals [8–10]. In bulk $CeO_2$ there is a single allowed Raman active triply degenerate $F_{2g}$ mode centered at about $\sim 465\,\mathrm{cm}^{-1}$. This mode can be viewed as a symmetric breathing vibrational mode of the O ions around each cation [11]. This mode is, therefore, very sensitive to the oxygen sublattice disorder resulting from processing or from the effects connected with a decrease of crystal dimension. It has been noticed that in $CeO_2$ nanocrystals the Raman peak energy of the $F_{2g}$ mode decreases, the line width increases and the spectral feature becomes asymmetric towards lower frequencies with decreasing size [10]. This change of the Raman line shape and position can be well described using a theoretical model that assumes the localization of the phonon wave function – the phonon confinement model (PCM) – with decreasing particle size. The PCM is almost exclusively applied to optical phonon confinement and is based on the fact that phonons from the whole Brillouin zone contribute to the Raman line intensity. The weight of the off-center phonons increases as the crystal size decreases and the phonon dispersion causes a wavenumber shift and asymmetrical broadening of the Raman modes [9, 12, 13]. Besides the phonon confinement other effects like stress, inhomogeneous strain broadening associated with the dispersion in particle size, defect states and non-stoichiometry can be possible reasons for variations of Raman spectra of $CeO_2$ particles [10, 14].

In various semiconductor, metal and insulator nanoparticles the low-frequency Raman modes were observed due to scattering from confined acoustic vibrations in nanoparticles. The elastic sphere model (ESM) was generally used to analyze the acoustic phonon confinement. This model describes the oscillations of a homogeneous elastic sphere and was successfully applied to explain the experimental spectra of various nanoparticles [15–18].

According to this model, the frequency of an acoustic Raman mode is scaled as the inverse of the dimension of particles. Thus, the size of the nanoparticles can be deduced from the frequency of these low-frequency Raman peaks.

In this paper we present low-frequency Raman spectra of $CeO_2$ nanoparticles. To the best of our knowledge, this is the first report of experimental evidence of acoustic phonon confinement in $CeO_2$ nanoparticles by Raman spectroscopy. To analyze our experimental spectra we have calculated characteristic frequencies of acoustic phonons confined in $CeO_2$ spherical nanoparticles by the ESM [18, 19] more accurately than in the theoretical work of Talati and Jha [20]. From the characteristic frequencies we obtained the information about the average particle size that coincides well with the size value deduced from the PCM.

## 2 Experimental results

The nanocrystalline $CeO_2$ samples were obtained by self-propagating room-temperature synthesis (SPRT) in

---

✉ Fax: +381-11-3160531, E-mail: rkostic@phy.bg.ac.yu

order to produce powders of high quality with a narrow particle size distribution in the nanometric range. The detailed sample preparation procedure has been described previously [21]. The nanocrystal phase was analyzed by X-ray diffraction (XRD). The calculated value of the $CeO_2$ crystallite size obtained from XRD measurements was about 6 nm.

Micro-Raman spectra were taken in the backscattering configuration and analyzed using a Jobin-Yvon T64000 spectrometer, equipped with a nitrogen-cooled charge-coupled-device detector. As an excitation source we used the 514.5-nm line of an Ar-ion laser.

Figure 1 shows Raman spectra of nano- and polycrystalline $CeO_2$ samples measured at room temperature. The strongest intensity mode at about 457 $cm^{-1}$ (in the polycrystalline sample at 464.3 $cm^{-1}$) represents the optical Raman $F_{2g}$ mode, which originates from oxygen stretching vibrations. This mode softens in a nanosample as a consequence of phonon confinement effects. We have already discussed in more detail the influence of the grain size upon the Raman spectra of $CeO_2$ in the optical phonon region [10]. In the inset of Fig. 1 we have shown the experimental Raman spectrum of nano-$CeO_2$ in the optical region together with the calculated Raman spectrum (full line) based on the PCM. This model accounts for size and inhomogeneous strain effects which arise in nanocrystals from non-uniform size of the powder particles, as described in the previous work [10]. The best-fit procedure gives the average particle size value of about 8 nm.

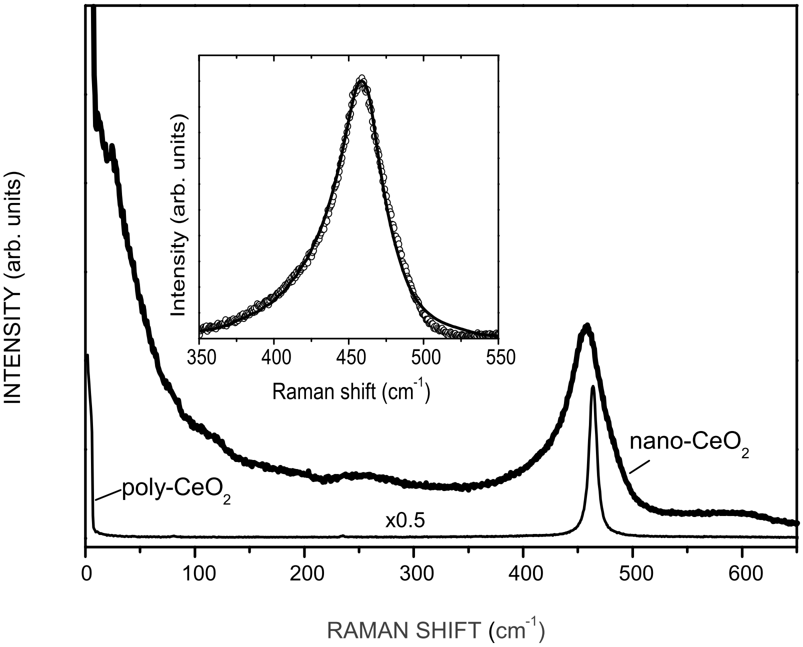

**FIGURE 1** Room-temperature Raman spectra of nano- and polycrystalline $CeO_2$. *Inset*: experimental (*open circles*) and calculated (*solid line*) $CeO_2$ Raman spectra in the 350–550 $cm^{-1}$ spectral range

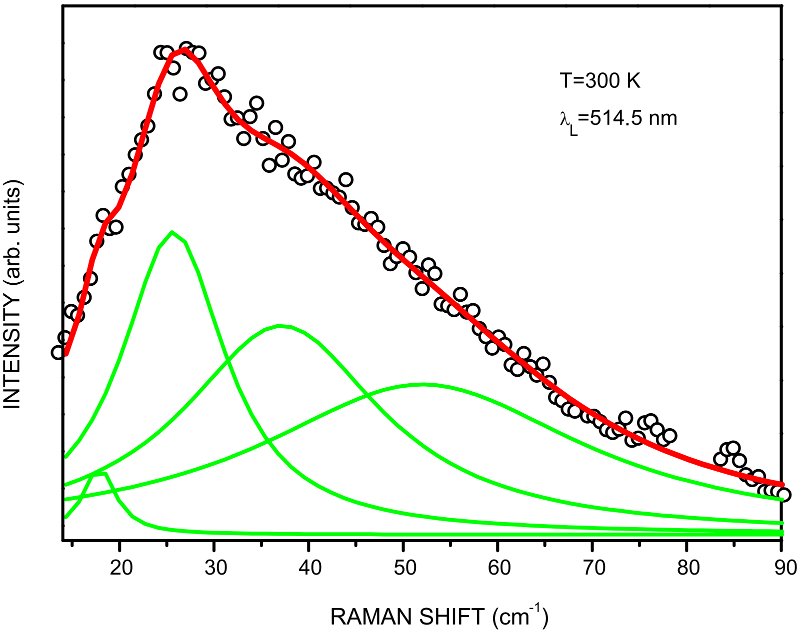

**FIGURE 2** Spectrum of low-frequency Raman scattering from $CeO_2$ nanoparticles (*open circles*). *Full line* is the Lorentzian peak profile fit

Weak intensity features at about 270 $cm^{-1}$ and about 600 $cm^{-1}$ in the Raman spectrum of nano-$CeO_2$ are ascribed to the second-order Raman features and intrinsic oxygen vacancies due to the sample non-stoichiometry [22], respectively [10, 23]. The concentration of the vacancies is increased with the decrease of the particle size and an increase of the particle surface to volume ratio. The Raman spectrum of nano-$CeO_2$ differs substantially from poly-$CeO_2$ in the low-frequency region (below 100 $cm^{-1}$, see Fig. 1). Further on, we will focus our attention on the low-frequency region of the nano-$CeO_2$ Raman spectrum only. At first, we subtracted the intensity of the elastic scattering background by the $A/\omega^n$ approximation [24]. The resulting spectrum is presented in Fig. 2 (open circles). The several modes were observed and deconvoluted in Fig. 2 using the Lorentzian line profile technique.

Four low-frequency modes are observed in the spectrum at the following frequencies: $18.0 \pm 0.4\,cm^{-1}$, $25.7 \pm 0.4\,cm^{-1}$, $37.2 \pm 2.0\,cm^{-1}$ and $52.0 \pm 8.0\,cm^{-1}$. Their line widths increase with the increase of the frequency and their FWHM values are $4.2 \pm 0.4\,cm^{-1}$, $13.4 \pm 3.0\,cm^{-1}$, $25.6 \pm 13.0\,cm^{-1}$ and $41.0 \pm 12.0\,cm^{-1}$, approximately. As these peaks definitely do not appear in the spectra of bulk $CeO_2$, we assumed that the radiation–vibration coupling involved vibrational eigenmodes characteristic for $CeO_2$ nanoparticles.

## 3 Calculation of the vibrational frequencies of a homogeneous elastic sphere of $CeO_2$

The vibrational theory of a continuous elastic body is often used to describe a long-wavelength acoustic phonon that propagates in an ideal bulk crystal. The equation of motion of the three-dimensional elastic body, formulated by Lamb, can be written as

$$\varrho \ddot{\boldsymbol{u}} = (\lambda + 2\mu)\nabla(\nabla \cdot \boldsymbol{u}) - \mu \nabla \times (\nabla \times \boldsymbol{u})\,. \tag{1}$$

Here $\boldsymbol{u}(\boldsymbol{r}, t) = \boldsymbol{u}(\boldsymbol{r})e^{-i\omega t}$ is the lattice displacement vector at position $\boldsymbol{r}$ and time $t$, $\lambda$ and $\mu$ are parameters of the material known as Lame's constants and $\varrho$ is the mass density. Lame's constants are related to the elastic constants of a cubic material as $\lambda + 2\mu = C_{11}$, $\lambda = C_{12}$ and $\mu = C_{44}$. In $CeO_2$ the elastic constants are $C_{11} = 4.03 \times 10^{11}\,N/m^2$, $C_{12} = 1.05 \times 10^{11}\,N/m^2$ and $C_{44} = 0.6 \times 10^{11}\,N/m^2$ [25]. The mass density of $CeO_2$ is 7300 $kg/m^3$. The transverse sound velocity is $v_T = 2890$ m/s. We point out that this velocity is quite different from the one (3890 m/s) assumed by Talati and Jha [20]. The longitudinal sound velocity is $v_L = 6600$ m/s. These velocities are parameters of (1). Equation (1) can be rewritten as

$$-\omega^2 \boldsymbol{u} = v_L^2 \nabla(\nabla \cdot \boldsymbol{u}) - v_T^2 \nabla \times (\nabla \times \boldsymbol{u})\,, \tag{2}$$

where $\boldsymbol{u} = \boldsymbol{u}(\boldsymbol{r})$.

As we want to describe a confined acoustic phonon in a small crystal we must consider the boundary conditions at the surface of the crystal, in our case a sphere, and combine them with (2) in spherical coordinates. We introduced a spherical coordinate system coherent with the symmetry of the problem as in [18, 19]. General solutions were obtained by introducing appropriate scalar and vector potentials. In order to calculate the coefficients that appear in the solution for the displacement field, $\boldsymbol{u} = \boldsymbol{u}(\boldsymbol{r})$, boundary conditions were chosen. It was useful to introduce dimensionless variables: $\eta = \omega R/v_T = \omega d/(2v_T)$ and $\xi = \omega R/v_L = \omega d/(2v_L)$, where $R$ is the radius of the particle ($d$ is the diameter).

As nanoparticles are usually embedded in a different material (matrix), appropriate boundary conditions must be used. If there is a great difference in properties (greater mass density of the matrix, mechanical parameters, structure) of nanoparticle and surrounding matrix, the matrix can disable movement of the surface of the nanoparticle. In the case of so-called rigid boundary conditions, as discussed in [16–18], there is no displacement at the particle surface, i.e. all $\boldsymbol{u}$ components are zero at the surface of the sphere.

If properties of a matrix make it possible for a nanoparticle to vibrate without restrictions, we can assume that there is no force acting on the particle surface, i.e. radial components of the stress tensor at the surface are zero (it is the case of so-called free-surface boundary conditions) as applied in [15–17]. This condition is completely fulfilled if the matrix is absent. Since there is no matrix in the case of interest we assumed the stress-free boundary conditions as in [18] in order to describe the behavior of $CeO_2$ nanoparticles in our samples. Two types of vibrational modes were obtained: spheroidal and torsional modes. In dimensionless variables, spheroidal vibrational motion satisfies secular equations:

$$\frac{\tan \xi}{\xi} = \frac{1}{1 - \left(\frac{v_L}{v_T}\right)^2 \xi^2}\,, \quad l = 0 \tag{3}$$

and

$$\begin{aligned} &\frac{\eta^2}{2}\left[(l-1)(2l+1) - \frac{\eta^2}{2}\right] j_l(\eta) j_l(\xi) \\ &\quad + [\eta^2 - (l^2-1)(l+2)]\xi j_{l+1}(\xi) j_l(\eta) \\ &\quad + [\eta^2 - l(l-1)(l+2)]\eta j_l(\xi) j_{l+1}(\eta) \\ &\quad + (l-1)(l+2)\xi\eta j_{l+1}(\xi) j_{l+1}(\eta) = 0\,, \quad l > 0\,. \end{aligned} \tag{4}$$

The torsional mode motion satisfies the equation

$$j_{l+1}(\eta) - \frac{l-1}{\eta} j_l(\eta) = 0\,, \quad l > 0\,. \tag{5}$$

Here $l$ is an angular momentum quantum number and $j_l$ is a spherical Bessel function of the first kind. There is no torsional movement characterized by $l = 0$.

For each $l$ we obtain a series of solutions $\eta$ ($\xi$), so-called eigensolutions. As $\omega = 2\eta v_T/d$ ($\omega = 2\xi v_L/d$), each solution $\eta$ ($\xi$) determines a specific linear dependence $\omega = f(1/d)$. Dimensionless solutions of equations for spheroidal modes, (3) and (4), strongly depend on the material through the ratio $v_T/v_L$. Solutions for torsional modes, (5), do not depend on the material. The first three solutions for spheroidal $l = 0$, $l = 1$ and $l = 2$ and torsional $l = 1$ and $l = 2$ modes are presented in Table 1.

A spheroidal mode is a vibration with dilatation while a torsional vibration is without dilatation. The lowest-frequency modes, $n = 0$, for $l = 0, 1$ correspond to the surface modes because the displacement vector, in this case, has large

| Spheroidal | | | Torsional | | |
|---|---|---|---|---|---|
| $l$ | $n$ | $\xi$ | $l$ | $n$ | $\eta$ |
| 0 | 0 | 2.583 | 0 | 0 | – |
| | 1 | 6.157 | | 1 | – |
| | 2 | 9.342 | | 2 | – |
| | $n$ | $\eta$ | | $n$ | $\eta$ |
| 1 | 0 | 3.685 | 1 | 0 | 5.763 |
| | 1 | 7.346 | | 1 | 9.095 |
| | 2 | 9.745 | | 2 | 12.323 |
| 2 | 0 | 2.655 | 2 | 0 | 2.501 |
| | 1 | 5.218 | | 1 | 7.136 |
| | 2 | 8.728 | | 2 | 10.515 |

**TABLE 1** Calculated values of dimensionless variables $\xi$ and $\eta$ for fundamental spheroidal (SPH) and torsional (TOR) modes in $CeO_2$. $v_L = 6600\,\mathrm{m/s}$ and $v_T = 2890\,\mathrm{m/s}$ [25]

amplitudes near the surface. For $l > 1$, $n = 1$ is usually a surface mode [26]. The higher-frequency modes, $n > 1$, correspond to the inner modes.

The solutions of (2) for a sphere must transform according to the irreducible representations of the three-dimensional rotation–inversion group O(3) labeled as $D_l^g$ and $D_l^u$. The spheroidal modes transform according to $D_0^g$, $D_1^u$, $D_2^g$, ... representations and the torsional modes transform according to $D_1^g$, $D_2^u$, $D_3^g$, ... representations. The Raman transition operator for dipole-allowed scattering transforms according to $D_0^g$ and $D_2^g$ representations. Hence, the spheroidal $l = 0$ and $l = 2$ modes are Raman active [27]. In experimental Raman spectra we expect to see $l = 0$ series of modes (which are often called spherical modes because the corresponding displacements in the particle are purely longitudinal) and $l = 2$ series (often named ellipsoidal modes because the corresponding displacement in the particle is of both longitudinal and transverse nature).

Size dependences of the acoustic mode frequencies, calculated with the use of eigensolutions $\eta$ or $\xi$ from Table 1, for five lowest energy levels ($l = 2, n = 0$; $l = 2, n = 1$; $l = 0$, $n = 0$; $l = 2, n = 2$ and $l = 0, n = 1$), are plotted in Fig. 3.

## 4 Discussion

The most intensive mode from Fig. 2, at about $25.7\,\mathrm{cm^{-1}}$, corresponds to the spherical ($l = 0$, $n = 0$) mode. Because of the nature of the $l = 0$, $n = 0$ mode, which is completely symmetrical, the theory implies that the lowest energy spherical mode ($l = 0$, $n = 0$) should be the most intensive among all the others in the $l = 0$ series of solutions. The same applies for the first quadrupolar mode ($l = 2$, $n = 0$) in the $l = 2$ series.

As mentioned previously, the eigensolutions of (2) represent different frequency dependences on the particle diameter and are useful for the determination of the particle size. The particle size diameter value that corresponds to the frequency $25.7\,\mathrm{cm^{-1}}$, according to the solution $\xi = 2.853$ obtained for $l = 0$, $n = 0$, is 7.8 nm. The value of 7.8 nm gained by the application of ESM calculations in the analysis of experimental data is in excellent agreement with the mean particle size of 8 nm deduced from the PCM. This can be taken as an additional confirmation of the assertion that the frequency of $25.7\,\mathrm{cm^{-1}}$ represents the spherical mode ($l = 0$, $n = 0$) in $CeO_2$ nanopowder.

From the ESM the frequency of the $l = 2$, $n = 0$ mode is expected to be around $10\,\mathrm{cm^{-1}}$ for the particle size $\sim 8$ nm, but unfortunately due to the screening by Rayleigh scattering this mode cannot be observed. The same uncertainty is present in determining the position of the $l = 2$, $n = 1$ vibrational mode, which is expected to be around $20\,\mathrm{cm^{-1}}$ (the deconvolution technique gives the value of $18.0\,\mathrm{cm^{-1}}$). The further modes in the experimental spectrum can be ascribed to the $l = 2$, $n = 2$ and $l = 0$, $n = 1$ branches with frequencies $37.2\,\mathrm{cm^{-1}}$ and $52.0\,\mathrm{cm^{-1}}$, respectively. It can be noted that these frequencies are close to the values of the frequencies calculated from the appropriate eigensolutions using the par-

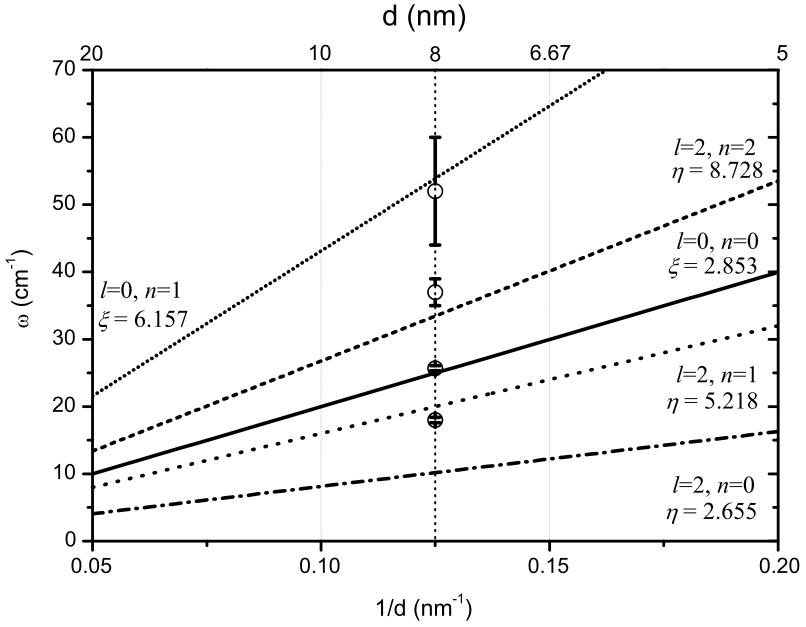

**FIGURE 3** Dependence of the low-frequency Raman bands on the inverse diameter of the $CeO_2$ nanoparticles. Plotted *lines* represent eigensolutions, presented also in Table 1, for spheroidal modes in the stress-free boundary approximation. *Symbols* are experimental results

ticle diameter value of 8 nm. From the calculations performed in [28] it follows that the intensity of the mode in each series (characterized by the value of $l$) decreases rapidly with the increase of the value of $n$. This was an additional reason for the previous assignment.

It is assumed here that each particle vibrates with the frequency which enables us to establish a relationship between the Raman line shape and the shape of the particle size distribution. Broadening of all of the lines observed in the experiment originates from the particle size distribution. Broadening is also determined by the slopes of curves representing the eigensolutions (Fig. 3). This is why we expected the mode $l = 0$, $n = 0$ to be the narrowest and $l = 0$, $n = 1$ the widest, as was confirmed by deconvolution. The diameter that corresponds to the maximum intensity in the low-frequency Raman spectrum does not precisely determine the mean particle diameter [24], which is somewhat smaller. This difference is determined by the width of the particle size distribution. We estimated that this difference is not so significant for the interpretation of our experimental spectra.

It should be noted that the non-stoichiometry of $CeO_2$, i.e. the presence of the Raman peak at the frequency of $\sim 600\,\mathrm{cm}^{-1}$ that corresponds to the intrinsic oxygen vacancies [23], does not make the use of the ESM less justified. The nanoparticles evidently experience vibrations that belong to the spectra of the eigenmodes of the homogeneous spheres.

## 5 Conclusion

In this work we reported the low-frequency Raman scattering spectrum of $CeO_2$ nanocrystals. We found that the observed peaks agree well with the calculated frequencies based on the ESM with parameters transferred from bulk material and the assumption of free-surface boundary conditions. As a result we identified these low-frequency Raman features as scattering from the acoustic vibrations: $l = 2$, $n = 1$; $l = 0$, $n = 0$; $l = 2$, $n = 2$ and $l = 0$, $n = 1$. From the most intensive acoustic mode ($l = 0$, $n = 0$) we determined the particle size, which is in good agreement with the results obtained from the PCM. Careful analysis of the Raman spectra would enable us to make a correspondence between Raman line shape and particle size distribution.

**ACKNOWLEDGEMENTS** This work is supported by the Serbian Ministry of Science, under Project No. 141047, and the OPSA-026283 project within the EC FP6 programme.

## REFERENCES

1 H. Feuer, J. Margalit, Am. Ceram. Soc. Bull. **83**, 12 (2004)
2 D.S. Lee, W.S. Kim, S.H. Choi, J. Kim, J.H. Lee, Solid State Ionics **176**, 33 (2005)
3 C. Lu, W.L. Worrell, C. Wang, S. Park, H. Kim, J.M. Vohs, R.J. Gorte, Solid State Ionics **152–153**, 393 (2002)
4 H. Chen, H. Chang, Ceram. Int. **31**, 795 (2005)
5 P. Shuk, M. Greenblatt, Solid State Ionics **116**, 217 (1999)
6 C. Hu, Z. Zhang, H. Liu, P. Gao, Z.L. Wang, Nanotechnology **17**, 5983 (2006)
7 A. Hartridge, A.K. Bhattacharya, J. Phys. Chem. Solids **63**, 441 (2002)
8 W.H. Weber, K.C. Hass, J.R. McBride, Phys. Rev. B **48**, 178 (1993)
9 I. Kasacki, T. Suzuki, V. Petrovsky, H.U. Anderson, P. Colomban, Solid State Ionics **149**, 99 (2002)
10 Z.D. Dohčević-Mitrović, M.J. Šćepanović, M.U. Grujić-Brojčin, Z.V. Popović, S.B. Bošković, B.M. Matović, M.V. Zinkevich, F. Aldinger, Solid State Commun. **137**, 387 (2006)
11 W.B. Lacina, P.S. Pershan, Phys. Rev. B **1**, 1765 (1969)
12 H. Richter, Z.P. Wang, L. Ley, Solid State Commun. **39**, 625 (1981)
13 I.H. Campbell, P.M. Fauchet, Solid State Commun. **58**, 739 (1986)
14 J.E. Spanier, R.D. Robinson, F. Zhang, S.-W. Chan, I.P. Herman, Phys. Rev. B **64**, 245 407 (2001)
15 A. Tanaka, S. Onari, T. Arai, Phys. Rev. B **47**, 1237 (1993)
16 L. Saviot, B. Champagnon, E. Duval, A.I. Ekimov, Phys. Rev. B **57**, 341 (1998)
17 L. Saviot, D.B. Murray, M. del C. Marco de Lucas, Phys. Rev. B **69**, 113 402 (2004)
18 L. Saviot, B. Champagnon, E. Duval, I.A. Kudriavtsev, I.E. Akimov, J. Non-Cryst. Solids **197**, 238 (1996)
19 E. Roca, C. Trallero-Giner, M. Cardona, Phys. Rev. B **49**, 13 704 (1994)
20 M. Talati, P.K. Jha, Physica E **28**, 171 (2005)
21 S. Bošković, D. Djurović, Z. Dohčević-Mitrović, Z. Popović, M. Zinkevich, F. Aldinger, J. Power Sources **145**, 237 (2005)
22 W.H. Weber, K.C. Hass, J.R. McBride, Phys. Rev. B **48**, 178 (1993)
23 Z.D. Dohčević-Mitrović, M. Grujić-Brojčin, M. Šćepanović, Z.V. Popović, S. Bošković, B. Matović, M. Zinkevich, F. Aldinger, J. Phys.: Condens. Matter **18**, S2061 (2006)
24 M. Ivanda, A.M. Tonejc, I. Djeradj, M. Gotić, S. Musić, G. Mariotto, M. Montagna, in *Nanoscale Spectroscopy and its Applications to Semiconductor Research* (Lect. Notes Phys.), ed. by Y. Watanabe, S. Heun, G. Salviati, Y. Yamamoto (Springer, Berlin, Heidelberg, 2002), pp. 16–27
25 A. Nakajama, A. Yoshihara, M. Ishigame, Phys. Rev. B **50**, 13 297 (1994)
26 L. Saviot, D.B. Murray, Phys. Rev. B **72**, 205 433 (2005)
27 E. Duval, Phys. Rev. B **46**, 5795 (1992)
28 M. Montagna, R. Dusi, Phys. Rev. B **52**, 10 080 (1995)

APPLIED PHYSICS LETTERS **91**, 203118 (2007)

# Temperature-dependent Raman study of $Ce_{0.75}Nd_{0.25}O_{2-\delta}$ nanocrystals

Z. D. Dohčević-Mitrović,[a] M. Radović, M. Šćepanović, M. Grujić-Brojčin, and Z. V. Popović
*Center for Solid State Physics and New Materials, Institute of Physics, Pregrevica 118, 11080 Belgrade, Serbia*

B. Matović and S. Bošković
*Institute of Nuclear Sciences "Vinča", 11001 Belgrade, Serbia*

(Received 20 June 2007; accepted 31 October 2007; published online 16 November 2007)

Raman spectra of Nd doped ceria nanocrystals were measured by gradual heating and cooling over the temperature range of 293–1073 K and analyzed using the phonon confinement model that incorporates inhomogeneous strain and anharmonic effects. We have demonstrated that in nanograins, four-phonon anharmonic processes are more dominant at higher temperatures than size effects. After the heat treatment, Nd doped ceria nanocrystals remain of nanometric range ($\sim$20 nm) while the concentration of oxygen vacancies is still high in ceria lattice, making this material convenient for solid oxide fuel cells application. © *2007 American Institute of Physics*. [DOI: 10.1063/1.2815928]

Cerium dioxide ($CeO_2$) attracts a lot of interest because of its applications in three-way catalysis,[1] gas sensor devices,[2] and as electrolyte material in solid oxide fuel cells.[3,4] Nanosized $CeO_2$ doped with rare earth elements is a promising solid electrolyte with excellent ionic conductivity at low temperature because of the high oxygen vacancy concentration.[5,6]

Although in recent years numerous investigations have been performed on the structural[7–9] and transport properties of doped ceria,[5,6] we are not aware of any other Raman work aimed to the examination of temperature-induced changes on the vibrational properties in these materials. In the present study, we investigated the temperature dependence of the Raman spectra of $Ce_{0.75}Nd_{0.25}O_{2-\delta}$ nanocrystals. The presence of oxygen vacancy Raman modes after heat treatment implies that Nd doped ceria can be a useful electrolyte material for fuel cells. High-temperature x-ray diffraction (HTXRD) measurements were performed in order to investigate the stability of this system and to estimate the particle size.

The $Ce_{0.75}Nd_{0.25}O_{2-\delta}$ nanocrystals were synthesized using self-propagating room temperature synthesis. The detailed powder preparation procedure has been described previously.[10] HTXRD measurements were carried out on Philips X'pert Pro XRD unit equipped with Anton Paar HTK attachment, in static air, using Co $K\beta$ radiation.

Raman experiments were performed in the backscattering configuration using Jobin Yvon T64000 spectrometer and TS1500 Linkam microscope heating stage. The Raman spectra were measured with the 514.5 nm $Ar^+$ laser line.

In Fig. 1 are displayed Raman spectra of the $Ce_{0.75}Nd_{0.25}O_{2-\delta}$ sample at room temperature (RT), during the heating (circles) and after gradual cooling (dashed lines) down to room temperature.

In $CeO_2$ nanocrystals, $F_{2g}$ Raman mode[11] at 464 $cm^{-1}$ shifts to lower frequencies with pronounced asymmetrical broadening depending on the particle size.[12] In $Ce_{0.75}Nd_{0.25}O_{2-\delta}$ sample, this mode, at RT, is positioned at about 450 $cm^{-1}$. With temperature increase the $F_{2g}$ mode shifts to lower frequencies and becomes less asymmetric while the linewidth continuously increases. Such a behavior is attributed to the presence of anharmonicity in the vibrational potential energy due to the decay of the optical phonon to two or three acoustic phonons.[12,13] The temperature dependence of the Raman mode frequency and linewidth, including three- and four-phonon anharmonic processes is[13]

$$\omega(T) = \omega_0 + C\left[1 + \frac{2}{e^x - 1}\right] + D\left[1 + \frac{3}{e^y - 1} + \frac{3}{(e^y - 1)^2}\right] = \omega_0 + \Delta\omega(T), \quad (1)$$

$$\Gamma(T) = \Gamma_1 + A\left[1 + \frac{2}{e^x - 1}\right] + B\left[1 + \frac{3}{e^y - 1} + \frac{3}{(e^y - 1)^2}\right] = \Gamma_1 + \Delta\Gamma, \quad (2)$$

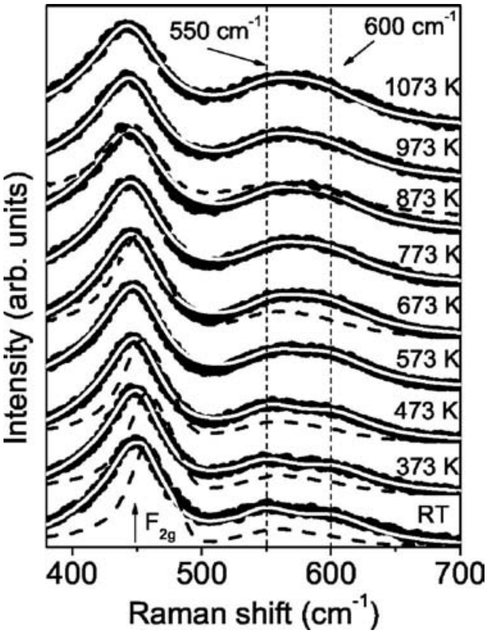

FIG. 1. Raman spectra of $Ce_{0.75}Nd_{0.25}O_{2-\delta}$ sample obtained upon heating (circles) and cooling (dashed lines). The solid lines are calculated spectra using PCM model.

---

[a] Electronic mail: zordoh@phy.bg.ac.yu

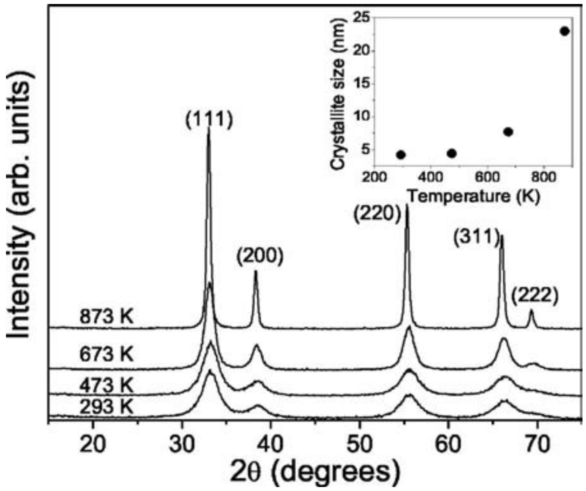

FIG. 2. X-ray diffraction patterns of the $Ce_{0.75}Nd_{0.25}O_{2-\delta}$ sample in the temperature range of 293–873 K.

where $\omega_0$ is the harmonic frequency, $x=\hbar\omega_0/2k_BT$, $y=\hbar\omega_0/3k_BT$, $\Gamma_1$ is a linewidth due to phonon confinement and inhomogeneous strain, and A, B, C, and D are anharmonic constants.

Raman spectra of the $Ce_{0.75}Nd_{0.25}O_{2-\delta}$ sample from Fig. 1 are fitted using phonon confinement model (PCM). In the PCM are included inhomogeneous strain effect through term $\Delta\omega_i(q,L)$, using Gaussian particle size distribution function $\rho(L)$,[12,14] and anharmonic effects through terms $\Delta\omega(T)$, $\Gamma(T)$:

$$I(\omega) = \sum_{i=1}^{3} \int_0^\infty \rho(L)dL \times \int_{BZ} \frac{\exp\left(-\dfrac{q^2L^2}{8\beta}\right)d^3q}{[\omega-(\omega_i(q)+\Delta\omega)]^2+[\Gamma(T)/2]^2}, \quad (3)$$

where the wave vector $q$ is expressed in units of $2\pi/a$ ($a$ is the lattice constant), $L$ is the particle diameter, $\Delta\omega=\Delta\omega_i(q,L)+\Delta\omega(T)$, and $\beta$ is an adjustable parameter concerning the strength of the phonon confinement in nanomaterials. The full lines in Fig. 1 are the calculated spectra based on Eq. (3). From the PCM model, we obtained that particle size increased from 6.6 to 11 nm during the heating (see inset of Fig. 4).

In Fig. 2 are presented XRD data collected in the temperature range of 293–873 K. The diffraction peaks became more intense, narrower, and sharper with temperature increase indicating particle agglomeration. No phase separation was detected confirming that $Ce_{0.75}Nd_{0.25}O_{2-\delta}$ solid solution is stable at higher temperatures. The estimated nanocrystal average size, using Scherrer's equation, ranged from 4.2 to 23 nm (see inset of Fig. 2). Our estimation of particle size from the PCM model is in a very good agreement with HTXRD results as well as with XRD measurements of Wang *et al.*[15]

In Fig. 3(a) is shown the $F_{2g}$ mode frequency downshift (squares) and linewidth increase (circles) with heating. The best fits of the peak position and linewidth [full lines in Fig. 3(a)] were obtained including only four-phonon processes contrary to the microceria sample where three-phonon processes are more probable.[12,16] Such a behavior suggests that phonon decay channels are different in nanocrystalline grain than that in larger grain. Taking into account that particles grow during the heating and assuming that size effects predominate, we would expect the upshift of the $F_{2g}$ mode frequency [triangles in Fig. 3(a)] and linewidth decrease, but because of evident redshift and broadening of the $F_{2g}$ mode during heating, we concluded that anharmonicity effects at higher temperatures have more influence on the frequency (linewidth) change than size effects.

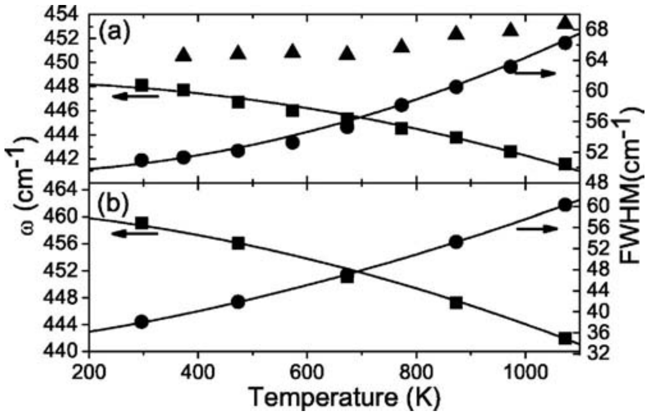

FIG. 3. Variation of the $F_{2g}$ mode frequency (■) and linewidth (●) upon heating (a) and upon gradual cooling (b). Full lines represent calculated values for the peak position and linewidth. The best fitting parameters during the heating are $\omega_0=448.5$ cm$^{-1}$, $C=0$ cm$^{-1}$, $D=-0.095$ cm$^{-1}$, $\Gamma_1=49$ cm$^{-1}$, $A=0$ cm$^{-1}$, and $B=0.25$ cm$^{-1}$, whereas those for cooling are $\omega_0=462$ cm$^{-1}$, $C=-1.1$ cm$^{-1}$, $D=-0.182$ cm$^{-1}$, $\Gamma_1=32$ cm$^{-1}$, $A=2.5$ cm$^{-1}$, and $B=0.17$ cm$^{-1}$. Triangles represent the calculated $F_{2g}$ mode position including only size and strain effects.

Upon cooling, the $F_{2g}$ mode frequency increases while linewidth decreases [Fig. 3(b)]. The temperature dependence of $F_{2g}$ mode frequency (squares) and linewidth (circles) is now well fitted including both terms in Eqs. (1) and (2). This behavior is more similar to the microceria sample.[12,16] The Raman spectrum of $Ce_{0.75}Nd_{0.25}O_{2-\delta}$ sample at room temperature after cooling is narrower, blueshifted with respect to starting spectrum (see Fig. 1), but at lower frequency (~457 cm$^{-1}$) than in the bulk counterpart. This implies that the particles were increased after the heat treatment but are still in the nanometric range (~20 nm at room temperature).

Beside $F_{2g}$ mode two additional Raman modes appear in $Ce_{0.75}Nd_{0.25}O_{2-\delta}$ sample. The mode at ~600 cm$^{-1}$ originates from intrinsic oxygen vacancies due to nonstoichiometry of ceria nanopowder.[7] The other mode at ~550 cm$^{-1}$ can be ascribed to the oxygen vacancies introduced into the ceria lattice whenever $Ce^{4+}$ ions are replaced with $Nd^{3+}$ cations.[7,17] This mode is pronounced during the heating and still exists after cooling. The defect concentration $N=3/(4\pi\xi^3)$, determined from the correlation length $\xi=L/\sqrt{8\beta}$,[9,16] is presented in Fig. 4 for the temperature range of 293–1073 K. In the inset is presented change of the particle size obtained from PCM with temperature. The defect concentration in $Ce_{0.75}Nd_{0.25}O_{2-\delta}$ decreases with temperature as a consequence of size effects[9,18] but is still high after heat treatment, almost three orders of magnitude higher than in polycrystalline sample.[8,9]

We examined the effects of temperature-induced changes on vibrational states of Nd doped ceria nanocrystals using Raman spectroscopy. This study revealed that four-phonon anharmonic processes predominate in $Ce_{0.75}Nd_{0.25}O_{2-\delta}$ nanocrystals contrary to polycrystals where three-phonon

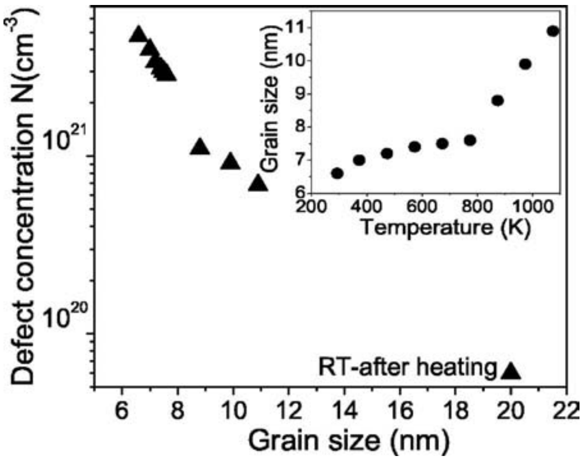

FIG. 4. Defect concentration for the temperature range of 293–1073 K as a function of the grain size. Inset: the particle size, obtained from the PCM model, as a function of temperature.

processes are more probable. The size effects have less influence on the Raman mode behavior than anharmonic effects at high temperatures. The Raman spectra before and after heat treatment differ significantly, as a consequence of particle growth, but the $Ce_{0.75}Nd_{0.25}O_{2-\delta}$ sample is still in nanometric range with a significant presence of oxygen vacancies in ceria lattice.

This work was supported by the MSRS under the Project No. 141047 and the OPSA-026283 Project within EC FP6 Programme. The authors thank Dr. Udo Wlezel, Max-Planck Institute, MPI, Stuttgart, Germany, for performing HTXRD measurements.

[1] A. Trovarelli, Catal. Rev. - Sci. Eng. **38**, 439 (1996).
[2] P. Jasinski, T. Suzuki, and H. U. Anderson, Sens. Actuators B **95**, 73 (2003).
[3] M. Mogensen, N. M. Sammes, and G. A. Tompsett, Solid State Ionics **129**, 63 (2000).
[4] T. S. Zhang, J. Ma, L. B. Kong, S. H. Chan, and J. A. Kilner, Solid State Ionics **170**, 209 (2004).
[5] X. M. Lin, L. P. Li, G. S. Li, and W. H. Su, Mater. Chem. Phys. **69**, 236 (2001).
[6] A. Sin, Yu. Dubitsky, A. Zaopo, A. S. Arico, L. Gullo, D. La Rosa, S. Siracusano, V. Antonucci, C. Oliva, and O. Ballabio, Solid State Ionics **175**, 361 (2004).
[7] J. R. McBride, K. C. Hass, B. D. Poindexter, and W. H. Weber, J. Appl. Phys. **76**, 2435 (1994).
[8] S. Patil, S. Seal, Y. Guo, A. Schulte, and J. Norwood, Appl. Phys. Lett. **88**, 243110 (2006).
[9] I. Kosacki, V. Petrovsky, H. U. Anderson, and P. Colomban, J. Am. Ceram. Soc. **85**, 2646 (2002).
[10] S. Boskovic, D. Djurovic, Z. Dohčević-Mitrović, Z. Popovic, M. Zinkevich, and F. Aldinger, J. Power Sources **145**, 237 (2005).
[11] W. H. Weber, K. C. Hass, and J. R. McBride, Phys. Rev. B **48**, 178 (1993).
[12] J. E. Spanier, R. D. Robinson, F. Zhang, S. W. Chan, and I. P. Herman, Phys. Rev. B **64**, 245407 (2001).
[13] M. Balkanski, R. F. Wallis, and E. Haro, Phys. Rev. B **28**, 1928 (1983).
[14] Z. D. Dohčević-Mitrović, M. J. Šćepanović, M. U. Grujić-Brojčin, Z. V. Popović, S. B. Bošković, B. M. Matović, M. V. Zinkevich, and F. Aldinger, Solid State Commun. **137**, 387 (2006).
[15] X. Wang, J. C. Hanson, G. Liu, J. A. Rodriguez, A. Iglesias-Juez, and M. Fernandez-Garcia, J. Chem. Phys. **121**, 5434 (2004).
[16] Z. V. Popović, Z. Dohčević-Mitrović, M. J. Konstantinović, and M. Šćepanović, J. Raman Spectrosc. **38**, 750 (2007).
[17] Z. D. Dohčević-Mitrović, M. Grujić-Brojčin, M. Šćepanović, Z. V. Popović, S. Bošković, B. Matović, M. Zinkevich, and F. Aldinger, J. Phys.: Condens. Matter **18**, S2061 (2006).
[18] J. H. Zhang, Y. Q. Yang, J. M. Shen, and A. Wang, J. Mol. Catal. A: Chem. **237**, 182 (2005).

*Science of Sintering*, **39** (2007) 281-286

doi: 10.2298/SOS0703281R

UDK 677.026.34:553.689

# Raman Study Of Ba-Doped Ceria Nanopowders

**M. Radović[1*)], Z. Dohčević-Mitrović[1], M. Šćepanović[1], M. Grujić-Brojčin[1], B. Matović[2], S. Bošković[2] Z. V. Popović[1]**
[1]Institute of Physics, Center for Solid State Physics and New Materials, Pregrevica 118, P.O. Box 68, 11080 Belgrade, Serbia,
[2]Institute of Nuclear Sciences 'Vinca', 11001 Belgrade, Serbia

---

***Abstract:***

*A series of $Ce_{1-x}Ba_xO_{2-y}$ ($5 \leq x \leq 0.20$) nanometric powders were synthesized by self-propagating room temperature synthesis. XRD and Raman scattering measurements were used to characterize the samples at room temperature. All the samples are solid solutions with fluorite type structure with an average crystallite size about 5 nm. The redshift and asymmetric broadening of the Raman $F_{2g}$ mode can be well explained with combined confinement and strain effects because of the nanocrystalline powders nature. The appearance of the additional peaks at ~560 $cm^{-1}$ and ~600 $cm^{-1}$, are attributed to extrinsic and intrinsic $O^{2-}$ vacancies in ceria lattice. Raman spectra of temperature treated $Ce_{0.80}Ba_{0.20}O_{2-\delta}$ sample revealed the instability of this system.*

***Keywords:*** *Ba doped ceria nanopowders, XRD method, Raman scattering, phase separation*

---

## 1. Introduction

Cerium dioxide is of interest because of its multiple applications such as catalysis in vehicle emissions-control systems [1], high storage capacitors [2], for high Tc superconducting structures [3], and for optical devices [4]. Recently, ceria based solid solutions have gained an increasing amount of attention due to their potential use as electrolyte material in solid oxide fuel cells [5] (SOFCs). Optimization of SOFCs, to operate at reduced temperatures can be performed with use of electrolyte materials, which have high ionic conductivity at moderate temperatures.

Monodisperse cerium nanoparticles have higher ionic conductivities than bulk material, due to the properties related to their nanostructured nature. Nanosized ceria doped with oxides of di- or trivalent metals exhibits high ionic conductivity at intermediate temperatures (400-700 $^0$C) and is a promising candidate for electrolyte SOFCs materials. Whenever the $Ce^{4+}$ ions are replaced with di- or trivalent rare earth ions large density of oxygen vacancies are formed in ceria lattice enhancing the ionic conductivity of these materials [6,7]. The ionic conductivity significantly depends on the ionic radius and the concentration of the dopant too [8,9].

In the present work we described briefly the SPRT method as a possible method for preparing Ba-doped ceria nanopowders. To the best of our knowledge this method is for the first time used to synthesize the $Ce_{1-x}Ba_xO_{2-y}$ ($5 \leq x \leq 0.20$) solid solutions. The influence of

---

[*)] Corresponding author: marrad@phy.bg.ac.yu doping and heating treatment on the Raman spectra of doped ceria powders is also investigated. Raman spectroscopy at room temperature was used to identify and distinguish the presence of oxygen vacancies introduced into ceria lattice with doping from the intrinsic vacancies that originate from nonstoichiometry in doped samples.

## 2. Experiment

The solid solutions of Ba doped $CeO_2$ samples were prepared by a self-propagating room temperature synthesis (SPRT) using metal nitrates and sodium hydroxide as the starting materials. The synthesis involves hand-mixing starting materials in alumina mortar for 5-7 minutes until the mixture got light brown. After being exposed to air for 3h, the mixture was suspended in water. Rinsing out of reaction byproduct ($NaNO_3$) was performed by centrifuge Centurion 1020D at 3500 rpm. This procedure was performed 3 times with distilled water and twice with ethanol [10].

Single solid-state solutions were obtained according to reaction:

$2[(1\text{-}x)Ce(NO_3)_36H_2O + xBaNO_3] + 6NaOH + (1/y)O_2 \rightarrow 2Ce_{1-x}Ba_xO_{2-y} + 6NaNO_3 + 9H_2O$

Compositions of $Ce_{1-x}Ba_xO_{2-y}$ were synthesized with x ranging from 0.05 to 0.20

The crystalline phases were identified by X-ray powder diffraction using Siemens D5000 diffractometer with Cu $K_\alpha$ radiation at room temperature. Diffractograms of the $Ce_{1-x}Ba_xO_{2-y}$ samples were recorded over the 2θ range from $20^0$ to $80^0$ using a position sensitive detector with $8^0$ acceptance angle. The average grain size was measured from the (111) XRD peak using the Scherrer formula. The average crystallite size was estimated to be 5 nm.

Room temperature Raman measurements were performed in the backscattering geometry using 514.5-nm line of Ar-ion laser, Jobin-Yvon U1000 monochromator and photomultiplier as a detector while high temperature Raman measurements were taken with same $Ar^+$ laser line using Jobin Yvon T64000 spectrometer equipped with Linkam TS 1500 microscope heating stage and nitrogen cooled charge-coupled-device detector (CCD). Overheating of the samples was avoided using a minimal laser power when no changes of the Raman spectra were noticed.

## 3. Results and discussion

According to the XRD spectra, Ba doped samples appeared to be of single phase for the whole doping range retaining the $CeO_2$ fluorite structure. Diffraction lines of Ba oxide were not registered in the whole doping range.

The XRD patterns for $Ce_{0.95}Ba_{0.05}O_{2-y}$, $Ce_{0.90}Ba_{0.10}O_{2-y}$ and $Ce_{0.85}Ba_{0.15}O_{2-y}$ samples are shown in Fig. 1 (a). Change of lattice parameter as a function of dopant concentration is shown in Fig.1 (b). Lattice parameter of pure $CeO_2$ is shown as reference one. The increasing of lattice constant with increasing dopant concentration is directly correlated with ionic size
$CeO_2$ with a fluorite structure has one Raman active triply degenerate $F_{2g}$ mode at 465 $cm^{-1}$.

This mode presents symmetrical stretching vibrations of $CeO_8$ vibrational unit and should be very sensitive to the oxygen sublattice disorder [11]. Raman study of $CeO_2$ nanoparticles have demonstrated that the $F_{2g}$ mode shifts to lower energies with increasing linewidth while the line shape becomes asymmetric on the low-energy side as the particle size gets smaller [12]. This evolution of the Raman line can be attributed to the combined effect of phonon confinement and inhomogeneous strain [12,13]. To explain properly the evident phonon softening and increased linewidth asymmetry of the main $F_{2g}$ mode in the $Ce_{1-x}Ba_xO_{2-y}$ samples we used the phonon confinement model (PCM) that incorporates size and strain effects [13]. Raman intensity is calculated over the whole Brillouin zone by the following relation:

$$I(\omega)=\sum_{1}^{3}\int_{0}^{\infty}\rho(L)dL\int_{BZ}\frac{\exp(-\frac{q^2L^2}{8\beta})}{[\omega-(\omega_i(q)+\Delta\omega_i(q,L))]^2+[\Gamma_0/2]^2}d^3q \qquad (1)$$

where $\rho(L)$ is Gaussian particle size distribution, L is particle size and $\Gamma_0$ is the linewidth of the Raman mode in bulk crystal. The factor $\beta$ is an adjustable parameter depending on the strength of the phonon confinement in different nanomaterials. It varies from $\beta=1$ to $\beta=2\pi^2$ for Richter [14] and Cambpell [15] model respectively. In order to obtain the best fits of our experimental spectra we used higher degree of phonon confinement $\beta\sim4\pi^2$.

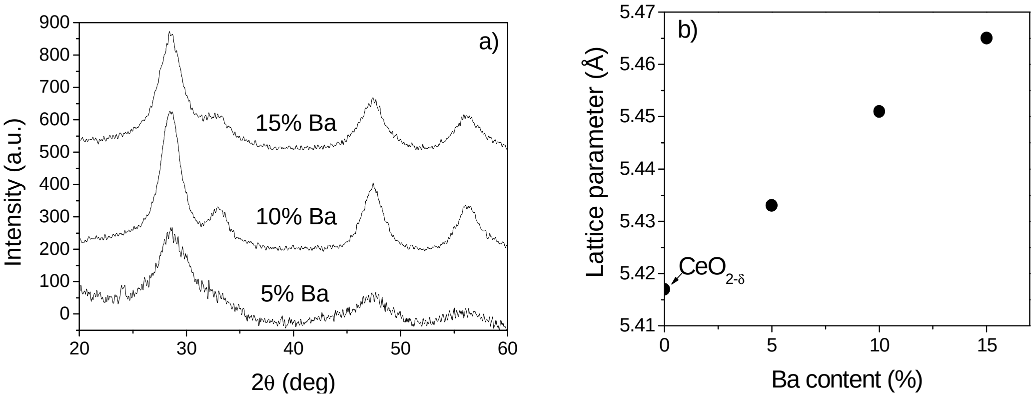

**Fig. 1** a) XRD spectra of $Ce_{0.95}Ba_{0.05}O_{2-y}$, $Ce_{0.90}Ba_{0.10}O_{2-y}$ and $Ce_{0.85}Ba_{0.15}O_{2-y}$ samples b) change of lattice parameter with dopant concentration.

Fig. 2 shows Raman spectra at room temperature of the Ba doped $CeO_2$ samples (circles) and numerical fits of the experimental data (lines) using PCM (Eq. 1).

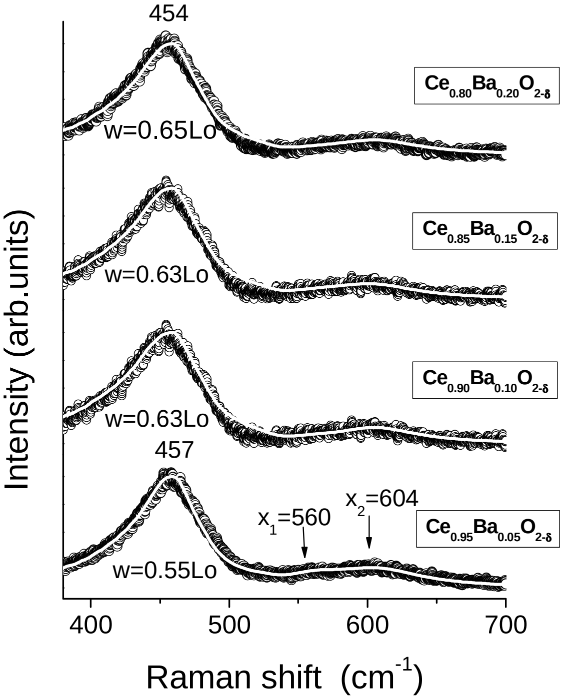

**Fig. 2** Raman spectra of Ba doped $CeO_2$ samples at room temperature.

The best accordance between the experimental and calculated curves is obtained for the average particle size *L*=6.6 nm value while the Gaussian width (*w*) is also given in Fig. 2 for each sample. As can be seen Raman spectra of $Ce_{1-x}Ba_xO_{2-y}$ samples show systematic shift of the $F_{2g}$ mode, positioned at ~ 457 $cm^{-1}$ for the lowest Ba doping concentration, to lower frequencies with increasing doping level (in a $Ce_{0.80}Ba_{0.20}O_{2-\delta}$ this mode is positioned at ~ 454 $cm^{-1}$) while the linewidth increases. Such a decrease in phonon energy is consistent with dilatation of unit cell parameter due to the incorporation of large $Ba^{2+}$ ions in cerium lattice. On the other hand the broadening of the $F_{2g}$ mode with increasing Ba content could be correlated with increasing $O^{2-}$ vacancy concentration with doping because this mode is very sensitive to disorder in oxygen sub-lattice [11].

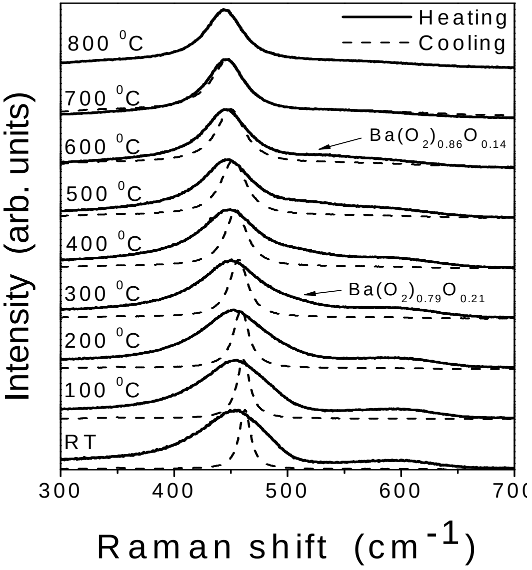

**Fig. 3** Raman spectra of $Ce_{0.85}Ba_{0.20}O_{2-y}$ sample during heating and cooling.

Besides the $F_{2g}$ Raman mode there are two additional modes at ~ 560 $cm^{-1}$ and ~ 600 $cm^{-1}$. These modes are assigned to the extrinsic oxygen vacancies introduced into the ceria lattice by substitution of $Ce^{4+}$ ions with $Ba^{2+}$ ions and intrinsic oxygen vacancies due to the nonstoichiometry of ceria nanopowders [5, 10].

One sample with the highest Ba concentration ($Ce_{0.80}Ba_{0.20}O_{2-\delta}$) was temperature treated in order to investigate the phonon behaviour and stability of this system at high temperatures. Raman spectra of $Ce_{0.80}Ba_{0.20}O_{2-\delta}$ sample, obtained by heating (lines) and gradual cooling (dashed lines) are shown in Fig. 3. Temperature dependence of mode frequency upon heating and cooling is shown in Fig. 4.

We have found that frequency and linewidth of the $F_{2g}$ mode continuously decreases by heating while the line shape becomes more symmetric up to 800 $^0$C when it becomes totally symmetric. In the Raman spectra at 300 $^0$C additional mode can be observed at 515 $cm^{-1}$. This mode can be ascribed to the Raman mode of $Ba(O_2)_{0.79}O_{0.21}$ system [16]. Frequency of this mode increases with temperature increase up to 527 $cm^{-1}$ at 600°C, which corresponds to the frequency of the $Ba(O_2)_{0.86}O_{0.14}$ system [16]. This mode disappears as the temperature further increases to 700°C. Therefore we concluded that at 300°C phase separation begins and certain types of $Ba(O_2)_{1-x}O_x$ oxide system are formed. At higher temperatures these oxides are unstable. This conclusion is valid if we have in mind that barium oxide (peroxide) begins to decompose at 500°C in air [17].

Two competitive effects could be responsible for frequency and linewidth change during heating: anharmonic and size effects. If the anharmonic effects are dominant we would expect the frequency red shift and linewidth increase with temperature, while the expected particle growth with temperature would produce an opposite trend. The frequency shift is consistent with the theory regarding the anharmonic effects in crystals [18] but the linewidth behaviour is not. The only plausible explanation for that is that phase separation on $CeO_2$ and $Ba(O_2)_{1-x}O_x$ takes place in $Ce_{1-x}Ba_xO_{2-\delta}$ samples during heating and at temperatures higher than 600 $^0$C Ba disappears from the ceria lattice. By cooling the frequency increases, reaching the value of 462.5 cm$^{-1}$ at room temperature. Linewidth continuously decreases, during cooling, down to 12.3 cm$^{-1}$ at room temperature. This behavior is typical for the anharmonic phonon behaviour in bulk samples and similar to that found in a $CeO_2$ polycrystalline sample [12] leading us to conclude that the $Ce_{0.80}Ba_{0.20}O_{2-\delta}$ sample transforms from nano to a polycrystalline $CeO_2$ sample by the above mentioned temperature treatment.

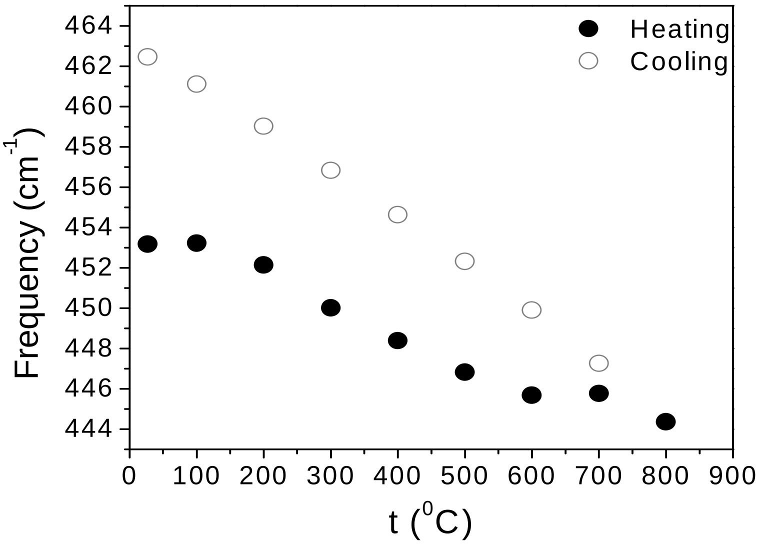

**Fig. 4** Temperature dependence of $F_{2g}$ mode frequency

Intensity of modes at 560 cm$^{-1}$ and 600 cm$^{-1}$ increases with temperature increase until 300 $^0$C when they start to decrease in intensity and become very weak at 800 $^0$C. This means that the concentration of oxygen vacancies decreases with temperature. The sample becomes more stoichiometric and the structure defects are probably removed by heat treatment.

## 4. Conclusions

In summary, $Ce_{1-x}Ba_xO_{2-\delta}$ nanocrystalline samples (5≤x≤0.20) were prepared by the SPRT method. From XRD and Raman measurements at room temperature we have concluded that $Ce_{1-x}Ba_xO_{2-\delta}$ samples are solid solutions with fluorite crystal structure in the whole doping range. The Raman spectra are well described using a spatial correlation model with combined size and inhomogeneous strain effects. At high temperatures a phase separation takes place between $CeO_2$ and $Ba(O_2)_{1-x}O_x$ systems. We demonstrated that Raman spectroscopy is a very effective diagnostic method in monitoring nanocrystalline size, detecting phase separation and the presence of intrinsic and introduced oxygen vacancies in the ceria lattice.

## Acknowledgements

This work was supported by the MSRS under the project No. 141047 and the OPSA-026283 Project within the EC FP6 Programme and SASA Project F/134.

## References

1. A. Trovarelli, Catal. Rev. Sci. Eng. 38 (1996) 439.
2. Z. Zhang, X. Du, W. Wang, J. Vac. Sci. Tech. A 18 (2000) 2928.
3. A. Walkenhorst, M. Schmitt, H. Adrian, K. Petersen, Appl. Phys. Lett. 64 (1994) 1871.
4. S. Kanakaraju, S. Mohan, A. K. Sood, Thin Solid Films 305 (1997) 191.
5. Z. Dohcevic-Mitrovic, M. Grujic-Brojcin, M. Scepanovic, Z. V. Popovic, S. Boskovic, B. Matovic, M. Zinkevich, F. Aldinger, J. Phys. Cond. Matt. 18 (2006) 1.
6. A. Sin, Y. Dubitsky, A, Zaopo, S. A. Aric`o, L. Gullo, D. La Rosa, S. Siracusano, V. Antonucci, C. Oliva, O. Ballabio, Solid State Ion. 175 (2004) 361.
7. C. Peng, Y. Wang, K. Jiang, Q. B. Bin, W. H. Liang, J. Feng and J. Meng, J. Alloys Compounds 349 (2003) 273.
8. H. Deguchi, H. Yoshida, T. Inagaki, M. Horiuchi, Solid State Ionics 176 (2005) 1817.
9. L. Minervini, M. O. Zacate, R. W. Grimes, Solid State Ionics 116 (1997) 339.
10. S. Boskovic, D. Djurovic, B. Matovic, M. Cancarevic, Z. Mitrovic-Dohcevic, Z. V. Popovic, M. Zinkevich, F. Aldinger, Materials Science Forum, 518 (2006) 95.
11. I. Kosacki, T. Suzuki, H. Anderson, P. Colomban, Solid State Ionics 149 (2002) 99.
12. J. E. Spanier, R. D. Robinson, F. Zhang, S. W. Chan, I. P. Herman, Phys. Rev. B 64 (2001) 245407.
13. Z. Dohcevic-Mitrovic, M. Grujic-Brojcin, M. Scepanovic, Z. V. Popovic, S. Boskovic, B. Matovic, M. Zinkevich, F. Aldinger, Solid State Commun. 137 (2006) 387.
14. H. Richter, Z. Wang, L. Ley, Solid State Commun. 39 (1981) 625.
15. I. H. Campbell, P. M. Fauchet, Solid State Commun. 58 (1986) 739.
16. D. de Waal, K. Range, M. Konigstein, W. Kiefer, J. Raman Spect. 29 (1998)109.
17. J. H. Lunsford, X. Yang, K. Haller, J. Laane, J. Phys. Chem. 97 (1993) 13810.
18. M. Balkanski, R.F. Wallis, E. Haro, Phys. Rev. B 28 (1983) 1928.

---

***Садржај:*** *Серија нанопрахова* $Ce_{1-x}Ba_xO_{2-y}$ *(*$5 \leq x \leq 0.20$*), добијена је методом самораспростируће синтезе на собној температури (SPRT). За карактеризацију узорака коришћене су методе дифракције рендгенских зрака (XRD)и Раман спектроскопије.Сви узорци су чврсти раствори флуоритне структуре чија је средња величина кристалиа око 5nm. Померај Раман* $F_{2g}$ *мода ка нижим енергијама и његово асиметрично ширење може се објаснити комбинованим ефектима фононског конфајнмента и стрејна. Појава додатних модова на ~560 cm*$^{-1}$ *и ~600 cm*$^{-1}$*, приписује се постојању уведених и својствених* $O^{2-}$ *ваканција у церијумовој решетки. Раман спектри одгреваног* $Ce_{0.80}Ba_{0.20}O_{2-\delta}$ *узорка указују на нестабилност овог система.*

***Кључне речи:*** *Ba допирани нанопрахови церијума, XRD метод, Рамановo расејање, сепарација фаза.*

---

Vol. **112** (2007) *ACTA PHYSICA POLONICA A* No. 5

---

Proceedings of the International School and Conference on Optics and
Optical Materials, ISCOM07, Belgrade, Serbia, September 3–7, 2007

# The Effects of Nonstoichiometry on Optical Properties of Oxide Nanopowders

M. Šćepanović[a], M. Grujić-Brojčin[a,*],
Z. Dohčević-Mitrović[a], K. Vojisavljević[b],
T. Srećković[b] and Z.V. Popović[a]

[a]Center for Solid State Physics and New Materials
Institute of Physics, Pregrevica 118, 11080 Belgrade, Serbia
[b]Institute of Multidisciplinary Research, Kneza Višeslava 1,
Belgrade, Serbia

In this paper we illustrate the change of optical properties of mechanically activated wurtzite ZnO powder and laser synthesized anatase $TiO_2$ nanopowder due to the nonstoichiometry caused by mechanical activation and/or laser irradiation in vacuum. Both of the investigated materials are widely used in optoelectronics and the examination of their optical properties under different preparation and environmental conditions is of great practical interest.

PACS numbers: 77.84.Bw, 73.63.Bd, 78.67.–n, 78.55.–m, 78.30.–j

## 1. Introduction

The high surface-to-volume ratio of nanocrystals suggests that the surface properties have significant effects on their structural and optical properties. This could be related to the presence of gap surface states arising from surface nonstoichiometry, unsaturated bonds, etc. [1]. Therefore the investigation and control of the surface processes is an important step toward understanding the optical properties of oxide nanocrystals.

Optical properties of as prepared and laser irradiated mechanically activated ZnO powder and laser synthesized anatase $TiO_2$ nanopowder were investigated by photoluminescence (PL) and Raman spectroscopy. The spectra excited by different lines of $Ar^+$ and He–Cd lasers at room temperatures in air and vacuum are compared.

## 2. Experiment

A commercial ZnO powder (Kemika, p.a. 99.96%) was mechanically activated by grinding in a vibro-mill with steel rings. The grinding time was

---

[*] corresponding author; e-mail: myramyra@phy.bg.ac.yu

30 and 300 minutes and the powders are labeled as ZnO(30) and ZnO(300), respectively. Average crystallite size obtained from X-ray diffraction (XRD) results are: 190 nm for ZnO(0), 106 nm for ZnO(30), and 44 nm for ZnO(300) [2]. Anatase $TiO_2$ nanopowder was synthesized by laser-induced pyrolysis, using titanium isopropoxide as a liquid precursor. The produced powder was calcined in air for 4 h at 500°C, and its average crystallite size obtained from XRD was about 18 nm.

Raman measurements were performed in the backscattering geometry using the 457.9 nm of $Ar^+$ and 442 nm line of HeCd laser, Jobin-Yvon U1000 monochromator and a photomultiplier as a detector. PL spectra were excited by 457.9 nm of $Ar^+$ laser, as well as UV (325 nm) and visible (442 nm) lines of a He–Cd laser, using the same equipment as in the Raman measurements. All experiments are performed at room temperature in air and vacuum.

## 3. Results and discussion

### *3.1. ZnO*

Raman spectra taken on non-activated ZnO powder (ZnO(0)) in air and vacuum are shown in Fig. 1, where the observed first-order Raman modes are assigned

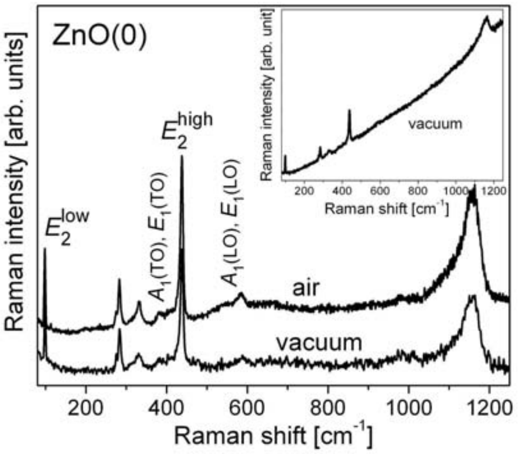

Fig. 1. Raman spectra of nonactivated ZnO powder in air and vacuum. The original Raman spectrum in vacuum before subtraction of backgrounddue to the luminescence is shown in the inset.

to the Raman spectrum of wurtzite ZnO [3, 4]: 100 ($E_2^{\rm low}$), 383 ($A_1$(TO)), 409 ($E_1$(TO)), 438.4 ($E_2^{\rm high}$), 543 ($A_1$(LO)), and 585 ($E_1$(LO)). Additionally, several second-order Raman modes positioned at 331, 776, 984, 1112, and 1159 cm$^{-1}$ were found. Two additional modes at 275 and 284 cm$^{-1}$ are related to intrinsic host lattice defects [2]. The spectrum in vacuum is obtained by subtracting background due to the luminescence from the original spectrum (inset). It is obvious that there is no substantial change in the position and shape of the Raman modes after irradiation in vacuum. Also there are no additional changes in mode behavior in the Raman spectra of activated samples due to irradiation in vacuum, but those ascribed to the tensile strain introduced by activation [2].

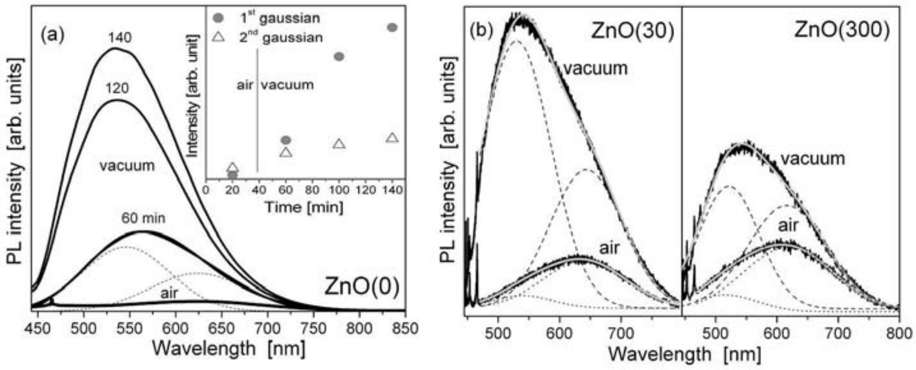

Fig. 2. PL spectra excited by 442 nm He–Cd laser line of (a) nonactivated and (b) activated for 30 and 300 min ZnO powder in air and vacuum, fitted to the sum of two Gaussians. Time dependences of Gaussian intensities of nonactivated ZnO are shown in the inset.

Figure 2 presents PL spectra of ZnO powders excited by 442 nm laser line in air and vacuum fitted to the sum of 2 Gaussians at about 540 and 640 nm. With irradiation in vacuum PL intensity rapidly increases in nonactivated ZnO powder, due to the increase in the broad green luminescence band at ≈ 540 nm, Fig. 2a. This emission attributed to electron transition, mediated by defect levels in the band gap [5], is strongly correlated to the density of singly ionized oxygen vacancies [6] located at the surface [7]. The PL spectra intensity in as-prepared activated ZnO powder, excited by the same energy, increase with activation time [2], with additional increase due to irradiation in vacuum, Fig. 2b. This was expected because the nonstoichiometry of activated ZnO powder is a consequence of both activation and irradiation in the vacuum.

Figure 3 presents PL spectra of the ZnO powders excited by the UV line of a He–Cd laser with a wavelength of 325 nm (3.81 eV) in air and vacuum. The spectra of nonactivated ZnO powder show strong emission peak at about 410 nm, with increasing intensity due to irradiation in vacuum. This violet luminescence probably originates from radiative defects related to oxygen vacancies. However, activated samples exhibit weak luminescence, both in UV and violet spectral ranges. As ZnO powders have luminescence in green and yellow/orange spectral region, PL spectra in visible range are fitted to the sum of 2 corresponding Gaussians. The intensity in this PL decreases with activation time [2], while there is no significant change in these spectra due to irradiation in vacuum. This indicates that oxygen vacancy complexes, as specific defects, are not a green luminescence center in ZnO excited by UV light; they may in fact act as the quenching centers [8].

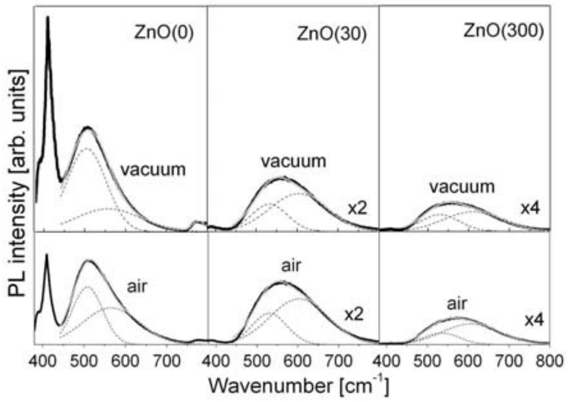

Fig. 3. PL spectra of nonactivated ZnO powder (ZnO(0)) and ZnO powder activated for 30 (ZnO(30)) and 300 min (ZnO(300)), excited by 325 nm He–Cd laser line, in air and vacuum, fitted to the sum of 2 Gaussians.

### *3.2. TiO*$_2$

Raman spectra of $TiO_2$ nanopowder in the air and vacuum, presented in Fig. 4a, confirm its anatase phase in both environments. The observed modes are assigned to the Raman spectrum of anatase single crystal: 145 ($E_g$), 197 ($E_g$), 399 ($B_{1g}$), 513 ($A_{1g}$), 519 ($B_{1g}$), and 639 cm$^{-1}$ ($E_g$) [9]. Laser irradiation in vacuum causes great intensity decrease in the Raman spectrum and small blueshift and broadening of $E_g$ mode. These changes can be ascribed to nonstoichiometry in anatase $TiO_2$ [10, 11].

Figures 4b and c show the PL spectra of anatase $TiO_2$ nanopowder excited by 457.9 nm line of $Ar^+$ laser with different irradiation times in vacuum and air, respectively. As the visible luminescence of anatase $TiO_2$ is attributed to 3 different physical origins: oxygen vacancies, surface states and self-trapped excitons [12, 13], the spectra are fitted by a sum of 3 Gaussian modes at about 1.95, 2.20, and 2.40 eV, respectively. Dependence of intensities of these Gaussians on the irradiation time in vacuum and air is presented in Fig. 4d. The intensity of all modes is greater in vacuum than in air, resulting in overall PL intensity increase with irradiation time in vacuum, and subsequent decrease in air. However, the position of PL maximum depends on the relative intensity of those 3 modes. Its redshift in vacuum can be related to the *greatest* increase in PL mode attributed to oxygen vacancies.

## 4. Conclusion

Nonstoichiometry in ZnO powders induced by mechanical activation and laser irradiation in vacuum has a great influence on the PL spectra, depending on activation time and laser excitation energy. It causes the prominent changes both in the PL intensity and position in the spectra excited by visible line of He–Cd

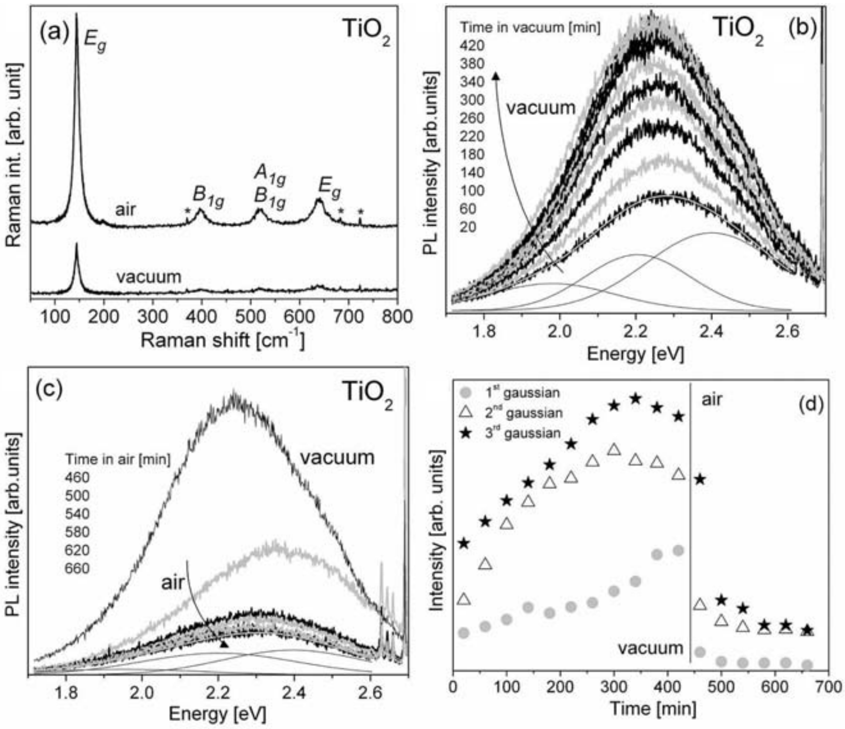

Fig. 4. (a) Raman spectra of anatase $TiO_2$ nanopowder in air and vacuum (* — plasma lines). PL spectra of $TiO_2$ nanopowder in vacuum (b) and air (c), excited by 457.9 nm $Ar^+$ laser line, with Gaussian intensity of PL bands (d).

laser. These changes are related to the enormous increase in green luminescence excited by visible light, which is strongly correlated to the density of oxygen vacancies located at the surface. Drastic decrease in PL intensity excited by UV line of He–Cd laser in activated ZnO suggests that the surface defects introduced by mechanical activation may act as quenching centers for such luminescence. Different behavior of green luminescence excited by visible and UV light after laser irradiation in vacuum indicates that it can originate from different defect-related transitions depending on the excitation energy.

The observed visible broad-band luminescence in anatase $TiO_2$ nanopowder is decomposed into 3 PL bands originating from oxygen vacancies, surface states, and self-trapped excitons. These bands are very sensitive to the surface defects introduced by oxygen deficiency. Therefore the intensity and position of the complex PL band are determined by intensities of particular bands and they are strongly dependent on irradiation conditions.

This study confirms crucial role of surface defects, especially oxygen vacancies, in the optical properties of oxide nanopowders and shows how these properties could be changed by preparation and laser irradiation under different conditions.

## Acknowledgments

This work was supported by the MSRS under the projects No. 141047 and 142040 and the OPSA-026283 project within EC FP6 Programme.

## References

[1] M.A. Hines, P. Guyot-Sionnest, *J. Phys. Chem.* **100**, 468 (1996).

[2] M. Šćepanović, T. Srećković, K. Vojisavljević, M.M. Ristić, *Sci. Sint.* **38**, 169 (2006).

[3] C.A. Arguello, D.L. Rousseau, S.P.S. Porto, *Phys. Rev.* **181**, 1351 (1969).

[4] J.M. Calleja, M. Cardona, *Phys. Rev. B* **16**, 3753 (1977).

[5] Y. Du, M.-S. Zhang, J. Hong, Y. Shen, Q. Chen, Z. Yin, *Appl. Phys. A* **76**, 171 (2003).

[6] K. Vanheusden, C.H. Seager, W.L. Warren, D.R. Tallant, J.A. Voigt, *Appl. Phys. Lett.* **68**, 403 (1996).

[7] D. Li, Y.H. Leung, A.B. Djurišć, Z.T. Liu, M.H. Xie, S.L. Shi, S.J. Xu, W.K. Chan, *Appl. Phys. Lett.* **85**, 1601 (2004).

[8] T. Ohsaka, F. Izumi, Y. Fujiki, *J. Raman Spectrosc.* **7**, 321 (1978).

[9] J.C. Parker, R.W. Siegel, *Appl. Phys. Lett.* **57**, 943 (1990).

[10] M.J. Šćepanović, M.U. Grujić-Brojčin, Z.D. Dohčević-Mitrović, Z.V. Popović, *Mater. Sci. Forum* **518**, 101 (2006).

[11] T. Sekiya, S. Kamei, S. Kurita, *J. Lumin.* **87-89**, 1140 (2000).

[12] Y. Lei, L.D. Zhang, G.W. Meng, G.H. Li, X.Y. Zhang, C.H. Liang, W. Chen, S.X. Wang, *Appl. Phys. Lett.* **78**, 1125 (2001).

[13] K. Vanheusden, C.H. Seager, W.L. Warren, D.R. Tallant, J. Caruso, M.J. Hampden-Smith, T.T. Kodas., *J. Lumin.* **75**, 11 (1997).

PHONONS 2007 IOP Publishing
Journal of Physics: Conference Series **92** (2007) 012042 doi:10.1088/1742-6596/92/1/012042

# Raman scattering from low frequency phonons confined in CeO$_2$ nanoparticles

**S Aškrabić, R Kostić, Z Dohčević-Mitrović and Z V Popović**

Centre for Solid State Physics and New Materials, Institute of Physics, P. O. Box 68, Pregrevica 118, 11080 Belgrade, Serbia

E-mail: `sonask@phy.bg.ac.yu`

**Abstract.** CeO$_2$ nanopowder samples synthesized by self-propagating room temperature method were investigated by Raman spectroscopy. The phonon modes observed in the low frequency region ($\omega < 70$ cm$^{-1}$) can be well described by the elastic continuum model, assuming that nanoparticles are of perfect spherical shape and isotropic. Both rigid boundary and stress-free surface cases were analyzed. The calculated vibrational frequency dependencies on the particle diameter were used to identify the modes: ($l$=2, $n$=0), ($l$=0, $n$=0) and ($l$=0, $n$=1). Using the facts that mode frequencies scale inversely with particle dimension ($\omega \sim 1/\mathrm{D}$) and that mode-radiation coupling coefficient for this type of vibrations is $1/\omega$, the correspondence between the particle size distribution and the Raman intensity was made. Particle diameter values ranging from 7 to 8 nm for the rigid boundary condition give the best description of the experimental spectra. This coincides well with the average particle diameter value of 8 nm acquired from the phonon confinement model.

## 1. Introduction

Raman scattering from confined acoustic vibrations in nanoparticles was observed in the low frequency part of spectra of various materials. The elastic sphere model (ESM) was generally used to analyze the acoustic phonon confinement. This model describes the oscillations of homogeneous elastic sphere and was successfully applied to explain the experimental spectra of nanoparticles [1, 2, 3, 4, 5]. According to ESM, the frequency of an acoustic Raman mode is scaled as the inverse of the dimension of a vibrating particle.

In this paper we give an overview of the possibilities for the extraction of information on nanoparticle size distribution from the low-frequency Raman spectra of CeO$_2$ nanoparticles. We calculated linear coefficients relating vibrational frequency and the particle diameter from ESM [2, 6]. We regarded our experimental spectrum as a superposition of several ESM modes and treated the inhomogenous broadening of the spectrum as a consequence of the non-uniform particle size distribution of the sample. Based on this, the average particle size was evaluated. Results were compared to the particle size value deduced from phonon confinement model (PCM) that accounts for the optical phonon confinement, size and inhomogeneous strain effects [7].

## 2. Experimental Results

The nanocrystalline CeO$_2$ samples were obtained by self propagating room temperature synthesis [7] and analyzed by X-ray diffraction. The CeO$_2$ crystallite size was about 6 nm.

Micro-Raman spectra were taken in the backscattering configuration and analyzed using a Jobin Yvon T64000 spectrometer, equipped with nitrogen cooled charge-coupled-device detector. As an excitation source we used the 514.5 nm line of Ar-ion laser.

Figure 1 shows Raman spectra of nano- and polycrystalline $CeO_2$ samples measured at room temperature. The strongest intensity mode at about 457 $cm^{-1}$ (in polycrystalline sample at 464.3 $cm^{-1}$) represents the optical Raman $F_{2g}$ mode, which softens in nano-sample as a consequence of phonon confinement effects. From the fits of optical $F_{2g}$ mode with PCM the average particle size value can be deduced and for this sample it is 8 nm.

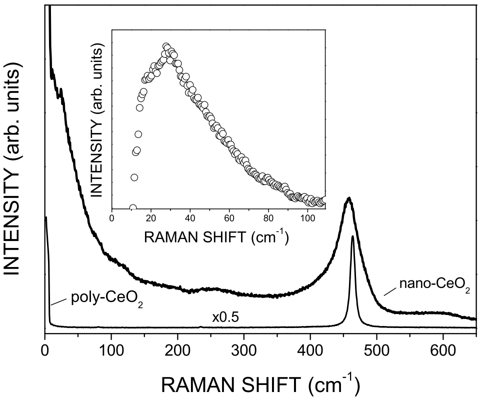

**Figure 1.** Room temperature Raman spectra of nano- and poly-crystalline $CeO_2$. Inset: corrected Raman spectrum of nano-$CeO_2$ in the 0-110 $cm^{-1}$ spectral range.

Weak intensity feature at about 270 $cm^{-1}$ is ascribed to the second order Raman scattering. In the inset of figure 1 we have shown corrected experimental Raman spectrum of nano-$CeO_2$ in the low-frequency region 0-110 $cm^{-1}$. The intensity of the elastic scattering background was subtracted by $A/\omega^n$ approximation [5].

## 3. Vibrations of homogenous elastic nanospheres of $CeO_2$

Low-frequency Raman peaks in nanocrystalline materials, ascribed to confined acoustic phonon-like vibrations, can be well interpreted as vibrations of a three-dimensional homogenous elastic sphere using Navier's equation and imposing spherical symmetry:

$$\rho\ddot{\mathbf{u}} = (\lambda + 2\mu)\nabla(\nabla\cdot\mathbf{u}) - \mu\nabla\times(\nabla\times\mathbf{u}), \tag{1}$$

where $\mathbf{u}$ represents mechanical displacement vector $\mathbf{u}(\mathbf{r},t) = \mathbf{u}(\mathbf{r})e^{-i\omega t}$ , while $\lambda$ and $\mu$ are parameters of material known as the Lame's constants and $\rho$ is the mass density. Mass density of $CeO_2$ is 7300 kg/m$^3$, transverse and longitudinal sound velocities are respectively: $v_T = \sqrt{\mu/\rho} =$ 2890 m/s and $v_L = \sqrt{(\lambda + 2\mu)/\rho} = 6600$ m/s [8].

Different boundary conditions were applied in solving Eq.(1): rigid boundary condition (no displacement at the particle surface) [2, 3, 6] and stress-free surface condition (no force acting on the particle surface) [1, 4, 5]. Two types of vibrational modes were obtained: spheroidal and torsional modes [2]. The calculated solutions express the linear dependence of $\omega$ on the inverse diameter of a nanoparticle. The Raman frequency is related to the particle diameter D as: $\omega^R_{ln} = \frac{\omega}{2\pi c} = \frac{\beta_{ln}}{D}$, where $\beta_{ln}$ characterize the solutions of the Eq.(1), $l$ is the angular momentum quantum number. The solutions $\beta_{ln}$ for spheroidal $l$=0, $l$=1 and $l$=2 and torsional $l$=1 and $l$=2 modes for two different boundary conditions are presented in Table 1 (a) and (b), respectively. According to the group theory analysis the spheroidal $l$=0 and $l$=2 modes are Raman active [9].

## 4. Results and discussion

Intensity of Raman scattering by small particles is expressed by formula [10] :

$$I(\omega) = A\frac{n(\omega)}{\omega}C(\omega)g(\omega) \tag{2}$$

**Table 1.** Calculated values of dimensionless variables $\beta_{ln}$ for fundamental spheroidal (SPH) and torsional (TOR) modes in $CeO_2$ for: rigid boundary (a) and stress-free surface condition (b).

| **(a)** | spheroidal | | | torsional | |
|---|---|---|---|---|---|
| $l$ | $n$ | $\beta_{ln} \cdot 10^7$ | $l$ | $n$ | $\beta_{ln} \cdot 10^7$ |
| 0 | 0 | 314.42 | 0 | 0 | - |
| | 1 | 540.62 | | 1 | - |
| | 2 | 763.31 | | 2 | - |
| 1 | 0 | 33.66 | 1 | 0 | 137.78 |
| | 1 | 114.07 | | 1 | 236.88 |
| | 2 | 137.79 | | 2 | 334.36 |
| 2 | 0 | 176.62 | 2 | 0 | 176.73 |
| | 1 | 222.31 | | 1 | 278.89 |
| | 2 | 278.73 | | 2 | 377.87 |

| **(b)** | spheroidal | | | torsional | |
|---|---|---|---|---|---|
| $l$ | $n$ | $\beta_{ln} \cdot 10^7$ | $l$ | $n$ | $\beta_{ln} \cdot 10^7$ |
| 0 | 0 | 199.96 | 0 | 0 | - |
| | 1 | 431.16 | | 1 | - |
| | 2 | 654.20 | | 2 | - |
| 1 | 0 | 113.00 | 1 | 0 | 176.73 |
| | 1 | 225.26 | | 1 | 278.89 |
| | 2 | 298.82 | | 2 | 377.87 |
| 2 | 0 | 81.41 | 2 | 0 | 76.69 |
| | 1 | 160.00 | | 1 | 218.82 |
| | 2 | 267.63 | | 2 | 322.43 |

where $n(\omega)$ is Bose-Einstein factor, $C(\omega)$ is the mode-radiation coupling factor, $g(\omega)$ is the density of states and A is the scaling constant. It had been shown that the mode-radiation coupling factor scales inversely with the vibrational frequency: $C(\omega) \sim \frac{1}{\omega}$ for small spherical particles [10]. According to ESM, Raman spectrum would consist of discrete peaks if all the particles were of same dimensions. We presumed that the density of states reflects the particle size distribution, N(D), through the relation: $g(\omega)$ =N(D= $\frac{\beta_{ln}}{\omega}$) [5]. The most often size distributions encountered in different nanomaterials can be well approximated with Gaussian ($\mathrm{N(D)} \sim e^{-\frac{(\mathrm{D}-\mathrm{D}_0)^2}{2\sigma^2}}$) or Log-normal ($\mathrm{N(D)} \sim e^{-\frac{(\ln(\mathrm{D}/\mathrm{D}_0))^2}{2\sigma^2}}$) distribution functions.

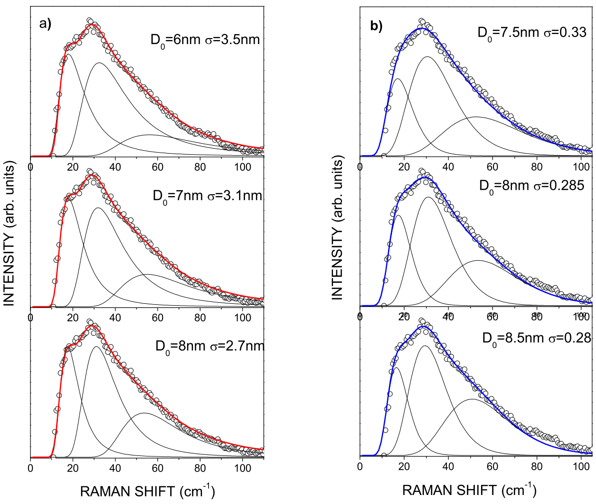

**Figure 2.** Experimental spectra (open circles) fitted with calculated Raman lines (solid lines) for rigid boundary condition: **(a)** Gaussian distribution, **(b)** Log-normal distribution.

In the low frequency region of the obtained Raman spectrum, there is a broad structure with two maxima positioned at the frequencies 18 $cm^{-1}$ and 28 $cm^{-1}$. Due to the significant broadening, the low frequency Raman spectrum was fitted with three ESM modes ($l$=2, $n$=0), ($l$=0, $n$=0) and ($l$=0, $n$=1). Intensities of these modes were calculated according to Eq.(2) including Gaussian or Log-normal particle size distribution. Most frequent diameter, $D_0$, distribution width, $\sigma$ and constants A corresponding to the three modes, were treated as free parameters. The position and broadening of each peak in the calculated spectra are determined by $\beta_{ln}$, $D_0$ and $\sigma$. A mode position shifts towards lower frequencies as $D_0$ and $\sigma$ increase and $\beta_{ln}$ decreases.

The theory implies that the spheroidal ($l$=0, $n$=0) mode should be the most intensive in the $l$=0 series of solutions [10]. The same applies for the first quadrupolar mode ($l$=2, $n$=0) in the $l$=2 series. From the results shown in Table 1 (a) and (b) it is obvious that $\beta_{00} > \beta_{20}$, which implies that the most intensive mode from figure 2, at about 28 $cm^{-1}$ corresponds to the spherical ($l$=0, $n$=0) mode, while the mode at 18 $cm^{-1}$ can be ascribed to ($l$=2, $n$=0) mode.

We analyzed the case of rigid boundary particles first. Curves plotted in the figure 2 (a) illustrate that the Gaussian distributions with $D_0$ having value from the interval $6-8$ `nm` coincide well with the experimental Raman spectra. The distributions with higher values of $D_0$ from this interval are more likely to occur since they need to be narrower and approach zero value more rapidly as the diameter approaches zero.The Log-normal distributions of the particle diameter for the values of $D_0$ in interval $7.5-8.5$ nm produced satisfactory fit of the experimental spectra (see figure 2 (b)). The best fits were acquired for the Gaussian distribution with parameters ($D_0$=7nm, $\sigma$=3.1nm), and Log-normal distribution with parameters $D_0$=8nm, $\sigma$=0.285. If the results from these fits are compared to the value of the mean particle size diameter of 8nm, acquired from PCM, it can be concluded that values of $D_0$ from the interval $7-8$ nm (in the rigid boundary case) describe best the particle size distribution of the investigated sample.

In the case of stress-free surface the values of $\beta_{20}$ and $\beta_{00}$ led to sufficiently distinct peaks in the Raman spectrum for $D_0$ ranging from 5 nm to 6.7 nm, without possibility to produce the satisfactory fit of the experimental data. Small size of the particles ($6-8$ nm) often leads to high particles' agglomeration which might be the reason for rigid boundary vibrations, since it can act as powder matrix [3].

## 5. Conclusion

We identified the low-frequency Raman feature as scattering from the vibrations of small spheres. Taking into account the correspondence between Raman intensity and particle size distribution, Raman intensity was calculated as the sum of three ESM modes intensities: ($l$=2, $n$=0), ($l$=0,$n$=0) and ($l$=0, $n$=1). The best agreement between experimental and calculated spectrum was obtained for the rigid boundary case and not for stress-free boundary condition. The reason can be found in high agglomeration of the nanoparticles when the particles are of small dimensions as in our case or in the presence of microstrain effects that influence strongly the optical Raman mode in ceria nanopowder. The mean particle diameter could not be determined exactly because of the resemblance of the calculated curves for the particle diameter interval $6-8$ nm in the case of Gaussian size distribution and for the interval $7.5-8.5$ nm for Log-normal distribution. The idealization imposed by ESM model might be the reason for the lack of unique interpretation of the experimental results, but the actual particle size distribution might also differ from those used in our calculations.

## Acknowledgments

This work is supported by the Ministry of Science of the Republic of Serbia, under the project No. 141047 and the OPSA-026283 project within EC FP6 Programme. S.A. wishes to thank M. Šćepanović for helpful discussions.

## References

[1] Tanaka A, Onari S and Arai T 1993 *Phys. Rev.* B **47** 1237
[2] Saviot L, Champagnon B, Duval E, Kudriavtsev I A and Akimov I E 1996 *J. of Noncryst. Solids* **197** 238
[3] Dieguez A, Romano-Rodriguez A, Morante J R, Barsan N, Weimar U and Gopel W 1997 *Appl. Phys. Lett.* **71** 1957
[4] Saviot L, Champagnon B, Duval E and Ekimov A I 1998 *Phys. Rev.* B **57** 341
[5] Ivanda M *et al.* 2007 *J. Raman Spectrosc.* **38** 647
[6] Roca E, Trallero-Giner C and Cardona M 1994 *Phys. Rev.* B **49** 13704
[7] Dohčević-Mitrović Z D, Šćepanović M J, Grujić-Brojčin M U, Popović Z V, Bošković S B, Matović B M, Zinkevich M V and Aldinger F 2006 *Solid State Commun.* **137** 387
[8] Nakajama A, Yoshihara A and Ishigame M 1994 *Phys. Rev.* B **50** 13297
[9] Duval E 1992 *Phys. Rev.* B **46** 5795
[10] Montagna M and Dusi R 1995 *Phys. Rev.* B **52** 10080

Vol. **116** (2009) *ACTA PHYSICA POLONICA A* No. 1

Proceedings of the Symposium A of the European Materials Research, Warsaw, September 2008

# Anharmonicity Effects in Nanocrystals Studied by Raman Scattering Spectroscopy

Z. Dohčević-Mitrović*, Z.V. Popović and M. Šćepanović
Center for Solid State Physics and New Materials, Institute of Physics, Belgrade, Serbia

Phonon–phonon interactions were investigated in various nanocrystalline powders like anatase $TiO_{2-\delta}$, pure $CeO_{2-\delta}$ and ceria doped with Nd(Gd) analyzing temperature dependent Raman spectra of these systems. Phonon confinement model based on size, inhomogeneous strain and anharmonic effects was used to properly describe the evident changes present in the Raman spectra of pure and doped ceria nanocrystalline samples. In small particles of pure and doped ceria nanocrystals, when size effects have minor impact on Raman modes, four phonon anharmonic processes prevail under the three-phonon ones. When nanopowdered particles are grown enough size effects provoke changes of the anharmonic interactions when three-phonon coupling prevails over the four-phonon anharmonic processes. In nanocrystalline anatase $TiO_2$ evident blueshift of the most prominent $E_g$ Raman mode probably originates from dominant four-phonon anharmonic interactions.

PACS numbers: 63.22.−m, 78.67.Bf, 78.30.−j, 61.72.uj

## 1. Introduction

Physical properties of materials are dependent on temperature. Temperature affects the population of the different levels for each normal mode provoking the change of the lattice parameters. Any change of the lattice parameters with temperature is attributed to the anharmonicity of the lattice potential. As an effect of the anharmonic interaction, a nonequilibrium phonon population decays into phonons of lower energy or is scattered by thermal phonons into modes of different frequencies.

The Raman spectra of various amorphous or crystalline materials show changes in line position and bandwidth with temperature [1–4]. This changes manifest in shift of line position and a change in line width and intensity. Any frequency shift or the variation of the half-width $\Gamma$ with temperature of the Raman modes are the measurements of the anharmonicity of the interactions. The phonon–phonon interactions are of special interest in nanostructured systems if we have in mind that in the literature there is still no adequate theory which describes the anharmonic effects in these systems [5, 6].

We investigated the anharmonic behaviour of the first-order Raman modes in vaious nanocrystalline materials like anatase $TiO_{2-\delta}$, pure $CeO_{2-\delta}$, and ceria doped with rare earth elements like Nd and Gd by the Raman spectroscopy method. The aim of this work was to examine the temperature-induced changes of the vibrational properties of these materials and to better understand the contribution of volume expansion and anharmonic intermode coupling to the Raman frequency shift and line width in these systems.

## 2. Experiment

Pure ceria nanocrystalline sample as well as ceria samples doped with Nd(Gd) were synthesized by self-propagating room temperature synthesis. The detailed powder preparation procedure is already described [7]. Sample of nanocrystalline anatase $TiO_2$ was supplied by Merck.

The vibrational properties of these nanopowders were studied by the Raman spectroscopy method. Micro-Raman spectra were collected in backscattering configuration using Jobin Yvon T64000 spectrometer equipped with a nitrogen cooled charge-coupled-device detector. Argon ion ($Ar^+$) laser line $\lambda = 514.5$ nm was used as an excitation source. The pure and doped ceria samples and $TiO_2$ sample were progressively heated in Linkam TS 1500 microscope heating stage, up to 1073 K and then gradually cooled down to room temperature.

## 3. Results and discussion

The variation of the frequency of the normal modes with temperature at constant pressure arises from two contributions: pure volume contribution which results from thermal expansion and pure-temperature contribution which results from cubic and quartic anharmonicities (self-energy shift). The complete expression for the frequency as a function of temperature can be expressed as

$$\omega(T) = \omega_0 + \Delta_{\mathrm{E}}(qj) + \Delta_{\mathrm{A}}(qj, \Omega) =$$

$$\omega_0 + \Delta_{\mathrm{E}} + \Delta_3 + \Delta_4, \qquad (1)$$

where $\omega_0$ is harmonic frequency, term $\Delta_{\mathrm{E}}$ arises from the thermal expansion while $\Delta_{\mathrm{A}}$ represents pure temperature contribution due to cubic ($\Delta_3$) and quartic anharmonicities ($\Delta_4$). In most solids $\Delta_{\mathrm{E}} < 0$ i.e. lattice dilation results in mode softening. Frequency shift due to thermal

---

* corresponding author; e-mail: zordoh@phy.bg.ac.yu

expansion can be evaluated from the following equation:

$$\Delta_{\mathrm{E}} = \omega_0 \left[ \exp\left( -3\gamma_i \int_0^T \alpha(T')\mathrm{d}T' \right) - 1 \right]. \tag{2}$$

Frequency shifts $\Delta_3$ and $\Delta_4$ arise from phonon–phonon interactions due to the lowest-order cubic and quartic terms in the interatomic potential. The multiphonon processes associated with the cubic terms give rise to a negative frequency shift $\Delta_3 < 0$, whereas the shift $\Delta_4$ associated with quartic anharmonicity can be either positive or negative [8]. The resultant frequency shift due to phonon–phonon interaction may be either positive or negative depending on the relative magnitudes of the anharmonic terms in the interatomic potential. The expression for $\Delta_{\mathrm{A}}$ arising from the cubic and quartic terms in the first approximation, is given [8]:

$$\begin{aligned}\Delta_{\mathrm{A}} = &-\frac{18}{\hbar^2} \sum_{q_1 q_2 j_1 j_2} \left| V \begin{pmatrix} 0 & q_1 & q_2 \\ j & J_1 & j_2 \end{pmatrix} \right|^2 \Big( \frac{n_1 + n_2 + 1}{\omega_1 + \omega_2 + 1} \\ &+ \frac{n_1 + n_2 + 1}{\omega_1 + \omega_2 - \Omega} + \frac{n_2 - n_1}{\omega_1 - \omega_2 + \Omega} + \frac{n_2 - 1}{\omega_1 - \omega_2 - \Omega} \Big) \\ &+ \frac{12}{\hbar^2} \sum_{q_1 j_1} V \begin{pmatrix} 0 & 0 & q_1 & -q_1 \\ j & j & j_1 & j_1 \end{pmatrix} (2n_1 + 1).\end{aligned} \tag{3}$$

The first term in Eq. (3) represents the cubic anharmonic term which comprises down and up conversion processes [9] whereas the second term relates to the first-order quartic term which is always positive. The $n_j(q)$ is the Bose–Einstein occupation factor of the $j$-th phonon mode with wave vector $q$ and frequency $\omega$ given as

$$n(T, \omega) = \exp\left( \frac{\hbar\omega}{k_{\mathrm{B}} T} \right) - 1. \tag{4}$$

Klemens assumed that the optical Raman phonon decays in two acoustical phonons of opposite $q$ belonging to the same branch ($j_1 = j_2$). In this case the equations for frequency and bandwidth change of Raman modes with temperature including three phonon-processes are simplified [10]:

$$\begin{aligned}\Delta(T) &= A \left( 1 + \frac{2}{\mathrm{e}^{\hbar\omega/2k_{\mathrm{B}}T} - 1} \right), \\ \Delta\Gamma(T) &= C \left( 1 + \frac{2}{\mathrm{e}^{\hbar\omega/2k_{\mathrm{B}}T} - 1} \right).\end{aligned} \tag{5}$$

Although this model is a great oversimplification, it has gained wide acceptance, specially after the work of Hart et al. on Si [11]. Balkanski et al. performed systematic temperature measurements of the line width and frequency shift of the Raman LO phonon in Si for the temperature range 5–1400 K [12] and deduced that at higher temperatures besides cubic terms the incorporation of quartic anharmonicity terms give satisfactory fits of the experimental values. In this case the frequency and bandwidth change of Raman modes with temperature looks like [12]:

$$\begin{aligned}\Delta(T) = &A \left( 1 + \frac{2}{\mathrm{e}^{\hbar\omega/2k_{\mathrm{B}}T} - 1} \right) \\ &+ B \left[ 1 + \frac{3}{\mathrm{e}^{\hbar\omega/3k_{\mathrm{B}}T} - 1} + \frac{3}{\left(\mathrm{e}^{\hbar\omega/3k_{\mathrm{B}}T} - 1\right)^2} \right],\end{aligned} \tag{6}$$

$$\begin{aligned}\Delta\Gamma(T) = &C \left( 1 + \frac{2}{\mathrm{e}^{\hbar\omega/2k_{\mathrm{B}}T} - 1} \right) \\ &+ D \left[ 1 + \frac{3}{\mathrm{e}^{\hbar\omega/3k_{\mathrm{B}}T} - 1} + \frac{3}{\left(\mathrm{e}^{\hbar\omega/3k_{\mathrm{B}}T} - 1\right)^2} \right],\end{aligned} \tag{7}$$

where $A$, $B$, $C$, $D$ are anharmonic constants.

### 3.1. Anharmonic effects in $CeO_{2-\delta}$ nanocrystals

In Fig. 1 there are given Raman spectra of $\mathrm{CeO}_{2-\delta}$ nanocrystals measured at different temperatures starting from room temperature (RT) up to 1273 K [13]. By heating, the $F_{2\mathrm{g}}$ Raman mode frequency continuously decreases and its line shape becomes less asymmetric indicating the change in crystallite size.

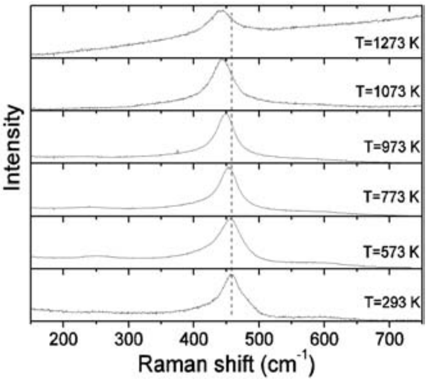

Fig. 1. Raman spectra of $\mathrm{CeO}_{2-\delta}$ nanocrystals at different temperatures.

Namely, the particle size effect provokes systematic changes in the Raman spectra of $\mathrm{CeO}_{2-\delta}$ nanocrystals when crystallite size decreases [14–16]. The evolution of the $F_{2\mathrm{g}}$ Raman mode (the mode frequency shift and asymmetrical broadening) strongly depends on the confinement and inhomogeneous strain effects due to the particle size change and is best described using phonon-confinement model (PCM) [17, 18]. On the other side, the temperature provokes the changes of the Raman line position and bandwidth. Such temperature dependence can be attributed to the phonon–phonon interactions originating from crystal anharmonicity. As an effect of anharmonic interactions an optical mode can interchange energy with other lattice modes in such a way that it decays to lower energy phonons or is scattered by thermal phonons into modes of different energy. Figure 2 shows the first-order Raman mode frequency and bandwidth change of first-order $F_{2\mathrm{g}}$ Raman mode in $\mathrm{CeO}_{2-\delta}$ nanocrystals at different temperatures.

By heating, the Raman frequency continuously decreases (circles in Fig. 2). In addition, as the temperature increases, the line shape becomes less asymmetric, and at about 1100 K it becomes totally symmetric, as

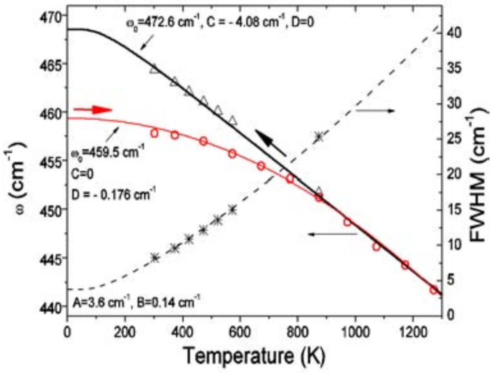

Fig. 2. Frequency (circles, triangles) and line width (asterisks) change of the $F_{2\mathrm{g}}$ Raman mode with temperature. The solid (dashed) lines are calculated data using Eqs. (6) and (7).

can be seen from Fig. 1. By cooling, the frequency of the $F_{2\mathrm{g}}$ mode increases (triangles in Fig. 2), reaching the value of 464 $\mathrm{cm}^{-1}$ at room temperature very close to the value of $\mathrm{CeO}_2$ single crystals [19, 20] while the line width decreases with temperature decrease. Temperature dependence of the Raman mode frequency and bandwidth based on the Klemens ansatz [10], was fitted using Eqs. (6) and (7). The results of the fitting procedure (full line) applied to the experimental frequency dependence on temperature during the heating demonstrated that the anharmonicity is dominated by four-phonon anharmonic processes. Namely, as can be seen from Fig. 2, the Raman mode frequency of the nanocrystals (circles) varies as $T^2$ ($C = 0$, $D = -0.176\ \mathrm{cm}^{-1}$). We concluded that in $\mathrm{CeO}_{2-\delta}$ nanocrystals, the anharmonicity is dominated by different phonon decay processes (four-phonon processes) [13]. Upon gradual cooling down to room temperature the same fitting analysis applied to frequency (open triangles) and line width (asterix) experimental values showed that three phonon processes became dominant (see fitting parameters in Fig. 2). Such behavior pointed out that our sample suffers a transformation from nano to polycrystalline one by above mentioned heating treatment. The subtle interplay between size and anharmonic effects, depending on the heat treatment, leads to different phonon–phonon interactions in nanostructured systems under consideration.

### 3.2. *High temperature Raman study of $Ce_{0.75}Nd_{0.25}O_{2-\delta}$ nanocrystals*

The Raman spectra of $\mathrm{Ce}_{0.75}\mathrm{Nd}_{0.25}\mathrm{O}_{2-\delta}$ sample obtained upon heating (circles) and cooling (dashed lines) are presented in Fig. 3. Raman spectra of the $\mathrm{Ce}_{0.75}\mathrm{Nd}_{0.25}\mathrm{O}_{2-\delta}$ sample from Fig. 3 were analyzed using the phonon confinement model-PCM that incorporates size, inhomogeneous strain and anharmonic effects [21].

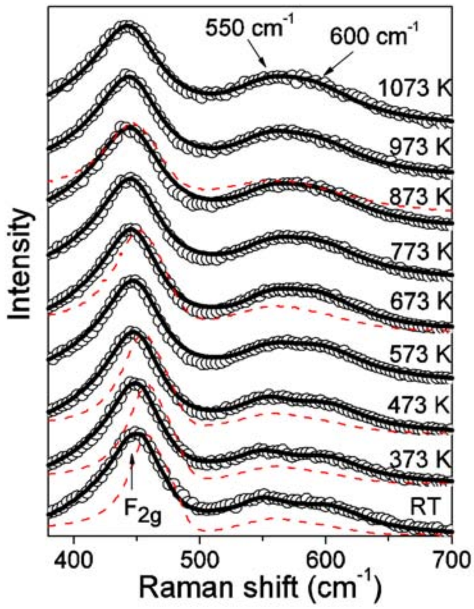

Fig. 3. Raman spectra of $\mathrm{Ce}_{0.75}\mathrm{Nd}_{0.25}\mathrm{O}_{2-\delta}$ sample obtained upon heating (circles) and cooling (dashed lines). The solid lines are calculated spectra using PCM model.

In the PCM there are included inhomogeneous strain effect through the term $\Delta\omega(q, L)$ using Gaussian particle size distribution function $\rho(L)$ and anharmonic effects through terms $\Delta\omega(T)$, $\Gamma(T)$:

$$I(\omega) = \sum_{i=1}^{3} \int_0^\infty \rho(L)\mathrm{d}L \times \int_{\mathrm{BZ}} \frac{\exp\left(-\frac{q^2L^2}{8\beta}\right)\mathrm{d}^3q}{[\omega - (\omega_i(q) + \Delta\omega)]^2 + [\Gamma(T)/2]^2}, \tag{8}$$

where the wave vector $q$ is expressed in units of $2\pi/a$ ($a$ is the lattice constant), $L$ is the particle diameter, $\Delta\omega = \Delta\omega_i(q, L) + \Delta\omega(T)$ and $\beta$ is an adjustable parameter concerning the strength of the phonon confinement in nanomaterials. The full lines in Fig. 3 are the calculated spectra based on Eq. (8). Using the PCM that incorporates anharmonic and size effects we were able to calculate the change of average particle size at higher temperatures and to estimate the particle growth influence on the $F_{2\mathrm{g}}$ Raman mode behaviour. From the PCM model we obtained that particle size increased from 6 nm to 12 nm during the heating [21]. The detailed study of the frequency (bandwidth) behavior upon heating revealed that four-phonon anharmonic processes dominate over size effects and three-phonon anharmonic processes in nanocrystalline grains (see Fig. 4a) similar to pure ceria nanocrystals. On the other side, if we take into account that particles grow during the heating we would expect the upshift of the $F_{2\mathrm{g}}$ mode frequency (triangles in Fig. 4a) and line width decrease. Experimentally evident redshift and broadening of the $F_{2\mathrm{g}}$ mode during heating, clearly points to the fact that anharmonicity effects at higher temperatures influence more the frequency (line width) change than size effects [21]. The temperature dependence of $F_{2\mathrm{g}}$ mode frequency and line width upon

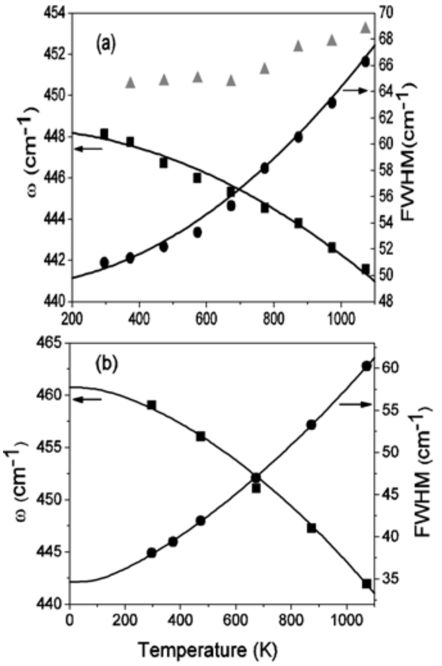

Fig. 4. Frequency and line width change (a) upon heating and (b) upon gradual cooling down to room temperature. The solid lines represent calculated data for the frequency (bandwidth) change with temperature. The best fitting parameters are given in Ref. [21].

cooling (see Fig. 4b) is similar to microceria sample where three phonon processes became dominant [21].

### 3.3. Phonon–phonon interactions in $Ce_{0.85}Gd_{0.15}O_{2-\delta}$ nanocrystals

The Raman spectra (circles) of $\mathrm{Ce_{0.85}Gd_{0.15}O_{2-\delta}}$ nanocrystalline sample from Fig. 5 in the temperature range 293–1100 K exhibit significant changes similar to pure and Nd-doped ceria samples. With increasing temperature the $F_{2g}$ mode shifts to lower frequencies and becomes less asymmetric while the line width increases. Such a behavior can be attributed to the anharmonicity interactions at elevated temperatures. The Raman spectra (circles) are analyzed by PCM model (Eq. (8)) and the calculated spectra are presented with solid lines. Detailed analysis of frequency (line width) behavior with temperature revealed the change of the phonon–phonon coupling in this system. Namely, careful analysis of the evolution of $F_{2g}$ Raman mode with temperature showed that temperature dependence of the bandwidth, given in Fig. 6b, is determined by four-phonon anharmonicity up to the 573 K (full line fit).

At higher temperatures when the particles are grown enough size effects provoke the changes in phonon–phonon interactions influencing the bandwidth of the Raman mode in such a way that three-phonon anharmonic interactions prevail over the four-phonon ones (dashed line fit). The best fit of the frequency (full line) during the heating up to 573 K was obtained including only the four-phonon anharmonic term (see Fig. 6a) while at higher temperatures three phonon decay processes became dominant (dashed line). Anharmonic fitting parameters for both quantities are also presented in Fig. 6a and b. From such an analysis, we concluded that different phonon decay channels dominate in nanocrystalline

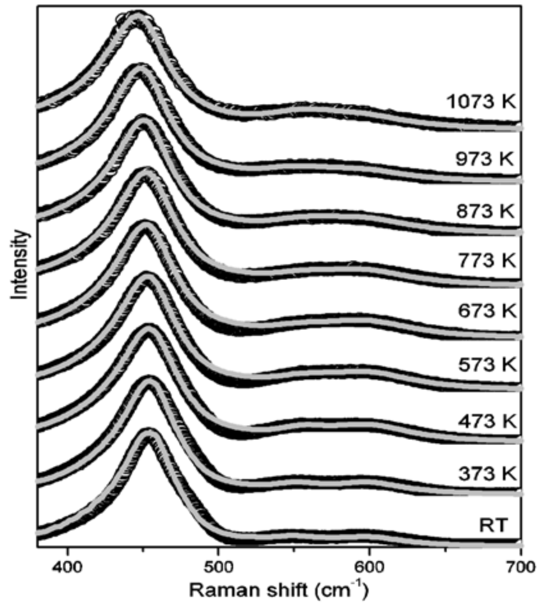

Fig. 5. Raman spectra of $\mathrm{Ce_{0.85}Gd_{0.15}O_{2-\delta}}$ sample at different temperatures (circles). The solid lines are calculated spectra using PCM.

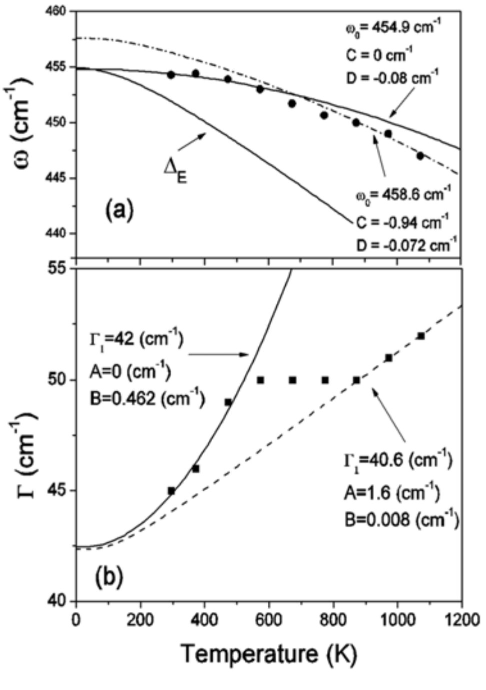

Fig. 6. Temperature dependence of the $F_{2g}$ Raman mode (a) frequency and (b) line width during heating.

grain than in larger grain and pure anharmonicity effects at temperatures up to 573 K have more influence on the frequency (bandwidth) than size effects [22]. At temperatures higher than 573 K three phonon processes became dominant. In Fig. 6a there is also presented the calculated frequency shift due to the pure-volume contribution — $\Delta_{\mathrm{E}}$ (line) [23]. The frequency redshift due to the thermal expansion would be higher than the experimentally obtained frequency shift. This suggests that anharmonic couplings of phonons influence more the frequency behaviour of $F_{2g}$ Raman mode during heating than thermal expansion. The Raman spectrum at room temperature after cooling (Fig. 7a) is narrower, blue shifted regarding the starting spectrum but still at lower frequency than in the bulk counterpart meaning that particles are in nanometric range. Upon cooling frequency shifts to higher values while bandwidth decreases (Fig. 7a). The best fit of the frequency (line width) behaviour with cooling down to room temperature, presented in Fig. 7b with full (dashed) lines, was obtained including three phonon anharmonic processes which become dominant. This implies that the particles are grown enough so the phonon–phonon interactions are more similar to polycrystalline ceria [22].

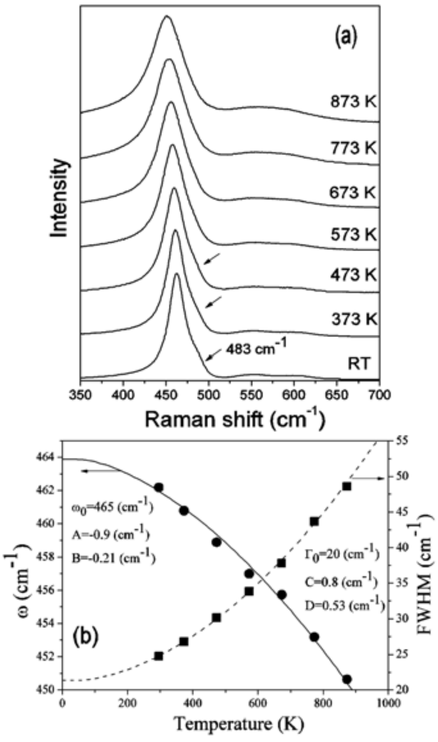

Fig. 7. (a) Raman spectra of $Ce_{0.85}Gd_{0.15}O_{2-\delta}$ sample upon gradual cooling down to room temperature and (b) variation of the $F_{2\mathrm{g}}$ mode frequency and line width upon gradual cooling. Full (dashed) lines represent fits of the line position and line width using Eqs. (6) and (7).

### 3.4. *Intrinsic anharmonicity in nanocrystalline anatase TiO2*

$TiO_2$ in anatase phase has six first-order Raman active modes among which low frequency $E_{\mathrm{g}(1)}$ and $E_{\mathrm{g}(2)}$ modes exhibit frequency shift up (hardening behavior) with increasing temperature while the other four modes exhibit softening behavior with rising temperature [24–26]. In Fig. 8 there is presented the temperature dependence of the $E_{\mathrm{g}(1)}$ mode frequency. The Raman shift dependence on temperature can be attributed to two effects, one being the thermal expansion or volume change and the other optical-phonon anharmonic couplings. The variation of the frequency of the Raman modes with temperature at constant pressure arises from two contributions: pure volume contribution which results from thermal expansion and pure-temperature contribution which results from cubic and quartic anharmonicities. Temperature dependence of each vibrational mode at constant pressure can be expressed

$$(\partial \ln \omega / \partial \ln T)p = -(\alpha/k)(\partial \ln \omega / \partial \ln P)_T$$
$$+(\partial \ln \omega / \partial \ln T)_V, \qquad (9)$$

where $\alpha$ is the volume thermal expansion coefficient and $k$ is the isothermal volume compressibility. Above equation can be written in terms of measured pressure and temperature dependence of the Raman-active mode as

$$(\Delta\omega_T)_P = -(\Delta\omega_P)_T + (\Delta\omega_T)_V =$$
$$\mathit{\Delta}_{\mathrm{E}}(qj) + \mathit{\Delta}_{\mathrm{A}}(qj, \mathit{\Omega}). \qquad (10)$$

In his work Osaka measured pressure and temperature dependence of each anatase mode and was able to separate the thermal expansion contribution from pure phonon–phonon interactions and to estimate their influence on each Raman mode in anatase $TiO_2$ [25]. From this study he deduced, as well as later Gao in nanocrystalline anatase [26], that anharmonic couplings of optical phonons become much stronger upon increasing temperature in the $E_{\mathrm{g}(1)}$ mode than quasiharmonic contribution arising from thermal expansion. Both authors deduced that strongly intrinsic anharmonicity is responsible for

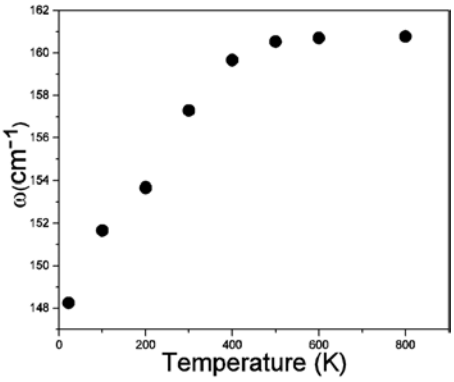

Fig. 8. Frequency of the $E_{\mathrm{g}(1)}$ mode versus temperature.

frequency blueshift of this mode upon increasing temperature. The unusual hardening behavior of the lowest-frequency $E_g$ mode was explained by Gao and others [25, 26] through three- and four-phonon processes where three-phonon anharmonic processes dominate over the four-phonon anharmonic interaction. If we have in mind that three-phonon decay (scattering) processes bring to mode softening while the quartic terms may be either positive or negative [8] we deduced that only quartic terms (see Eq. (3)) dominate and suppress the contribution from thermal expansion and from cubic anharmonic terms. This means that contrary to Gao and other authors temperature dependence of the main Raman mode seeks for new explanation and this will be strong motiv for our further investigation.

## 4. Conclusion

We examined the effects of temperature-induced changes on vibrational states of nanocrystalline materials like $CeO_{2-\delta}$, ceria doped with Nd (Gd) and $TiO_{2-\delta}$ using the Raman spectroscopy. At high temperatures, in pure and Nd doped ceria nanomaterials, four-phonon anharmonic processes dominate over three-phonon processes and the size effects have less influence on the Raman mode behavior than anharmonic effects. In a case of Gd doped ceria nanocrystals up to 300°C four-phonon coupling dominates but with further temperature increase the three-phonon coupling prevails indicating that the particles are grown enough to behave similar to polycrystalline sample. The Raman spectra after heat treatment demonstrated that these samples are still in nanometric range but anharmonic behavior is similar to their bulk counterparts. The unusual hardening of the lowest-frequency $E_g$ mode in anatase nanopowders can be assigned to the intrinsic anharmonicity due to the dominant contribution of positive quartic terms.

## Acknowledgments

This work was supported by the Ministry of Science and Technological Development of Republic of Serbia under the project No. 141047, the OPSA-026283 Project within the EC FP6 Programme and SASA project F-134.

## References

[1] G. Morell, W. Pérez, E. Ching-Prado, R.S. Katiyar, *Phys. Rev. B* **53**, 5388 (1996).

[2] N.S. Yuksek, N.M. Gasanly, A. Aydinli, *J. Raman Spectrosc.* **35**, 55 (2004).

[3] P. Verma, S.C. Abbi, K.P. Jain, *Phys. Rev. B* **51**, 16660 (1995).

[4] J. Serrano, M. Cardona, T.M. Ritter, B.A. Weinstein, A. Rubio, C.T. Lin, *Phys. Rev. B* **66**, 245202 (2002).

[5] K.A. Alim, V.A. Fonoberov, A.A. Balandina, *Appl. Phys. Lett.* **86**, 053103 (2005).

[6] M.X. Gu, L.K. Pan, B.K. Tay, C.Q. Sun, *J. Raman Spectrosc.* **38**, 780 (2007).

[7] S. Boskovic, D. Djurovic, Z. Dohcevic-Mitrovic, Z. Popovic, M. Zinkevich, F. Aldinger, *J. Power Sources* **145**, 237 (2005).

[8] A.A. Maradudin, A.E. Fein, *Phys. Rev.* **128**, 2589 (1962).

[9] J. Kulda, A. Debernardi, M. Cardona, F. de Geuser, E.E. Haller, *Phys. Rev. B* **69**, 045209 (2004).

[10] P.G. Klemens, *Phys. Rev.* **148**, 845 (1966).

[11] T.R. Hart, R.L. Aggarwal, Benjamin Lax, *Phys. Rev. B* **1**, 638 (1970).

[12] M. Balkanski, R.F. Wallis, E. Haro, *Phys. Rev. B* **28**, 1928 (1983).

[13] Z.V. Popović, Z. Dohčević-Mitrović, A. Cros, A. Cantarero, *J. Phys., Condens. Matter* **19**, 496209 (2007).

[14] I. Kosacki, V. Petrovsky, H.U. Anderson, P. Colomban, *J. Am. Ceram. Soc.* **85**, 2646 (2002).

[15] Z.D. Dohčević-Mitrović, M.J. Šćepanović, M.U. Grujić-Brojčin, Z.V. Popović, S.B. Bošković, B.M. Matović, M.V. Zinkevich, F. Aldinger, *Solid State Commun.* **137**, 387 (2006).

[16] M.D. Hernandez-Alonso, A.B. Hugria, A. Martinez--Arias, J.M. Coronado, J.C. Conesa, J. Soria, M. Fernandez-Garcia, *Phys. Chem. Chem. Phys.* **6**, 3524 (2004).

[17] H. Richter, Z.P. Wang, L. Ley, *Solid State Commun.* **39**, 625 (1981).

[18] I.H. Campbell, P.M. Fauchet, *Solid State Commun.* **58**, 739 (1986).

[19] T. Sato, S. Tateyama, *Phys. Rev. B* **26**, 2257 (1982).

[20] W.H. Weber, K.C. Hass, J.R. McBride, *Phys. Rev. B* **48**, 178 (1993).

[21] Z.D. Dohčević-Mitrović, M. Radović, M. Šćepanović, M. Grujić-Brojčin, Z.V. Popović, B. Matović, S. Bošković, *Appl. Phys. Lett.* **91**, 203118 (2007).

[22] S. Aškrabić, Z.D. Dohčević-Mitrović, M. Radović, M. Šćepanović, Z.V. Popović *J. Raman Spectrosc.*, DOI 10.1002/jrs.2177.

[23] H. Hayashi, M. Kanoh, C.J. Quan, H. Inaba, S. Wang, M. Dokiya, H. Tagawa, *Solid State Ionics* **132**, 227 (2000).

[24] K.R. Zhu, M.S. Zhang, Q. Chen, Z. Yin, *Phys. Lett. A* **340**, 220 (2005).

[25] T. Ohsaka, *J. Phys. Soc. Japan* **48**, 1661 (1980).

[26] K. Gao, *Physica B* **398**, 33 (2007).

Vol. 116 (2009) ACTA PHYSICA POLONICA A No. 1

Proceedings of the Symposium A of the European Materials Research, Warsaw, September 2008

# Use of Phonon Confinement Model in Simulation of Raman Spectra of Nanostructured Materials

M. Grujić-Brojčin*, M.J. Šćepanović, Z.D. Dohcević-Mitrović and Z.V. Popović
Center for Solid State Physics and New Materials, Institute of Physics
Pregrevica 118, Belgrade 11080, Serbia

The simulation of the Raman spectra of nanostructured materials, where the effects of frequency shift and asymmetric broadening of the Raman modes play an important role, can be very useful in systematic characterization of these materials. Use of phonon confinement model for calculating Raman spectra of different nanomaterials is considered both from the viewpoint of different confinement function and the confinement strength, as well as the dimensionality of the confinement model. The phonon dispersion relations and the choice of their approximation are also studied. The influence of particle size distribution on the shape of the calculated spectra is discussed and contributions of Gaussian and asymmetric Gaussian distribution are compared. The effects of average and inhomogeneous strain on the behavior of simulated Raman spectra are also discussed. The results of the phonon confinement model are compared to the experimental spectra of $CeO_2$ and anatase $TiO_2$ nanopowders.

PACS numbers: 81.07.Wx, 78.30.−j, 63.22.−m, 07.05.Tp

## 1. Introduction

Phenomenological phonon confinement model (PCM) is widely used method in modeling Raman spectra of nanomaterials. For spherical particle of diameter $L$ and Gaussian confinement function, the resulting Raman intensity $I(\omega)$ can be presented as [1, 2]:

$$I(\omega) \propto \sum_{i=1}^{m} \int_0^\infty \rho(L)\,\mathrm{d}L \int_{\mathrm{BZ}} \frac{\exp\left(\frac{-q^2L^2}{8\beta}\right)\mathrm{d}^3q}{[\omega-\omega_i(q)]^2+(\Gamma/2)^2}, \qquad (1)$$

where $\rho(L)$ is the particle size distribution (PSD), $q$ is wave vector in units of $\pi/a$ ($a$ — unit cell parameter), and $\Gamma$ is the intrinsic mode line width. The sum is carried over $m$ dispersion curves $\omega_i(q,T)$, depending on mode degeneration $m$.

## 2. Results and discussion

The confinement factor $\beta$ in literature often varies from $\beta = 1$ in the Richter confinement model [1] to $\beta = 2\pi^2$ in the Campbell model [2], depending on confinement boundary conditions in different nanomaterials. Higher confinement factor leads to greater shift and broadening of the Raman spectrum, comparing to bulk (when $\beta \to 0$).

The confinement dimension is also important factor in calculating Raman intensity, offering a lot of possibilities in modeling different types of nanomaterials [3]. The three-dimensional (3D) PCM is appropriate for 0D objects such as powders, quantum dots, etc. where the infinitesimal volume element in Eq. (1) can be written as $\mathrm{d}^3q \propto q^2\mathrm{d}q$. For 2D confinement (1D objects such as quantum wires, etc.) it is $\mathrm{d}^3q \propto q\mathrm{d}q$ and for 1D confinement (2D objects — quantum wells, nanolayers etc.) $\mathrm{d}^3q \propto \mathrm{d}q$. With 3D confinement the broadening of Raman spectrum is the most pronounced [4].

To calculate the contributions of the optical phonons over a whole Brillouin zone (BZ) to the Raman spectra of nanoparticles, the phonon dispersion relations $\omega_i(q)$ are included in PCM. However, dispersion relations sometimes cannot be explicitly determined. In this way, the phonon dispersions for $E_\mathrm{g}$ mode of anatase $TiO_2$ used by different authors [5–8] presented in Fig. 1a, show obvious discrepancy, especially away from center of BZ. Also, the choice of approximations for dispersion relations has great influence on the shape of the Raman spectrum. Two phonon dispersions of anatase $E_\mathrm{g}$ mode in $\Gamma$–$X$ direction, calculated by Mikami et al. [9], fitted by cosine, $\omega(q) = A + B(1 - \cos qa)$, and polynomial, $\omega(q) = A + B_1q + B_2q^2 + \ldots + B_5q^5$ functions, are shown in Fig. 1b. Corresponding Raman intensities are calculated along upper branch only (Fig. 1c) and both branches together (Fig. 1d). Although polynomial functions fit calculated phonon dispersions more precisely, the behaviour of both the linewidth and shape of corresponding Raman spectrum (Fig. 1(d)) suggests cosine dispersion as more proper for simulating Raman spectra of anatase $TiO_2$ [8].

The Raman mode asymmetry is the result not only of phonon confinement in whole BZ, but also the PSD. In

---

* corresponding author; e-mail: myramyra@phy.bg.ac.yu

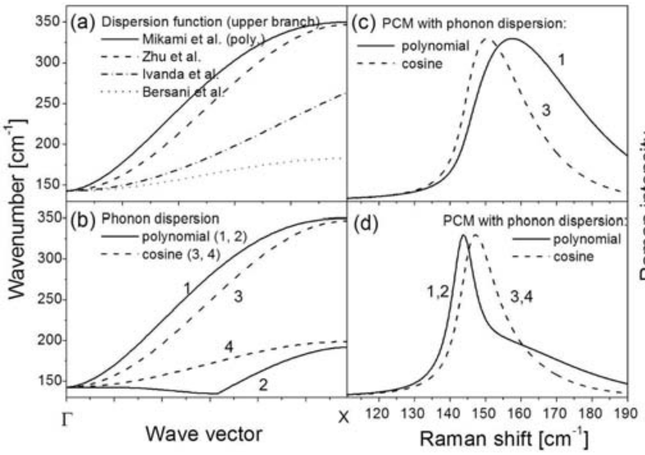

Fig. 1. The comparison of phonon dispersion functions for anatase $E_\mathrm{g}$ Raman mode in $\Gamma$–$X$ direction (a) published by different authors and (b) fitted by cosine (dashed line) and polynomial function (full line). $E_\mathrm{g}$ Raman mode intensity calculated by PCM using cosine (dashed line) and polynomial (full line) fit for dispersion functions: (c) upper dispersion branch only and (d) both branches in $\Gamma$–$X$ direction of BZ. Parameters of $\mathrm{TiO_2}$: $L_0 = 12$ nm, $\Gamma_0 = 8\ \mathrm{cm^{-1}}$, $\omega_0 = 144\ \mathrm{cm^{-1}}$, $\beta = 2\pi^2$.

Eq. (1) PSD is included by distribution function $\rho(L)$. Gaussian PSD $\rho(L) = (1/\sigma\sqrt{2\pi})\exp(-(L-L_0)^2/2\sigma^2)$ is the most used distribution for nanoparticles [10], with $L_0$ as average particle size, and $\sigma$ as standard deviation (whereas FWHM is $w = 2\sigma\sqrt{\ln 4}$). In Fig. 2a the anatase $E_\mathrm{g}$ Raman mode calculated by PCM with symmetrical Gaussian PSD are shown.

If the results of some relevant measurement (scanning electron microscopy (SEM), transmission electron microscopy (TEM), atomic force micoscopy (AFM)) point out to asymmetric particle size distribution, then asymmetric Gaussian distribution can be used. It is given by

$$\rho(L) = C/\sqrt{2\pi\sigma}\cdot\Big\{[1-h(L-L_0)] \times\exp\Big(-(L-L_0)^2/2\sigma_L\Big) + h(L-L_0)\exp\Big(-(L-L_0)^2/2\sigma_D\Big)\Big\}, \tag{2}$$

with $h(L-L_0)$ — step function, $L_0$ — particle size where asymmetric Gaussian has maximum, $\sigma_L$ and $\sigma_D$ — standard deviations corresponding to left and right side of the asymmetric curve, and $\sigma = (\sigma_L + \sigma_D)/2$. In Fig. 2b anatase $E_\mathrm{g}$ Raman mode calculated by PCM with asymmetrical Gaussian PSD are shown. The distribution with $\sigma_L > \sigma_D$ increases mode asymmetry and shifts spectrum towards higher frequencies. Let us note that use of asymmetrical Gaussian PSD with proper choice of parameters gives similar results as using PCM with log-normal distribution [11].

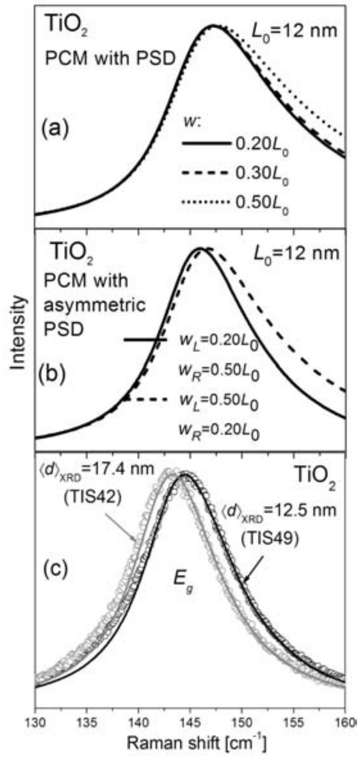

Fig. 2. $E_\mathrm{g}$ Raman mode of anatase calculated by PCM with (a) symmetric and (b) asymmetric Gaussian PSD; (c) the experimental spectra of anatase nanopowders (circle) fitted by PCM (line) with asymmetric Gaussian PSD. Parameters: $\Gamma = 8.5\ \mathrm{cm^{-1}}$, $\omega_{q=0} = 142\ \mathrm{cm^{-1}}$, phonon dispersion calculated in cosine form, with the integration in all directions of BZ [8].

The experimental Raman spectra of anatase $\mathrm{TiO_2}$ nanopowders presented by circles in Fig. 2c show the influence of particle size decreasing. It reflects through greater shift and broadening of Raman mode for sample with smaller nanoparticles, TIS49 (with mean particle size obtained from X-ray diffraction (XRD) data $\langle d\rangle_\mathrm{XRD} = 12.5$ nm), in comparison to sample TIS42 (with $\langle d\rangle_\mathrm{XRD} = 17.4$ nm). The results of PCM with asymmetric Gauss PSD with $w_L/w_D = 0.25/0.60$ for TIS49, and $w_L/w_D = 0.45/0.55$ for TIS42 (lines in Fig. 2c) show good agreement with experimental spectra.

The change of lattice parameters (lattice volume) with nanoparticle size $L$ decrease is registered in nanomaterials due to effect of microstrain [12, 13]. To include the influence of strain on the Raman spectra, the dispersion function $\omega_i(q)$ in Eq. (1) must be replaced with $\omega_i(q) + \Delta\omega_i(q)$, where $\Delta\omega_i(q)$ is the term related to microstrain, given as [10, 14]:

$$\Delta\omega_i(q) = -\gamma_i\omega_i(q)\Delta V/V_0, \tag{3}$$

where $\gamma$ is the Grüneisen parameter and $V$ volume of unit cell. In Fig. 3a the results of PCM with different kinds of strain for the Raman $F_{2\mathrm{g}}$ mode in $\mathrm{CeO_2}$ are shown. The dependence of lattice parameter $a$ in $\mathrm{CeO_2}$ cubic lattice is given by $a(L) = a_0 + k/L^2$, where $a_0$ is bulk lattice parameter (Fig. 3a, inset), whereas $\gamma = 1.23$ for $F_{2g}$ mode in $CeO_2$ [10]. When the PSD is uniform ($L_0 = \text{const}$) PCM with so-called average strain included (dashed black line, Fig. 3a) gives mode with the same shape, but redshifted in comparison with mode obtained without strain (dashed gray line).

However, with nonuniform (Gaussian) PSD, the inhomogeneous strain is introduced in PCM, according to Eq. (3). It results both in frequency shift and pronounced asymmetric broadening of calculated Raman mode (black line). For cubic lattice, where $V = a^3$, Eq. (3) can be written as $\Delta\omega_i(q) = -3\gamma_i\omega_i(q)\Delta a/a_0$. In Fig. 3b the results of PCM are compared with the experimental Raman spectrum of $CeO_{2-\delta}$ nanopowder. The Raman $F_{2g}$ mode calculated by PCM with inhomogeneous strain, symmetric Gaussian PSD ($L_0 = 7$ nm, $w = 0.52L_0$) and phonon confinement $\beta = 4\pi^2$ [14] (full line), fits the broadening of experimental spectrum better than PCM with average (dots), or inhomogeneous (dashed line) strain with $\beta = 2\pi^2$ [2, 10].

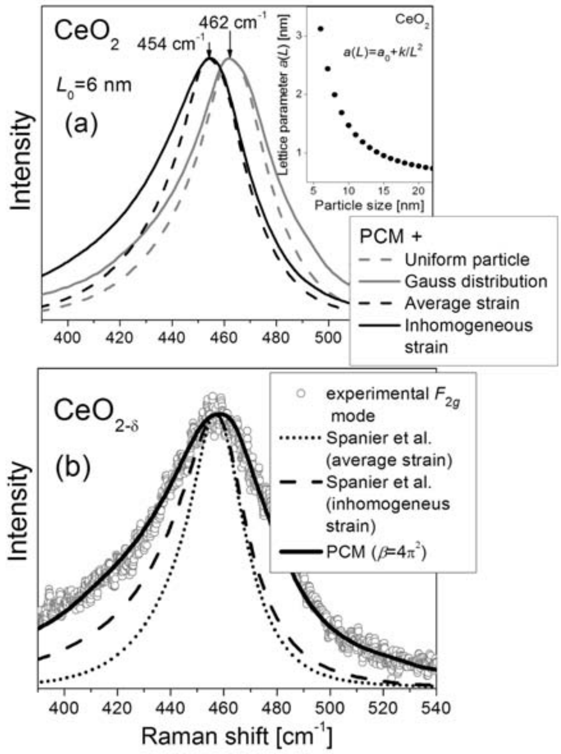

Fig. 3. (a) The comparison of PCM results for Raman $F_{2g}$ mode in $CeO_{2-\delta}$ nanopowder with $L_0 = 6$ nm (inset: the lattice parameter vs. particle size [10, 14]); (b) experimental and PCM results for $F_{2g}$ mode in $CeO_{2-\delta}$.

Opposite to $CeO_2$, the lattice parameters of tetragonal anatase $TiO_2$ decrease with nanopartical size decreasing (Fig. 4b) due to compressive strain [12, 15]. Therefore, the unit cell volume can be approximated by: $V(L) = V_0 - k_1/L^{k_2}$, with bulk unit cell volume $V_0 = a_0^2c_0$, and adjustable parameters $k_1$ and $k_2$ [15].

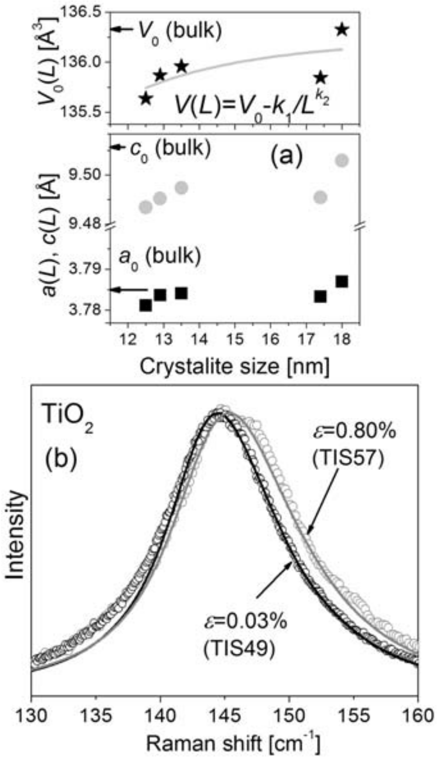

Fig. 4. (a) Lattice parameters ($a$, $c$) and unit cell volume ($V$) vs. particle size from XRD measurements [15]. (b) Experimental spectra of $E_g$ Raman mode (circles) with PCM results (lines) for anatase $TiO_2$ nanopowders.

The experimental spectra of $TiO_2$ nanopowders (TIS49 and TIS57) with different strain values $\varepsilon_{\mathrm{XRD}}$, obtained from XRD analyses, together with the results of PCM are shown in Fig. 4. Fitted spectrum for TIS49 with small strain value ($\varepsilon_{\mathrm{XRD}} = 0.03\%$) is obtained by PCM with no strain included (as in Fig. 2), whereas appropriate blueshift of $E_g$ mode caused by relatively great strain ($\varepsilon_{\mathrm{XRD}} = 0.80\%$) in TIS57 sample is simulated by PCM with inhomogeneous strain, calculated by Eq. (3) with Grüneisen parameter for anatase $E_g$ mode $\gamma_i = 4.23$ [15].

## 3. Conclusion

The results of phonon confinement model are compared to the experimental spectra of $CeO_2$ and anatase $TiO_2$ nanopowders. It is shown that proper choice of confinement parameters, phonon dispersion relations, particle size distribution and the strain type (tensile or compressive), in accordance with physical properties of the nanomaterials allows precise modeling of their Raman spectra. This confirms use of the phonon confinement model in simulation of the Raman spectra of nanostructured materials as favorable method in estimation of their nanostructural characteristics.

## Acknowledgments

This work is supported by the Serbian Ministry of Science and Technological Development under project No. 141047 and the OPSA-026283 project within the EC FP6 program.

## References

[1] H. Richter, Z.P. Wang, L. Ley, *Solid State Commun.* **39**, 625 (1981).

[2] I.I. Campbell, P.M. Fauchet, *Solid State Commun.* **58**, 739 (1986).

[3] A.K. Arora, M. Rajalakshmi, T. R. Ravindran, V. Sivasubramanian, *J. Raman Spectrosc.* **38**, 604 (2007).

[4] M.J. Šćepanović, M. Grujić-Brojčin, Z. Dohčević-Mitrović, Z.V. Popović, *J. Optoel. Adv. Mater.* **9**, 178 (2007).

[5] D. Bersani, P.P. Lottici, X.Z. Ding, *Appl. Phys. Lett.* **72**, 73 (1998).

[6] M. Ivanda, S. Music , M. Gotić , A. Turković , A.M. Tonejc, O. Gamulin, *J. Mol. Struct.* **480-481**, 641 (1999).

[7] K.R. Zhu, M.S. Zhang, Q. Chen, Z. Yin, *Phys. Lett. A* **340**, 220 (2005).

[8] M.J. Šćepanović, M. Grujić-Brojčin, Z. Dohčević-Mitrović, Z.V. Popović, *Appl. Phys. A* **86**, 365 (2007).

[9] M. Mikami, S. Nakamura, O. Kitao, H. Arakawa, *Phys. Rev. B* **66**, 1552131 (2002).

[10] J.E. Spaneir, R.D. Robinson, F. Zhang, S.-W. Chan, I.P. Herman, *Phys. Rev. B* **64**, 2454071 (2001).

[11] M. J. Šćepanović, M. Grujić-Brojčin, Z. Dohčević-Mitrović, Z.V. Popović, *Sci. Sintering* **41**, 67 (2009).

[12] V. Swamy, D. Menzies, B.C. Muddle, A. Kuznetsov, L.S. Dubrovinsky, *Appl. Phys. Lett.* **88**, 243103 (2006).

[13] F. Zhang, S.-W. Chan, J.E. Spanier, E. Apak, Q. Jin, R.D. Robinson, I.P. Herman, *Appl. Phys. Lett.* **80**, 127 (2002).

[14] Z.D. Dohčević-Mitrović, M.J. ćepanović, M.U. Grujić-Brojčin, Z.V. Popović, S.B. Boković, B.M. Matović, M.V. Zinkevich, F. Aldinger, *Solid State Commun.* **137**, 387 (2006).

[15] M.J. Šćepanović, M.U. Grujić-Brojčin, Z.D. Dohčević-Mitrović, Z.V. Popović, *Mater. Sci. Forum* **518**, 101 (2006).

Vol. **116** (2009) *ACTA PHYSICA POLONICA A* No. 1

Proceedings of the Symposium A of the European Materials Research, Warsaw, September 2008

# Raman Scattering from Acoustic Phonons Confined in Spherical Nanoparticles

R. Kostić*

Centre for Solid State Physics and New Materials, Institute of Physics
P.O. Box 68, Pregrevica 118, 11080 Belgrade, Serbia

Low-frequency Raman scattering from small spherical particles is analyzed. Frequencies of vibrational modes are calculated in elastic continuum approximation, which considers one nanoparticle as homogeneous elastic sphere. Parameters of this model are transverse ($v_{\mathrm{T}}$) and longitudinal ($v_{\mathrm{L}}$) sound velocities of material, i.e. elastic properties of bulk material. Frequencies of vibrational modes are scaled as function of mentioned bulk parameters for symmetric $l = 0$ and quadrupolar $l = 2$ spheroidal modes, in the case of stress-free boundary conditions. Calculated values are compared with the low-frequency Raman experimental results from literature (Ge, Si, CdS, CdSe, $\mathrm{CeO_2}$, ...). These calculated relations can be practically used to examine nanoparticles of any bulk material. We presented also a procedure how to establish $v_{\mathrm{L}}$ and $v_{\mathrm{T}}$ of material from low-frequency Raman spectra and dimension $d$ of particles.

PACS numbers: 61.46.Df, 63.22.–m

## 1. Introduction

The validity of elasticity theory in case of very small particles was the subject of continuous interest. Good agreement was found between results in valence-force-field model [1, 2], or atomistic approach [3] and the vibration frequencies of acoustic modes calculated using elasticity theory up to particle dimension of few nanometers.

The aim of this paper is to present some conclusions that follow from the basic case: a homogeneous spherical particle without surrounding medium in elastic continuum approximation.

## 2. Model and results

The vibrational theory of continuous elastic body is often used to describe a long-wavelength acoustic phonon that propagates in an ideal bulk crystal. Equation of motion parameters of the three-dimensional elastic body are mass density and elastic constants i.e. transverse $v_{\mathrm{T}}$ and longitudinal $v_{\mathrm{L}}$ sound velocities. As we attend to describe a confined acoustic phonon in a small crystal we must consider the boundary conditions at the surface of crystal, in our case sphere, and combine them with equation of motion in spherical coordinates [4–8].

Nanoparticles are often embedded in different material (matrix). Matrix can disable movement on the surface of nanoparticle. If there is no displacement at the particle surface, it is the case of so called rigid boundary conditions [6]. If properties of a matrix make it possible for a nanoparticle to vibrate without restrictions we can assume that there is no force acting on the particle surface, i.e. radial components of the stress tensor at the surface are zero (it is the case of so-called free-surface boundary conditions) as applied in [6]. This condition is completely fulfilled if matrix is absent.

In this paper we present results of calculation for the stress-free boundary conditions. If we assume that particles are small spheres, equation of motion must be solved in spherical coordinate. It is useful to introduce dimensionless variables: $\eta = \frac{\omega R}{v_{\mathrm{T}}} = \frac{\omega d}{2 v_{\mathrm{T}}}$ and $\xi = \frac{\omega R}{v_{\mathrm{L}}} = \frac{\omega d}{2 v_{\mathrm{L}}}$, where $R$ is radius of the particle ($d$ is diameter).

In spherical case, each value of angular momentum quantum number $l$ ($l = 0, 1, 2, \ldots$) gives a series of solutions. We numerate these solutions $n$ ($n = 0, 1, 2, \ldots$). Eigen solutions are labeled as $\eta^{nl}(\xi^{nl})$, and eigenstates are labeled as $(n, l)$. Two types of vibrational modes are obtained: spheroidal and torsional modes. As $\omega^{nl} = 2\eta^{nl} v_{\mathrm{T}}/d$ i.e. $\omega^{nl} = 2\xi^{nl} v_{\mathrm{L}}/d$, each solution gives one linear dependence $\omega^{nl} = f(1/d)$.

According to the group theory analysis the spheroidal $l = 0$ and $l = 2$ modes are Raman active. Theory implies that the spheroidal mode (0, 0) is the most intensive in the $l = 0$ series, and the most intensive of all Raman active modes. In a lot of low-frequency Raman scattering spectra only this mode was detected. The first quadrupolar mode is the most intensive in $l = 2$ series. The frequency of (0, 2) mode is almost always lower than the (0, 0) mode frequency.

We scaled $l = 0$ and $l = 2$ solutions as function of $v_{\mathrm{L}}/v_{\mathrm{T}}$. Results of these calculations are presented in Fig. 1.

---

* e-mail: rkostic@phy.bg.ac.yu

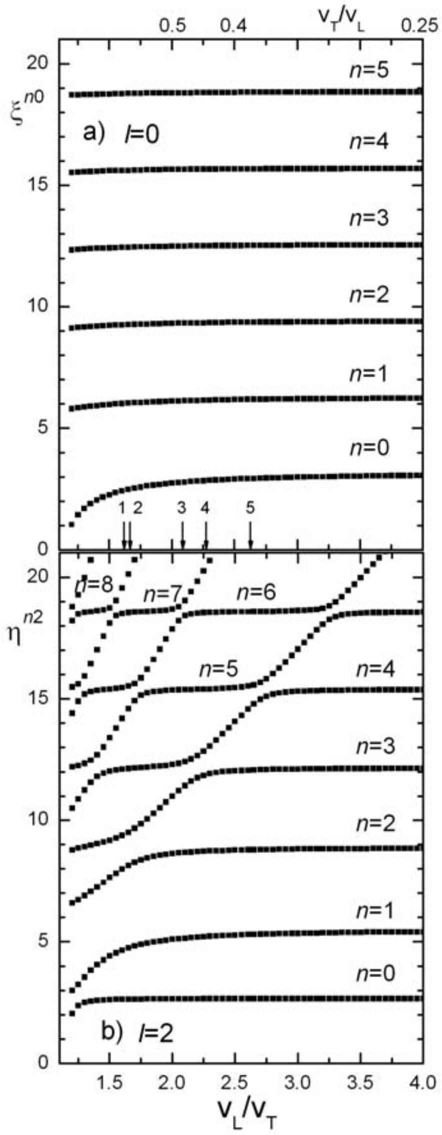

Fig. 1. Dimensionless eigensolutions: (a) $\xi^{n0}$ as function of $v_L/v_T$ for $l = 0$, $n = 0, 1, 2, \ldots, 5$; (b) $\eta^{n2}$ as function of $v_L/v_T$ for $l = 2$, $n = 0, 1, 2, \ldots, 8$. $v_L/v_T$ values of Ge(1), Si(2), Ag(3), CdSe, CeO$_2$ and CdS(4) and Au(5) are assigned by arrows at the bottom of (a).

Sound velocity $v_L$ is always bigger than $v_T$. We scaled $v_L/v_T$ interval from 1.2 to 4. We present values of $\xi^{n0}$ up to 20 i.e. $n = 5$, Fig. 1a. As we mentioned, intensity of Raman active modes decrease rapidly with increase of $n$ and modes with higher $n$ are not expected to be registered in experimental spectra. In case $v_L/v_T \gg 1$ eigensolutions converge to constant values.

In Fig. 1b we present values of $\eta^{n2}$ up to 20. For $l = 2$ case $\eta^{n2}$ eigensolutions are commonly presented to emphasize that displacements in the particle have both longitudinal and transversal nature.

If we have in mind relations $\omega^{nl} = 2\eta^{nl} v_T/d$ and $\omega^{nl} = 2\xi^{nl} v_L/d$, and calculated values presented in Fig. 1, we can establish any of relations $\frac{\omega^{n_1 l_1}}{\omega^{n_2 l_2}} = \frac{\xi^{n_1 l_1}}{\eta^{n_2 l_2}} \frac{v_L}{v_T} = \frac{\xi^{n_1 l_1}}{\xi^{n_2 l_2}} = F\left(\frac{v_L}{v_T}\right)$. These ratios do not depend on particle dimension $d$, nor material parameters $v_L$ or $v_T$ directly. They do depend on $v_L/v_T$ ratio, only.

As mode (0, 0) is the most intensive in Raman spectra, we will form relationships between frequency $\omega^{00}$ and frequencies from the series $l = 0$, $n = 0, 1, 2, \ldots$ as $\frac{\omega^{n0}}{\omega^{00}} = \frac{\xi^{n0}}{\xi^{00}} = F_0\left(\frac{v_L}{v_T}\right)$. Results of these calculations are presented in Fig. 2a.

As we mentioned, ratios $\omega^{n0}/\omega^{00}$ are independent of $d$. So, if we examine small spheres of material of known value $v_L/v_T$, characteristic ratio of frequencies $\omega^{10}/\omega^{00}$ and $\omega^{20}/\omega^{00}$ will be the same for all dimensions. This is one piece of information in attempt to interpret experimental spectra.

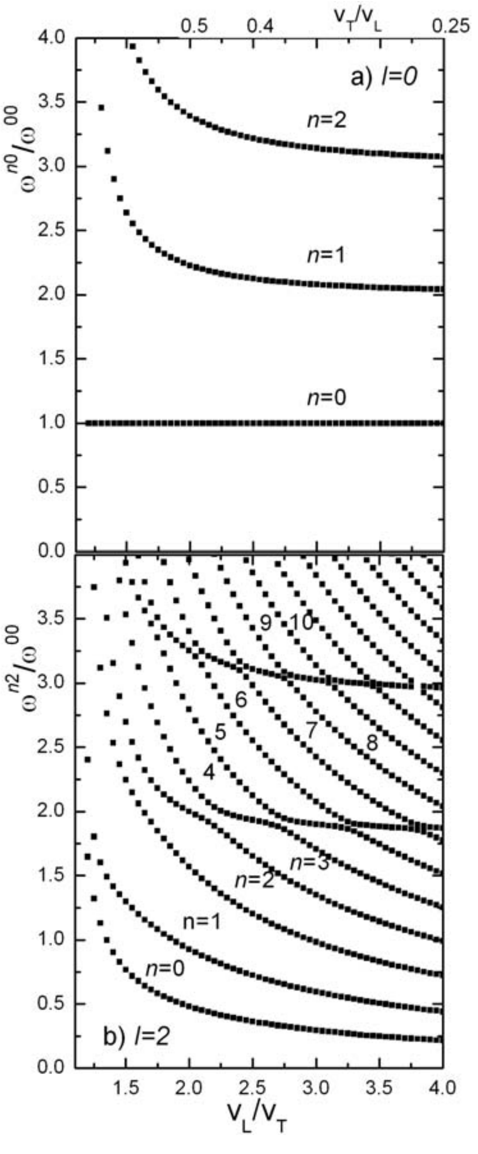

Fig. 2. (a) Frequency $\omega^{n0}/\omega^{00}$ ratio as a function of $v_L/v_T$ for $l = 0$, $n = 0, 1, 2$; (b) frequency $\omega^{n2}/\omega^{00}$ ratio as a function of $v_L/v_T$ for $l = 2$, $n = 0, 1, 2, \ldots$

If $v_\mathrm{L}/v_\mathrm{T}$ decreases below 2, $\omega^{10}/\omega^{00}$ and $\omega^{20}/\omega^{00}$ increase drastically. Similar behavior is found for $n > 2$ values that are not presented in Fig. 2a. In case $v_\mathrm{L}/v_\mathrm{T} > 2$, values of $\omega^{n0}/\omega^{00}$ coverage to constant values become less informative about $v_\mathrm{L}/v_\mathrm{T}$ value.

We also form relationships between frequency $\omega^{00}$ and frequencies from the series $l = 2$, $n = 0, 1, 2, \ldots$, $\frac{\omega^{n2}}{\omega^{00}} = \frac{\xi^{n2}}{\xi^{00}} = F_2\left(\frac{v_\mathrm{L}}{v_\mathrm{T}}\right)$. Results of these calculations are presented in Fig. 2b.

All $l = 2$ solutions are rather sensitive to $v_\mathrm{L}/v_\mathrm{T}$ value. Raman intensity of $l = 2$ modes is less than of $l = 0$ modes, and practically only first few modes from $l = 2$ series are expected to be registered and included in analysis. Mode (0, 2) is the most prominent one in $l = 2$ series. $\omega^{02} > \omega^{00}$ in a small region $v_\mathrm{L}/v_\mathrm{T} \leq 1.3$, $\omega^{02} \approx \omega^{00}$ at $v_\mathrm{L}/v_\mathrm{T} \approx 1.3$ and it is impossible to distinguish these two modes; $\omega^{02} < \omega^{00}$ in region $v_\mathrm{L}/v_\mathrm{T} > 1.3$ and $\omega^{02}/\omega^{00}$ decreases with $v_\mathrm{L}/v_\mathrm{T}$ increase. Parameters of the most materials are in $v_\mathrm{L}/v_\mathrm{T} > 1.3$ region. $\omega^{02}$, as the strongest in $l = 2$ series, is often detected in experimental Raman spectra. As $v_\mathrm{L}/v_\mathrm{T}$ increases, $\omega^{02}$ decreases and goes into the very low frequency region.

At the bottom of Fig. 1a $v_\mathrm{L}/v_\mathrm{T}$ values of a few materials are assigned. Low-frequency Raman spectra for these, already studied, materials confirm results of this analysis.

Therefore, if one central feature in low-frequency Raman spectrum is registered it can be tentatively attributed to $\omega^{00}$. Features below $\omega^{00}$, if registered, are probably $\omega^{02}$ or $\omega^{12}$ frequency. Spectral features in spectral region over $\omega^{00}$ are probably $\omega^{10}$ (if $\omega_2 \approx 2\omega^{00}$) or some of the $\omega^{n2}$ modes from $l = 2$ series.

These results can be directly used if there are at least two features in low-frequency Raman spectra at frequencies $\omega_1$ and $\omega_2$. It is reasonable to assume the most intensive Raman feature $\omega_1$ to be $\omega^{00}$. We must assume which mode from the $l = 0$ or $l = 2$ series corresponds to mode of $\omega_2$ frequency. From $\omega_2/\omega_1$ value and curves from Fig. 2, $v_\mathrm{L}/v_\mathrm{T}$ value can be determined. When $v_\mathrm{L}/v_\mathrm{T}$ value is established, $\xi^{00}$ value from $\xi^{00}(v_\mathrm{L}/v_\mathrm{T})$ (Fig. 1a) can be determined. As we already know dimension $d$, we have assumed that $\omega^{00} = \omega_1$ and using relation $v_\mathrm{L} = \omega^{00}d/2\xi^{00}$ values of $v_\mathrm{L}$ and $v_\mathrm{T}$ can be calculated. Rest of features, if any, should be at the positions that correspond to calculated values $v_\mathrm{L}$ and $v_\mathrm{T}$. These values have to be reasonable for the group of materials we are dealing with. If so, these $v_\mathrm{L}$ and $v_\mathrm{T}$ values can be adopted as new parameters of nanoparticle material. If not, we can try with some other assignment of $\omega_2$ frequency, and follow the same procedure.

## 3. Conclusion

Dimensionless eigensolutions of Raman active vibrational modes of elastic sphere are scaled as function of bulk elastic parameters. We formulated rules that characteristic frequencies must obey. If there is more than one mode registered in low-frequency Raman spectra, calculated results give possibility to establish elastic parameters of the nanosphere material.

## Acknowledgments

This work was supported by Serbian Ministry of Science and Technological Development, under project No. 141047 and OPSA-026283 project within the EC FP6 programme.

## References

[1] W. Cheng, S.F. Ren, P.Y. Yu, *Phys. Rev. B* **71**, 174305 (2005).

[2] W. Cheng, S.F. Ren, *Phys. Rev. B* **68**, 193309 (2003).

[3] N. Combe, J.R. Huntziger, A. Mlayah, *Phys. Rev. B* **76**, 205425 (2007).

[4] L. Saviot, B. Champagnon, E. Duval, I.A. Kudriavtsev, I.E. Akimov, *J. Non-Cryst. Solids* **197**, 238 (1996).

[5] E. Roca, C. Trallero-Giner, M. Cardona, *Phys. Rev. B* **49**, 13704 (1994).

[6] L. Saviot, D.B. Murray, Maria del Carmen Marco de Lucas, *Phys. Rev. B* **69**, 113402 (2004).

[7] L. Saviot, D.B. Murray, *Phys. Rev. B* **72**, 205433 (2005).

[8] M. Montagna, *Phys. Rev. B* **77**, 045418 (2008).

Vol. **116** (2009) *ACTA PHYSICA POLONICA A* No. 1

Proceedings of the Symposium A of the European Materials Research, Warsaw, September 2008

# Effect of $Fe^{2+}$ ($Fe^{3+}$) Doping on Structural Properties of $CeO_2$ Nanocrystals

M. Radović[a], Z. Dohčević-Mitrović[a,*], N. Paunović[a], M. Šćepanović[a], B. Matović[b] and Z.V. Popović[a]

[a]Center for Solid State Physics and New Materials, Institute of Physics, Belgrade, Serbia

[b]Institute of Nuclear Sciences "Vinča", 11001 Belgrade, Serbia

We have measured the Raman scattering and magnetization of pure and $Fe^{2+}$($Fe^{3+}$) doped $CeO_2$ nanopowders at room temperature. The Raman scattering spectra revealed the existence of $CeO_2$ fluorite cubic structure for all investigated samples. The Raman active mode at about 600 $cm^{-1}$, seen in all samples, can be ascribed to the $CeO_2$ intrinsic oxygen vacancies. Additional Raman modes at 720 $cm^{-1}$, 1320 $cm^{-1}$ and 1600 $cm^{-1}$, which appear in the spectra of doped samples, can be assigned to maghemite ($\gamma$-$Fe_2O_3$) cation deficient structure, to $2\omega_{LO}$ IR-allowed overtone and two magnon structure, respectively. This implies that our powders are composed of mixed valence states and have defective structure. Presence of oxygen defect states and magnetic ions can be responsible for the observed ferromagnetism at room temperature in both pure and Fe doped samples.

PACS numbers: 61.72.uj, 78.30.−j, 75.50.Tt

## 1. Introduction

Nanostructured $CeO_2$ based materials have reached significant impact in practical applications due to general improvement of catalytic [1], electrical [2], optical [3] and electrooptical [4] properties. Technology of solid oxide fuel cells is currently the most relevant field where $CeO_2$ found applications [5].

Various methods of preparation, such as sol-gel [4], spray pyrolysis [6], sputtering [3], have been used to obtain nanosized $CeO_2$. One of the major challenges for the preparation of these nanostructured oxides is precise control of particle size. In our recent studies [7–9], nanoparticles of $CeO_2$ doped with Nd, Y, and Ba were prepared with self propagating room temperature (SPRT) synthesis. With this cost and time effective method we were able to produce nanocrystalline materials with an average particle size below 10 nm. $CeO_2$ nanocrystals doped with $3d$ elements such as Fe, were obtained for the first time by this method of preparation.

Vibrational properties of nanocrystalline systems are dependent on the reduction of crystallite size. Room temperature Raman scattering measurements of $CeO_2$ nanoparticles revealed that the energy of the $F_{2g}$ Raman active mode decreases and the line width increases followed by an asymmetrical broadening with decreasing particle size [10]. Several factors as inhomogeneous strain, phonon confinement, particle size distribution and the presence of defect states were considered to explain such changes [7].

The magnetic properties of $CeO_2$ nanocrystals have been the subject of several studies [11, 12]. The existence of room temperature ferromagnetism in $CeO_2$ nanoparticles is discovered recently whereas bulk counterpart are diamagnetic. It is assumed that the origin of ferromagnetism may be the exchange interactions between unpaired electron spins arising from oxygen vacancies presented at the surfaces of nanoparticles [11].

In the present work, we used Raman scattering and magnetic measurements to determine the effect of $Fe^{2+}$ and $Fe^{3+}$ doping on structural and magnetic properties of $CeO_2$ nanocrystals.

## 2. Experiment

Nanocrystalline $Ce_{1-x}Fe_x^{2+}(Fe_x^{3+})O_{2-y}$ ($x = 0.12$ and 0.06) samples were prepared by the SPRT synthesis using metal nitrates and sodium hydroxide as the starting materials. The synthesis involves hand-mixing of starting materials in alumina mortar for 5–7 min until the mixture gets light brown. After being exposed to air for three hours, the mixture was suspended in water. Rinsing out of reaction byproduct ($NaNO_3$) was performed by centrifuge Centurion 1020D at 3500 rpm. This procedure was performed three times with distilled water and twice with ethanol. The $Fe^{2+}$ doped solid-state solution was obtained according to reaction

$$2[(0.88)Ce(NO_3)_3 \cdot 6H_2O + (0.12)FeNO_3] + 6NaOH + (1/y)O_2 \rightarrow 2Ce_{0.88}Fe_{0.12}O_{2-y} + 6NaNO_3 + 9H_2O, \qquad (1)$$

whereas $Fe^{3+}$ doped solid state solution was obtained according to reaction

---

* corresponding author; e-mail: zordoh@phy.bg.ac.yu

$$2[(0.88)\mathrm{Ce(NO_3)_3}\cdot 6\mathrm{H_2O} + (0.12)\mathrm{Fe(NO_3)_3}\cdot 6\mathrm{H_2O}]$$
$$+6\mathrm{NaOH} + (1/2 - y)\mathrm{O_2}$$
$$\rightarrow 2\mathrm{Ce_{0.88}Fe_{0.12}O_{2-y}} + 6\mathrm{NaNO_3} + 15\mathrm{H_2O}. \qquad (2)$$

Unpolarized Raman scattering measurements were performed in the backscattering configuration using micro-Raman Jobin Yvon T64000 system. As an excitation source 514.5 nm line of Ar$^+$ laser was used. In order to avoid sample heating we used very low laser power on the sample (0.24 mW).

Magnetic moment measurements at room temperature were performed using vibrating sample magnetometer (VSM 200) of 14 T cryogen free measurement system (Cryogenic Ltd.).

## 3. Results and discussion

In Fig. 1 we present room temperature Raman spectra of the $\mathrm{Ce}_{1-x}\mathrm{Fe}_x^{2+}(\mathrm{Fe}_x^{3+})\mathrm{O}_{2-y}$ ($x = 0.12$ and 0.06) samples together with the Raman spectrum of pure nanocrystalline CeO$_2$ sample. The first order $F_{2\mathrm{g}}$ Raman active mode of CeO$_2$ nanocrystals appears at 454 cm$^{-1}$. Besides the $F_{2\mathrm{g}}$ mode there are additional modes at 600 cm$^{-1}$ and 1048 cm$^{-1}$ which are assigned to intrinsic oxygen vacancies ($\mathrm{V_{Ce3+}}$) [7] and the second order Raman mode at $X$-point of the Brillouin zone [13], respectively.

In the Raman spectrum of Fe$^{2+}$ doped sample ($\mathrm{Ce_{0.88}Fe_{0.12}^{2+}O_{2-y}}$), the $F_{2\mathrm{g}}$ mode is located at nearly the same frequency as the $F_{2\mathrm{g}}$ mode of pure CeO$_2$ nanocrystalline sample, with slightly increased line width. Beside the $F_{2\mathrm{g}}$ and oxygen vacancy modes, a weak band appears at 720 cm$^{-1}$ (marked with * in Fig. 1), which is assigned to maghemite ($\gamma$-Fe$_2$O$_3$) cation deficient structure [14]. $2\omega_{\mathrm{LO}}$ (IR-active) overtone, characteristic for hematite ($\alpha$-Fe$_2$O$_3$), appears at 1320 cm$^{-1}$ [14]. The appearance of modes characteristic for different iron oxide crystal structures can be a consequence of oxidation of mixed valence iron oxide (magnetite Fe$_3$O$_4$), probably caused by laser irradiation.

In the Raman spectrum of Fe$^{3+}$ doped sample ($\mathrm{Ce_{0.88}Fe_{0.12}^{3+}O_{2-y}}$), the $F_{2\mathrm{g}}$ mode is shifted to lower energies and is broader than in the spectra of pure, Fe$^{2+}$ and Fe$^{2+}$/Fe$^{3+}$ ceria doped samples. Red shift and broadening of the $F_{2\mathrm{g}}$ mode can be ascribed to the size and strain effects [7, 10] or can be a consequence of electron molecular vibrational coupling due to the increased concentration of defects in oxygen sub-lattice of CeO$_2$ and presence of magnetic ions in ceria lattice.

The intensity of intrinsic oxygen vacancy Raman active mode ($\mathrm{V_{Ce3+}}$) in $\mathrm{Ce_{0.88}Fe_{0.12}^{3+}O_{2-y}}$ sample is more pronounced than in other samples. Such behavior confirms our previous statement that incorporation of trivalent iron in ceria lattice provokes a formation of more defective structure, i.e. higher concentration of oxygen vacancies is formed with Fe$^{3+}$ doping. The Raman active mode at 1320 cm$^{-1}$ can be assigned to $2\omega_{\mathrm{LO}}$ IR-allowed overtone of Fe$_2$O$_3$, whereas a weak structure at about 1600 cm$^{-1}$ can be ascribed to two-magnon peak of Fe$_2$O$_3$ phase [14].

In Fig. 1 there are also shown the Raman spectra of mixed valence Fe-doped ceria sample ($\mathrm{Ce_{0.88}Fe_{0.06}^{2+}Fe_{0.06}^{3+}O_{2-y}}$). The frequency of the $F_{2\mathrm{g}}$ mode, for this sample, lies between the $F_{2\mathrm{g}}$ values for Fe$^{2+}$ and Fe$^{3+}$ doped samples. The intensity of $2\omega_{\mathrm{LO}}$ IR-allowed overtone and two magnon mode of Fe$_2$O$_3$ in this sample is significantly higher than in ($\mathrm{Ce_{0.88}Fe_{0.12}^{3+}O_{2-y}}$) sample. The appearance of iron oxide Raman modes implies high structural disorder in this sample.

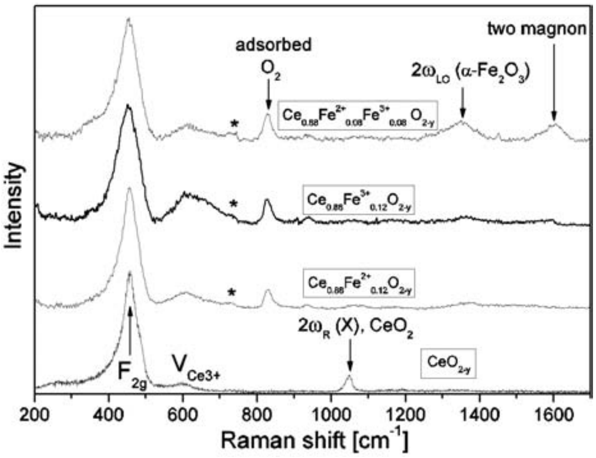

Fig. 1. Room temperature Raman spectra of Fe$^{2+}$/Fe$^{3+}$ doped and pure CeO$_2$ nanocrystalline samples.

Interesting feature in the Raman spectra of all doped samples, is a mode located at about 830 cm$^{-1}$, which is not observed in the spectra of pure CeO$_2$. This mode is characteristic for adsorbed oxygen species on the surface of CeO$_2$ nanoparticles [15] suggesting that doping with iron can lead to better chemical activity of ceria nanoparticles.

In Fig. 2 there is shown magnetization versus magnetic field for polycrystalline and nanocrystalline CeO$_2$ samples, measured at 300 K. The bulk sample shows a weak diamagnetic response, as it can be expected for CeO$_2$ with Ce$^{4+}$ ions in the $4f^0$ electronic configuration. On the other hand, CeO$_2$ nanocrystals show weak ferromagnetic behavior. It has been observed that nonmagnetic oxides at room temperature become weakly ferromagnetic when the samples are in the form of small nanoparticles [11, 12] or very thin films [16].

It was suggested that the origin of this ferromagnetism may be exchange interaction between unpaired electron spins arising from oxygen vacancies formed at surface of nanoparticles [16, 11]. We believe that $4f^1$ unpaired electron spins in Ce$^{3+}$, formed at nanoparticles surface, are responsible for room temperature ferromagnetism in nano CeO$_2$. Saturation magnetization of our CeO$_2$ nanocrystals is about 0.0055 emu/g which is comparable with previous results [11, 12].

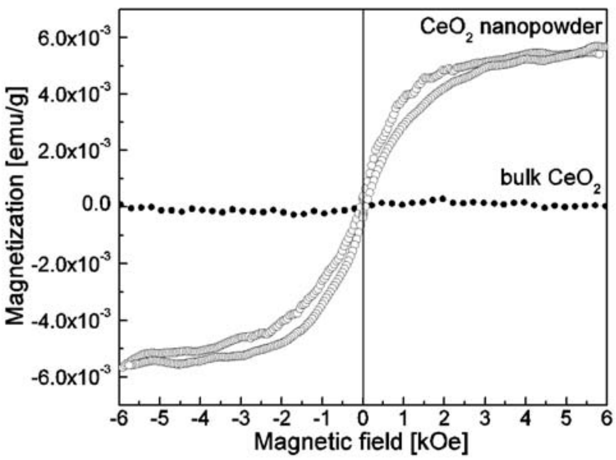

Fig. 2. Room temperature magnetization versus magnetic field for bulk and nanopowdered $CeO_2$ samples.

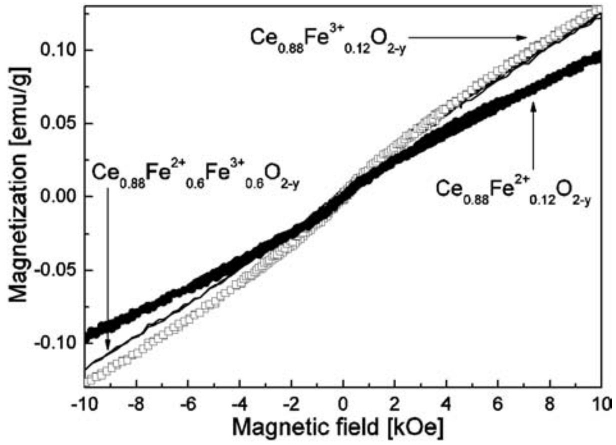

Fig. 3. Magnetization versus magnetic field for the $Ce_{1-x}Fe_x^{2+}(Fe_x^{3+})O_{2-y}$ ($x = 0.12$ and 0.06) samples measured at 300 K.

In Fig. 3 there is shown magnetization versus magnetic field for the $Ce_{1-x}Fe_x^{2+}(Fe_x^{3+})O_{2-y}$ ($x = 0.12$, 0.06) samples, measured at 300 K. It can be seen that Fe-doped $CeO_2$ samples show paramagnetic response with small ferromagnetic component in these samples.

The ferromagnetic component only, obtained by subtracting the linear paramagnetic background from $M(H)$ curves in Fig. 3 is given in Fig. 4. The hysteresis loop for the $Fe^{2+}/Fe^{3+}$ doped sample (Fig. 4) is between the loops for $Fe^{2+}$ and $Fe^{3+}$ doped samples. Saturation magnetizations (at 10 kOe) can be roughly estimated to be 0.009, 0.014 and 0.018 emu/g for the $Fe^{2+}$, $Fe^{2+}/Fe^{3+}$ and $Fe^{3+}$ doped samples, respectively.

This means that the value of saturation magnetization for the sample doped with $Fe^{2+}$, $Fe^{3+}$ is roughly in the middle between the values of saturation magnetization for $Fe^{2+}$ and $Fe^{3+}$ doped samples, i.e. saturation magnetization of this ferromagnetic component increases with the increase of oxidation state of Fe dopant.

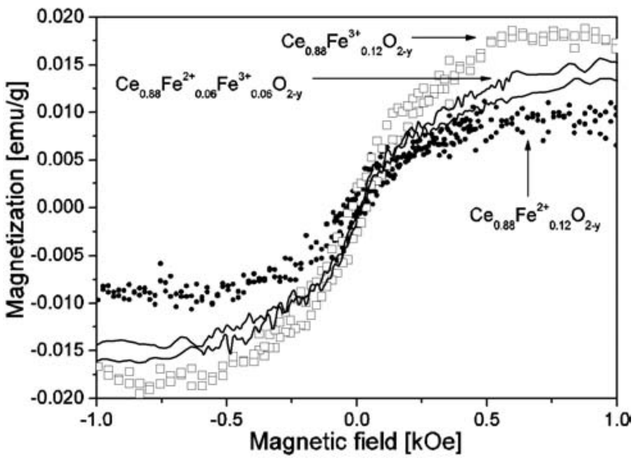

Fig. 4. Hysteresis loops for the $Ce_{1-x}Fe_x^{2+}(Fe_x^{3+})O_{2-y}$ ($x = 0.12$ and 0.06) samples measured at 300 K.

As we already mentioned the existence of $Ce^{3+}$ states may be the origin of room temperature ferromagnetism in nano $CeO_2$. The exchange interaction between $4f^1$ nonpaired electrons in $Ce^{3+}$ can result in weak ferromagnetism experimentally found in nano $CeO_2$ (see Fig. 2). By doping with Fe we can expect different behavior in the case of 2+ and 3+ valence state. Iron has $3d^6 + 4s^2$ valence electrons. In the case of low spin state of $Fe^{2+}$ ions all $3d^6$ ions are compensated ($\uparrow\downarrow\uparrow\downarrow\uparrow\downarrow$, $S = 0$) and they do not contribute to the total magnetic moment of nanoceria. In this case iron as dopant produces higher disorder in ceria structure i.e. an increase of oxygen vacancy concentration which further increases the $Ce^{3+}$ ion concentration. In this way, the ferromagnetic exchange interaction is also stronger and magnetization saturation value in $Fe^{2+}$ doped sample is a little bit higher than in pure nano $CeO_2$ (see Fig. 2 and Fig. 4). In $Fe^{3+}$ doped samples, $3d^5$ electrons in the low spin state can participate in ferromagnetic ordering ($\uparrow\downarrow\uparrow\downarrow\uparrow$, $S = 1/2$). In this case, both $Fe^{3+}$ and $Ce^{3+}$ electron spins contribute to ferromagnetic ordering. Consequently, we can expect dramatic increase in magnetization of $Fe^{3+}$ doped sample, which is experimentally observed in Figs. 3 and 4. In such a way we concluded that the existence of both $Ce^{3+}$–oxygen vacancies complexes and $Fe^{3+}$ ions in the low spin state contribute to the weak ferromagnetism in nanoceria and not only oxygen vacancies as previously stated [11, 16].

## 4. Conclusion

Nanocrystalline $Ce_{1-x}Fe_x^{2+}(Fe_x^{3+})O_{2-y}$ ($x = 0.12$ and 0.06) samples were synthesized by self propagating room temperature synthesis method. Raman spectroscopy at room temperature was applied to determine the influence of $Fe^{2+}/Fe^{3+}$ doping on structural and vibrational properties of cerium dioxide nanopowders. Doping with trivalent iron causes redshift and broadening of the $F_{2g}$ mode as a consequence of electron molecular vibrational coupling due to the increased concentration of $Ce^{3+}$–oxygen vacancies complexes and magnetic $Fe^{3+}$ ions. The existence of second order Raman modes characteristic for iron oxide suggest that there is a high structural disorder in our samples. From magnetic measurements it was established that nanocrystalline $CeO_2$ sample exhibit ferromagnetic behavior at room temperature. The Fe-doped ceria samples also exhibit small ferromagnetism at room temperature. The saturation magnetization in all doped samples is higher than in pure ceria and increases with an increase of oxidation state of Fe dopant. The presence of $Ce^{3+}$ and $Fe^{3+}$ spin electrons is responsible for observed ferromagnetism.

## Acknowledgments

This work was supported by the Ministry of Science and Technological Development of Republic of Serbia under the project No. 141047, the OPSA-026283 project within the EC FP6 Programme and SASA project F-134.

## References

[1] T. Masui, T. Ozaki, K. Machida, G. Adachi, *J. Alloys Comp.* **303**, 49 (2000).

[2] Y.-M. Chiang, E.B. Lavik, I. Kosacki, H.L. Tuller, J.Y. Ying, *Appl. Phys. Lett.* **69**, 8 (1996).

[3] S. Guo, H. Arwin, S.N. Jacobsen, K. Järrendahl, U. Helmersson, *J. Appl. Phys.* **77**, 5369 (1995).

[4] N. Ozer, *Sol. Energy Mater. Sol. Cells* **68**, 391 (2001).

[5] B.C.H. Steele, *Solid State Ionics* **129**, 95 (2000).

[6] J.L.M. Rupp, A. Infortuna, L.J. Gauckler, *Acta Mater.* **54**, 1721 (2006).

[7] Z.D. Dohčević-Mitrović, M.J. Šćepanović, M.U. Grujić-Brojčin, Z.V. Popović, S.B. Bošković, B.M. Matović, M.V. Zinkevich, F. Aldinger, *Solid State Commun.* **137**, 387 (2006).

[8] Z.D. Dohčević-Mitrović, M. Grujić-Brojčin, M. Šćepanović, Z.V. Popović, S. Bošković, B. Matović, M. Zinkevich, F. Aldinger, *J. Phys., Condens. Matter* **18**, 1 (2006).

[9] M. Radović, Z.D. Dohčević-Mitrović, M. Šćepanović, M. Grujić-Brojčin, B. Matović, S. Bošković, Z.V. Popović, *Sci. Sinter.* **39**, 281 (2007).

[10] J.E. Spanier, R.D. Robinson, F. Zhang, S.W. Chan, I.P. Herman, *Phys. Rev. B* **64**, 245407 (2001).

[11] A. Sundaresan, R. Bhargavi, N. Rangarajan, U. Siddesh, C.N.R. Rao, *Phys. Rev. B* **74**, 161306(R) (2006).

[12] Y. Liu, Z. Lockman, A. Aziz, J. MacManus-Driscoll, *J. Phys., Condens. Matter* **20**, 165201 (2008).

[13] G.A. Kourouklis, A. Jayaraman, G.P. Espinosa, *Phys. Rev. B* **37**, 4250 (1988).

[14] M.J. Massey, U. Baier, R. Merlin, W.H. Weber, *Phys. Rev. B* **41**, 7822 (1990).

[15] Y.M. Choi, H. Abernathy, H.T. Chen, M.C. Lin, M. Liu, *Chem. Phys. Chem.* **7**, 1957 (2006).

[16] M. Venkatesan, C.B. Fitzgerald, J.M.D. Coey, *Nature* **430**, 630 (2004).

Vol. **116** (2009) *ACTA PHYSICA POLONICA A* No. 1

Proceedings of the Symposium A of the European Materials Research, Warsaw, September 2008

# Low-Frequency Raman Spectroscopy of Pure and La-Doped $TiO_2$ Nanopowders Synthesized by Sol-Gel Method

M. Šćepanović[a,*], S. Aškrabić[a], M. Grujić-Brojčin[a], A. Golubović[a], Z. Dohčević-Mitrović[a], A. Kremenović[b] and Z.V. Popović[a]

[a]Center for Solid State Physics and New Materials, Institute of Physics, Belgrade, Serbia

[b]Faculty of Mining and Geology, Laboratory for Crystallography, University of Belgrade, Serbia

Pure and La-doped titania ($TiO_2$) nanopowders are synthesized by sol-gel technology. The crystallite sizes determined by X-ray diffraction measurements range from 10 to 15 nm. Dependence of structural and morphological characteristics of nanopowders on synthesis conditions and $La^{3+}$ content is investigated by the Raman spectroscopy. Very intensive modes observed in the Raman spectra of all nanopowder samples are assigned to anatase phase of $TiO_2$. Additional Raman modes of extremely low intensity can be related to the presence of a small amount of brookite amorphous phase in nanopowders, which is in accordance with the results of X-ray diffraction analysis. The particle size distribution in $TiO_2$ nanopowders was estimated from the low frequency Raman spectra, using the fact that the phonon modes in nanosized $TiO_2$ observed in the low frequency region ($\omega < 40$ cm$^{-1}$) can be well described by the elastic continuum model, assuming that nanoparticles are of perfect spherical shape and isotropic. The nanosized particle distribution obtained by this method is used for the calculation of the frequency and shape of the most intensive $E_g$ Raman mode in anatase $TiO_2$ by the phonon confinement model. The calculated broadening of this mode, associated with the particle size distribution, coincides well with the characteristics of $E_g$ mode observed in measured Raman spectra of $TiO_2$ nanopowders. This confirms the Raman spectroscopy method as a powerful tool for determination of particle size distribution in nanosized materials.

PACS numbers: 81.20.Fw, 81.07.Wx, 78.30.−j, 63.22.−m

## 1. Introduction

Titanium dioxide ($TiO_2$) has three polymorphic modifications: rutile (tetragonal, $P42/mnm$), anatase (tetragonal, $I41/amd$), and brookite (orthorhombic, $Pbca$). All of them have numerous applications as important industrial materials. In recent years, nanosized $TiO_2$, especially anatase $TiO_2$, has attracted much attention as key material for photocatalysts [1], dye-sensitized solar cells [2], gas sensors [3] and electrochromic devices [4]. The applications of nanosized anatase $TiO_2$ are primarily determined by its physicochemical properties such as crystalline structure, particle size, surface area, porosity and thermal stability. The aim of this study is to investigate the variations in anatase structure induced by doping of nanopowders with lanthanum. In our previous paper [5] it was shown that La-doping improves thermal stability of sol-gel synthesized $TiO_2$ nanopowders. The Raman spectroscopy method is primarily used here to correlate the amount of brookite phase, as well as the particle size and particle size distribution in anatase phase, with the content of La-dopant.

## 2. Experimental details

$TiCl_4$ was used as the precursor in the synthesis. The $Ti(OH)_4$ hydrogel was obtained by hydrolysis of $TiCl_4$ at 0°C with controlled addition of 2.5 wt.% aqueous ammonia into the aqueous solution of $TiCl_4$ (0.3 mol/l) and careful control of the pH value of the solution. After aging in the mother liquor for 5 h, filtering and washing out with deionized water, obtained $Ti(OH)_4$ hydrogel was converted to its ethanol-gel by repeated exchange with anhydrous ethanol for several times. The obtained alcogel was placed in a vessel, dried at 280°C and calcined at temperature of 550°C, and after that converted to the nanoparticles. In the case of La-doped $TiO_2$, $LaCl_3{\cdot}7H_2O$ was used.

Powder X-ray diffraction (XRD) was used for the identification of crystalline phases, quantitative phase analysis and estimation of crystallite size and strain. The XRD patterns were collected on a Philips diffractometer (PW1710) employing Cu $K_{\alpha_{1,2}}$ radiation.

Raman measurements were performed using 514 nm laser line of an $Ar^+/Kr^+$ laser and Jobin Yvon T64000 triple spectrometer system, equipped with confocal microscope and a nitrogen-cooled CCD detector. Low-frequency Raman measurements were performed in the backscattering geometry using the 442 nm line of a He–Cd laser as an excitation source, a Jobin Yvon U1000

---

[*] corresponding author; e-mail: maja@phy.bg.ac.yu

monochromator and a photomultiplier as a detector. All Raman scattering measurements were performed at room temperature in air.

## 3. Results and discussion

Relevant and the most intensive diffraction peaks in the XRD patterns of all samples belong to anatase crystal structure of TiO$_2$ (JCPDS card 78-2486). The presence of low-intensity diffraction peak at $2\theta \approx 30.8°$ that can be ascribed to the brookite phase of TiO$_2$ was observed in all XRD patterns (JCPDS card 29-1360). Structure refinements were performed by the Rietveld method [6]. The obtained average anatase (brookite) crystallite size was 12 nm (35 nm) and 10 nm (26 nm) for pure TiO$_2$ and TiO$_2$ doped with 1 wt.% of La, respectively. The average strain in anatase was $4.2 \times 10^{-3}$ in pure TiO$_2$, whereas its value was $5.7 \times 10^{-3}$ in La-doped TiO$_2$. The percent of brookite phase obtained by quantitative phase analysis is 16% and 24% in pure and La-doped TiO$_2$, respectively. These results show that doping with 1 wt.% of La induced crystallite size decrease, whereas strain value and brookite content increased. The large values of the average strain in brookite crystallites ($\approx 20 \times 10^{-3}$) indicate that this phase is highly disordered both in pure and La-doped samples.

In the Raman spectra of both pure and La-doped TiO$_2$ samples the dominant modes (Fig. 1a) can be assigned to the Raman active modes of the anatase crystal [7]: $\approx 143$ ($E_{g(1)}$), 197 ($E_{g(2)}$), 399 ($B_{1g(1)}$), 519 ($A_{1g}$, $B_{1g(2)}$) and 639 cm$^{-1}$ ($E_{g(3)}$). The additional Raman modes at about 243, 294, 323 and 362 cm$^{-1}$ (Fig. 1b), can be ascribed to the brookite phase of titania [8]. Low intensities and large widths of these modes confirm great disorder and partial amorphization of brookite in all the samples. The content of brookite for TiO$_2$ doped with La up to 4 wt.% [5] is higher or close to the amount in pure TiO$_2$, whereas for greater La wt.% brookite content decreases.

The position of anatase $E_{g(1)}$ Raman mode for different TiO$_2$ samples ranges between 143 and 144 cm$^{-1}$, whereas its line width varies from 12.1 to 13.7 cm$^{-1}$. Several factors can contribute to the changes in the peak position, line width and shape of this mode in TiO$_2$ nanopowders ([9] and references therein). Dominance of one or more of these factors, observable in Raman spectra, is determined by the structural characteristics of a TiO$_2$ nanopowder: particle size distribution [9–11], existence of mixed phases (anatase in combination with considerable amount of rutile or brookite phase) [5], value and type of the strain (compressed or tensile) [9, 11], discrepancy from stoichiometry [12] as well as type of defects [5, 9], etc. We assumed that the main factors that influenced the behavior of $E_{g(1)}$ mode in our samples were the confinement effect due to anatase nanoparticle size distribution, disorder induced by existence of considerable amount of brookite phase and the strain effects caused by introducing of La$^{3+}$ ions into the TiO$_2$ lattice.

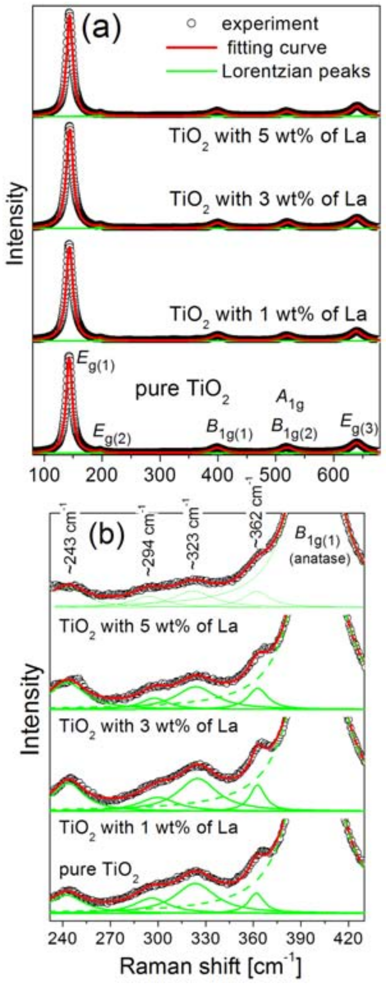

Fig. 1. Raman spectra of pure and La-doped TiO$_2$ samples. Lorentzian fits of anatase (a) and brookite (b) modes in the experimental Raman spectra (○).

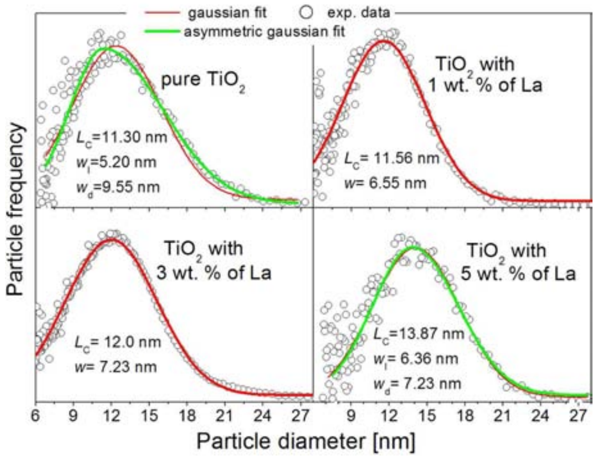

Fig. 2. Particle size distributions in pure and La-doped TiO$_2$ nanopowders estimated from low-frequency Raman spectra.

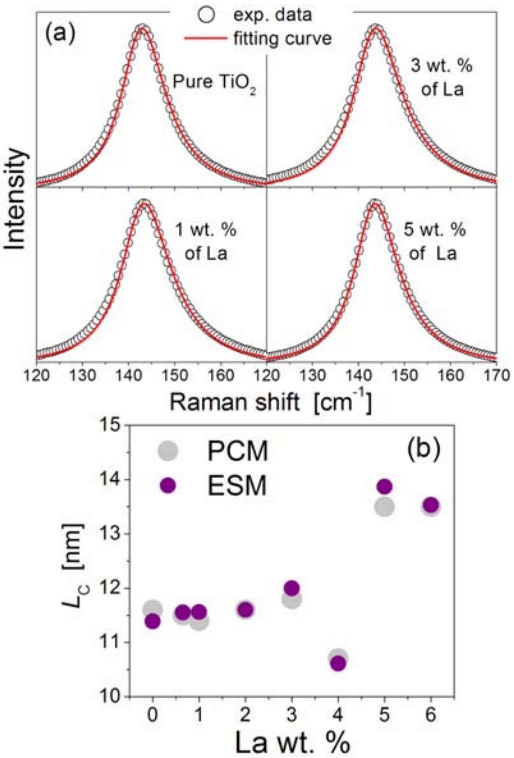

Fig. 3. PCM fits of $E_{g(1)}$ Raman mode for pure and La-doped anatase samples (a). Most frequent particle size $L_C$ obtained by ESM (black circles) and PCM (gray circles) in dependence of wt.% of La in $TiO_2$ nanopowders (b).

Raman scattering from confined acoustic vibrations in nanoparticles was observed in low frequency part of spectra of various materials. The elastic sphere model (ESM) was generally used to analyze the acoustic phonon confinement. This model describes the oscillations of homogeneous elastic sphere and was successfully applied to explain the experimental spectra of nanoparticles [13–15]. According to ESM, the frequency of an acoustic Raman mode is scaled as the inverse of the dimension of a vibrating particle: $\omega = \beta_L/D$, where $\beta_L$ is a coefficient calculated from ESM [14, 15]. In this paper we used procedure proposed by Ivanda et al. [15] for the extraction of information on nanoparticle size distribution from the low-frequency Raman spectra of $TiO_2$ nanoparticles. Values of longitudinal and transversal sound velocities for rutile $TiO_2$ were used ($v_L = 9017$ m/s, $v_T = 5394$ m/s, respectively) in calculations, due to the lack of this data for anatase. Calculated $\beta_L$ was 239.6. Inhomogeneous broadening of the spectrum as a consequence of the non-uniform particle size distribution of the sample was incorporated. The evaluated particle size distributions in pure and La-doped $TiO_2$ are presented in Fig. 2 together with the best fits of these distributions obtained by Gaussian and asymmetric Gaussian functions. The parameters $L_C$ — most frequent particle size, $w$ — symmetric Gaussian halfwidth, and $w_l$ and $w_d$ — left and right halfwidths of asymmetric Gaussian, are shown in Fig. 2. Let us note that the value $L_C$ is equal to average particle size $L_0$ in symmetric Gaussian distribution, as in $TiO_2$ with 1 wt.% of La ($L_0 = L_C \approx 11.6$ nm). However, in nanopowders with asymmetrical Gaussian distributions, the values of $L_C$ and $L_0$ are different, as in pure $TiO_2$ where $L_0 \approx 13$ nm while $L_C \approx 11.3$ nm.

The intensities of $E_{g(1)}$ mode for pure and La-doped $TiO_2$ nanopowders were calculated by phonon confinement model (PCM), described in detail in our previous papers [5, 9, 10]. The particle size distributions obtained by ESM were used as initial distributions for the best-fit calculations of the $E_{g(1)}$ mode by PCM (Fig. 3a). The dependence of the most frequent particle size $L_C$ on La content in $TiO_2$ nanopowders is shown in Fig. 3b. The values of $L_C$ in the distributions used finally in PCM (gray circle) are very close to the corresponding values of $L_C$ in the distributions obtained by ESM (black circle). The values of the average particle size estimated from the Raman spectra is a little bit greater than the average anatase crystallite size obtained by XRD, which can be a consequence of presence of brookite crystallites in the powders. Finally, we had to include the effects of compressive strain in PCM of Raman $E_{g(1)}$ mode in nanopowders with higher La content.

## 4. Conclusion

A detailed Raman study of sol-gel synthesized anatase $TiO_2$ nanopowders doped with lanthanum ions ($La^{3+}$) in the range from 0 to 6 wt.% was presented. Very intensive modes observed in the Raman spectra of all nanopowders were assigned to anatase phase of $TiO_2$, whereas the additional modes of extremely low intensity can be related to the presence of small amount of brookite phase. The particle size distributions in $TiO_2$ nanopowders estimated from the low frequency Raman spectra by ESM coincide with the distributions used for the best-fit calculation of the anatase $E_g$ Raman mode by the PCM. Obtained results show that the particle size in $TiO_2$ nanopowders doped with La up to 4 wt.%, is close to or smaller than in the pure $TiO_2$, whereas nanoparticles are larger for higher La content. Also, PCM analysis implies existence of compressive strain in nanopowders with more than 3 wt.% of La.

## Acknowledgments

This work is supported by the Serbian Ministry of Science and Technological Development under project No. 141047, the OPSA-026283 project within the EC FP6 programme and SASA project F-134.

## References

[1] S. Sakka, *J. Sol-Gel Sci. Techn.* **37**, 135 (2006).
[2] J.N. Hart, D. Menzies, Y-B. Cheng, G. P. Simon, L. Spiccia, *J. Sol-Gel Sci. Techn.* **40**, 45 (2006).

[3] D. Kim, A. Rothschild, D-J. Yang, H. L. Tuller, *Sensor Actuat. B, Chem.* **130**, 9 (2008).

[4] C.G. Granqvist, A. Azens, J. Isidorsson, M. Kharrazi, L. Kullman, T. Lindström, G.A. Niklasson, C.-G. Ribbing, D. Rönnow, M. Stromme Mattsson, M. Veszelei, *J. Non-Cryst. Solids* **218**, 273 (1997).

[5] M. Šćepanović, S. Akrabić, V. Berec, A. Golubović, Z. Dohčević-Mitrović, A. Kremenović, Z.V. Popović, *Acta Phys. Pol. A* **115**, 771 (2009).

[6] A. Kremenovic, J. Blanusa, B. Antic, P. Colomban, V. Kahlenberg, C. Jovalekic, J. Dukic, *Nanotechnology* **18**, 145616 (2007).

[7] T. Ohsaka, F. Izumi, Y. Fujiki, *J. Raman Spectrosc.* **7**, 321 (1978).

[8] S. Yin, K. Ihara, B. Liu, Y. Wang, R. Li, T. Sato, *Phys. Scr. T* **129**, 268 (2007).

[9] M.J. Šćepanović, M. Grujić-Brojčin, Z. Dohčević-Mitrović, Z.V. Popović, *Mater. Sci. Forum* **518**, 101 (2006).

[10] M.J. Šćepanović, M. Grujić-Brojčin, Z.D. Dohčević-Mitrović, Z.V. Popović, *Appl. Phys. A* **86**, 365 (2007).

[11] J.E. Spanier, R.D. Robinson, F. Zhang, S-W. Chan, I.P. Herman, *Phys. Rev. B* **64**, 245407 (2001).

[12] J.C. Parker, R.W. Siegel, *Appl. Phys. Lett.* **57**, 943 (1990).

[13] L. Saviot, B. Champagnon, E. Duval, I.A. Kudriavtsev, A.I. Ekimov, *J. Noncryst. Solids* **197**, 238 (1996).

[14] R. Kostić, S. Aškrabić, Z. Dohčević-Mitrović, Z.V. Popović, *Appl. Phys. A* **90**, 679 (2008).

[15] M. Ivanda, K. Furi, S. Musi, M. Risti, M. Goti, D. Risti, A.M. Tonejc, I. Djerdj, M. Mattarelli, M. Montagna, F. Rossi, M. Ferrari, A. Chiasera, Y. Jestin, G.C. Righini, W. Kiefer, R.R. Gonçalves, *J. Raman Spectrosc.* **38**, 647 (2007).

Research Article

Journal of RAMAN SPECTROSCOPY

Received: 1 August 2008 Accepted: 28 November 2008

(www.interscience.wiley.com) DOI 10.1002/jrs.2177

# Phonon–phonon interactions in $Ce_{0.85}Gd_{0.15}O_{2-\delta}$ nanocrystals studied by Raman spectroscopy

S. Aškrabić, Z. D. Dohčević-Mitrović,* M. Radović, M. Šćepanović and Z. V. Popović

**Phonon–phonon interactions and phase stability of Gd-doped ceria nanocrystals were examined over the temperature range 293–1100 K by Raman spectroscopy. The phonon confinement model (PCM) based on size, inhomogeneous strain and anharmonic effects was used to properly describe the anharmonic interactions in this system. The interplay between size and anharmonic effects influenced different phonon decay channels in nano grains than in larger grains. After the gradual cooling down to room temperature (RT), the Raman study revealed the phase separation in this system pointing to the phase instability of $Ce_{0.85}Gd_{0.15}O_{2-\delta}$ nanocrystals after heat treatment. The concentration of extrinsic (intrinsic) oxygen vacancies was also studied by Raman spectroscopy during the heat treatment of the $Ce_{0.85}Gd_{0.15}O_{2-\delta}$ nanocrystalline sample. Copyright © 2009 John Wiley & Sons, Ltd.**

**Keywords:** Gd-doped ceria; Raman scattering; phonon–phonon interaction; oxygen vacancies

## Introduction

Cerium dioxide has been widely studied theoretically and experimentally, because of its various applications such as catalyst in vehicle emission control system,[1] electrolyte for solid oxide fuel cells,[2] high storage capacitors,[3] superconductor structures,[4] UV blocking filters,[5] neuroprotection[6] and other. Use of ceria-based nanomaterials as an electrolyte for solid oxide fuel cells is determined by its good ionic conductivity at intermediate temperatures 600–700 °C. The ionic conductivity is dependent on the concentration of oxygen vacancies present in the electrolyte material. These vacancies in nanocrystalline ceria can be intrinsic, originating from the reduction of the grain size and enlargement of the surface-to-volume ratio of the sample, or they can be induced by doping ceria with trivalent ions of rare earth elements.[7,8] This is precisely why the gadolinium-doped ceria nanocrystals are interesting for investigation. The properties of these materials at working temperatures of solid oxide fuel cells are of special interest from the point of view of materials stability and oxygen vacancy behavior. On the other hand, the phonon–phonon interactions in these nanocrystalline systems are scarcely investigated in the literature and the interplay between anharmonic interactions and the size effects is still not well understood in nanostructured materials.

The purpose of this article was to investigate the anharmonic processes in nanocrystalline ceria doped with 15% of gadolinium, $Ce_{0.85}Gd_{0.15}O_{2-\delta}$ by means of Raman spectroscopy during the gradual heating up to 1073 K and cooling down to room temperature (RT). Raman spectra at different temperatures were influenced by the different phonon–phonon interactions which on the other side are dependent on the nanocrystalline size. The extrinsic (intrinsic) oxygen vacancy behavior at working temperatures of this potential solid oxide fuel cells electrolyte material was also analyzed.

## Experimental

A $Ce_{0.85}Gd_{0.15}O_{2-\delta}$ nanocrystalline sample was synthesized by self-propagating RT synthesis. The detailed powder preparation procedure is already described.[9]

The crystalline phase of $Ce_{0.85}Gd_{0.15}O_{2-\delta}$ nanocrystals was studied by X-ray diffraction (XRD) method using a Siemens D-5000 diffractometer with Cu K$\alpha$ radiation, at RT. Diffraction patterns were recorded over the 2$\theta$ range from 20 to 80° using a position sensitive detector with 8° acceptance angle.

Atomic force microscope (AFM) images were taken before and after heat treatment using the Omicron B002645 SPM PROBE VT AFM 25 in noncontact mode in order to investigate the particle size changes with temperature treatment.

The vibrational properties of $Ce_{0.85}Gd_{0.15}O_{2-\delta}$ nanopowders were studied by Raman spectroscopy. Micro-Raman spectra were collected in the backscattering configuration using a Jobin Yvon T64000 spectrometer equipped with a nitrogen-cooled charge-coupled-device detector. The argon ion ($Ar^+$) laser line with $\lambda = 514.5$ nm was used as an excitation source. The $Gd^{3+}$ doped sample was progressively heated in a Linkam TS 1500 microscope heating stage, up to 1073 K, with a 100-K step, and then gradually cooled down to RT. All the measurements were performed in the air.

---

* Correspondence to: Z. D. Dohčević-Mitrović, Center for Solid State Physics and New Materials, Institute of Physics, 11080 Belgrade, Pregrevica, 118, Serbia. E-mail: zordoh@phy.bg.ac.yu

Center for Solid State Physics and New Materials, Institute of Physics, Pregrevica 118, 11080 Belgrade, Serbia

## Results and Discussion

X-ray diffraction patterns of $Ce_{0.85}Gd_{0.15}O_{2-\delta}$ nanocrystalline sample are shown in Fig. 1 together with a XRD spectrum of pure $CeO_{2-\delta}$ nanocrystals for comparison. The XRD spectrum of $Ce_{0.85}Gd_{0.15}O_{2-\delta}$ sample clearly shows the existence of a fluorite structure, without the presence of a crystalline phase of $Gd_2O_3$ indicating that the sample is a solid solution. The broad diffraction peaks suggest that the particles are within the nanometric range and the average crystallite size of about 7 nm was determined from the full width at half maximum (FWHM) of the (111) peak using the well known Scherrer formula.

RT AFM images (250 nm × 250 nm) of $Ce_{0.85}Gd_{0.15}O_{2-\delta}$ nanocrystals are shown in Fig. 2, before heat treatment (a) and after cooling down to RT (b). It can be seen from Fig. 2(a) that particles of the $Ce_{0.85}Gd_{0.15}O_{2-\delta}$ nanocrystalline sample, before heat treatment, are predominantly of spherical shape with diameters in a narrow range with average particle size less than 10 nm. After sample cooling down to RT, the particles became agglomerated and irregularly shaped with average particle size between 15 and 20 nm (Fig. 2(b)).

### Heating

Cerium dioxide of fluorite type structure has a single allowed triply degenerate Raman active mode of $F_{2g}$ symmetry. Raman spectra of $Ce_{0.85}Gd_{0.15}O_{2-\delta}$ solid solution in the temperature range 293–1100 K are shown in Fig. 3. In the Raman spectra at RT, three modes at 453, 550 and 600 $cm^{-1}$ are present. The Raman mode at 453 $cm^{-1}$ is assigned to the $F_{2g}$ mode of the $CeO_2$ fluorite structure and represents the symmetrical stretching vibration of the $CeO_8$ vibrational unit.[10] In the nanocrystalline sample this mode is broader, asymmetric and shifted to lower wavenumbers, comparing to the single-crystal value.[11]

The other two modes are second order Raman modes attributed to the oxygen vacancies due to the nonstoichiometry of nano ceria (600 $cm^{-1}$) and generated as charge compensating defects induced by the incorporation of trivalent metal cations ($Gd^{3+}$) into the ceria lattice (550 $cm^{-1}$).[12,13] $CeO_2$ experiences the loss of oxygen ions when its average particle size decreases down to nanometric dimensions. The entire sample surface-to-volume ratio increases, which enables the oxygen ions to leave the crystal lattice with high probability (this refers especially to the oxygen ions located near the grain surface). Apart from this, the substitution of $Ce^{4+}$ ions with $Gd^{3+}$ ions imposes the loss of oxygen ions $O^{2-}$ in order to keep the electro neutrality of the material.

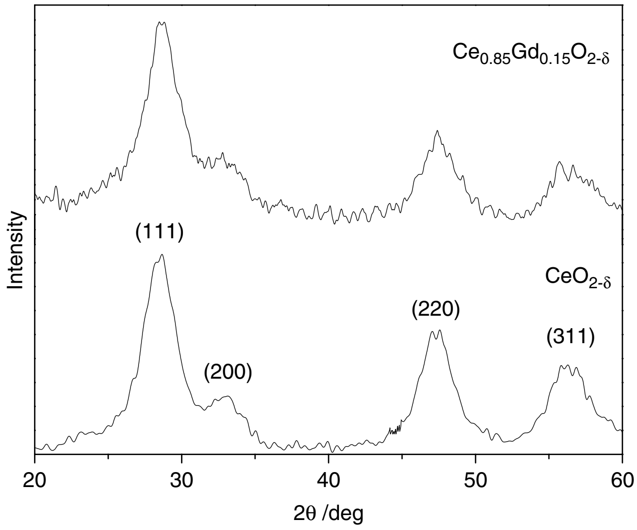

**Figure 1.** XRD patterns of the $Ce_{0.85}Gd_{0.15}O_{2-\delta}$ and pure $CeO_{2-\delta}$ samples.

Raman spectra at higher temperatures display significant changes. With increasing temperature, the $F_{2g}$ mode exhibits a systematic shift to lower wavenumber values and becomes less asymmetric while the linewidth increases with increasing temperature. Such a behavior can be attributed to the anharmonic interactions due to the decay of optical phonon to lower energy phonons i.e. so called down-conversion processes.[14]

The experimental spectra (circles) are fitted using the phonon confinement model (PCM) based on the size, inhomogeneous strain using the Gaussian size distribution function $\rho(L)$ and anharmonic effects.[15] In such a case the intensity of the Raman mode can be calculated as:

$$I(\omega, T) = \sum_{i=1}^{3} \int_{0}^{\infty} \rho(L) \mathrm{d}L \int_{BZ} \frac{\exp\left(\frac{-\mathbf{q}^2 L^2}{8\beta}\right) d^3\mathbf{q}}{\{\omega - [\omega_i(q) + \Delta\omega(q, L) + \Delta\omega(T)]\}^2 + \left(\frac{\Gamma(T)}{2}\right)^2} \quad (1)$$

where $\mathbf{q}$ is the wave vector, $L$ is the particle size, $\beta$ is adjustable parameter depending on the strength of the phonon confinement, $\omega_i(q)$ represents phonon dispersion curves for bulk,[12] while $\Delta\omega(q, L)$ is the wavenumber shift due to the inhomogeneous strain.[16] The terms $\Delta\omega(T)$ and $\Gamma(T)$ describe the temperature dependent wavenumber shift and bandwidth due to the phonon–phonon interactions, respectively.[16,17] Temperature dependence of the Raman mode wavenumber and bandwidth based on the Klemens' model,[18,19] including three and four-phonon anharmonic processes, can be presented with following equations:

$$\omega(T) = \omega_0 + C\left[1 + \frac{2}{e^x - 1}\right] + D\left[1 + \frac{3}{e^y - 1} + \frac{3}{(e^y - 1)^2}\right] = \omega_0 + \Delta\omega(T) \quad (2)$$

$$\Gamma(T) = \Gamma_1 + A\left[1 + \frac{2}{e^x - 1}\right] + B\left[1 + \frac{3}{e^y - 1} + \frac{3}{(e^y - 1)^2}\right] = \Gamma_1 + \Delta\Gamma(T) \quad (3)$$

where $\omega_0$ is the zero temperature wavenumber, $x = \frac{\hbar\omega_0}{2k_B T}$, $y = \frac{\hbar\omega_0}{3k_B T}$, $\Gamma_1$ is the broadening due to phonon confinement and inhomogeneous strain, $\Delta\Gamma(T)$ is the temperature–dependent linewidth because of the phonon coupling decay and $A$, $B$, $C$, $D$ are the anharmonic constants. Equation (2) and (3), which are related to the anharmonic processes, were incorporated in Eqn (1), through proper choice of the anharmonic constants $A, B, C, D$ and $\Gamma_1$ to reproduce the experimental Raman spectra of $Ce_{0.85}Gd_{0.15}O_{2-\delta}$ nanocrystalline sample obtained at high temperatures. Calculated Raman spectra using PCM model are presented with solid lines in Fig. 3.

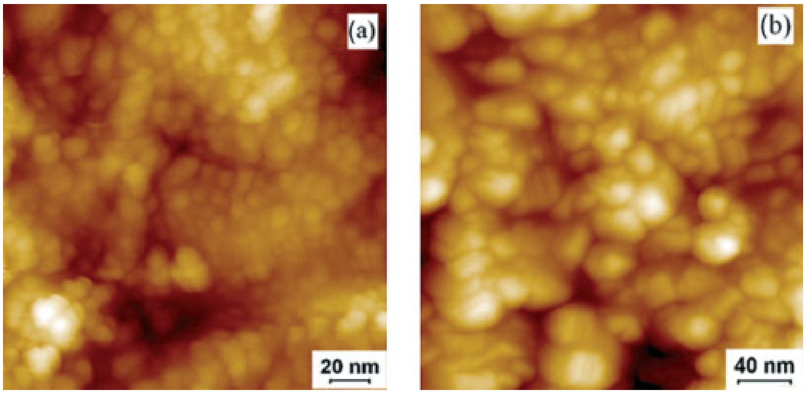

**Figure 2.** AFM images of $Ce_{0.85}Gd_{0.15}O_{2-\delta}$ nanocrystals before (a) and after (b) heat treatment.

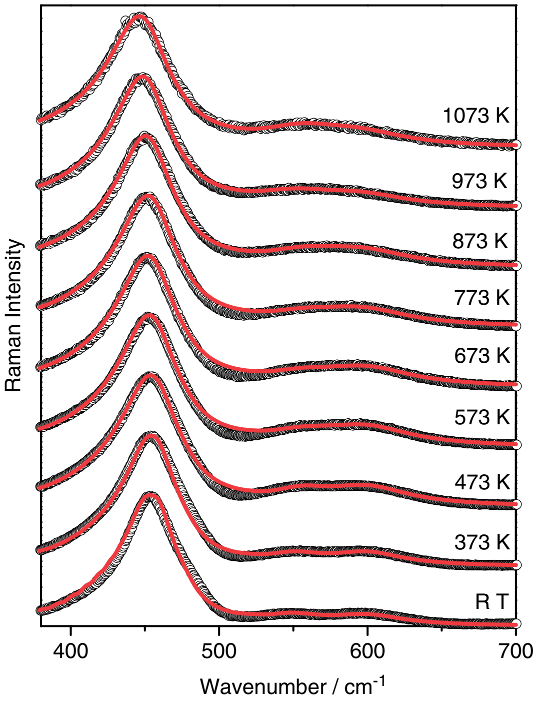

**Figure 3.** Raman spectra of $Ce_{0.85}Gd_{0.15}O_{2-\delta}$ sample taken during the heating (circles). The spectra calculated from PCM are represented by solid lines.

From the PCM, which incorporates anharmonic, size and inhomogeneous strain effects we were able to obtain the average particle size ($L_0$) at higher temperatures and to estimate the particle growth influence on the $F_{2g}$ Raman mode behavior. The change of the average particle size ($L_0$), strength of phonon confinement ($\beta$) and the width ($w$) of the Gaussian particle size distribution with temperature are given in Table 1. The strength of the phonon confinement decreases ($\beta$) as particle size increases with temperature implying that confinement effects become weaker as particles grow with temperature. The width of the Gaussian particle size distribution ($w$) also increases with temperature indicating the change in particle size distribution. In Fig. 4, we present the average particle size calculated from PCM. As can be seen from this figure, the average particle size ranges from 7 nm at RT, what is in a good accordance with the AFM result from Fig. 2(a), up to 10 nm at temperature of 1073 K.

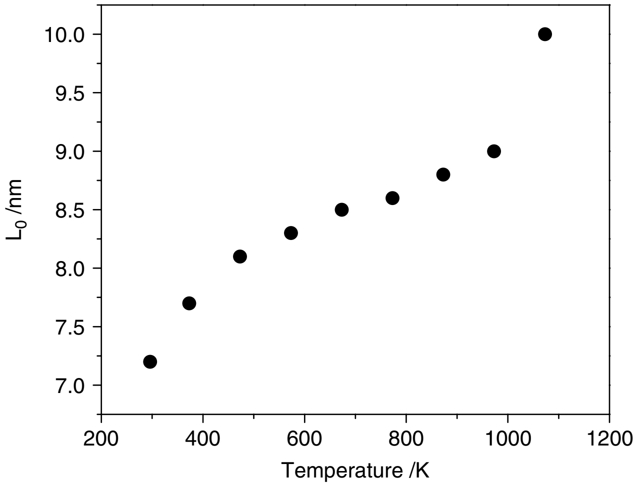

**Figure 4.** Change of the average particle size with temperature calculated from the PCM.

**Table 1.** Change of the average particle size, strength of the phonon confinement and width of the Gaussian particle size distribution with temperature

| *T*/K | 296 | 373 | 473 | 573 | 673 | 773 | 873 | 973 | 1073 |
|---|---|---|---|---|---|---|---|---|---|
| $L_0$/nm | 7.2 | 7.7 | 8.1 | 8.3 | 8.5 | 8.6 | 8.8 | 9 | 10 |
| $\beta$ | 38 | 38 | 37 | 36 | 35 | 35 | 33 | 32 | 30 |
| w/nm | 2.88 | 3.38 | 4.05 | 4.15 | 4.42 | 4.64 | 5.02 | 5.22 | 6.50 |

From Fig. 3, it can be seen that the Raman mode wavenumber decreases with increasing temperature up to 1073 K while the bandwidth increases. The wavenumber red shift and bandwidth increase with increasing temperature are ascribed to the optical-phonon anharmonic couplings in $Ce_{0.85}Gd_{0.15}O_{2-\delta}$ nanocrystalline sample.

The $F_{2g}$ mode wavenumber and bandwidth dependence on the temperature is shown in the Fig. 5(a) and (b).

The best fit of the wavenumber values (full line) during the heating up to 573 K was obtained including only the four-phonon anharmonic term, while at higher temperatures three-phonon decay processes became dominant (dashed line) similar to the polycrystalline $CeO_2$. On the other side, the bandwidth behavior up to 573 K is well fitted only including the four-phonon anharmonic

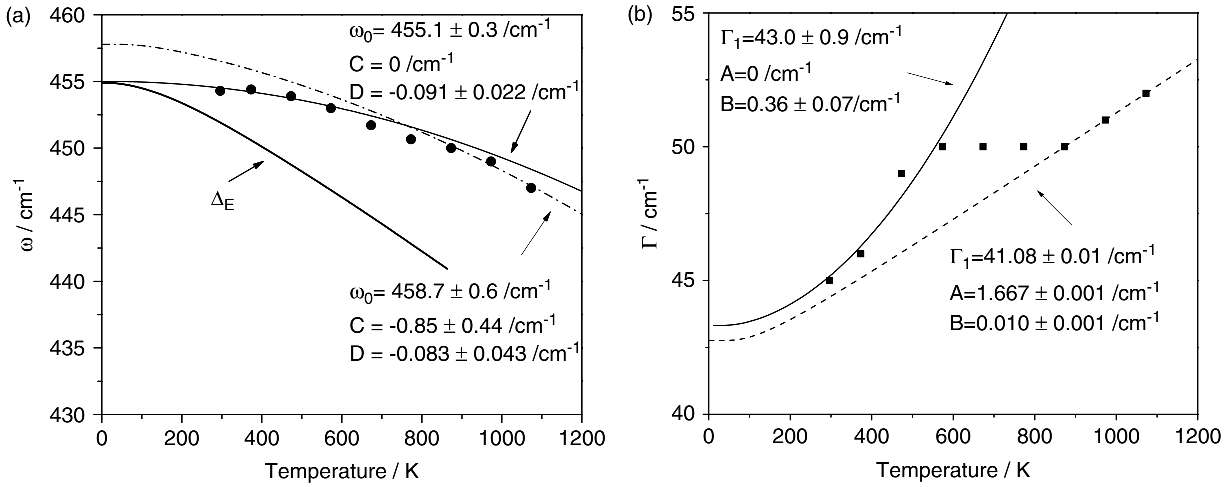

**Figure 5.** Temperature dependence of the $F_{2g}$ Raman mode (a) wavenumber and (b) line width during heating. The fitting parameters are also presented on the graphs together with the calculated thermal expansion contribution.

term. Between 573 and 873 K there is an evident plateau and then with further temperature increase, the bandwidth increases according to the three-phonon coupling processes. If we have in mind that the bandwidth of the Raman mode determines the phonon lifetime[20] and therefore reflects the change in phonon–phonon interactions in the material under investigation, we concluded that in small nano grains up to temperature of 573 K the four-phonon decay processes are more probable than the three-phonon decay processes and have more influence on the wavenumber (bandwidth) behavior than the size effects. At higher temperatures, when the particles are grown enough, size effects provoke the changes in phonon–phonon interactions influencing the wavenumber (bandwidth) of the Raman mode in such a way that three-phonon anharmonic interactions prevail over the four-phonon ones. Such behavior is much alike to the microceria sample although the particles are still in the nanometric range (Fig. 4). In Fig. 5(a) is also presented the calculated wavenumber shift due to the pure-volume contribution – $\Delta_E$ (line) which can be evaluated from the following equation[21]:

$$\Delta_E = \omega_0 \left\{ \exp\left[ -3\gamma_i \int_0^T \alpha(T')dT' \right] - 1 \right\} \qquad (4)$$

where $\alpha$ is the linear coefficient of the thermal expansion and $\gamma_i$ is the mode Grüneisen parameter. The temperature dependent thermal expansion coefficients $\alpha$ for Gd-doped ceria are taken from the work of Hayashi *et al.*[21] while the value of $\gamma = 1.24$ is taken from Ref. [11] because of the lack of literature data for Gd-doped ceria nanosized samples. It is obvious that the wavenumber shift due to thermal expansion will provoke a higher red shift of the $F_{2g}$ mode wavenumber indicating that most likely the values for $\alpha$ and $\gamma$ are overestimated for small nanoparticles. This was already suggested by Spanier *et al.*[22] Namely, in their work Spanier *et al.* deduced that the phonon coupling is not enhanced in the nanoparticles compared to larger particles. Contrary to their conclusion, we deduced that different phonon decay channels dominate in the nanocrystalline grain and pure anharmonic coupling of phonons influence more the wavenumber behavior of $F_{2g}$ Raman mode at high temperatures than the size effect and thermal expansion.

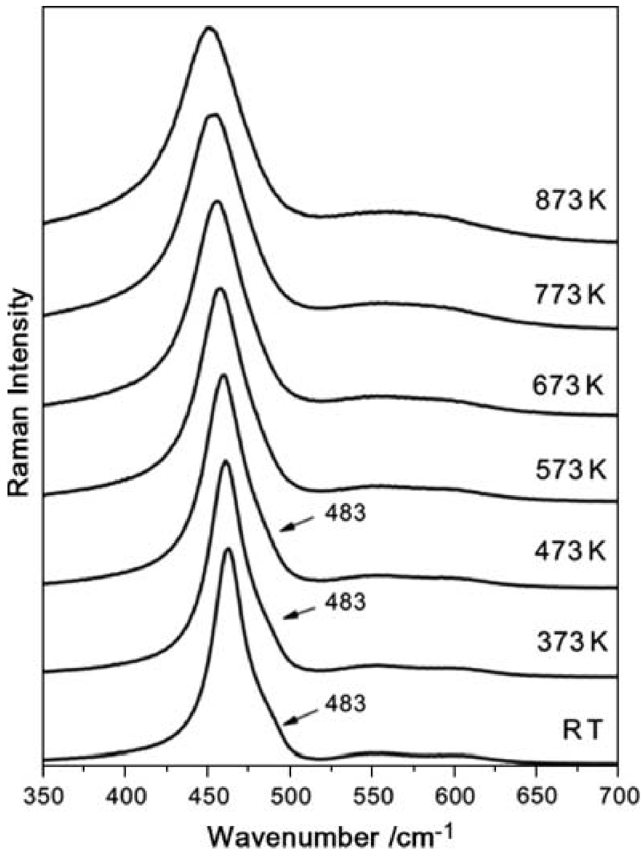

**Figure 6.** Raman spectra of $Ce_{0.85}Gd_{0.15}O_{2-\delta}$ sample taken during the cooling down to room temperature (RT).

## Cooling

After annealing, the sample was cooled down to the RT. Raman spectra were taken at the temperatures from 873 K to RT downwards with a-100 K step (Fig. 6). The temperature dependence of the $F_{2g}$ mode wavenumber (triangles) and linewidth (squares) is presented in Fig. 7 and now is well fitted including both terms in Eqns (2) and (3). The three-phonon contribution is more dominant

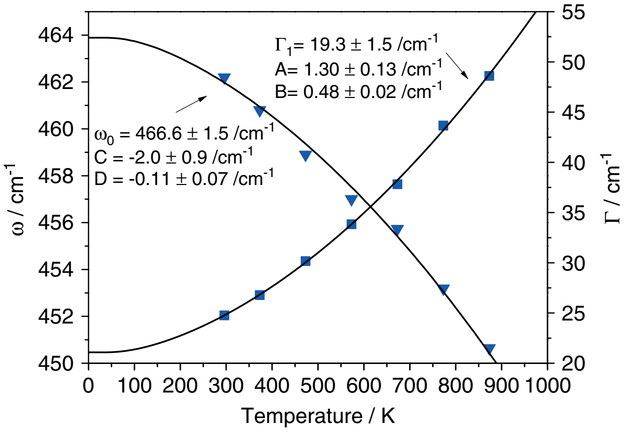

**Figure 7.** Variation of the $F_{2g}$ mode wavenumber and line width upon gradual cooling. Full lines represent fits of the peak position and line width using Eqns (2) and (3).

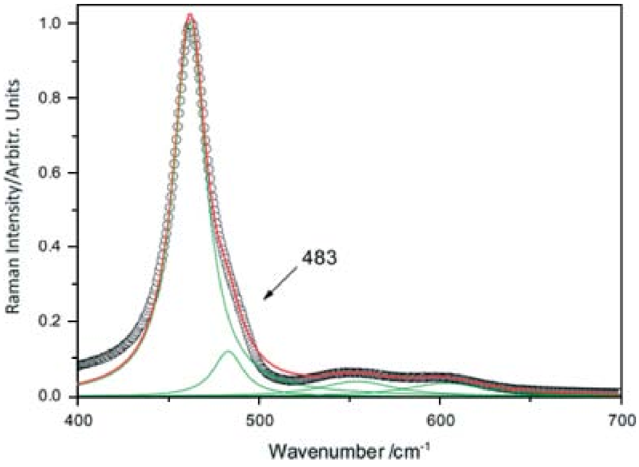

**Figure 8.** Raman spectra of $Ce_{0.85}Gd_{0.15}O_{2-\delta}$ nanocrystalline sample after heat treatment. Deconvolution of the spectrum with Lorentzian-type profile revealed the presence of $CeO_2$ and $Gd_2O_3$ oxide phase.

than the four-phonon anharmonic terms what can be seen from the ratio of the constants $C/D$ and $A/B$. This behavior is more similar to the polycrystalline ceria sample because the particles are grown enough and we can consider that nanosized effects are almost negligible.

The Raman spectrum at RT after cooling is narrower, blue shifted regarding the starting spectrum and at lower wavenumber than in the bulk counterpart. A deconvolution with the Lorentzian-line profile technique (Fig. 8) revealed that the $F_{2g}$ mode consists of two modes with wavenumbers of 462 and 483 $cm^{-1}$. The second mode represents the Raman mode of $Gd_2O_3$ phase compared to the Raman wavenumber of bulk gadolinium oxide.[23] This result confirms that a phase separation took place, i. e. $CeO_2$ and $Gd_2O_3$ phases were formed after heat treatment. In our previous work,[24] we have demonstrated the advantage of Raman spectroscopy over the XRD method to detect the phase separation in the $CeO_2$–$Gd_2O_3$ system for small Gd concentrations. In fact, all high-intensity diffraction peaks of $CeO_2$ and $Gd_2O_3$ are overlapping and for smaller concentrations of the $Gd_2O_3$, the phase XRD pattern of pure and Gd-doped $CeO_2$ did not show any difference. Only in the heavily doped samples, (80% $Gd_2O_3$) there is an appearance of a $Gd_2O_3$ phase in the XRD spectrum. On the other side, Raman spectra showed clearly the evidence of a phase separation even for the sample with 15% of Gd-doped ceria.

From the PCM model, it was deduced that average particle size after heating and gradual cooling is higher than 15 nm. This is in accordance with AFM result obtained from the $Ce_{0.85}Gd_{0.15}O_{2-\delta}$ nanocrystals after heat treatment and presented in Fig. 2(b).

Besides the $F_{2g}$ Raman active mode, two additional modes appear in the region of interest. These modes are centered at the approximate wavenumbers of 550 and 600 $cm^{-1}$. Both of these modes are connected to the defect spaces related to the oxygen vacancies present in the structure of $Ce_{0.85}Gd_{0.15}O_{2-\delta}$ nanocrystalline sample.[13] $CeO_2$ experiences the loss of oxygen ions when its average particle size decreases down to nanometric dimensions. The ratio of the entire sample surface to its volume increases what enables oxygen ions to leave the crystal lattice with high probability (this refers especially to the oxygen ions located near the grain surface). Apart from this, another reason for such behavior lies in the fact that doped $Gd^{3+}$ ions, which substitute $Ce^{4+}$ ions in the lattice lead to the loss of oxygen ions $O^{2-}$ in order to keep the electro neutrality of the material. This is why for every two substituted $Gd^{3+}$ ions, one oxygen ion $O^{2-}$ leaves the crystal lattice. According to Nakajima *et al.*,[12] the vibrational states with wavenumber near the value of 600 $cm^{-1}$ are attributed to the defect spaces including or neighboring the intrinsic oxygen vacancies, while the mode at 550 $cm^{-1}$ is associated with oxygen vacancies induced by doping $CeO_2$ with $Gd^{3+}$ (extrinsic vacancies). The intensity of the intrinsic vacancy mode increases with temperature up to 773 K (Fig. 9). With further temperature increase, the intensity of this mode decreases and then abrupt intensity increase happens at 1073 K. The intensity of extrinsic mode increases up to 573 K and than has a minor decrease till the temperature of 773 K after which again increases. The decrease in intensity of the vacancy modes can be explained in terms of the formation of different microdomains as proposed by Zhang *et al.*[25] which include $Gd^{3+}$ ions and $O^{2-}$ vacancies or $Ce^{3+}$ ions and vacancies. If these nanosized domains have a higher degree of ordering, this can have a negative impact on ionic conductivity.[26] On the other side, Zhang *et al.*[25] suggested that above the critical temperature (in a case of Gd-doped ceria system the critical temperature is about 400 °C), the vacancies become mobile and are not necessarily associated with $Gd^{3+}$

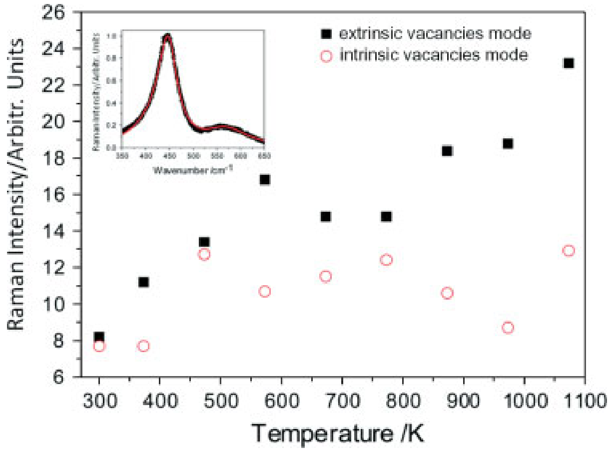

**Figure 9.** Intensity changes of extrinsic and intrinsic oxygen vacancies modes in Raman spectra with temperature. The inset: Fitted Raman spectra of $Ce_{0.85}Gd_{0.15}O_{2-\delta}$ nanocrystalline sample at 1073 K.

ions. Smaller number of complex defects would lead to weaker intensity of the corresponding vibrational modes. Maybe this effect is also responsible for a small intensity decrease of the extrinsic $O^{2-}$ vacancy mode in the temperature range 573–773 K. The pronounced intensity drop of the intrinsic vacancy mode at temperatures above 773 K can be explained by the additional fact that at higher temperatures the accelerated intake of oxygen ions from atmosphere and its positioning in the lattice takes place leading to improved sample stoichiometry. At 1073 K both intensities increase. We performed the fitting of the Raman vacancy modes at this temperature first with two Lorentzians and then with only one (inset of Fig. 9) because it was observed that the incorporation of a second Lorentzian band does not improve the fitting-quality. Such a result may suggest that at these high temperatures, different oxygen vacancy complexes which include both $Gd^{3+}$, $Ce^{3+}$ and $O^{2-}$ vacancy ions are formed but the final explanation is left to be found in further analysis.

## Conclusion

We examined the effects of temperature-induced changes on vibrational states of nanocrystalline $Ce_{0.85}Gd_{0.15}O_{2-\delta}$ solid solutions using Raman spectroscopy. Raman spectra were collected at different temperatures between RT and 1073 K and afterwards during the gradual cooling of the sample. The Raman spectra during the heating are well described using a PCM model with combined size, inhomogeneous strain and anharmonic effects. At temperatures up to 573 K four-phonon anharmonic processes dominate and the size effects have less influence on the Raman mode behavior than the anharmonic effects. With further temperature increase, the three-phonon coupling prevails indicating that the particles are grown enough to behave similar to the polycrystalline sample. The Raman spectra after heat treatment demonstrated that the $Ce_{0.85}Gd_{0.15}O_{2-\delta}$ sample is still in the nanometric range but phase separation took place, i.e. $CeO_2$ and $Gd_2O_3$ oxides are formed pointing to the instability of this system. Analyzing the behavior of the intrinsic (extrinsic) oxygen vacancy Raman modes it was deduced that at different temperatures different oxygen vacancy complexes (ordering) in nanosized domains can be formed. Overall increase of modes intensity, i.e. the oxygen vacancy concentration points out that Gd-doped ceria can be a very convenient material for intermediate temperature solid oxide fuel cells application.

### Acknowledgement

This work was supported by the MSRS under the Project No. 141047 and the OPSA-026283 Project within EC FP6 Program.

## References

[1] A. Trovarelli, *Catal. Rev. – Sci. Eng.* **1996**, *38*, 439.
[2] M. Mogensen, N. M. Sammes, G. A. Tompsett, *Solid State Ionics* **2000**, *129*, 63.
[3] A. Walkenhorst, M. Schmitt, H. Adrian, K. Petersen, *Appl. Phys. Lett.* **1994**, *64*, 1871.
[4] S. Kanakaraju, S. Mohan, A. K. Sood, *Thin Solid Films* **1997**, *305*, 191.
[5] M. Yamashita, K. Kameyama, S. Yabe, S. Yoshida, Y. Fujishiro, T. Kawai, T. Sato, *J. Mater. Sci.* **2002**, *37*, 683.
[6] D. Schubert, R. Dargusch, J. Raitano, S. W. Chan, *Biochem. Biophys. Res. Commun.* **2006**, *342*(1), 86.
[7] A. Sin, Y. Dubitsky, A. Zaopo, A. S. Aricò, L. Gullo, D. La Rosa, S. Siracusano, V. Antonucci, C. Oliva, O. Ballabio, *Solid State Ionics* **2004**, *175*, 361.
[8] W. Bai, K. L. Choy, N. H. J. Stelzer, J. Schoonman, *Solid State Ionics* **1999**, *116*, 225.
[9] S. Bošković, D. Djurović, Z. Dohčević-Mitrović, Z. V. Popović, M. Zinkevich, F. Aldinger, *J. Power Sources* **2005**, *145*, 237.
[10] J. R. McBride, K. C. Hass, B. D. Poindexter, W. H. Weber, *J. Appl. Phys.* **1994**, *76*, 2435.
[11] W. H. Weber, K. C. Hass, J. R. McBride, *Phys. Rev. B* **1993**, *48*, 178.
[12] A. Nakajima, A. Yoshihara, M. Ishigame, *Phys. Rev. B* **1994**, *50*, 13297.
[13] Z. D. Dohčević-Mitrović, M. Grujić-Brojčin, M. Šćepanović, Z. V. Popović, S. Bošković, B. Matović, M. Zinkevich, F. Aldinger, *J. Phys.: Condens. Matter* **2006**, *18*, S2061.
[14] J. Menendez, M. Cardona, *Phys. Rev. B* **1984**, *29*, 2051.
[15] Z. D. Dohčević-Mitrović, M. Radović, M. Šćepanović, M. Grujić-Brojčin, Z. V. Popović, B. Matović, S. Bošković, *Appl. Phys. Lett.* **2007**, *91*, 203118.
[16] Z. D. Dohčević-Mitrović, M. J. Šćepanović, M. U. Grujić-Brojčin, Z. V. Popović, S. B. Bošković, B. M. Matović, M. V. Zinkevich, F. Aldinger, *Solid State Commun.* **2006**, *137*, 387.
[17] V. G. Kravets, V. Y. Kolmykova, *Opt. Spectrosc.* **2005**, *99*(1), 68.
[18] P. G. Klemens, *Phys. Rev. B* **1966**, *148*, 845.
[19] M. Balkanski, R. Wallis, E. Haro, *Phys. Rev. B* **1983**, *28*, 1928.
[20] P. G. Klemens, *Phys. Rev. B* **1975**, *11*, 3206.
[21] H. Hayashi, M. Kanoh, C. J. Quan, H. Inaba, S. Wang, M. Dokiya, H. Tagawa, *Solid State Ionics* **2000**, *132*, 227.
[22] J. E. Spanier, R. D. Robinson, F. Zhang, S. W. Chan, I. P. Herman, *Phys. Rev. B* **2001**, *64*, 245407.
[23] J. Zarembowitch, J. Gouteron, A. M. Lejus, *J. Raman Spectrosc.* **1980**, *9*, 263.
[24] Z. V. Popović, Z. Dohčević-Mitrović, M. J. Konstantinović, M. Šćepanović, *J. Raman Spectrosc.* **2007**, *38*, 750.
[25] T. S. Zhang, J. Ma, L. B. Kong, S. H. Chan, J. A. Kilner, *Solid State Ionics* **2004**, *170*, 209.
[26] D. R. Ou, T. Mori, F. Ye, T. Kobayashi, *Appl. Phys. Lett.* **2006**, *89*, 171911.

*Science of Sintering*, **41** (2009) 67-73

---

doi: 10.2298/SOS0901067S

UDK 661.882-14:681.785Y6

# Characterization of Anatase $TiO_2$ Nanopowder by Variable-Temperature Raman Spectroscopy

**M. J. Šćepanović, M. Grujić-Brojčin, Z. D. Dohčević-Mitrović,**
**Z. V. Popović**
Center for Solid State Physics and New Materials, Institute of Physics, Pregrevica 118,11080 Belgrade, Serbia

---

***Abstract:***

*Raman spectroscopy has been used for characterization of commercial nanosized $TiO_2$ powder with declared grain size of 5 nm. The Raman spectra measured in Stokes and anti-Stokes regime confirm the anatase phase of $TiO_2$ powder in temperature range 25-1173 K. It is shown that phonon-confinement (due to small grain size) and nonstoichiometry (caused by laser irradiation in vacuum) have a great influence on blueshift and broadening of the main $E_g$ Raman mode at low temperatures, while the influence of the strong anharmonic effect becomes dominant at higher temperatures. The phonon confinement effect decreases due to the crystallite growth at temperatures above 673 K.*

***Keywords**: Anatase $TiO_2$ nanopowder, Raman spectroscopy*

---

## 1. Introduction

Recent interest in nanocrystalline anatase $TiO_2$ has been driven by its potential in a variety of technological applications, as well as in fundamental studies of size-induced modifications of the physical properties and phase stability of nanoscale inorganic systems [1, 2]. Raman spectroscopy is a powerful tool in the study of microstructure of nanosized materials, and therefore a promising technique for characterization of TiO2 nanopowders [3]. The changes in the Raman spectrum of nanocrystalline anatase, the phase most commonly synthesized at ambient conditions, have been variously interpreted as originating from the phonon confinement [4-6], non-stoichiometry [7] or internal stress⁄surface tension effects [8]. Although the majority of published studies point out phonon confinement as the main factor responsible for the changes observed in the Raman spectrum of nanocrystalline anatase [4-6], some researchers have interpreted their results favoring other factors, depending on structural characteristics of nanopowders.

In the present work we investigate the temperature dependence of Raman spectra of commercial anatase $TiO_2$ nanocrystals with a declared average crystallite size of about 5 nm using variable-temperature Raman scattering. The Stokes and anti-Stokes Raman spectra at different temperatures in the range from about 23 to 1173 K are shown. We demonstrated that, depending on temperature, phonon confinement, anharmonic and nonstoichiometric effects have different influence on the frequency shift and the broadening of the lowest frequency $E_g$ Raman mode. A Comparison between experimental spectra of anatase $TiO_2$

---

[*)] Corresponding author: maja.scepanovic@phz.bg.ac.rs nanopowder and spectra calculated by the phonon confinement model with anisotropic dispersion relations and temperature dependant parameters reveals information about the structure, stoichiometry and crystallite size at all given temperatures.

## 2. Experimental details

In this study $TiO_2$ nanopowder (Aldrich 637254-50G, 99.7%) with a declared average crystallite size of about 5 nm was investigated.

Low frequency Raman measurements were performed at room temperature in the backscattering geometry using the 514.5-nm line of an $Ar^+$ laser, Jobin–Yvon U1000 monochromator and a photomultiplier as the detector. Raman measurements at low temperatures were performed by the same equipment in vacuum in the cryostat system.

High temperature Raman measurements were taken with same $Ar^+$ laser line using a Jobin Yvon T64000 spectrometer equipped with a Linkam TS 1500 microscope heating stage and nitrogen cooled charge-coupled-device detector (CCD). Overheating of the samples was avoided using a minimal laser power when no changes of the Raman spectra were noticed.

## 3. Results and discussion

Fig. 1 shows nanosize particle distribution estimated by the procedure for the evaluation of the particle size from the low frequency Raman (LFR) spectrum proposed by Ivanda et al. [9]. A room temperature LFR spectrum is presented in the inset of the same figure. The existence of two modes in LFR spectrum resulted in the distribution with two maxima. As the particle frequency corresponding to the second maximum is very low, only the distribution from the first maximum was fitted by log-normal function with the parameters 7.28 nm and 0.20.

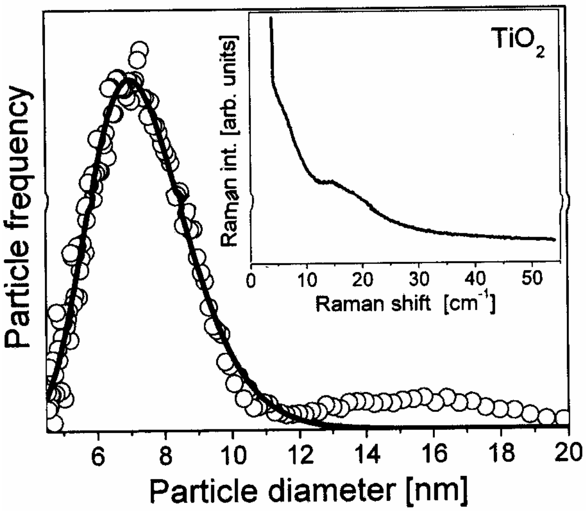

**Fig. 1.** Size distribution (open circles) of $TiO_2$ nanopowder obtained from room temperature LFR spectrum (inset) and its fit by a log-normal function (full line).

All Raman spectra measured at temperatures between 23 and 1173 K confirm the anatase phase of this $TiO_2$ nanopowder (some of them are shown in Fig. 2). Raman modes can be assigned to the Raman spectra of the anatase single crystal [10]: ~144 ($E_g$), 197 ($E_g$), 399

($B_{1g}$), 513 ($A_{1g}$), 519 ($B_{1g}$) and 639 cm$^{-1}$ ($E_g$). With temperature increasing above room temperature, the linewidth of all noted modes increases, while the frequencies of three modes (two $E_g$ and one $B_{1g}$ mode) exhibit different temperature dependence. The frequencies of $B_{1g}$ mode at 396 cm$^{-1}$ and $E_g$ mode at 637 cm$^{-1}$ at room temperature shift to lower frequencies with the increasing temperature, in accordance to literature [11]. The blueshift and broadening of the lowest frequency anatase $E_g$ Raman mode at different temperatures will be particularly analyzed. Note that the increase of temperature above 1173 K is followed by a partial transformation of anatase to rutile $TiO_2$, as expected [12].

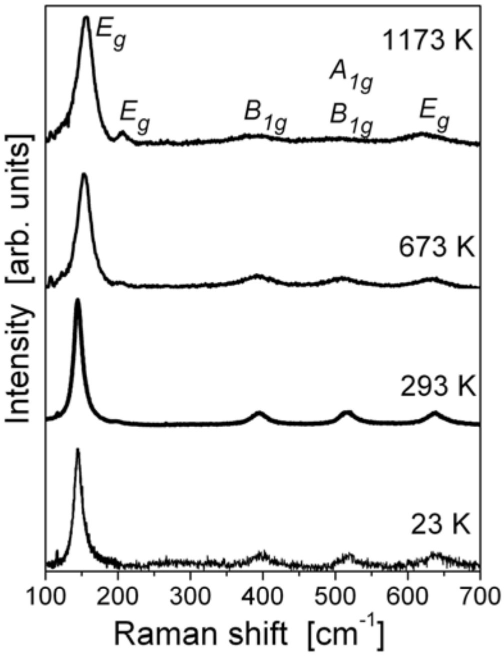

**Fig. 2** Raman spectra of anatase $TiO_2$ taken at 23, 293, 673 and 1173 K.

The Stokes and anti-Stokes Raman spectra of the lowest frequency $E_g$ mode at different temperatures in $TiO_2$ nanopowder are shown in Fig. 3(a) and (b). Lower temperatures ($T < 300$ K) were obtained by the cryostat system in vacuum. Higher temperatures were achieved by the microscope heating stage in air.

Several factors like phonon confinement [2-5, 8, 13, 14], strain [8, 15], non–homogeneity of the size distribution [8], defects and nonstoichiometry [7, 8], as well as anharmonic effects due to temperature increase [16] can contribute to changes in the peak position, linewidth and shape of the $E_g$ Raman mode in anatase $TiO_2$ nanopowder.

The asymmetric shape of the $E_g$ modes at room and lower temperatures points to a pronounced phonon confinement effect, while at higher temperatures its more symmetric broadening indicates that a strong anharmonic effect is dominant.

The redshift and narrowing of the Raman $E_g$ mode in anatase $TiO_2$ nanopowder, in comparison to the room temperature position and linewidth, are expected at low temperatures [17]. The absence of this effect here can be ascribed to discrepancy from the stoichiometry and the presence of a specific kind of nonstoichiometric defects, due to laser irradiation in vacuum, which usually cause blueshift and broadening of the Raman $E_g$ mode [7, 8]. That effect compensates the expected redshift and narrowing at low temperatures.

According to the phenomenological work of Richter et al. [13] and Campbell et al. [14] for spherical particles of diameter $L$ and Gaussian confinement function, the resulting

Raman intensity $I(\omega)$ can be presented as a superposition of weighted Lorentzian contributions over the whole Brillouin zone [14, 15]:

$$I(\omega)=\sum_{i=1}^{m}\int_{0}^{\infty}\rho(L)\,dL\int_{BZ}\frac{\exp\left(\frac{-q^{2}L^{2}}{8\beta}\right)d^{3}q}{[\omega-\omega_{i}(q,T)]^{2}+\left(\frac{\Gamma(T)}{2}\right)^{2}}\ , \qquad (1)$$

where $\rho(L)$ is the particle size distribution, $q$ is wave vector expressed in units of $\pi$ divided by value of unit cell parameter, and $\Gamma(T)$ is the mode line width at temperature $T$. The sum is carried over $m$ dispersion curves $\omega_i(q, T)$, depending on mode degeneration [15]. Then, according to theoretical curves of anatase calculated by Mikami et al. [18], the dispersion relations were approximated in cosine form [17], $\omega_i(q,T)=\omega_0(T)+B_i(1-\cos(2\pi\cdot q))$, where $\omega_0(T)$ is frequency in the center of Brillouin zone at temperature $T$, and $B_i$ are fitting parameters. The angular integral in a wave vector space in the Brillouin zone was performed by integrating along the Γ-X, Γ-N, and G-Z symmetry directions, weighting each by the number of equivalent symmetry directions [17]. Confinement factor is assumed to be $\beta\approx7$. The values of $\omega_0(T)$, as well as those of $\Gamma(T)$, at a specified temperature were treated as adjusting parameters in the fitting procedure. We supposed a log-normal particle size distribution with the average crystallite size of $L_0$=7.3 nm and standard deviation $\sigma$=0.20 obtained from LFR measurements.

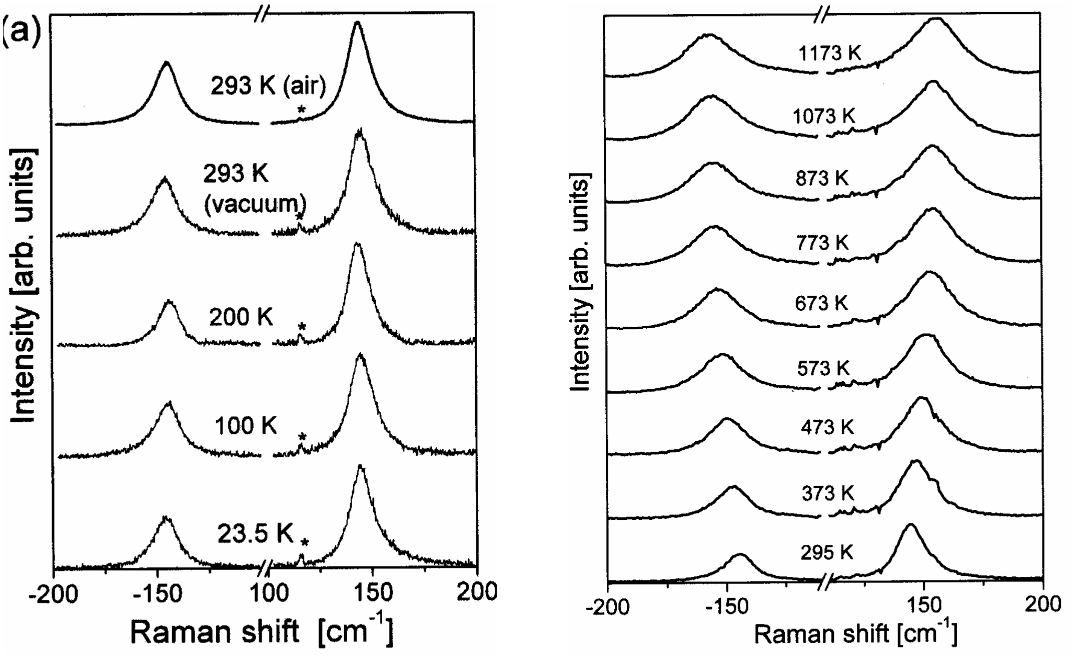

a) b)

**Fig. 3** Stokes and anti-Stokes Raman shift of $E_g$ mode anatase $TiO_2$ measured at different temperature ranges: 23 to 293 K (a) and 295 to 1173 K (b).

The comparison of the normalized experimental and calculated spectra according to described procedure at several temperatures (23, 295, 673, and 1073 K) is shown in Fig. 4. A good agreement between these results confirms the proper choice of particle size distribution taken according to LFR measurements.

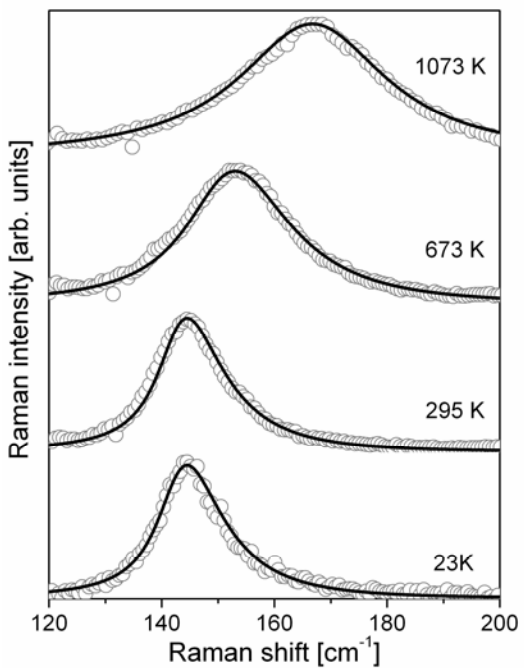

**Fig. 4** Normalized experimental (*open circles*) and calculated (*solid lines*) spectra of anatase $TiO_2$ nanopowder measured at different temperatures.

It is evident that frequency and linewidth increases by heating above room temperature, while the lineshape of $E_g$ mode becomes more symmetric. As-read experimental (open symbols) and fitted (full symbols) positions $\omega_0(T)$ and linewidths $\Gamma(T)$ of Raman $E_g$ mode are compared in Fig. 5(a). The influence of phonon confinement effect can be estimated through the difference between measured and calculated values, which decreases with temperature increases above 673 K (500°C). It is related to the crystallite size increase shown in Fig. 5(b), obtained by the fitting procedure described above, where it is changed from 7.3 to 35 nm, when the temperature grows from 673 to 1173 K. This coincides with the results of Balaji et al. [12], where upon annealing at temperatures at and below 400°C the crystallite size does not change significantly, while this size grows continuously as the annealing temperature is raised to 900°C.

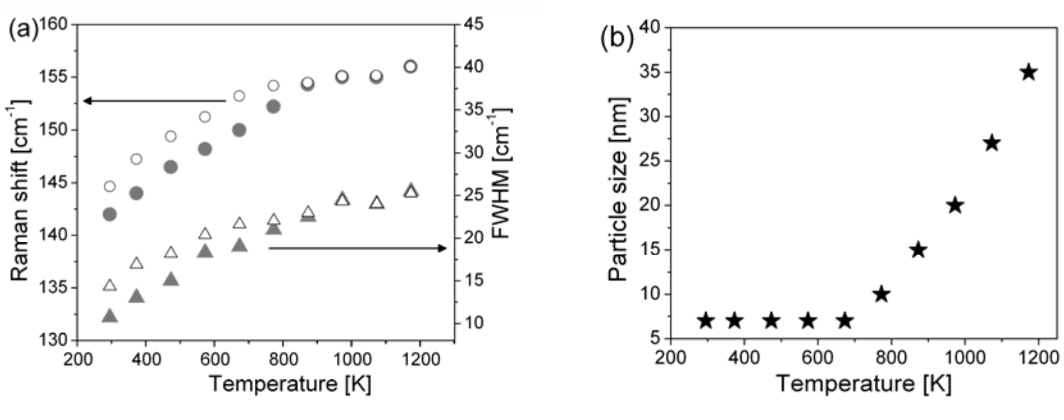

a) b)

**Fig. 5** As-read experimental (open symbols) and fitted (full symbols) positions and halfwidths of Raman $E_g$ mode (a) and the temperature dependence of particle size obtained from fitting procedure (b).

The Raman spectrum of $TiO_2$ nanopowder measured at room temperature after heating at 900°C (1173 K), shown in Fig. 6, confirms crystallite growth due to heating. Namely, the position (143.5 $cm^{-1}$) and linewidth (8.8 $cm^{-1}$) of the lowest frequency $E_g$ Raman mode in this spectrum are close to their values characterstic for the Raman spectrum of polycrystalline anatase $TiO_2$ [16].

## 4. Conclusion

Commercial $TiO_2$ nanopowder in the anatase phase was temperature treated in order to investigate the phonon behavior and stability of this nanocrystalline material. The temperature dependence of the Raman spectra of anatase $TiO_2$ nanocrystals was measured in the temperature range 23-1073 K. Variations of the frequency and linewidth of Raman modes with temperature were demonstrated. The blueshift and broadening of the lowest frequency $E_g$ Raman mode are particularly analyzed by the phonon confinement model, including anisotropic dispersion relations with temperature dependant parameters.

The study shows the utilisation of Raman spectroscopy for determination of structure and crystallite size of nanocrystalline $TiO_2$. These results have shown that the contributions of confinement effect and nonstoichiometry due to laser irradiation in vacuum are pronounced at low temperatures. However, at high temperatures the contribution due to anharmonic effect is dominant. Decreasing of phonon confinement effect with temperature increase above 673 K is ascribed to crystallite growth at higher temperatures.

## Acknowledgement

This work was supported by the MSRS under the projects No. 141047 and the OPSA-026283 Project within EC FP6 Programme.

## References

1. V. Swamy, A. Kuznetsov, L. S. Dubrovinsky, R. A. Caruso, D. G. Shchukin, B. C. Muddle, Phys. Rev. B 71 (2005) 184302.
2. H. Zhang, J. F. Banfield, J. Mater. Chem. 8 (1998) 2073.
3. A. Li Bassi, D. Cattaneo, V. Russo, C. E. Bottani, E. Barborini, T. Mazza, P. Piseri, P. Milani, F. O. Emst, K. Wegner, S. E. Pratsinis, J. Appl. Phys. 98 (2005) 074305.
4. S. Kelly, F. H. Pollak, M. Tomkiewicz, J. Phys. Chem. B 101 (1997) 2730.
5. D. Bersani, P. P. Lottici, Appl. Phys. Lett. 72 (1998) 73.
6. W. F. Zhang, Y. L. He, M. S. Zhang, Z. Yin, Q. Chen, J. Phys. D: Appl. Phys. 33 (2000) 912.
7. J. C. Parker, R. W. Siegel, Appl. Phys. Lett. 57 (1990) 943.
8. M. J. Šćepanović, M. U. Grujić-Brojčin, Z. D. Dohčević-Mitrović, Z. V. Popović, Mater. Sci. Forum 518 (2006) 101.
9. M. Ivanda, K. Furić, S. Musić, M. Ristić, M. Gotić, D. Ristić, A. M. Tonejc, I. Djerdj, M. Mattarelli, M. Montagna, F. Rossi, M. Ferrari, A. Chiasera, Y. Jestin, G. C. Righini, W. Kiefer, R. R. Goncalves, J. Raman Spectrosc. 38 (2007) 64.
10. T. Ohsaka, F. Izumi, Y. Fujiki, J. Raman Spec. 7 (1978) 321.
11. Y.L. Du, Y. Deng, M.S. Zhang, J. Phys. Chem. Solids 67 (2006) 2405.
12. S. Balaji, Y. Djaoued, J. Robichaud, J. Raman Spectrosc 37 (2006) 1416.
13. H. Richter, Z.P. Wang, L. Ley, Solid State Commun. 39 (1981) 625.
14. I. H. Campbell, P.M. Fauchet, Solid State Commun. 58 (1984) 739.

15. J. E. Spanier, R. D. Robinson, F. Zhang, S. W. Chan, I. P. Herman, Phys. Rev. B 64 (2001) 245407.
16. K. R. Zhu, M. S. Zhang, Q. Chen, Z. Yin, Phys. Lett. A 340 (2005) 220.
17. M. J. Šćepanović, M. Grujić-Brojčin, Z. D. Dohčević-Mitrović, Z. V. Popović, Appl. Phys. A 86 (2007) 365.
18. M. Mikami, S. Nakamura, O. Kitao, H. Arakawa, Phys. Rev. B 66 (2002) 155213.

***Садржај:*** *Метода Рамановe спектроскопије употребљена је за карактеризацију комерцијалног* $TiO_2$ *нанопраха, декларисане величине зрна од 5 nm. Раманови спектри, мерени у Стоксовом и анти-Стоксовом режиму, потврдили су анатас фазу* $TiO_2$ *праха у температурном опсегу 25-1173 K. Показано је да фононско ограничење (услед мале величине зрна) и нестехиометрија (изазвана ласерским озрачивањем у вакууму) имају велики утицај на плави помак и ширење најинтензивнијег* $E_g$ *Раман мода на ниским температурама, док утицај јаког анхармонијског ефекта постаје доминантан на вишим температурама. Ефекат фононског ограничења смањује се услед повећања кристалита на температурама вишим од 673 K.*

***Кључне речи****: Анатас* $TiO_2$ *нанопрах, Раманова спектроскопија*

J Sol-Gel Sci Technol (2009) 49:311–319
DOI 10.1007/s10971-008-1872-3

ORIGINAL PAPER

# Raman study of the variation in anatase structure of $TiO_2$ nanopowders due to the changes of sol–gel synthesis conditions

**A. Golubović · M. Šćepanović · A. Kremenović ·
S. Aškrabić · V. Berec · Z. Dohčević-Mitrović ·
Z. V. Popović**

Received: 18 August 2008 / Accepted: 25 November 2008 / Published online: 10 December 2008

**Abstract** $TiO_2$ nanopowders were produced by sol–gel technique under different synthesis conditions. XRD results have shown that obtained nanopowders are in anatase phase, with the presence of a small amount of highly disordered brookite phase, whereas nanocrystallite size and amount of brookite slightly depend on sol–gel synthesis conditions. Raman measurements confirm these results. The analyses of the shift and width of the most intensive anatase $E_g$ Raman mode by phonon confinement model suggest that anatase crystallite size should be in the range between 11 and 15 nm, what is in excellent correlation with XRD results. Obtained results have shown that Raman spectroscopy is a highly sensitive method for the estimation of anatase crystallite size as well as brookite content in $TiO_2$ nanopowders synthesized by variable sol–gel synthesis conditions.

**Keywords** Nanostructures · Sol–gel synthesis · X-ray diffraction · Raman spectroscopy

**Abbreviation**

| | |
|---|---|
| XRD | X-ray diffraction |
| PCM | Phonon confinement model |
| JCPDS | Joint committee on powder diffraction standards |

A. Golubović (✉) · M. Šćepanović · S. Aškrabić · V. Berec ·
Z. Dohčević-Mitrović · Z. V. Popović
Institute of Physics, Pregrevica 118, P.O. Box 68,
11080 Zemun, Serbia
e-mail: golubovic@phy.bg.ac.yu

A. Kremenović
Faculty of Mining and Geology, University of Belgrade,
Djušina 7, P.O. Box 162, 11000 Belgrade, Serbia

## 1 Introduction

Titanium dioxide ($TiO_2$) is an important industrial material as a main component of paints, pigments, a variety of glass products, biomedical implants and in cosmetics [1, 2]. It has been also used for optical coatings, beam splitters and anti-reflection coatings because of its high dielectric constant and refractive index. Pure $TiO_2$ has three polymorphs: rutile (tetragonal, $P4_2/mnm$), anatase (tetragonal, $I4_1/amd$), and brookite (orthorhombic, $Pbca$). Recently, nanosized anatase $TiO_2$ has attracted much attention for its numerous applications as key material for photocatalysts [3], dye-sensitized solar cells [4], gas sensors [5] and electrochromic devices [6]. Furthermore, $TiO_2$ nanocrystals are non-toxic compounds and can be candidate for the biological applications [7]. The applications of nanosized anatase $TiO_2$ are primarily determined by its physicochemical properties such as crystalline structure, particle size, surface area, porosity and thermal stability. Proper control of these properties, especially crystalline structure depending on the preparation conditions of nanosized $TiO_2$, represents some of the key issues in this area.

Sol–gel process is a relatively novel technique for the preparation of nanocrystalline $TiO_2$. It has been demonstrated that using the sol–gel process, the physicochemical and electrochemical properties of $TiO_2$ can be modified in order to improve its application [8]. This technique provides a simple and easy means of synthesizing nanoparticles at ambient temperature under atmospheric pressure. Since this process occurs in a solution, it has all the advantages over other preparation techniques regarding the purity, homogeneity, possibility of introducing large concentration of dopants, stoichiometry control, simplicity of processing and composition control. Through the sol–gel process, the growth of $TiO_2$ colloids in submicrometer range can be effectively controlled by systematic change of the parameters relevant for the hydrolysis and condensation of titanium alkoxides in aqueous solution.

To achieve a certain control of $TiO_2$ nanostructural properties it is necessary to find a sensitive and reliable method for fast estimation of small variations of above mentioned properties depending on the material preparation conditions. Among various conventional characterization techniques Raman Spectroscopy has already proven to be such a technique [9]. Namely, correct interpretation of the Raman spectra of $TiO_2$ nanopowders enables the estimation of various properties, such as: existence of mixed phases (anatase in combination with considerable amount of rutile or brookite phase), particle size and particle size distribution, discrepancy from stoichiometry as well as type of stoichiometric defects, etc. [10–13]. The aim of this paper is to investigate the subtle variations in structure of anatase nanopowders by Raman spectroscopy and to correlate these variations with the parameters of the sol–gel synthesis process.

## 2 Experimental details

$TiCl_4$ was used as the precursor in the synthesis process. The $Ti(OH)_4$ hydrogel was obtained by hydrolysis of $TiCl_4$ at 0 °C with controlled addition of 2.5 wt% aqueous ammonia into the aqueous solution of $TiCl_4$ (0.3 mol/l) and careful control of the pH value of the solution (9.3 and 10.3). $TiCl_4$ is soluble in water but it experiences rigorous reaction at 20 °C what can be very important to perform this reaction at lower temperature. After aging in the mother liquor for 5 h, the as-prepared hydrogel was filtered and washed out with deionized water until complete removal of chlorine ions. The obtained $Ti(OH)_4$ hydrogel was converted to its ethanol–gel by repeated exchange with anhydrous ethanol for several times (by repeated introduction of anhydrous ethanol). The obtained alcogel represents the starting point for production of $TiO_2$ nanoparticles. Alcogel was placed in a vessel, dried at 280 °C and calcined at temperatures below 600 °C, after which it was converted to the nanoparticles.

All chemicals used in this experiment were analytical grades (Merck Chemicals) and were used as received.

Atomic Force Microscope (Omicron B002645 SPM PROBE VT AFM 25) in noncontact mode was use to create an image of the surface topology of the samples. All measurements were performed in high vacuum conditions ($10^{-10}$ mbar) with standard $Si_3N_4$ needle for surface layer recording in the noncontact mode.

Powder X-ray diffraction (XRD) was used for identification of crystalline phases, quantitative phase analysis and estimation of crystallite size and strain. The XRD patterns were collected with Philips diffractometer (PW1710) employing $CuK\alpha_{1,2}$ radiation. Step scanning was performed with $2\theta$ ranging from 10 to 135°, step size of 0.06° and the fixed counting time of 41s/step. The XRD patterns were used to refine crystallographic structure and microstructural parameters using the procedure explained elsewhere [14, 15]. The Fullprof computer program was used [14].

Raman measurements were performed at room temperature using the Jobin-Yvon T64000 triple spectrometer system, equipped with confocal microscope and a nitrogen-cooled CCD detector. The 514-nm laser line of a mixed $Ar^+/Kr^+$ laser was used as an excitation source.

## 3 Results and discussion

### 3.1 Synthesis conditions

Sol–gel chemistry has recently evolved into a general and powerful approach for preparing inorganic materials [16]. The properties of obtained materials are determined by the main parameters of the sol–gel synthesis process: the precursor type, pH value in hydrolysis process, duration and temperature of hydrolysis (so called aging), alcogel, duration and temperature of drying and, as the most important ones, the parameters of calcination process—heating rate, temperature, duration and cooling rate of calcination.

$TiCl_4$ is the primary starting material for the commercial production of titania powders, known as the "chloride" process in the titania industry. The sol–gel method typically entails hydrolysis of a solution of a precursor molecule aiming to obtain first a suspension of colloidal particles (the sol) and then a gel composed of aggregated sol particles. The gel is then thermally treated yielding to the desired material. The reaction can be written as follows:

$$TiCl_4 \rightarrow Ti(OH)_4 \rightarrow \text{alcogel} \tag{1}$$

The corresponding chemical reactions are:

$$TiCl_4 + 4NH_4OH \rightarrow Ti(OH)_4 \downarrow + 4NH_4Cl \tag{2}$$

$$Ti(OH)_4 \rightarrow TiO_2 + \ 2H_2O \tag{3}$$

The pH value of the precursor solution is a decisive factor in controlling the final particle size and shape, crystal phase and agglomeration [17] due to its influence on the relative rates of hydrolysis and polycondensation. Aruna et al. [18] have found that the main hydrolyzate in this reaction is $[Ti(OH)_n(H_2O)_{6-n}]^{(4-n)+}$, where the amount of water varies with the relative rates of hydrolysis and polycondensation. The titanium monomers, formed during the reaction in precursor solution, play a significant role in the condensation process [19] and in the formation of the final gel structure containing precursor molecules [20]. $[Ti(OH)_7]^{3-}$

represents the preponderant titanium coordination complex in alkali solutions (pH = 9). Not only that all water molecules are completely replaced by hydroxyl ions, but some excessive hydroxyl ions are localized at the neighbouring sites of the $TiO_6$ octahedrons. Hence, the dehydration reaction involves two close hydroxyl ions while water molecules should remain in the precursor structure. According to the proposed model, the presence of excessive $[OH]^-$ will hinder the orientation movement of crystal nucleus. In such a way the disordered precursor structure will easily crystallize into the anatase phase. Since the intention was to obtain $TiO_2$ nanopowders in anatase form, pH values of the solution during the hydrolysis process, were chosen to be 9.3 ($pH_1$) and 10.3 ($pH_2$). These values are in accordance with the pH value of 9.4 used by Venz et al. [21] for the same sol state and tetraisopropyl titanate used as a precursor. These authors have shown that the pH values, several pH units above the pH value where zeta-potential is zero (isoelectric point), are suitable for obtaining the stable sol with maximal reduction of particle aggregations.

Aging is a process during which the gel physical properties can be changed as a result of polymerization, coarsening and phase transformation [22]. Nanocrystallite growth can be regarded as the coalescence of small neighbouring crystallites that become oriented due to the atomic diffusion or discrete orientation attachment. The aging conditions were the same in all experiments, with the temperature of 0 °C and process duration of 5 h which is in accordance with the literature data [23, 24]. In such a way the influence of aging on the properties of synthesized anatase nanoparticles was eliminated.

In order to obtain crystalline nanoparticles of titania by sol–gel technique, titanium hydroxide was dried and calcined at high temperature. In our experiments drying temperature was always 280 °C, while the process duration was 4 h.

Anatase nanopowders obtained by sol–gel method are amorphous in phase but with increasing the temperature up to 350 °C or higher the transition from amorphous to anatase phase happens [25]. However, calcination temperature must be kept lower than 600 °C, because of the phase transition from anatase to rutile phase [26]. Apart from this, high calcination temperature would result in the growth of nanocrystalline particles and the rapid decrease of specific surface area. In order to obtain ultrafine nanocrystalline $TiO_2$ powders with high specific surface area, a reasonable pathway would be to lower the temperature of the phase transition. The influence of the calcination parameters on the properties of anatase nanopowders was examined by changing the calcination temperature in the range between 400 and 550 °C, with two different heating rates, $Tr_1$ and $Tr_2$ (about 60 and 135 °C/h, respectively) and constant duration and cooling rate of calcination.

Some of the sol–gel synthesis parameters for chosen $TiO_2$ samples are listed in Table 1.

### 3.2 The results of AFM measurement

The surface topology of the sample A2 recorded by AFM in noncontact mode is shown in Fig. 1. As can be seen from this image the size of most particles ranges from 10 to 15 nm. However, as grain boundaries are not clearly defined it is very hard to obtain reliable distribution of particle size from this image. Correspondingly, this method cannot be used for the accurate estimation of subtle variations in average particle size due to the difference in synthesis conditions.

### 3.3 The results of XRD diffraction

The most intensive diffraction peaks in the XRD patterns of sol–gel produced samples can be ascribed to the anatase crystal structure (JCPDS card 78-2486). The XRD patterns of some chosen samples are presented in Fig. 2a, while the position of diffraction lines, together with corresponding Miller indices, is listed in Table 2. The obtained values for the unit cell parameters of anatase are as follows: $a = 3.7844(1)$ Å and $c = 9.4838(4)$ Å for sample $A_2$, $a = 3.7856(1)$ Å and $c = 9.4860(4)$ Å for sample $A_3$, and $a = 3.7884(1)$ Å and $c = 9.4980(3)$ Å for sample $A_6$. These results show that the value of the parameter $a$ varies around its reference value ($a_0 = 3.78479(3)$ Å), while the value of the $c$ parameter in our samples is slightly smaller than the reference one ($c_0 = 9.51237(12)$ Å). The presence of low-intensity diffraction peak at $2\theta \approx 30.8°$, which can be ascribed to the brookite phase of $TiO_2$, is observed in all XRD patterns (JCPDS card 29-1360). The variation of the intensity of this peak is also shown in Fig. 2b.

**Table 1** The parameters of sol–gel process for some $TiO_2$ samples

| Sample | Aging | | Drying | | | Calcination | | | |
|---|---|---|---|---|---|---|---|---|---|
| | Time [h] | T [°C] | Heating time [h] | T [°C] | Time [h] | Heating rate [°C/h] | T [°C] | Time [h] | Cooling rate [°C/h] |
| A2 | 5 | 0 | 2 | 280 | 4 | 55 | 500 | 7 | 36.46 |
| A3 | 5 | 0 | 2 | 280 | 4 | 67.5 | 550 | 7 | 37.42 |
| A6 | 5 | 0 | 2 | 280 | 4 | 135 | 550 | 7 | 37.42 |

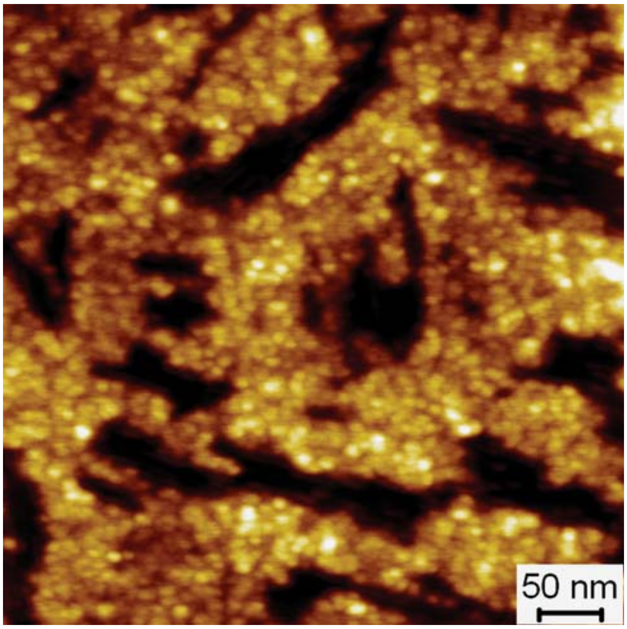

**Fig. 1** AFM image of sample A2 (500 × 500 nm) obtained at room temperature

Structure refinements were performed by the Rietveld method. Low values of agreement factors between the model, both structure and microstructure, and XRD data (A2–$R_p$: 6.86, $R_{wp}$: 8.94, $R_{exp}$: 5.90, $\chi^2$: 2.29, Bragg R-factor for anatase: 2.31 and Bragg R-factor for brookite: 5.19, A3–$R_p$: 8.86, $R_{wp}$: 13.8, $R_{exp}$: 5.97, $\chi^2$: 5.37, Bragg R-factor for anatase: 1.69 and Bragg R-factor for brookite: 4.17 and A6–$R_p$: 8.59, $R_{wp}$: 14.0, $R_{exp}$: 6.18, $\chi^2$: 5.16, Bragg R-factor for anatase: 2.08 and Bragg R-factor for brookite: 4.15) indicates high accuracy of obtained results. The obtained average crystallite size and average strain in anatase and brookite phase, as well as quantitative phase analysis results (brookite content), were summarized in Table 3. Large values of the average strain in brookite crystallites indicate that this phase is highly disordered in all the samples.

### 3.4 The results of Raman spectroscopy

Raman spectra of $TiO_2$ samples produced under different sol–gel synthesis conditions were measured at room temperature. Some of these spectra are shown in Fig. 3. In the spectra of all $TiO_2$ samples the dominant Raman modes can be assigned to the Raman active modes of the anatase crystal [27]: ~143 $cm^{-1}$ ($E_{g(1)}$), 197 $cm^{-1}$ ($E_{g(2)}$), 399 $cm^{-1}$ ($B_{1g(1)}$), 540 $cm^{-1}$ (combination of $A_{1g}$ and $B_{1g(2)}$ that can not be resolved at room temperature) and 639 $cm^{-1}$ ($E_{g(3)}$). The position of $E_{g(1)}$ Raman mode

**Fig. 2** XRD diffractograms of chosen $TiO_2$ samples (**a**). Enlarged diffraction peak ascribed to brookite phase (**b**)

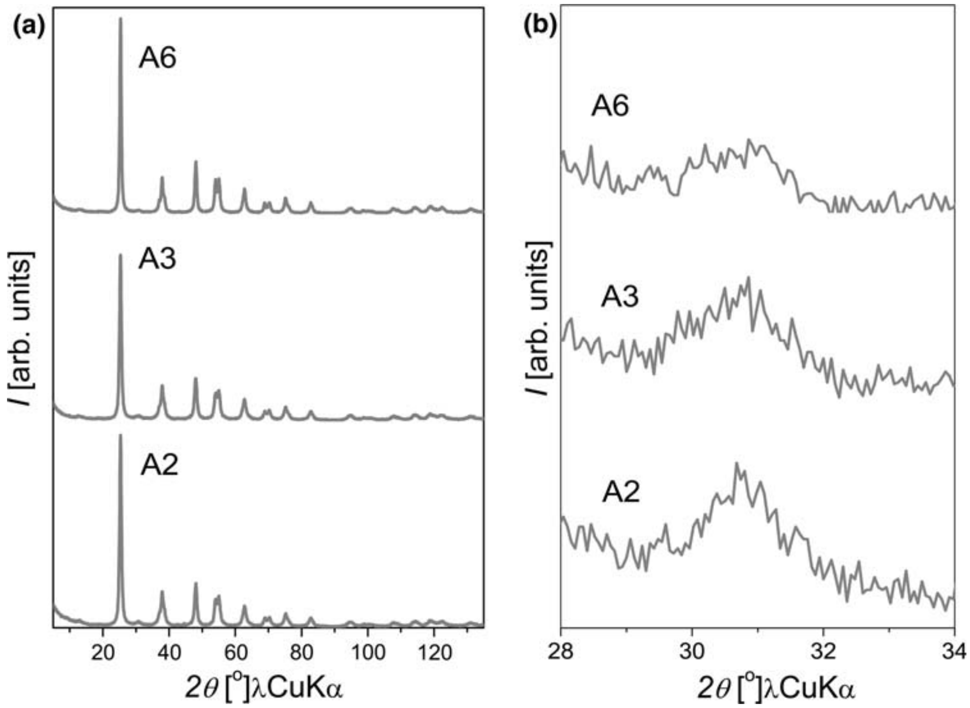

**Table 2** The positions of diffraction lines for patterns presented in Fig. 2a, together with corresponding Miller indices (JCPDS card 78-2486)

| 2θ [°] | 12.19 | 37.19 | 47.83 | 49.40 | 53.85 | 54.89 | 62.48 | 74.92 |
|---|---|---|---|---|---|---|---|---|
| (hkl) | 101 | 004 | 200 | 202 | 105 | 211 | 204 | 215 |

**Table 3** The results of Rietveld analyses (average crystallite size and average strain in anatase and brookite phase) and content of brookite phase for several $TiO_2$ samples

| Samples | Anatase crystallite size [nm] | Average strain in anatase crystallites | Brookite content [%] | Brookite crystallite size [nm] | Average strain in brookite crystallites |
|---|---|---|---|---|---|
| A2 | 12 | $4.5 \times 10^{-3}$ | 17 | 12 | $16.9 \times 10^{-3}$ |
| A3 | 12 | $4.2 \times 10^{-3}$ | 16 | 35 | $19.6 \times 10^{-3}$ |
| A6 | 15 | $3.4 \times 10^{-3}$ | 10 | 58 | $16.8 \times 10^{-3}$ |

for different $TiO_2$ samples ranges between 142.6 and 143.3 $cm^{-1}$, while its linewidth varies from 10.2 to 12.7 $cm^{-1}$, as can be seen in Fig. 4 The Raman linewidth and position of other modes change a little (within ±0.2 $cm^{-1}$) in different samples.

Several factors such as phonon confinement [10, 28–33], strain [28, 34], non–homogeneity of the size distribution [28, 29, 35], defects and nonstoichiometry [28, 36], as well as anharmonic effects due to temperature increase [29, 37] can contribute to the changes in the peak position, linewidth and shape of the $E_{g(1)}$ Raman mode in anatase $TiO_2$ nanopowders. Which of these factors play an important role in Raman spectra depends on the structural characteristics of a $TiO_2$ nanopowders like: grain size and grain size distribution, existence of mixed phases (anatase in combination with considerable amount of rutile or brookite phase), value and type of the strain (compressed or tensile), discrepancy from stoichiometry as well as type of stoichiometric defects, etc. [28]. Observed variations of position and linewidth of $E_{g(1)}$ mode in the $TiO_2$ samples, produced under different synthesis conditions shown in Fig. 4, imply that more than one of the mentioned factors influence the behaviour of this mode. Namely, broadening and blueshift of this mode don't have the same behaviour, i.e. greater broadening is not always followed by greater blueshift, as can be expected when only one factor (for instance phonon confinement due to small size of the particles) determines the behaviour of $E_{g(1)}$ mode. Strain

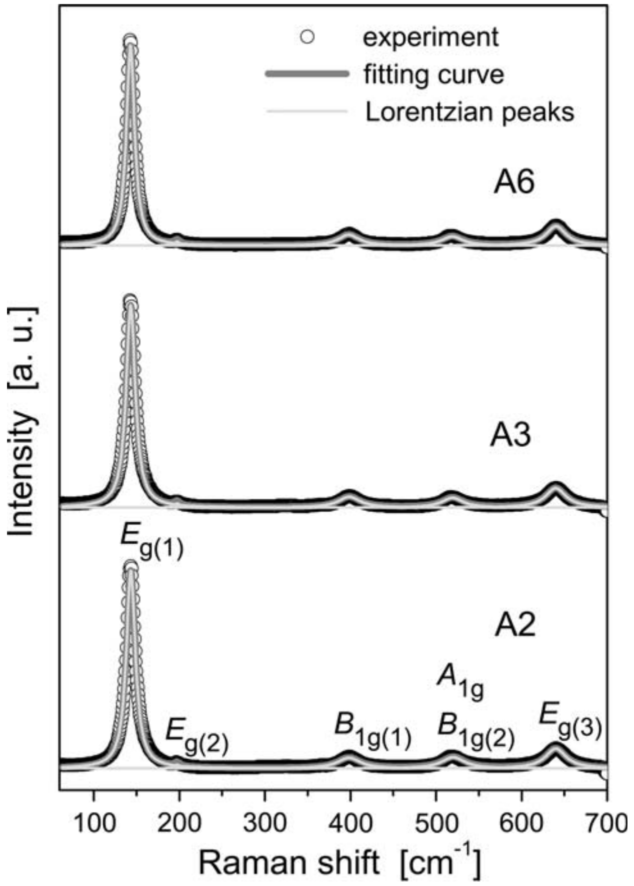

**Fig. 3** Raman spectra of several sol–gel synthesized $TiO_2$ samples

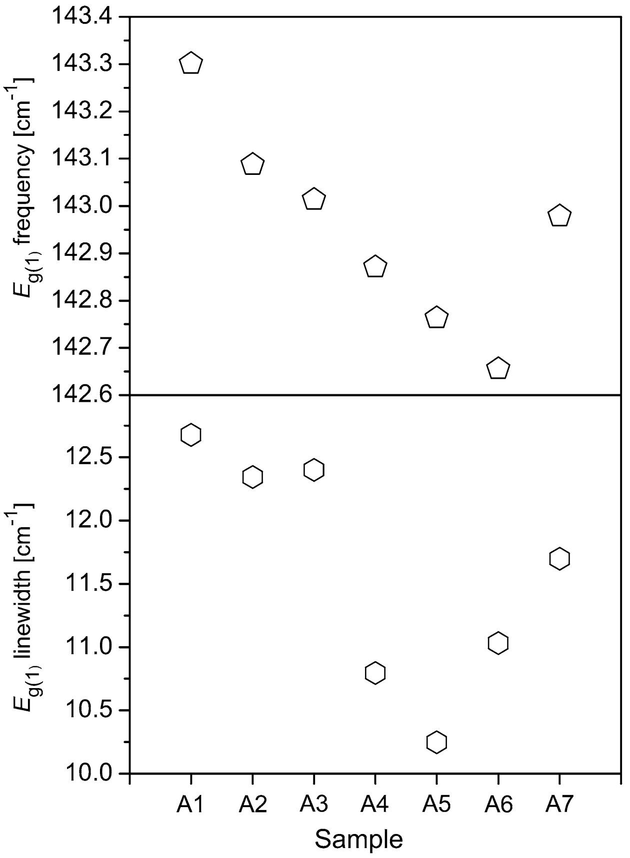

**Fig. 4** Frequency and linewidth of $E_{g(1)}$ Raman mode for different $TiO_2$ samples

and discrepancy from stoichiometry cannot be dominant factors in different behaviour of Raman spectra as all the samples have similar strain values (ranging from $3.4 \times 10^{-3}$ to $4.5 \times 10^{-3}$) and stoichiometry (due to similar calcination conditions). Also, as Raman spectra were measured at room temperature, the anharmonicity of the ionic potential must have similar effect on the Raman modes in all the samples. Therefore, the main factors which influence the behaviour of $E_{g(1)}$ mode in our samples synthesized by sol–gel method should be the grain size and grain size distribution, as well as the presence of disorder induced by the existence of considerable amount of brookite phase in combination with anatase. Considering the previous conclusions, the confinement effect due to small particle size was analyzed first, and afterwards the attention was paid to the presence of several modes of very low intensity that can be related to the brookite phase $TiO_2$.

The phonons in nanocrystal are confined in space and all the phonons over the entire Brillouin zone are expected to contribute to the first-order Raman spectra. The weight of the off-centre phonons increases as the crystal size decreases and the phonon dispersion causes an asymmetrical broadening and the shift of the Raman mode. According to the phenomenological work of Richter et al. [33] and Campbell et al. [34] for spherical particle of diameter $L$, presuming Gaussian confinement function, the resulting Raman intensity $I(\omega)$ can be presented as a superposition of weighted Lorentzian contributions over the whole Brillouin zone [34]:

$$I(\omega)=\sum_{i=1}^{m}\int_{0}^{\infty}\rho(L)\,dL\int_{BZ}\frac{\exp\left(\frac{-q^{2}L^{2}}{8\beta}\right)d^{3}q}{[\omega-\omega_{i}(q)]^{2}+\left(\frac{\Gamma_{0}}{2}\right)^{2}} \qquad (4)$$

where $\rho(L)$ is the particle size distribution, $q$ is wave vector expressed in units of $\pi$ divided by value of unit cell parameter, and $\Gamma_0$ is the intrinsic linewidth of Raman mode at given temperature. The sum is taken over $m$ dispersion curves $\omega_i(q)$, depending on mode degeneration. The factor $\beta$ varies from $\beta = 1$ in the Richter confinement model to $\beta = 2\pi^2$ in the Campbell model depending on the confinement boundary conditions in different nanomaterials. In the calculations of the intensity of $E_{g(1)}$ Raman mode in our sol–gel synthesized $TiO_2$ nanopowders we used $\beta = 12$.

According to phonon dispersion relations of anatase computed by Mikami et al. [38], the dispersion relations in this paper are approximately expressed in the cosine form [37]:

$$\omega_i(q) = \omega_0 + B_i(1 - \cos(q\pi)) \qquad (5)$$

where $\omega_0$ is the zone-centre frequency of the $E_{g(1)}$ mode at room temperature. The values of $B_i$ constants are calculated to match the theoretical phonon dispersion curves [38], depending on the direction throughout Brillouin zone. We assumed $B_1 = 102$ cm$^{-1}$ and $B_2 = 28$ cm$^{-1}$ in Γ–X direction, $B_3 = 52$ cm$^{-1}$ and $B_4 = 15$ cm$^{-1}$ in Γ–N direction, and $B_5 = 18$ cm$^{-1}$ in Γ–Z direction [29]. The angular integral in a wave vector space in the Brillouin zone is performed by integrating along the Γ–X, Γ–N, and Γ–Z symmetry directions, each weighting by the number of equivalent symmetry directions [29, 35].

The shape of the particle size distribution was assumed to be asymmetric Gaussian with the ratio of the left (corresponding to smaller particles, $L < L_0$) to the right (corresponding to larger particles, $L > L_0$) Gaussian halfwidths varying between 0.66 and 1. $L_0$ is the position of central maximum in the particle size distribution.

The intensities of $E_{g(1)}$ mode for different samples calculated by described phonon confinement model (PCM) coincide well with the experimental spectra, as can be seen from Fig. 5. The parameter $L_0$ of different $TiO_2$ nanocrystalline samples obtained from PCM is shown in Fig. 6. It varies from 11.5 to 15 nm and corresponding average nanoparticles sizes for the chosen samples are very close to the values obtained by XRD analyses shown in Table 1 (XRD). Intrinsic linewidth of $E_{g(1)}$ Raman mode, used in PCM as adjusting parameter, is in the range from 8.5 to 10.2 cm$^{-1}$, as can be seen from Fig. 7. It should be noted that the value of the lower limit of this range is close to the intrinsic linewidth for polycrystalline samples which amounts about 8 cm$^{-1}$ [28]. On the other hand, the values of intrinsic linewidth higher than 10 cm$^{-1}$ indicate structural disorder in the sample.

In order to investigate the presence of brookite phase by Raman spectroscopy Raman spectra were measured with high resolution, long exposure time and high number of accumulations. Enlarged parts of Raman spectra in the

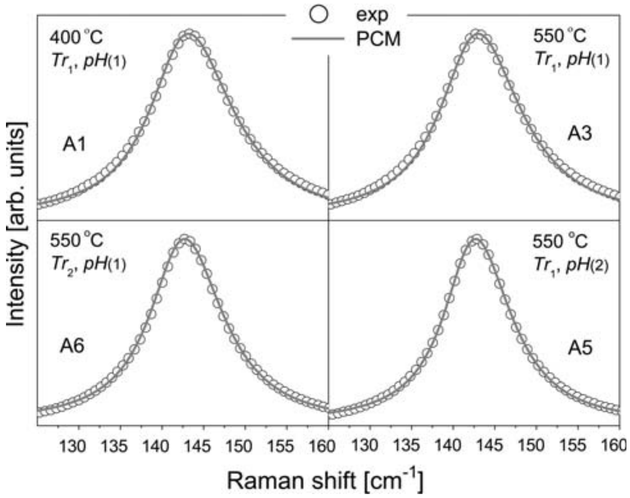

**Fig. 5** PCM fits of anatase $E_{g(1)}$ Raman mode for samples synthesized under different temperature and heating rate (*Tr*) of calcination and pH value of hydrolyzes

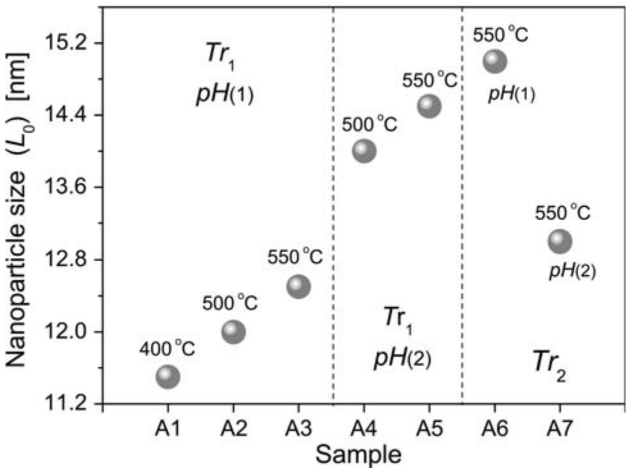

**Fig. 6** Nanoparticle size (parameter $L_0$) of different titania nanopowdered samples obtained from PCM

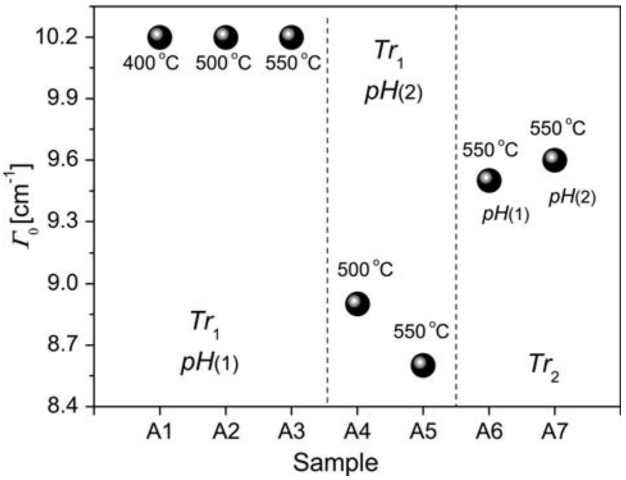

**Fig. 7** $E_{g(1)}$ Raman mode intrinsic linewidth obtained from PCM fits

range 230–430 cm$^{-1}$ for several samples are shown in Fig. 8. Additional Raman modes at about 243, 294, 323 and 362 cm$^{-1}$ can be ascribed to the brookite phase of titania [39–41]. Low intensities and large widths of these modes indicate great disorder and partial amorphization of brookite in all the samples. To estimate the amount of brookite phase, the sum of the integrated intensities of Lorentzian peaks originating from the brookite modes was compared to the intensity of Lorentzian peak related to the $B_{1g}$ mode of anatase phase. The intensity ratio of brookite modes to anatase one ($I_{B(\Sigma)}/I_{A(B1g)}$) is shown in Fig. 9. Although these results are mainly qualitative, they confirm the results obtained by XRD analyses. It can be seen from Fig. 9 that brookite content for the samples A2 and A3 estimated from Raman spectra is similar but higher then the content in the sample A6. The amount of brookite phase estimated by XRD was about 16% in the samples A2 and A3, and 10% for the sample A6.

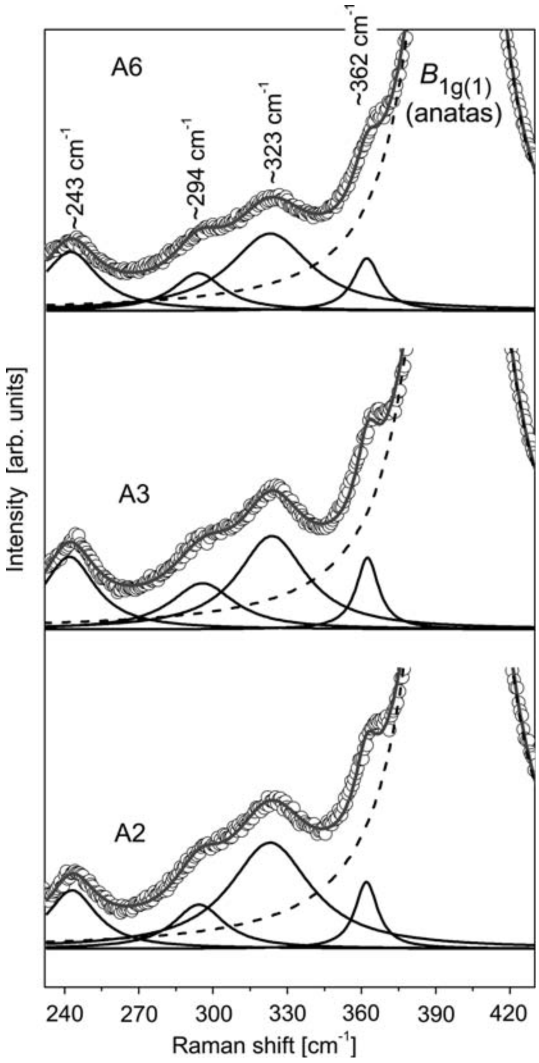

**Fig. 8** Lorentzian fits of brookite modes in experimental Raman spectra

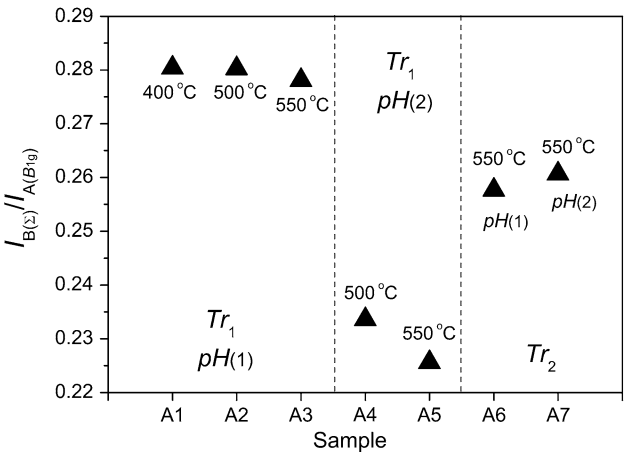

**Fig. 9** The intensity ratio of the sum of brookite modes and the anatase $B_{1g}$ Raman mode for different samples

Finally, the comparison of the obtained values for brookite to anatase ratio ($I_{B(\Sigma)}/I_{A(B1g)}$) with the behaviour of intrinsic linewidth ($\Gamma_0$) of $E_{g(1)}$ Raman mode in different samples suggests very interesting conclusion: larger amount of brookite in a sample induces larger values of $\Gamma_0$. This can be a consequence of the structural disorder of anatase due to the presence of brookite phase, but we also must have in mind that the most intensive Raman mode of brookite is at $\sim 150\ \mathrm{cm}^{-1}$ [38] and its presence can influence the width of the $E_{g(1)}$ Raman mode at $\sim 143\ \mathrm{cm}^{-1}$ (ascribed to anatase).

Although XRD diffraction can give good quantitative results relating to structural and microstructural properties of $TiO_2$ nanopowders, the collecting of the high resolution XRD patterns and their interpretation as well, are usually time-consuming process. The results presented in this section confirm great potential of Raman spectroscopy in determination of structural properties of $TiO_2$ nanopowders and the ability of this method to verify a very small variation in these properties as well.

### 3.5 Correlation between the results

Correlating the parameters of the sol–gel synthesis process with the resulting properties of nanostructured systems is necessary for the systematic control of the material properties. This section describes the influence of the variation of some synthesis parameters on the change in structural properties of obtained anatase nanoparticles, examined by XRD and Raman spectroscopy. Both XRD and Raman spectroscopy could enable more precise determination of the average particle size, compared to AFM measurements. Namely, from the obtained AFM images it wasn't possible to detect subtle variations in the particle size, of the order of few nanometres.

The influence of calcination temperature on anatase nanoparticles size was investigated earlier by several authors [9, 42]. The tendency of particle size to increase with increasing calcination temperature demonstrated in their papers was confirmed by our results shown in Fig. 6. When all other synthesis parameters are fixed higher calcination temperature leads to the formation of larger nanoparticles, although the results presented in Fig. 9 imply that calcination temperature doesn't affect the $I_{B(\Sigma)}/I_{A(B1g)}$ ratio.

The pH value of the hydrothermal solution can influence significantly polymorphous structure of $TiO_2$ nanopowders. Low and neutral pH values result in production of titania powders containing brookite and sometimes rutile. The alkalic solution with high pH values leads to the formation of anatase powders with high stability during calcination [43]. In our experiments pH values were set to 9.3 and 10.3, what was convenient for obtaining pure anatase powders, but in both XRD and Raman spectra the small content of amorphous brookite phase was observed. The same results were found in the literature (XRD peak at $2\theta = 30.8$) [44–46], but without any comments about brookite phase. Our results presented in Figs. 6 and 9, confirm the decreasing tendency of brookite content (and increasing particles size) with increasing pH value from 9.3 to 10.3 for relatively low heating rate of calcination process $Tr_1 = 60$ °C/h. However, the samples A6 and A7 produced with high heating rate $Tr_2 = 135$ °C/h show anomalous behaviour. They have almost the same ratio of brookite to anatase contents although they were prepared using different pH values of the hydrothermal solution. It seems that alkalic pH value is not high enough to avoid formation of brookite from $TiCl_4$ precursor although the literature suggests that brookite phase was observed only in acidic solutions [47].

Presented results show that properties of $TiO_2$ nanopowders depend not only on one parameter of sol–gel synthesis process. The nanoparticles size and content of brookite in produced nanopowders are the result of subtle interplay between many synthesis parameters such as the type of precursor, temperature and heating rate of calcination process and pH value of the hydrothermal solution.

## 4 Conclusion

A detailed Raman study of anatase $TiO_2$ nanopowders synthesized by sol–gel method with crystallite size varying between 11 and 15 nm was presented in this paper. It was demonstrated that the frequency shift and broadening of the most intensive anatase $E_{g(1)}$ Raman mode are the consequence of both confinement effect due to the nanosized nature of anatase crystallites and the presence of brookite phase in the samples. This enables not only basic phase identification but also the estimation of the nanoparticle size and brookite content in $TiO_2$ nanopowders following the subtle changes in the Raman spectra.

This study allows us to investigate the structural variations of nanosized $TiO_2$ arisen from the change in the sol–gel synthesis conditions. It was shown that nanostructured characteristics of the produced $TiO_2$ powders are the result of subtle interplay of several synthesis parameters: temperature and heating rate of calcination process and pH value of the hydrothermal solution. Presented results imply that the $TiCl_4$ as precursor may be responsible for the presence of small amount of disordered brookite phase in all samples despite of the alkalic solution used in the process of hydrolysis.

**Acknowledgement** Authors express thanks to Mirjana Grujić-Brojčin for the original software solutions which enabled the application of the PCM for numerical simulation of Raman spectra of investigated samples. Authors are also grateful to Toma Radić and Marko Radović for their help during AFM measurements. This work is supported by the Serbian Ministry of Science under project no. 141047, the OPSA-026283 project within the AC FP6 programme and SASA project F-134.

## References

1. Venz PA, Kloprogge JT, Frost RL (2000) Langmuir 16:4962. doi:10.1021/la990830u
2. Murugan AV, Samuel V, Ravi V (2006) Mater Lett 60:479. doi:10.1016/j.matlet.2005.09.017
3. Sakka S (2006) J Sol-Gel Sci Technol 37:135. doi:10.1007/s10971-006-6433-z
4. Hart JN, Menzies D, Cheng Y-B, Simon GP, Spiccia L (2006) J Sol-Gel Sci Technol 40:45. doi:10.1007/s10971-006-8387-6
5. Kim I-D, Rothschild A, Yang D-J, Tuller HL (2008) Sens Actuators B Chem 130:9. doi:10.1016/j.snb.2007.07.092
6. Granqvist CG, Azens A, Isidorsson J, Kharrazi M, Kullman L, Lindström T, Niklasson GA, Ribbing C-G, Rönnow D, Strømme Mattsson M, Veszelei M (1997) J Non-Cryst Solids 218:273. doi:10.1016/S0022-3093(97)00145-2
7. Zhang J, Wang X, Zheng W-T, Kong X-G, Sun Y-J, Wang X (2007) Mater Lett 61:1658. doi:10.1016/j.matlet.2006.07.093
8. Venkatachalam N, Palanichamy M, Arabindoo B, Murugesan V (2007) Mater Chem Phys 104:454. doi:10.1016/j.matchemphys.2007.04.003
9. Gouadec G, Colomban P (2007) Prog Cryst Growth Char Mater 53:1
10. Zhang WF, He YL, Zhang MS, Yin Z, Chen Q (2000) J Phys D Appl Phys 33:912. doi:10.1088/0022-3727/33/8/305
11. Du YL, Deng Y, Zhang MS (2006) J Phys Chem Solids 67:2405. doi:10.1016/j.jpcs.2006.06.020
12. Gao K (2007) Phys B 398:33. doi:10.1016/j.physb.2007.04.013
13. Zhang J, Li MJ, Feng ZC, Chen J, Li C (2006) J Phys Chem B 110:927. doi:10.1021/jp0552473
14. Rodriguez-Carvajal J (1998) FullProf computer program. ftp://charybde.saclay.cea.fr/pub/divers/fullprof.98/windows/winfp98.zip
15. Kremenovic A, Blanusa J, Antic B, Colomban P, Kahlenberg V, Jovalekic C, Dukic J (2007) Nanotechnology 18:145616
16. Lakshmi BB, Dorhout PK, Martin CR (1996) Chem Mater 9:857. doi:10.1021/cm9605577
17. Zhang W, Chen S, Yu S, Yin Y (2007) J Cryst Growth 308:122. doi:10.1016/j.jcrysgro.2007.07.053
18. Aruna ST, Tirosh S, Zaban A (2000) J Mater Chem 10:2388. doi:10.1039/b001718n
19. Sun J, Gao L (2002) J Am Ceram Soc 85:2382. doi:10.1111/j.1151-2916.2002.tb00467.x
20. Díaz-Díez MÁ, Macías-García A, Silvero G, Gordillo R, Caruso R (2003) Ceram Int 29:471. doi:10.1016/S0272-8842(02)00189-X
21. Venz PA, Frost RL, Kloprogge JT (2000) J Non-Cryst Solids 276:95. doi:10.1016/S0022-3093(00)00267-2
22. Wang P, Wang D, Xie T, Li H, Yang M, Wei X (2008) Mater Chem Phys 109:181. doi:10.1016/j.matchemphys.2007.11.019
23. He D, Lin F (2007) Mater Lett 61:3385. doi:10.1016/j.matlet.2006.11.075
24. Hari-Bala, Guo Y, Zhao X, Zhao J, Fu W, Ding X, Jiang Y, Yu K, Lv X, Wang Z (2006) Mater Lett 60:494. doi:10.1016/j.matlet.2005.09.030
25. Liu AR, Wang SM, Zhao YR, Zheng Z (2006) Mater Chem Phys 99:131. doi:10.1016/j.matchemphys.2005.10.003
26. Sugimoto T, Zhou X, Muramatsu A (2003) J Colloid Interface Sci 259:43. doi:10.1016/S0021-9797(03)00036-5
27. Ohsaka T, Izumi F, Fujiki Y (1978) J Raman Spectrosc 7:321. doi:10.1002/jrs.1250070606
28. Šćepanović MJ, Grujić-Brojčin MU, Dohčević-Mitrović ZD, Popović ZV (2006) Mater Sci Forum 518:101
29. Šćepanović MJ, Grujić-Brojčin M, Dohčević-Mitrović Z, Popović ZV (2007) Appl Phys A 86:365. doi:10.1007/s00339-006-3775-x
30. Li Bassi A, Cattaneo D, Russo V, Bottani CE, Barborini E, Mazza T, Piseri P, Milani P, Emst FO, Wegner K, Pratsinis SE (2005) J Appl Phys 98:074305. doi:10.1063/1.2061894
31. Kelly S, Pollak FH, Tomkiewicz M (1997) J Phys Chem B 101:2730. doi:10.1021/jp962747a
32. Bersani D, Lottici PP (1998) Appl Phys Lett 72:73. doi:10.1063/1.120648
33. Richter H, Wang ZP, Ley L (1981) Solid State Commun 39:625. doi:10.1016/0038-1098(81)90337-9
34. Campbell IH, Fauchet PM (1984) Solid State Commun 58:739. doi:10.1016/0038-1098(86)90513-2
35. Spanier JE, Robinson RD, Zhang F, Chan SW, Herman IP (2001) Phys Rev B 64:245407. doi:10.1103/PhysRevB.64.245407
36. Parker JC, Siegel RW (1990) Appl Phys Lett 57:943. doi:10.1063/1.104274
37. Zhu KR, Zhang MS, Chen Q, Yin Z (2005) Phys Lett A 340:220. doi:10.1016/j.physleta.2005.04.008
38. Mikami M, Nakamura S, Kitao O, Arakawa H (2002) Phys Rev B 66:155213. doi:10.1103/PhysRevB.66.155213
39. Ivanda M, Tonejc AM, Djerdj I, Gotić M, Music S, Mariotto G, Montagna M (2002) Nanoscale spectroscopy and its applications in semiconductor research, Lecture Notes in Physics, vol 588. Springer, Berlin, p 24
40. Djaoued Y, Brüning R, Bersani D, Lottici PP, Badilescu S (2004) Mater Lett 58:2618. doi:10.1016/j.matlet.2004.03.034
41. Yin S, Ihara K, Liu B, Wang Y, Li R, Sato T (2007) Phys Scr T 129:268. doi:10.1088/0031-8949/2007/T129/060
42. Bersani D, Lottici PP, Lopez T, Ding X-Z (1998) J Sol-Gel Sci Technol 13:849. doi:10.1023/A:1008602718987
43. Ovenstone J, Yanagisawa K (1999) Chem Mater 11:2770. doi:10.1021/cm990172z
44. Deshpande SB, Potdar HS, Khollam YB, Patil KR, Pasricha R, Jacob NE (2006) Mater Chem Phys 97:207. doi:10.1016/j.matchemphys.2005.02.014
45. Khanna PK, Singh N, Charan S (2007) Mater Lett 61:4725. doi:10.1016/j.matlet.2007.03.064
46. Khan R, Woo Kim S, Kim T-J, Nam C-M (2008) Mater Chem Phys 112:167
47. Pottier A, Chanéac C, Tronc E, Mazerolles L, Jolivet J-P (2001) J Mater Chem 11:116. doi:10.1039/b100435m

Vol. **115** (2009) *ACTA PHYSICA POLONICA A* No. 4

Proceedings of the Tenth Annual Conference of the Materials Research Society of Serbia, September 2008

# Characterization of La-Doped $TiO_2$ Nanopowders by Raman Spectroscopy

M. Šćepanović[a,*], S. Aškrabić[a], V. Berec[a], A. Golubović[a], Z. Dohčević-Mitrović[a],
A. Kremenović[b] and Z.V. Popović[a]

[a]Center for Solid State Physics and New Materials, Institute of Physics
Pregrevica 118, 11080 Belgrade, Serbia
[b]Faculty of Mining and Geology, Laboratory for Crystallography
University of Belgrade, Djušina 7, 11000 Belgrade, Serbia

Titanium dioxide ($TiO_2$) nanopowders doped with 0.65, 1, 2, 3 and 4 wt.% of lanthanum ions ($La^{3+}$) were synthesized by sol-gel technology. Dependence of structural and morphological characteristics of nanopowders on $La^{3+}$ content and synthesis conditions is investigated by the Raman spectroscopy. Very intensive modes observed in the Raman spectra of all nanopowder samples are assigned to anatase phase of $TiO_2$. Additional Raman modes of extremely low intensity can be related to the presence of certain amount of highly disordered brookite phase in nanopowders. Dependence of the intensity ratio of the Raman modes which originate from anatase and brookite on doping conditions is specially analyzed. In order to estimate the variation of nanocrystallite size with dopant content, shift and asymmetrical broadening of the most intensive $E_g$ Raman mode of anatase are analyzed by phonon confinement model. The obtained results are compared with the results of X-ray diffraction spectroscopy. Special attention is dedicated to the changes in the Raman spectra of pure and La-doped $TiO_2$ nanopowders observed after high temperature treatment.

PACS numbers: 81.20.Fw, 81.07.Wx, 78.30.−j, 07.05.Tp

## 1. Introduction

Titanium dioxide has three polymorphs: rutile (tetragonal, $P42/mnm$), anatase (tetragonal, $I41/amd$), and brookite (orthorhombic, $Pbca$). All of them have numerous applications as important industrial materials. In recent years, nanosized $TiO_2$, especially anatase $TiO_2$, has attracted much attention as key material for photocatalysts [1], dye-sensitized solar cells [2], gas sensors [3] and electrochromic devices [4]. The applications of nanosized anatase $TiO_2$ are primarily determined by its physicochemical properties such as crystalline structure, particle size, surface area, porosity and thermal stability. The aim of this paper is to investigate the variations in structure of anatase nanopowders, synthesized by sol-gel method, induced by doping with lanthanum. Structural properties, such as: existence of mixed phases (anatase in combination with considerable amount of rutile or brookite phase), particle size and particle size distribution, as well as value and type of the strain (compressed or tensile) determined by the Raman spectroscopy are correlated to the content of La-dopant.

## 2. Experimental details

$TiCl_4$ was used as the precursor in the synthesis process. The $Ti(OH)_4$ hydrogel was obtained by hydrolysis of $TiCl_4$ at 0°C with controlled addition of 2.5 wt.% aqueous ammonia into the aqueous solution of $TiCl_4$ (0.3 mol/l) and careful control of the pH value of the solution (9.3). $TiCl_4$ is soluble in water but it experiences rigorous reaction at 20°C which can be very important to perform this reaction at lower temperature. After aging in the mother liquor for 5 h, the as-prepared hydrogel was filtered and washed out with deionized water until complete removal of chlorine ions. The obtained $Ti(OH)_4$ hydrogel was converted to its ethanol-gel by repeated exchange with anhydrous ethanol for several times (by repeated introduction of anhydrous ethanol). The obtained alcogel represents the starting point for production of $TiO_2$ nanoparticles. Alcogel was placed in a vessel, dried at 280°C and calcined at temperature of 550°C, after which it was converted to the nanoparticles. In the case of La-doped $TiO_2$, $LaCl_3{\cdot}7H_2O$ was used. All chemicals used in this experiment were analytical grades (Merck Chemicals) and were used as received.

Powder X-ray diffraction (XRD) was used for the identification of crystalline phases, quantitative phase analysis and estimation of crystallite size and strain. The XRD patterns were collected on a Philips diffractometer (PW1710) employing Cu $K_{\alpha_{1,2}}$ radiation. Step scanning was performed with $2\theta$ ranging from 10 to 135°, step size of 0.06° and the fixed counting time of 41 s/step. The XRD patterns were used to refine crystallographic structure and microstructural parameters using the procedure explained elsewhere [5, 6]. The Fullprof computer program was used [5].

---

[*] corresponding author; e-mail: maja@phy.bg.ac.yu

The Raman measurements were performed at room temperature using the Jobin-Yvon T64000 triple spectrometer system, equipped with confocal microscope and a nitrogen-cooled CCD detector. The 514 nm laser line of an $Ar^+$ laser was used as an excitation source.

## 3. Results and discussion

Relevant and the most intensive diffraction peaks in the XRD patterns of all samples belong to anatase crystal structure of $TiO_2$ (JCPDS card 78-2486). The patterns of pure $TiO_2$ sample and $TiO_2$ doped with 1 wt.% of La, together with the corresponding unit cell parameters of anatase (the values in parenthesis represent estimated standard deviations), are presented in Fig. 1. These results show that value of the parameter $a$ in both samples varies around its reference value ($a_0 = 3.78479(3)$ Å). However, the value of the $c$ parameter is smaller than the reference one ($c_0 = 9.51237(12)$ Å), especially in La-doped sample. Decrease in $c$ parameter value with La doping could be a consequence of the lattice contraction induced by doping. The presence of low-intensity diffraction peak at $2\theta \approx 30.8°$ that can be ascribed to the brookite phase of $TiO_2$ is observed in all XRD patterns (JCPDS card 29-1360).

Structure refinements were performed by the Rietveld method. Low values of agreement factors between the model, both for structure and microstructure, and XRD data indicate high accuracy of obtained results. The obtained average crystallite size and average strain in anatase and brookite phase, as well as quantitative phase analysis results (brookite content), were summarized in Table. These results showed that doping with 1 wt.% of La induced crystallite size decrease, whereas strain value and brookite content increased. The large values of the average strain in brookite crystallites indicate that this phase is highly disordered both in pure and La-doped samples.

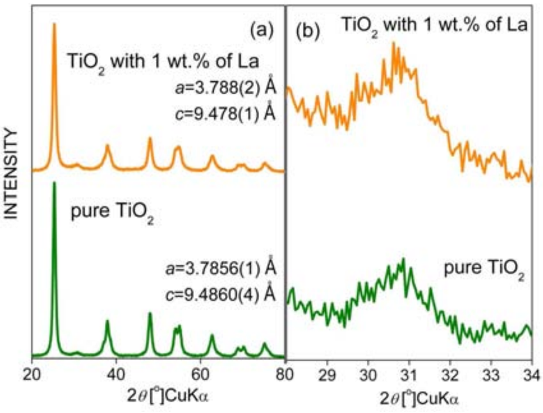

Fig. 1. (a) XRD diffractograms of pure and La-doped $TiO_2$ samples XRD diffractograms. (b) Enlarged diffraction peak ascribed to brookite phase.

TABLE

The results of the Rietveld analyses (average crystallite size and average strain in anatase and brookite phase) and content of brookite phase for pure $TiO_2$ and $TiO_2$ doped with 1 wt.% of La.

| Samples | Anatase crystallite size [nm] | Average strain in anatase | Brookite content [%] | Brookite crystallite size [nm] | Average strain in brookite |
|---|---|---|---|---|---|
| Pure $TiO_2$ | 12 | $4.2 \times 10^{-3}$ | 16 | 35 | $19.6 \times 10^{-3}$ |
| La-doped $TiO_2$ | 10 | $5.7 \times 10^{-3}$ | 24 | 26 | $22.0 \times 10^{-3}$ |

The Raman spectra of pure and La-doped $TiO_2$ samples produced by sol-gel method were measured at room temperature. Some of these spectra are shown in Fig. 2a. In the spectra of all $TiO_2$ samples the dominant Raman modes can be assigned to the Raman active modes of the anatase crystal [7]: ≈ 143 $cm^{-1}$ ($E_{g(1)}$), 197 $cm^{-1}$ ($E_{g(2)}$), 399 $cm^{-1}$ ($B_{1g(1)}$), 540 $cm^{-1}$ (combination of $A_{1g}$ and $B_{1g(2)}$ that cannot be resolved at room temperature) and 639 $cm^{-1}$ ($E_{g(3)}$). The position of $E_{g(1)}$ Raman mode for different $TiO_2$ samples ranges between 143 and 144 $cm^{-1}$, while its linewidth varies from 12.1 to 13.7 $cm^{-1}$, as can be seen in Fig. 3b.

Several factors such as phonon confinement [8–12], strain [8, 13], non-homogeneity of the particle size distribution [8, 9, 13], defects and nonstoichiometry [8, 14], as well as anharmonic effects [9, 15] can contribute to the changes in the peak position, linewidth and shape of the $E_{g(1)}$ Raman mode in anatase $TiO_2$ nanopowders. However, the separation between these various contributions is not straightforward [16]. Dominance of one or more of these factors, observable in the Raman spectra, is determined by the structural characteristics of a $TiO_2$ nanopowder: grain size and grain size distribution, existence of mixed phases (anatase in combination with considerable amount of rutile or brookite phase), value and

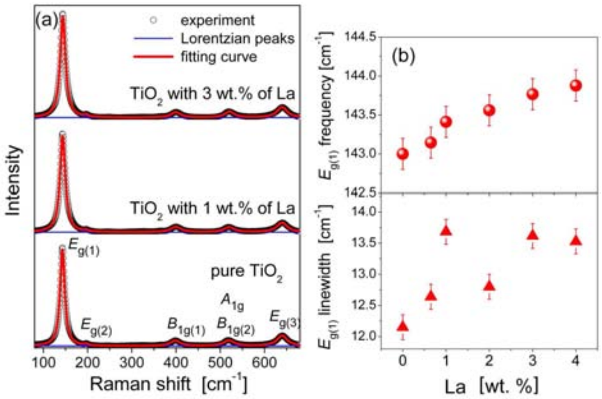

Fig. 2. (a) Raman spectra of pure and La-doped $TiO_2$ samples. (b) Frequency and linewidth of $E_{g(1)}$ Raman mode for $TiO_2$ with 0 to 4 wt.% of La. The error bars correspond to experimental error.

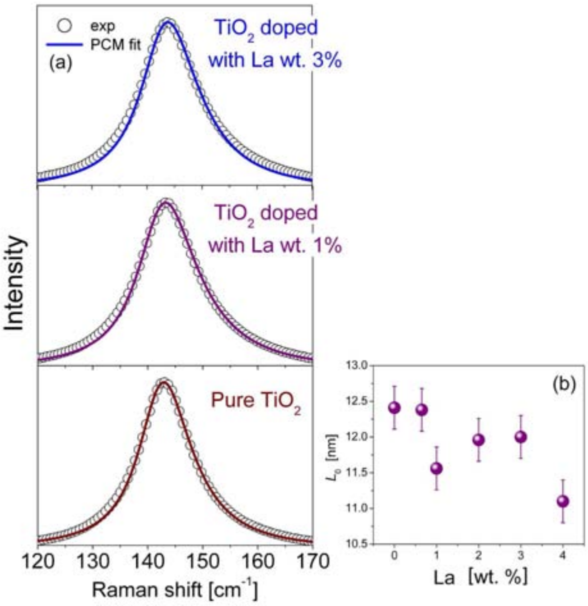

Fig. 3. (a) PCM fits of anatase $E_{g(1)}$ Raman mode for pure and La-doped samples. (b) Average particle dimensions for $TiO_2$ with 0 to 4 wt.% of La, obtained from PCM. The error bars correspond to the estimated statistical errors.

type of the strain (compressed or tensile), discrepancy from stoichiometry as well as type of defects, etc. [8]. The main factors that influence the behavior of $E_{g(1)}$ mode in our samples synthesized by sol-gel method should be the grain size and the grain size distribution, as well as the disorder induced by existence of considerable amount of brookite phase in combination with anatase and by introducing of $La^{3+}$ ions into the $TiO_2$ lattice.

The intensities of $E_{g(1)}$ mode for different samples calculated by phonon confinement model (PCM), described in detail in our previous papers [9, 17], coincide well with the experimental spectra, as can be seen from Fig. 3a. Average sizes of anatase nanoparticles for different $TiO_2$ samples obtained from PCM (Fig. 3b) vary from 11 to 12.4 nm and coincide well with the values obtained by XRD analyses shown in Table.

The results of the investigation of brookite phase presence by Raman spectroscopy are shown in Fig. 4. The additional Raman modes at about 243, 294, 323 and 362 $cm^{-1}$ (shown in Fig. 4a), can be ascribed to the brookite phase of titania [17–19]. Low intensities and large widths of these modes indicate great disorder and partial amorphization of brookite in all the samples. To estimate the amount of brookite phase, the sum of the integrated intensities of Lorentzian peaks originating from the brookite modes was compared to the intensity of Lorentzian peak related to the $B_{1g}$ mode of anatase phase. The intensity ratio of brookite modes to anatase one $(I_{B(\Sigma)}/I_{A(B1g)})$ is shown in Fig. 4a. Although these results are mainly qualitative, they confirm the results obtained by XRD analyses. It can be seen from Fig. 4b that brookite content for sample doped with 1 wt.% of La estimated from the Raman spectra are higher than the content in the pure $TiO_2$ sample. The amount of brookite phase for the samples with the other values of La wt.% is similar to the value in pure $TiO_2$.

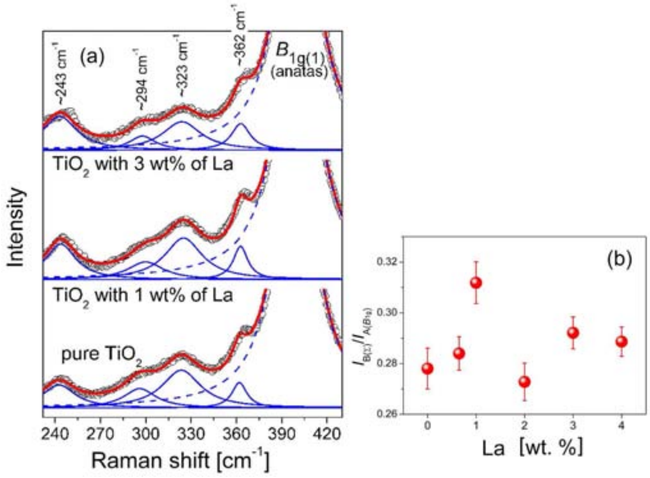

Fig. 4. (a) Lorentzian fits of brookite modes in the experimental Raman spectra. (b) The ratio of the total brookite modes intensity and the anatase $B_{1g}$ Raman mode intensity for $TiO_2$ with 0 to 4 wt.% of La. The error bars correspond to the errors obtained by fit analysis.

It is well known that the phase transition from anatase to rutile occurs at ≈ 600°C. In order to investigate the influence of La doping on phase stability of nanostructured $TiO_2$, pure $TiO_2$ and $TiO_2$ doped with 3 wt.% of La were treated at high temperatures up to 800°C. The Raman spectra of these samples, before and after thermal treatment, are shown in Fig. 5. It could be observed that the heating of pure $TiO_2$ to 800°C causes redshift and narrowing of anatase $E_g$ Raman mode which im-

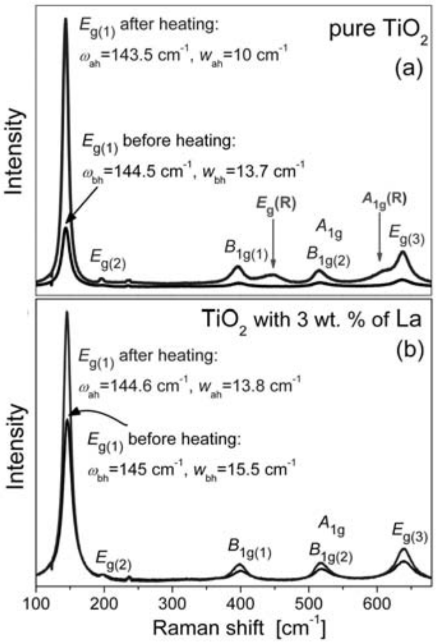

Fig. 5. Raman spectra of pure $TiO_2$ and $TiO_2$ doped with 3 wt.% of La at room temperature before and after heating to 800°C. $\omega$ is the mode frequency and $w$ is the linewidth of $E_{g(1)}$ Raman mode before (bh) and after (ah) heating. $R$ denotes rutile modes.

plies anatase crystallite growth. Also, the appearance of the new Raman modes assigned to rutile phase was registered. After the same heating treatment of the La-doped sample neither such drastic changes of $E_g$ Raman mode nor the appearance of peaks in the spectrum, belonging to rutile phase, were registered. This allowed us to conclude that La doping stabilized $TiO_2$ nanostructure at high temperatures and shifted the temperature of anatase–rutile phase transition to values higher than 800°C.

## 4. Conclusion

A detailed Raman study of sol-gel synthesized anatase $TiO_2$ nanopowders doped with lanthanum ions ($La^{3+}$) in the range from 0 to 4 wt.% was presented in this paper. It was demonstrated that the frequency shift and broadening of the most intensive anatase $E_{g(1)}$ Raman mode are the consequences of both confinement effect due to the nanosize dimensions of anatase crystallites and the disorder induced by the presence of brookite phase and La dopant in the samples. This enables not only basic phase identification but also the estimation of the nanoparticles size and brookite contents in $TiO_2$ nanopowders with different La content.

This study allows us to investigate the structural variations of nanosized $TiO_2$ arisen from the change in doping conditions and it confirms that doping of $TiO_2$ by $La^{3+}$ ions significantly improves phase and nanostructure stability of $TiO_2$ powders at high temperatures.

## Acknowledgments

Authors express their thanks to Mirjana Grujić-Brojčin for the original software solutions which enabled application of PCM for numerical simulation of the Raman spectra of the investigated samples. This work is supported by the Serbian Ministry of Science under project No. 141047, the OPSA-026283 project within the AC FP6 programme and SASA project F-134.

## References

[1] S. Sakka, *J. Sol-Gel Sci. Technol.* **37**, 135 (2006).

[2] J.N. Hart, D. Menzies, Y.-B. Cheng, G.P. Simon, L. Spiccia, *J. Sol-Gel Sci. Technol.* **40**, 45 (2006).

[3] D. Kim, A. Rothschild, D.-J. Yang, H.L. Tuller, *Sensor Actuat. B-Chem.* **130**, 9 (2008).

[4] C.G. Granqvist, A. Azens, J. Isidorsson, M. Kharrazi, L. Kullman, T. Lindström, G.A. Niklasson, C.-G. Ribbing, D. Rönnow, M. Strømme Mattsson, M. Veszelei, *J. Non-Cryst. Solids* **218**, 273 (1997).

[5] J. Rodriguez-Carvajal, 1998, FullProf computer program; `ftp://charybde.saclay.cea.fr/pub/divers/fullprof.98/windows/winfp98.zip` .

[6] A. Kremenovic, J. Blanusa, B. Antic, Ph. Colomban, V. Kahlenberg, C. Jovalekic, J. Dukic, *Nanotechnology* **18**, 145616 (2007).

[7] T. Ohsaka, F. Izumi, Y. Fujiki, *J. Raman Spectrosc.* **7**, 321 (1978).

[8] M.J. Šćepanović, M.U. Grujić-Brojčin, Z.D. Dohčević-Mitrović, Z.V. Popović, *Mater. Sci. Forum* **518**, 101 (2006).

[9] M.J. Šćepanović, M. Grujić-Brojčin, Z. Dohčević-Mitrović, Z.V. Popović, *Appl. Phys. A* **86**, 365 (2007).

[10] D. Bersani, P.P. Lottici, *Appl. Phys. Lett.* **72**, 73 (1998).

[11] H. Richter, Z.P. Wang, L. Ley, *Solid State Commun.* **39**, 625 (1981).

[12] I.H. Campbell, P.M. Fauchet, *Solid State Commun.* **58**, 739 (1984).

[13] J.E. Spanier, R.D. Robinson, F. Zhang, S.W. Chan, I.P. Herman, *Phys. Rev. B* **64**, 245407 (2001).

[14] J.C. Parker, R.W. Siegel, *Appl. Phys. Lett.* **57**, 943 (1990).

[15] K.R. Zhu, M.S. Zhang, Q. Chen, Z. Yin, *Phys. Lett. A* **340**, 220 (2005).

[16] G. Gouadec, P. Colomban, *Prog. Cryst. Growth Charact. Mater.* **53**, 56 (2007).

[17] A. Golubović, M. Šćepanović, A. Kremenović, S. Aškrabić, V. Berec, Z. Dohčević-Mitrović, Z.V. Popović, *J. Sol-Gel Sci. Technol.* **49**, 311 (2009).

[18] Y. Djaoued, R. Brüning, D. Bersani, P.P. Lottici, S. Badilescu, *Mater. Lett.* **58**, 2618 (2004).

[19] S. Yin, K. Ihara, B. Liu, Y. Wang, R. Li, T. Sato, *Phys. Scr. T* **129**, 268 (2007).